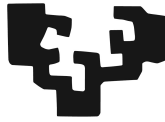eman ta zabal zazu

Universidad del País Vasco   **Euskal Herriko Unibertsitatea**

Ab-Initio Theoretical Study of Electronic Excitations and Optical Properties in Nanostructures

Federico Marchesin
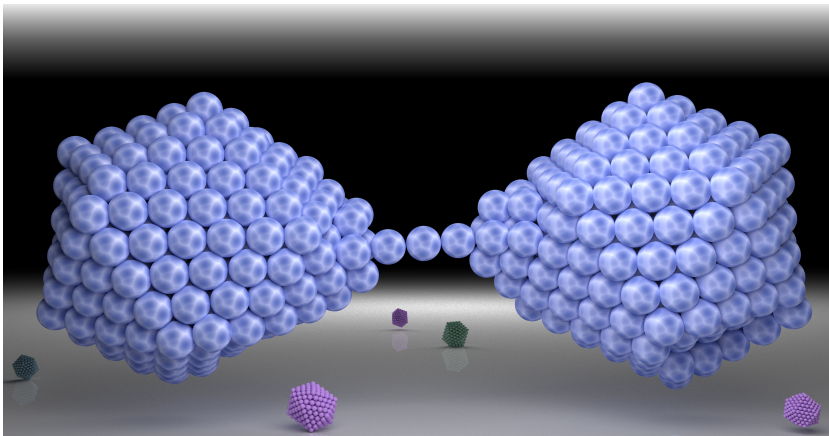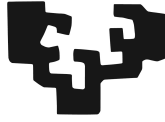
Donostia - San Sebastian 2017

eman ta zabal zazu

Universidad del País Vasco **Euskal Herriko Unibertsitatea**

Ab-Initio Theoretical Study of Electronic Excitations and Optical Properties in Nanostructures

Federico Marchesin

Supervisors:

Dr. Daniel Sánchez-Portal
Dr. Peter Koval

Donostia - San Sebastian 2017

CONTENTS

ABBREVIATIONS

Δ**SCF** Self-Consistent Field. 16, 17, 43, 186

AC ArmChair. 3, 55, 61, 65–67, 69–74, 76, 77, 79, 87, 90, 91, 95–98, 100, 140, 161, 162, 215

ALDA Adiabatic Local Density Approximation. 26, 104, 115

BDP Bonding Dipolar Plasmon. 107, 108, 120, 121, 123, 126, 127, 131, 138, 163

BO Born-Oppenheimer. 6, 7, 9

BS Bethe-Salpeter. 43

BSE Bethe-Salpeter Equation. 3, 40

BZ Brillouin Zone. 52, 53, 76, 77

CA Ceperley-Alder. 104, 113

CCD Cambridge Cluster Database. 112

CRF Coulombic Restoring Force. 158, 159

CTP Charge Transfer Plasmon. 108, 111, 120, 122, 123, 126, 127, 130, 131, 133, 136–139, 163, 164

CTP' high-energy Charge Transfer Plasmon. 120, 123, 126, 127, 131, 163, 164

CVD Chemical Vapour Deposition. 51, 54

DC Direct Current. 133

DFT Density Functional Theory. 2–5, 8, 15–17, 20, 27, 40–42, 52, 55–57, 60, 74, 76, 77, 90, 95, 104, 112–114, 116, 161, 162, 164, 176

DOS Density Of States. 95

DZ Double-ζ. 42, 59

DZP Double-ζ Polarized. 42, 57–61, 90, 104, 112, 144

E$_\text{F}$ Fermi Energy. 52, 53

e-h electron - hole. 38, 39, 101, 142, 146, 153, 156, 158–160, 164, 184

FFT Fast Fourier Transform. 35, 156

GGA Generalized Gradient Approximation. 26, 27, 48, 49, 112–114

GMRES Generalized Minimal RESidue. 3, 47

GPL General Public Licence. 2, 41

GWA GW Approximation. 3, 40, 43

HEX HEXagonal. 55

HK Hohenberg-Kohn. 2, 3, 8, 9, 12

HOMO Highest Occupied Molecular Orbital. 16, 17, 57, 58, 73, 77, 95–97, 150, 153, 156, 162

HWHM Half-Width at Half-Maximum. 24

JM Jellium Model. 107, 108, 111

KS Khon-Sham. 4, 13–17, 20, 24, 25, 27, 30, 33, 34, 48, 60, 64, 73, 75, 76, 90, 91, 96, 100, 101, 142, 146–151, 153, 156, 160, 162, 164

LCAO Linear Combination Atomic Orbitals. 42, 43, 64

LDA Local Density Approximation. 26, 27, 62, 90, 104, 107, 113–115

LR Linear. 161

LUMO Lowest Unoccupied Molecular Orbital. 16, 17, 57, 58, 73, 96, 150, 153, 162

MBPT-LCAO Many Body Perturbation Theory - Linear Combination Atomic Orbitals. 3, 4, 40, 41, 43, 44, 49, 56, 90, 104, 107, 161, 178

NGS Nominal Gap Size. 114–118, 120, 122, 125, 131, 134–136, 163, 164

NR N-representable. 10, 11

PAH Polycyclic Aromatic Hydrocarbon. 3, 88–91, 95, 96, 98, 100, 101, 162

PAO Pseudo-Atomic Orbitals. 42, 186

PBE Perdew-Burke-Erzenhorf. 27, 112, 113

Acknowledgement

During the years of my PhD I had the pleasure and the luck to work under the supervision of Dr. Daniel Sánchez-Portal and Dr. Peter Koval. They always supported me, guiding me over the whole period of the doctorate but at the same time giving me the chance to make my own decisions about my work. Moreover, they have always been glad to answer any question I came up with and clarifying any doubt I had. In particular at the beginning of my PhD Peter was a great help as he was following my work on daily basis.

In addition, I would like to thank Prof. Mark E. Casida who was willing to welcome me for three months in his team at the University of Grenoble, France. It has been a pleasure to work with him and an important working experience. Moreover, I have to thank his postdoc and my friend Dr. Hamanaden Mineni who helped me with my work during that period.

I would also like to thank Prof. Javier Aizpurua, as a result of our fruitful collaboration we managed to publish a paper, and it has been a pleasure to work with him.

I have to thank Javier and all the other organizers of the CFM-DIPC sagardotegi event taking place every year during spring, oh I will miss that. It was a moment in which one could get to know the CFM-DIPC people in a more relaxed environment and have the possibility to socialise with them.

A particular thanks goes to all the friends that made may stay in Donosti and in the CFM-DIPC really special. I would like to thank my friends Alvise Verso, Giuseppe Foti and Mikolai Smidth. It has been a pleasure to share with them my experience. I have made many friends during these years, too many to be mentioned here, a special thanks goes to all of them.

I have to thank the Centro de Fśica de Materiales (CFM-MPC) and the Donostia International Physics Center (DIPC) for the financial support they provided me.

Finally, I would also like to thank my girlfriend and my family for being always present in my daily life.

INTRODUCTION

Ab initio[(1)] theories can be used to study a broad variety of systems by changing a set of system-dependent parameters, without reconsidering the internal working methodology of the theory. In the scope of *ab initio* approaches for material modelling the Density Functional Theory (DFT) and its Time-Dependent (TD) extension (TDDFT), have attracted much attention, due to its favorable computational complexity scaling with the system size.[1] Both *ab initio* theories, DFT and TDDFT, have rapidly become popular along with the increasing computational capability of computers.[(2)] Furthermore, nowadays, it is possible to manufacture relatively small nanodevices containing only several tens or hundreds of atoms such as nanoflakes, nanodots,[2] nanoparticles,[3] nanoantennas,[4,5] which can be tackled computationally by means of *atomistic*, *ab initio* approaches.[6–11] This overlap of theory and experiment increases the importance of computer simulations and makes the theoretical material modelling essential in computer-aided material design.[12] DFT is employed to obtain information about the *ground state properties* – such as system total energy or equilibrium geometry – for finite or periodic systems. TDDFT describes the behaviour of a system influenced by a TD potential. Thus, it is used to calculate properties such as excitation energies, photoabsorption spectra, induced density, and other time-dependent properties.

In principle, DFT uses the electronic density as the central quantity to study the electronic properties of all systems.[1] This basic idea behind the DFT approach was first introduced independently by Llewellyn Thomas[13] and Enrico Fermi[14] in 1927. In their semi-classical approach, a statistical model is used to approximate the electron distribution where the total energy is presented as a functional of the electron density alone. But only after the advent of the Hohenberg-Kohn (HK) theorems, which prove the one-to-one correspondence between the electron density and the potential that generated it, the DFT was recognized as an *ab initio* theory. Since then, DFT has attracted the interest of the scientific community increasing the efforts to advance the theory that led to the development of dozens of DFT codes, now available in the market. The SIESTA (Spanish Initiative for Electronic Simulations with Thousands of Atoms)[6,7] code is a GPL (General Public Licence) DFT package and it is the code-of-choice used throughout the thesis to perform ground-state calculations.

TDDFT is the extension of DFT to study systems whose Hamiltonian includes time-

---

[(1)]From the latin ab[from] + initium[beginning], from the beginning.

[(2)]The growth in computer power has followed for years the so-called *Moore's law*, which states that the number of transistors in an integrated circuit doubles roughly every two years.

dependent potentials. The Runge-Gross theorems[15](3) are the time-dependent equivalent of the HK theorems and provide a solid ground for the use of the theory. In the linear response regime, when the time-dependent part of the Hamiltonian can be treated perturbatively, TDDFT can be formulated via the *density response function formalism*. The density response function obeys a Dyson-like equation derived by the Petersilka, Gossmann and Gross.[16] This equation is used in our TDDFT package MBPT-LCAO (Many Body Perturbation Theory with Linear Combination of Atomic Orbitals)[17–19] to compute the optical response. MBPT-LCAO makes use of an optimal basis[17,20] to compute the response function and a clever iterative procedure involving the use of a Generalized Minimal RESidue (GMRES)[17,20] method to calculate the observables (absorption spectrum, structure factor, induced fields, energy loss probability) of finite and periodic systems. MBPT-LCAO is a composite code consisting of a block that allows computing the quasiparticle self-energy within the GW Approximation (GWA),[21] a block to solve the Bethe-Salpeter Equation (BSE),[22] and a block to perform TDDFT simulations.[17–19] In particular, MBPT-LCAO is used in tandem with SIESTA – initial DFT calculations provide the information to be used as input in the following TDDFT calculations. In this thesis we present the results obtained with the TDDFT block on a variety of finite systems (organic molecules, metallic clusters, graphene flakes ...) and the work done on the development of the code.

In Chapters 3, 4, 5, 6 the results obtained for the different systems under investigation are presented. In addition, the most important DFT and TDDFT theoretical aspects and a thorough overview of the codes employed are included in Chapters 1 and 2, respectively.

In particular, in Chapter 3 a review of the absorption properties of graphene nanoflakes is presented. Graphene is a relatively novel material first isolated in 2004[23,24] and since then, graphene and its derivatives such as nanoribbons and nanodots have been intensively investigated because of many of their promising properties.[25] In this thesis we consider graphene nanodots of different shapes, and sizes and study their optical properties. Specifically, we show that the edge type – ArmChair (AC) versus ZigZag (ZZ) – and the edge functionalization play a fundamental role in determining the low-energy features of the spectra.

In Chapter 4 we study Polycyclic Aromatic Hydrocarbons (PAHs). The vast number of different shapes and sizes opens the way to a high degree of tunability in terms of optical properties. PAHs can be viewed as small graphene flakes. In particular, we show that the optical response of triangular shaped AC PAHs is very sensitive to charge doping as opposed to triangular ZZ PAHs, which are found to be relatively insensitive to doping. The analysis of the DFT orbital energies allows to clarify the origin of such insensitivity to doping. The origin of this behavior turns out to be the presence of edge states in the ZZ PAHs, in fact, ZZ edges create degenerate molecular levels at the Fermi energy.

In Chapter 5 we consider two metallic nanoclusters that form a plasmonic cavity. Each icosahedral nanocluster contains 380 sodium atoms. The optical properties are studied for different plasmonic cavity sizes and for different cluster orientations. Moreover, we study the effects of geometry relaxation while approaching and eventually retracting the two clusters. We report the jump-to-contact instability while approaching the clusters and the formation of atom-sized metal contacts while retracting them. We established the following relation: plastic nanocontact deformation → metal contact cross-section

---

(3)These theorems prove the existence of an invertible relation between the electron density and the time-dependent potential up to an additive time-dependent function

reduction → abrupt drop of the quantized contact current → decrease of the intensity of the corresponding plasmonic mode, highlighting the effects of atomic-scale details on the optical properties of such system. Moreover, we show that structural rearrangements – for systems of nanometer-scale dimensions like those considered here – involving very few atoms or even a single atom are reflected in the far-field optical spectrum of the system.

In Chapter 6 we tackle the problem of the definition and identification of collective excitations in molecules (plasmons). *Molecular plasmons* have been discussed in the literature,[26–31] however, their definition and identification remains less clear than the plasmonic excitations in 3D periodic systems. Very often, resonances found in the interacting cross-section spectrum that are missing in the non-interacting spectrum are labelled as plasmons, since the plasmonic character, given by a collective electron behaviour, is considered to be taken into account in the interacting absorption spectrum. In the chapter we try to find a practical operative definition for molecular plasmons. Our method includes the analysis in momentum domain of the transition density matrix.[32,33] We show that the analysis based on the character of the non-interacting Kohn-Sham (KS) transition density matrix is not appropriate for studying the resonant plasmonic character. For this study the Casida's approach is used to obtain the optical cross section, the method allows to get information about the precise resonance energies and eigenvectors.

Finally, in the conclusions chapter the topics addressed and the most relevant results obtained in this thesis will be summarized.

I would like to underline that the work that I have done, necessary for completing this doctoral thesis, combining two important aspects involved in scientific computer simulations: test and development. On the one side, I have worked as a user on some ab initio codes, mainly the DFT SIESTA code and the TDDFT MBPT-LCAO code. On the other side, I have implemented new features in the MBPT-LCAO source code.

1 | Theory

1.1 Density Functional Theory

Density Functional Theory (DFT) is a fundamental ab-initio quantum-mechanical theory widely used in physics and chemistry for analyzing electronic ground-state properties of multi-electron systems. DFT can be regarded as a dramatic simplification of a wave-function based formalism.[1] The non-relativistic wave-function formalism is based on the Schrödinger equation. DFT uses the *electron density* as the fundamental quantity rather than the electronic wave-function, and this fact greatly facilitates the solution of many-electron problems. In fact, while the wave-function formalism deals with $3N$ variables, with N being the total number of electrons, the DFT approach allows to describe the interacting electrons by means of a 3-dimensional quantity.[1] In this section, for the sake of didactic clarity, we are going to start by discussing the Schrödinger equation for many-body systems.

1.1.1 Schrödinger Equation

A great variety of physical phenomena in the microscopic world can be well understood using the Schrödinger formalism.

All the properties of the electronic structure in matter are governed by the time-dependent Schrödinger equation. For time-independent interactions, the Schrödinger equation can be written as

$$\hat{H}\tilde{\Psi} = E_{tot}\tilde{\Psi} \tag{1.1}$$

where E_{tot} and $\tilde{\Psi} = \tilde{\Psi}(\mathbf{r}_1, \mathbf{r}_2, \ldots, \mathbf{r}_N; \mathbf{R}_1, \mathbf{R}_2, \ldots, \mathbf{R}_M)$ are the total energy of the system and the many-body wavefunction containing information about the N-electrons and the M-nuclei of the system. $\hat{H}$ is the Hamiltonian operator given by

$$\hat{H} = \hat{T}_e + \hat{T}_n - \hat{V}_{en} + \hat{V}_{nn} + \hat{V}_{ee} \ , \tag{1.2}$$

$$\hat{T}_e = -\frac{\hbar^2}{2} \sum_i^N \frac{\nabla_i^2}{m_i} \ \hat{T}_n = -\frac{\hbar^2}{2} \sum_I^M \frac{\nabla_I^2}{m_I} \tag{1.3}$$

$$\hat{V}_{ne} = \sum_i^N \sum_I^M \frac{Z_I e}{|\mathbf{r}_i - \mathbf{R}_I|} \ \hat{V}_{nn} = \sum_{I<J}^M \frac{Z_I Z_J e^2}{|\mathbf{R}_I - \mathbf{R}_J|} \tag{1.4}$$

$$\hat{V}_{ee} = \sum_{i<j}^N \frac{e^2}{|\mathbf{r}_i - \mathbf{r}_j|} \ . \tag{1.5}$$

Here Z_I is the number of protons in the nucleus I, $\mathbf{R}_I$ is the position of the Ith-nucleus and $\mathbf{r}_i$ is the position of the ith-electron. m_i and m_I are the masses of the ith-electron and of the Ith-nucleus. The first two quantities on the right side of equation 1.2 represent the kinetic energy of electrons and nuclei respectively. The potential $\hat{V}_{en}$ represents the electron-nucleus interaction, $\hat{V}_{nn}$ the nucleus-nucleus interaction and $\hat{V}_{ee}$ is the electron-electron interaction. In the equation above and for the rest of the thesis the atomic units will be used, i.e. $m_e = \hbar = e = 1$ and $\epsilon_0 = 1/4\pi$.

1.1.2 Born-Oppenheimer Approximation

In order to solve the Equation 1.2, we use the Born-Oppenheimer (BO) approximation,[34] which consists in considering electrons as moving in a fixed background of positively charged nuclei. This approximation is based on the fact that nuclei are at least three order of magnitude heavier than electrons, $m_I > 1800 m_i$. Thus, within the BO approximation the total wavefunction can be factorized into an electronic and a nuclear part,

$$\tilde{\Psi}(\mathbf{r}, \mathbf{R}) = \Psi_{\mathbf{R}}(\mathbf{r})\chi(\mathbf{R}) \ , \tag{1.6}$$

$$\hat{H}_r \Psi_{\mathbf{R}}(\mathbf{r}) = E_{\mathbf{R}} \Psi_{\mathbf{R}}(\mathbf{r}) \ , \tag{1.7}$$

$$\hat{H}_{\vec{R}} \chi(\mathbf{R}) = E_{tot} \chi(\mathbf{R}) \ , \tag{1.8}$$

with

$$\hat{H}_{\vec{R}} = \hat{T}_n + V_{nn} + E_{\mathbf{R}} \ \hat{H}_r = \hat{T}_e + \hat{V}_{ee} + \hat{V}_{ne}. \tag{1.9}$$

In additions, above we used the abbreviations $\mathbf{r} = \{\mathbf{r}_i\}$ and $\mathbf{R} = \{\mathbf{R}_i\}$. Note that all the terms that couple the electron and nucleus dynamics have been dropped in Equations 1.7 and 1.8. The function $\Psi_{\mathbf{R}}(\mathbf{r})$ is the electronic part of the total wavefunction which contains parametrically the nuclei positions $\mathbf{R}$, while $\chi(\mathbf{R})$ is the nuclear wavefunction. Once we separate the total wavefunction, we can solve the electronic part assuming the electron to move in the potential created by the positive nuclei at fixed positions and eventually calculate the nuclear wavefunction $\chi(\mathbf{R})$. The nuclear wavefunction $\chi(\mathbf{R})$ accounts for rotational and vibrational motion of the nuclei. The BO approximation has some limitations,

although is valid for most systems of interest, it is not suitable when the electronic potential energy surface of the ground and excited states are very close, i.e. whenever the $E_{n,\mathbf{R}}$ calculated for all $\mathbf{R}$ are not well separated. If we insert the BO approximation given by Equations 1.6, 1.7 and 1.8 in Equation 1.1 we get

$$
\begin{aligned}
\left[T_n + V_{nn} + \hat{H}_r\right]\Psi_{\mathbf{R}}(\mathbf{r})\chi(\mathbf{R}) = {} & \Psi_{\mathbf{R}}(\mathbf{r})\left[-\frac{1}{2}\nabla_I^2 + V_{nn} + E_{\mathbf{R}}\right]\chi(\mathbf{R}) \\
& -\frac{1}{2}\left[\nabla_I^2\Psi_{\mathbf{R}}(\mathbf{r})\right]\chi(\mathbf{R}) - \left[\nabla_I\Psi_{\mathbf{R}}(\mathbf{r})\right]\left[\nabla_I\chi(\mathbf{R})\right].
\end{aligned}
\tag{1.10}
$$

The non-adiabatic correction terms are shown in the last line in 1.10 and they come from the coupling of the electronic and nuclear wavefunctions due to the nuclear kinetic operator. Glancing at the last equation we see that, the BO approximation consists of neglecting the contribution coming from the first-order term $\nabla_I\Psi_{\mathbf{R}}(\mathbf{r})$ and the second-order term $\nabla_I^2\Psi_{\mathbf{R}}(\mathbf{r})$ on the assumption that, due to the difference between the electrons mass and the nuclei mass, the nuclear wavefunction is more localized than the electronic wavefunction, i.e. $\nabla_I\Psi_{\mathbf{R}}(\mathbf{r}) \ll \nabla_I\chi(\mathbf{R})$. If we set to 0 the non-adiabatic contribution coming from the last line of 1.10 we are left with Equation 1.8. In this work we will focus on electronic degrees of freedom, assuming the validity of the BO approximation. The Schrödinger equation for electrons within the BO approximation can be re-written as Equation 1.7

1.1.3 Electron Density

Although the BO approximation helps to separate the total wavefunction into nuclear and electronic wavefunction, the task of solving the Equation 1.7 still remains highly non-trivial since the many-body wavefunction depends on $3N$ variables, with N being the total number of electrons. This multi-dimensional equation is impossible to solve by numerical methods except for a very small number of electrons.[1] However, in many practical calculations, we can avoid using the full N-electron wavefunction, at least in principle, by introducing the density matrix. We can define the first and second order density matrix, respectively as

$$
D_1(\mathbf{r}_1', \mathbf{r}_1) = N \int \Psi^*(\mathbf{r}_1', \mathbf{r}_2, \ldots, \mathbf{r}_N)\Psi(\mathbf{r}_1, \mathbf{r}_2, \ldots, \mathbf{r}_N)\mathrm{d}\mathbf{r}_2\mathrm{d}\mathbf{r}_3\ldots\mathrm{d}\mathbf{r}_N
\tag{1.11}
$$

and

$$
\begin{aligned}
D_2(\mathbf{r}_1', \mathbf{r}_2'; \mathbf{r}_1, \mathbf{r}_2) &= \binom{N}{2} \int \Psi^*(\mathbf{r}_1', \mathbf{r}_2', \mathbf{r}_3, \ldots, \mathbf{r}_N)\Psi(\mathbf{r}_1, \mathbf{r}_2, \mathbf{r}_3, \ldots, \mathbf{r}_N)\mathrm{d}\mathbf{r}_3\mathrm{d}\mathbf{r}_4\ldots\mathrm{d}\mathbf{r}_N \\
&= \frac{N(N-1)}{2} \int \Psi^*(\mathbf{r}_1', \mathbf{r}_2', \mathbf{r}_3, \ldots, \mathbf{r}_N)\Psi(\mathbf{r}_1, \mathbf{r}_2, \mathbf{r}_3, \ldots, \mathbf{r}_N)\mathrm{d}\mathbf{r}_3\mathrm{d}\mathbf{r}_4\ldots\mathrm{d}\mathbf{r}_N.
\end{aligned}
\tag{1.12}
$$

The diagonal part of the first and second order density matrix are used to determine, respectively, the expected values of one- and two- particle operators in the electronic Hamiltonian, Equation 1.9. Consequently, the quantities D_1 and D_2 of reduced dimensionality are sufficient to determine the electronic energy E

$$
E = \langle\Psi|\hat{H}|\Psi\rangle = \mathrm{Tr}(DH).
\tag{1.13}
$$

In this quest of reducing dimensionality, we shall go one step further by using the Hohenberg-Kohn (HK) theorems,[35] which validate the use of the electron density $n(\mathbf{r}) = D(\mathbf{r}, \mathbf{r})$ as the only variable to define the energy of the system. The electron density represents the number of electrons per unit volume in the quantum ground state. The HK theorems, discussed in Section 1.1.4, guarantee the possibility to describe a system of N electrons with a scalar function $n(\mathbf{r})$, which depends only on the 3 Cartesian variables, where we omit the spin variable. The corresponding electron-density operator is defined as $\hat{n} = \sum_i \delta(\mathbf{r} - \mathbf{r}_i)$ and leads to

$$n(\mathbf{r}) = \langle \Psi | \sum_i \delta(\mathbf{r} - \hat{\mathbf{r}}_i) | \Psi \rangle = N \int |\Psi(\mathbf{r}, \mathbf{r}_2, \mathbf{r}_3, \ldots, \mathbf{r}_N)|^2 \mathrm{d}\mathbf{r}_2 \mathrm{d}\mathbf{r}_3 \ldots \mathrm{d}\mathbf{r}_N \ . \quad (1.14)$$

As a matter of fact, electrons are fermions with spin $1/2$ and obey the Pauli exclusion principle.[36] Thus, for a system of N independent electrons, the exact total wavefunction can be written in determinant form

$$\Psi(\mathbf{r}_1, \mathbf{r}_2, \ldots, \mathbf{r}_N) = \frac{1}{\sqrt{N!}} \begin{vmatrix} \psi_1(\mathbf{r}_1) & \psi_2(\mathbf{r}_1) & \ldots & \psi_N(\mathbf{r}_1) \\ \psi_1(\mathbf{r}_2) & \psi_2(\mathbf{r}_2) & \ldots & \psi_N(\mathbf{r}_2) \\ \vdots & \vdots & \ddots & \vdots \\ \psi_1(\mathbf{r}_N) & \psi_2(\mathbf{r}_N) & \ldots & \psi_N(\mathbf{r}_N) \end{vmatrix} = \frac{1}{\sqrt{N!}} |\psi_1, \psi_2, \ldots, \psi_N| \ ,$$

$$(1.15)$$

$\psi_i(\mathbf{r})$ are a set of orthogonal functions representing *single-particle* wavefunctions. The resulting wavefunction $\Psi(\mathbf{r}_1, \mathbf{r}_2, \ldots, \mathbf{r}_N)$ is anti-symmetric with respect to particle permutations. Inserting Eq. 1.15 in Eq. 1.14 we obtain the density operator in terms of orthogonal functions ψ_i

$$n(\mathbf{r}) = 2 \sum_i^{N/2} |\psi_i(\mathbf{r})|^2 \quad (1.16)$$

where the factor 2 has been added added to account for the spin, assuming double occupancy of the one-electron levels. The possibility of using the electron density as the main variable for solving many-electron problems is warranted by the Hohenberg and Kohn theorems,[35] which are discussed in Section 1.1.4, and this possibility is behind the success of modern DFT. DFT became a popular method for studying many-body problems substituting in many applications previous methods such as the Hartree-Fock method.[37]

1.1.4 HOHENBERG-KOHN THEOREMS

The idea of using a 3-dimensional quantity to describe the electron system was first introduced by Llewellyn Thomas[13] and Enrico Fermi,[38,39] who reformulated the Schrödinger equation in terms of the electron density. The proposal of using the electron density as the only quantity for solving many-electron problems was mathematically justified later by the DFT. The DFT is based on two theorems proved by the Hohenberg and Kohn.[35] The HK theorems state that:

1. *The external potential $V_{ext}(\mathbf{r})$ is determined by the electron density $n(\mathbf{r})$ up to a constant.*[35]

2. *If we consider a trial electron density $\tilde{n}(\mathbf{r})$ normalized to the total number of electrons ($\int \tilde{n}(\mathbf{r})\mathrm{d}\mathbf{r} = N$) and such that $\tilde{n}(\mathbf{r}) \geq 0$, then*

$$E_0 \leq E[\tilde{n}(\mathbf{r})] \tag{1.17}$$

where E_0 is the true ground-state energy of the system and $E[\tilde{n}(\mathbf{r})]$ is the energy functional of the trial density.[35]

The first theorem establishes an important relation between the density distribution of electrons $n(\mathbf{r})$ and the external potential $V_{ext}(\mathbf{r})$ exerted to these electrons. In the BO approximation, the external potential $V_{ext}(\mathbf{r})$ is given by the Coulomb nucleus-electron attraction potential $V_{ne}(\mathbf{r})$, see Equation 1.4. To prove this theorem let us consider two external potentials $V(\mathbf{r})$ and $V'(\mathbf{r})$ which differ by more than a constant. We suppose these potentials to give the same ground-state electron density but different Hamiltonians H and H', wavefunctions Φ and Φ' and total energies E and E'. According to the Rayleigh variational principle any trial wavefunction Φ' will have a greater Hamiltonian expectation value $\langle\Phi'|\hat{H}|\Phi'\rangle$ than the ground state energy $\langle\Phi|\hat{H}|\Phi\rangle$, so that

$$\begin{aligned}
E_0 = \langle\Phi|\,H\,|\Phi\rangle &< \langle\Phi'|\,H\,|\Phi'\rangle = \langle\Phi'|\,H'\,|\Phi'\rangle + \langle\Phi'|\,H - H'\,|\Phi'\rangle \\
&= E_0' + \int n(\mathbf{r})(V(\mathbf{r}) - V'(\mathbf{r}))\mathrm{d}\mathbf{r}
\end{aligned} \tag{1.18}$$

where $H = T + V_{ee} + V$ and $H' = T + V_{ee} + V'$. For the ground state energy of H', we can write a similar equality,

$$E_0' < E_0 - \int n(\mathbf{r})(V(\mathbf{r}) - V'(\mathbf{r}))\mathrm{d}\mathbf{r} \ . \tag{1.19}$$

By adding 1.18 and 1.19 we get $E_0 + E_0' < E_0' + E_0$ which is a contradiction. Thus, the initial assumption was wrong, there cannot be two different external potentials giving the same ground-state electron density.

This theorem implies that the total energy E_0 is defined by the density, i.e. it is a functional of the density, so that the expected values of T, V_{ee} and V_{ne} are also functionals of the density. In particular, we define the so-called universal functional F as

$$F[n] = T[n] + V_{ee}[n], \tag{1.20}$$

which is called universal because it does not depend on the particular disposition of the nuclei in the system.

The second theorem is a variational theorem for the Schrödinger equation asserting that that the minimization of energy is given by the true wavefunction where the total energy of a system is $E[\Psi] = F[n] + \int n(\mathbf{r})v(\mathbf{r})\mathrm{d}\mathbf{r}$. From the first HK theorem we already know that the density implicitly defines a unique Hamiltonian and a unique wavefunction Ψ leading to the conclusion that the true electron density minimizes the total energy. The variational principle together with the particle number conservation

$$\int n(\mathbf{r})\mathrm{d}\mathbf{r} = N \ , \tag{1.21}$$

where N is the total number of electrons leads to the stationary condition

$$\delta\left[E[n] - \mu\left(\int n(\mathbf{r})\mathrm{d}\mathbf{r} - N\right)\right] = 0 \ . \tag{1.22}$$

The electron density $n(\mathbf{r})$ minimizes the energy $E[n]$ under the constraint that the density provides the correct number of electrons. The Lagrange multiplier μ represents the chemical potential. Evaluating the variational derivative of Eq. 1.22 with respect to the density we get

$$\frac{\delta\left[E[n] - \mu\left(\int n(\mathbf{r})\mathrm{d}\mathbf{r} - N\right)\right]}{\delta n(\mathbf{r})} = \frac{\delta\left(F[n] + V_{ne}[n]\right)}{\delta n(\mathbf{r})} - \frac{\delta\mu\left(\int n(\mathbf{r})\mathrm{d}\mathbf{r} - N\right)}{\delta n(\mathbf{r})} = 0 \quad (1.23)$$

$$\downarrow$$

$$\frac{\delta F[n]}{\delta n(\mathbf{r})} + V_{ne}(\mathbf{r}) - \mu = 0 \ . \tag{1.24}$$

Thus, the knowledge of the exact universal functional of the density $F[n]$ would lead to the exact ground-state electron density by solving Equation 1.24. However, it is difficult to find an explicit form for $F[n]$. Approximate solutions have to be found in order to turn DFT into a practical tool.

1.1.5 v- and N-Representability

In this section we will enter a bit more in detail and we will clarify the relation between external nucleus-electron potential $V_{ne}[n]$, electron density $n(\mathbf{r})$ and wavefunction $\Psi(\mathbf{r})$. However, it is not essential for the understanding of the rest of thesis, result chapters included.

An electron density is said to be v-representable (VR) if it is associated with an anti-symmetric ground state wavefunction of a Hamiltonian of the form $\hat{H} = \hat{T} + \hat{V}_{ee} + V_{ext}(\mathbf{r})$, determined by some external potential $V_{ext}(\mathbf{r})$. The first Hohenberg-Kohn theorem guarantees the existence of a given electron density $n(\mathbf{r})$ for a given external potential $V_{ext}(\mathbf{r})$, however, it requires the density to be v-representable (VR) because the universal functional of the density $F[n]$ (Eq.1.20) is defined through the ground state wavefunction Ψ. Thus, it depends explicitly on the ground-state wavefunction Ψ which has an associated density. For a VR density the first Hohenberg-Kohn theorem ensures a one-to-one mapping between the ground state wavefunction and the external potential allowing us to determine in principle all the ground state properties of the system. However, as a side remark, we note that not always the density is VR.[40]

Let us now introduce and define the concept of N-representable (NR) density. An NR density can be obtained from some antisymmetric wavefunction that may not be the ground state wavefunction for a system described by a given Hamiltonian. The N-representability condition is weaker than the v-representability condition, thus, easier to fulfill. It is good then that we can extend the first Hohenberg-Kohn theorem to all the NR densities. Density functional theory requires only the density to be NR.[40] The conditions for a density to be

NR are the following,[40]

$$n(\mathbf{r}) \geq 0 \qquad \int n(\mathbf{r})\mathrm{d}\mathbf{r} = N \qquad \int |\nabla n(\mathbf{r})|^2 \mathrm{d}\mathbf{r} < \infty . \qquad (1.25)$$

There are an infinite number of wavefunctions Ψ that provide the same electron density $n(\mathbf{r})$, however, thanks to the Levy formulation[41] we can select a single ground-state wave function by using the minimum-energy principle and showing that the first Hohenberg-Kohn theorem is valid for NR densities. The minimum-energy principle states that

$$\langle \Psi_0 | \hat{T} + \hat{V}_{ee} | \Psi_0 \rangle + \int V_{ne}(\mathbf{r}) n_0(\mathbf{r})\mathrm{d}\mathbf{r} \leq \langle \Psi_{n_0} | \hat{T} + \hat{V}_{ee} | \Psi_{n_0} \rangle + \int V_{ne}(\mathbf{r}) n_0(\mathbf{r})\mathrm{d}\mathbf{r}$$
$$(1.26)$$

where Ψ_0 is the ground-state wavefunction and Ψ_{n_0} is a trial wavefunction generating the ground-state density n_0. The contribution from the external potential describing the nucleus-electron interaction is a functional of the density and it is the same in the two cases. Thus, $\langle \Psi_0 | \hat{T} + \hat{V}_{ee} | \Psi_0 \rangle \leq \langle \Psi_{n_0} | \hat{T} + \hat{V}_{ee} | \Psi_{n_0} \rangle$. $\langle \Psi_0 | \hat{T} + \hat{V}_{ee} | \Psi_0 \rangle$ is the universal functional $F[n_0]$ defined in Equation 1.20. This introduces another constraint on the trial wavefunction Ψ_{n_0}. Namely, the wavefunction Ψ_{n_0} has to provide the ground-state electron density and at the same time minimize the F operator,

$$\langle \Psi_{n_0} | \sum_i \delta(\mathbf{r} - \mathbf{r}_i) | \Psi_{n_0} \rangle = n_0(\mathbf{r}) \qquad (1.27)$$

$$\langle \Psi_0 | \hat{T} + \hat{V}_{ee} | \Psi_0 \rangle = \mathrm{Min} \, \langle \Psi_{n_0} | \hat{T} + \hat{V}_{ee} | \Psi_{n_0} \rangle \qquad (1.28)$$

Equation 1.28 extends the first Hohenberg-Kohn theorem for cases of degeneration in the ground state because with the use of 1.28 we are able to pick out one of the degenerate wavefunctions.

The concept is clear if we re-write the Levy principle as,

$$E_0 = \underset{\Psi}{\mathrm{Min}} \, \langle \Psi | \, (\hat{T} + \hat{V}_{ee} + \hat{V}_{ne}) \, | \Psi \rangle$$
$$= \underset{n}{\mathrm{Min}} \left[\underset{\Psi \to n}{\mathrm{Min}} \, \langle \Psi | \, (\hat{T} + \hat{V}_{ee} + \sum_i^N v(\mathbf{r}_i)) \, | \Psi \rangle \right] \qquad (1.29)$$
$$= \underset{n}{\mathrm{Min}} \left\{ \underset{\Psi \to n}{\mathrm{Min}} \left[\langle \Psi | \, (\hat{T} + \hat{V}_{ee}) \, | \Psi \rangle \right] + \int v(\mathbf{r}) n(\mathbf{r}) \right\}$$

where $v(\mathbf{r}_i) = \sum_I^N \frac{Z_I}{|\mathbf{r}_i - \mathbf{r}_I|}$.

In order to better understand the relation between the ground-state wavefunction, the electron density and the external potential we show below in Fig. 1.1 a visual explanation of the minimization process.[40] Each color represents a different density and each of these colored areas contains all the wavefunctions corresponding the electron density, denoted as $n_1, n_2, ..., n_{13}$ in Fig. 1.1. The minimization $\underset{\Psi \to n}{\mathrm{Min}} \, \langle \Psi | \, (\hat{T} + \hat{V}_{ee}) \, | \Psi \rangle$ selects a set of wavefunctions for each particular density. These particular sets are indicated in Fig. 1.1 by dark dots. A further minimization $\underset{n}{\mathrm{Min}} \{ F[n] + \int v(\mathbf{r}) n(\mathbf{r}) \}$ will select the right density among all the dark dots.
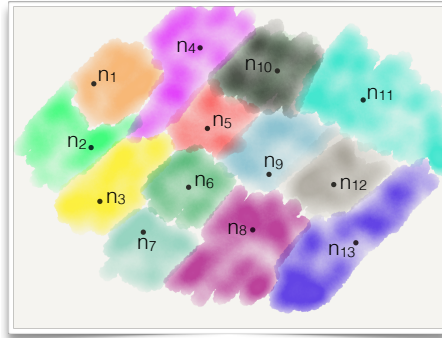
Figure 1.1: Illustration of the Levy principle. Areas with the same color have the same density and represent the collection of wavefunction sets providing this electron density $n_1, n_2, ..., n_{13}$. The minimization process chooses among all these sets of wavefunctions the one that minimizes the universal functional. The system wavefunction is then identified by minimizing the total energy with respect to the density.[40]

In Fig.1.2 the connection between different sets of wavefunctions, the density and the external potential is shown. For an N-representable density it is always possible to connect the density and the external potential, necessary condition for HK theorems to work (section 1.1.4). Moreover, it is also always possible to find a ground state through the minimization-energy principle.[41,42] Thus, a biunivocal relation for the transformation $n \rightarrow V_{ext}$ and $\Psi \rightarrow n$ can be found, as illustrated in Fig. 1.2. HK theorems and Levy theorem guarantee a one-to-one correspondence between the ground-state wave function, the electron density $n(\mathbf{r})$ and the external potential V_{ext}.
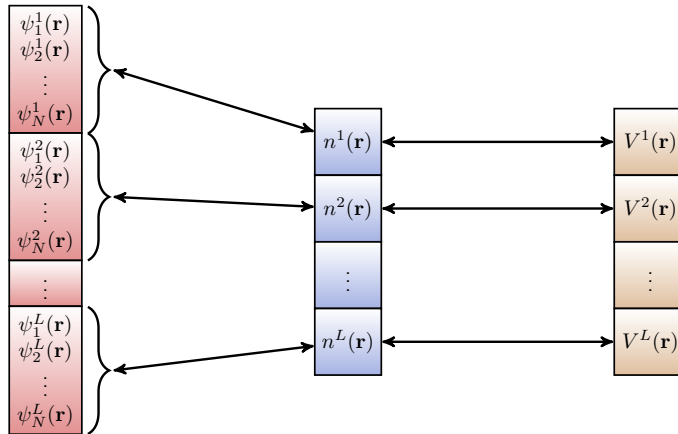
Figure 1.2: A two-stage splitting of different sets of wavefunctions $\psi_i(\mathbf{r})$, the density $n(\mathbf{r})$, and the external potential V_{ext} used in the minimization procedure.

1.1.6 KOHN-SHAM EQUATIONS

The obstacle for solving Equation 1.24 resides in the fact that we do not know the universal functional $F[n]$ exactly. In particular, the kinetic energy functional has proven to be a great challenge.[43] Therefore, it is necessary to work out an approximation that would allow a simple, and yet accurate, description of the kinetic energy. In the Kohn-Sham (KS) approach the system of interacting electrons is mapped onto a system of N non-interacting electrons, both having the same electron density. Other simpler approximations exist, but in general, they are not sufficiently accurate.[44] For an *interacting* electron system the electron density is written as

$$n(\mathbf{r}) = \sum_i^N f_i \sum_\sigma |\psi_i(\mathbf{r}, \sigma)|^2 \ , \tag{1.30}$$

and the kinetic energy, being one-electron operator, reads

$$T = -\frac{1}{2} \sum_i^{\tilde{N}} f_i \langle \psi_i| \nabla^2 |\psi_i \rangle \ . \tag{1.31}$$

Here ψ_i, in this case, are the natural spin orbitals and f_i their occupation numbers. The occupation number is $0 \le f_i \le 1$ due to the Pauli principle. In the KS framework the kinetic energy is approximated with

$$T_s = -\frac{1}{2} \sum_i^N \langle \psi_i| \nabla^2 |\psi_i \rangle \ , \tag{1.32}$$

which represents the kinetic energy for a system of *non-interacting* electrons that is described exactly by a single-determinantal wavefunction

$$\Psi_s = \frac{1}{\sqrt{N!}} |\psi_1, \psi_2, \ldots, \psi_N| \ . \tag{1.33}$$

The associated electron density is

$$n(\mathbf{r}) = \sum_i^N \sum_\sigma |\psi_i(\mathbf{r}, \sigma)|^2 \ . \tag{1.34}$$

This corresponds to Equation 1.30 when we set the coefficients $f_i = 1$ for $0 \le i \le N$ and equal to 0 otherwise. Henceforward, we should call the one-particle orbitals ψ_i the Kohn-Sham orbitals. Within this non-interacting picture the energy functional can be written as a sum of the external nucleus-electron interaction term V_{ne}, the new non-interacting kinetic-energy functional T_s, an electrostatic classical functional term V_H (Hartree energy) and the so-called Exchange-Correlation Energy functional $E_{xc}[n]$. The energy functional $E_{xc}[n]$ includes the non-classical contributions to the Coulomb energy and the error in the kinetic energy $(T - T_s)$, and together with the Hartree term should reproduced the electron-electron interaction term $V_{ee}[n]$.

$$E[n] = F[n] + V_{ne} \tag{1.35}$$

$$F[n] = T[n] + V_{ee}[n] = T_s[n] + V_H[n] + E_{xc}[n] \tag{1.36}$$

$$E_{xc}[n] = T[n] - T_s[n] - V_H[n] + V_{ee}[n] \tag{1.37}$$

The Hartree term $V_H[n] = \frac{1}{2} \int \int \frac{n(\mathbf{r})n(\mathbf{r}')}{|\mathbf{r}-\mathbf{r}'|} \mathrm{d}\mathbf{r}\mathrm{d}\mathbf{r}'$ accounts for the electrostatic self-interaction energy of a classical charge density $n(\mathbf{r})$. Equation 1.24 becomes

$$
\begin{aligned}
\mu &= \frac{\delta T_s[n]}{\delta n} + \frac{\delta E_{xc}[n]}{\delta n} + \frac{\delta E_H[n]}{\delta n} + V_{ne}(\mathbf{r}) \\
&= \frac{\delta T_s[n]}{\delta n} + V_{xc}(\mathbf{r}) + \int n(\mathbf{r}')v(\mathbf{r},\mathbf{r}')\mathrm{d}\mathbf{r}' + V_{ne}(\mathbf{r}) \\
&= \frac{\delta T_s[n]}{\delta n} + V_{eff}(\mathbf{r}) \; .
\end{aligned}
\tag{1.38}
$$

Where $v(\mathbf{r},\mathbf{r}') = \frac{1}{|\mathbf{r}-\mathbf{r}'|}$. The effective potential $V_{eff}(\mathbf{r})$ is given by the sum of $V_{xc}(\mathbf{r})$, $V_H(\mathbf{r})$ and $V_{ne}(\mathbf{r})$. The energy minimization problem, given by Eq. 1.38 can also be re-written in term of the Kohn-Sham (KS) orbitals rather than in terms of electron density.

$$
\begin{aligned}
0 = &-\frac{1}{2}\frac{\delta\big(\sum_i^N \int \psi_i^*(\mathbf{r})\nabla^2\psi_i(\mathbf{r})\mathrm{d}\mathbf{r}\big)}{\delta\psi_\lambda^*(\mathbf{r})} + \frac{\delta \int \big(V_{eff}(\mathbf{r})n(\mathbf{r})\mathrm{d}\mathbf{r}\big)}{\delta\psi_\lambda^*(\mathbf{r})} \\
&-\frac{\delta\big(\sum_i \sum_j \epsilon_{ij} \int \psi_j^*(\mathbf{r})\psi_i(\mathbf{r})\mathrm{d}\mathbf{r}\big)}{\delta\psi_\lambda^*(\mathbf{r})} = -\frac{1}{2}\nabla^2\psi_\lambda(\mathbf{r}) + V_{eff}(\mathbf{r})\psi_\lambda(\mathbf{r}) - \sum_j \epsilon_{\lambda j}\psi_j(\mathbf{r}) \; .
\end{aligned}
\tag{1.39}
$$

Eq. 1.39 has been obtained using the constraints

$$
\sum_{ij}^N \int \psi_i^*(\mathbf{r})\psi_j(\mathbf{r})\mathrm{d}\mathbf{r} - \delta_{ij} = 0
\tag{1.40}
$$

that guarantee the orthogonality of the KS orbitals and so, for non-interacting particle systems, is equivalent to the constraint 1.21. The Hamiltonian $H_{eff} = T_S + V_{eff}$ is a hermitian operator because $V_{eff}(\mathbf{r})$ is a local operator. Consequently, the matrix whose elements are $\epsilon_{\lambda j}$ is hermitian and can be diagonalized by a unitary transformation which leaves the determinant defining the total wavefunction (1.33) invariant. Therefore, also the density (1.34) and $H_{eff}[n]$ remain unchanged leading to the KS equations

$$
\left(-\frac{1}{2}\nabla^2 + V_{eff}(\mathbf{r})\right)\psi_\lambda(\mathbf{r}) = \hat{H}_{eff}\psi_\lambda(\mathbf{r}) = \epsilon_\lambda \psi_\lambda(\mathbf{r}) \; .
\tag{1.41}
$$

This is an eigenvalue equation. By diagonalizing $\hat{H}_{eff}$ all the eigenenergies ϵ_λ can be found.

Note that the total energy of the system E is not equal to the sum of the occupied eigenvalues of Eq. 1.41. This is due to the definition of the functional derivative, see

appendix F. In particular,

$$
\begin{aligned}
\sum_i^N \epsilon_i &= \sum_i^N \sum_\sigma \int \psi(\mathbf{r}, \sigma) \left[-\frac{1}{2}\nabla^2 + V_{eff}(\mathbf{r}) \right] \psi(\mathbf{r}, \sigma) \mathrm{d}\mathbf{r} \\
&= T_s[n] + \int V_{eff}(\mathbf{r}) n(\mathbf{r}) \mathrm{d}\mathbf{r} \\
&= T_s[n] + \int V_H(\mathbf{r}) n(\mathbf{r}) \mathrm{d}\mathbf{r} + \int V_{xc}(\mathbf{r}) n(\mathbf{r}) \mathrm{d}\mathbf{r} + \int V_{ne}(\mathbf{r}) n(\mathbf{r}) \mathrm{d}\mathbf{r} \\
&= T_s[n] + \int \int \frac{\delta n(\mathbf{r}')}{|\mathbf{r} - \mathbf{r}'|} n(\mathbf{r}) \mathrm{d}\mathbf{r} \mathrm{d}\mathbf{r}' + \int \frac{\delta E_{xc}[n]}{\delta n(\mathbf{r})} n(\mathbf{r}) \mathrm{d}\mathbf{r} + \int V_{ne}(\mathbf{r}) n(\mathbf{r}) \mathrm{d}\mathbf{r} \\
&= T_s[n] + 2E_H[n] + \int \frac{\delta E_{xc}[n]}{\delta n(\mathbf{r})} n(\mathbf{r}) \mathrm{d}\mathbf{r} + V_{ne}[n] \,,
\end{aligned}
\tag{1.42}
$$

so the total energy defined as $E = T_s[n] + E_H[n] + E_{xc}[n] + V_{ne}[n]$ is equal to

$$
E = \sum_i^N \epsilon_i - E_H[n] - \int \frac{\delta E_{xc}[n]}{\delta n(\mathbf{r})} n(\mathbf{r}) \mathrm{d}\mathbf{r} + E_{xc}[n] \,.
\tag{1.43}
$$

SELF-CONSISTENT PROCEDURE

The Kohn-Sham Equations 1.41 are self-consistent equations, i.e. one has to know $\hat{H}_{eff}$ to determine $n(\mathbf{r})$. However, in turn, $\hat{H}_{eff}$ depends on $n(\mathbf{r})$. Such kind of non-linear problems can be solved iteratively through the following steps:

1. An initial trial density is used to calculate the effective potential.

2. The potential is inserted in the Kohn-Sham equations, which will provide a new estimate for the KS orbitals $\psi(\mathbf{r})$ and so a new electron density $n(\mathbf{r})$.

3. The new density is used to calculate the new effective potential.

These steps are repeated trying to reach convergence. It usually requires some level of mixing (either of the density or of the Hamiltonian) to achieve self-consistency. In Fig.1.3 the iterative procedure used in DFT codes is shown.
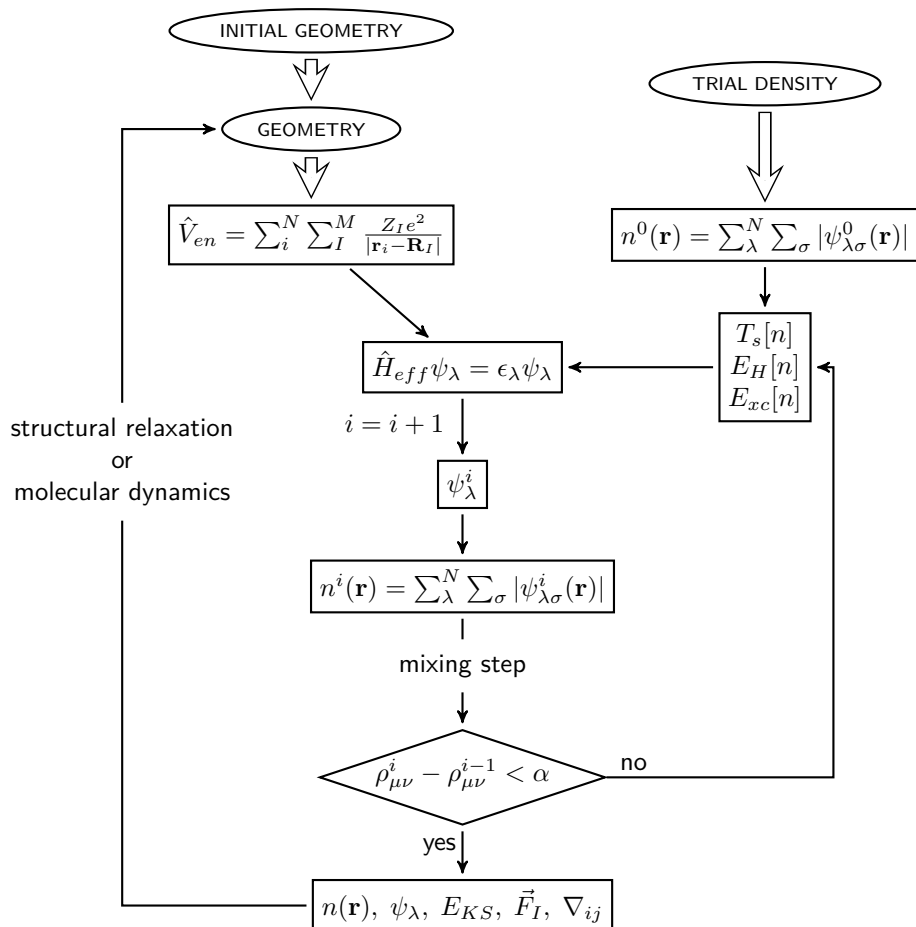
Figure 1.3: Iterative procedure used in DFT codes. $\vec{F}_I$, and ∇_{ij} stand for forces acting on nuclei and the stress tensor, respectively.

1.1.7 Δ SELF-CONSISTENT FIELD APPROACH

The ΔSCF (Self-Consistent Field) approach can be used to calculate excitation energies, ionization energy and electron affinity without employing the more sophisticated TDDFT. The difference in total energy calculated from two different DFT calculations with different constraints in the electron density often provides a decent estimate of corresponding excitation energies. This procedure works better for the ionization potential, since it is sometimes difficult to bind extra electrons to small molecules with most common DFT functionals.

HOMO-LUMO EXCITATION ENERGY

By forcing an electron to be promoted to the first KS orbital, leaving a hole behind is possible to calculate the HOMO-LUMO excitation energy, see Fig. 1.4(a).

Electron Affinity

In the same way it is possible to perform a DFT calculation by adding an electron in the LUMO. The difference ΔSCF gives the electron affinity (E.A.), see Fig. 1.4(b).

Ionization Potential

A calculation can be made where an electron is removed in the HOMO. The energy difference between the pristine and charged system gives the ionization potential (I.P.), see Fig. 1.4(c).

(a) ΔSCF = ESCF - ESCF-GS

(b) ΔSCF = E.A. = ESCF - ESCF-GS

(c) ΔSCF = I.P. = ESCF - ESCF-GS
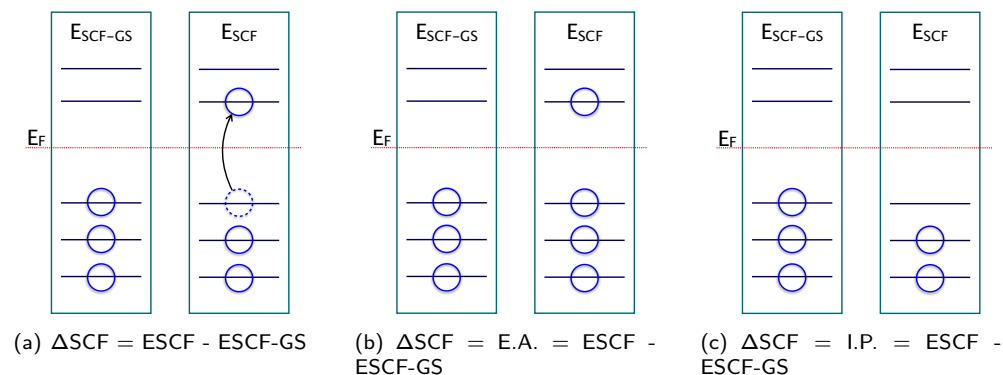
Figure 1.4: ΔSCF scheme for the calculation of the HOMO-LUMO excitation energy (a), electron affinity (b) and ionization potential (c).

1.2 Time Dependent Density Functional Theory (TDDFT)

DFT is a time-independent theory. Thus, DFT is employed whenever we want to compute the ground-state properties of a given electron system in which the external potential does not depend on time. However, when in the system Hamiltonian a time-dependent potential term is added, then a time-dependent extension of DFT is needed. Time-dependent fields are involved, for example, whenever we want to calculate photoabsorption spectra, excitation energies, etc. In this section we shall tackle the question of how to generalize the Hohenberg-Kohn theorems to time-dependent situations.

Next, we will discuss the Runge-Gross Theorem,[15] that extends the validity of the KS scheme TDDFT approach. Moreover, similarly to DFT, a time-dependent density functional theory can be formulated so that the problem of interacting electrons moving in an external time-dependent potential $V_{ext}(\mathbf{r}, t)$ can be mapped onto a problem involving non-interacting particles subjected to a time-dependent effective potential $V_{eff}(\mathbf{r}, t)$, this effective potential being a function of the time-dependent density n($\mathbf{r}$,t).

1.2.1 RUNGE-GROSS THEOREMS

The TDDFT approach has a formal ground thanks to the Runge-Gross theorems[15]. Similarly to the Hohenberg-Kohn theorems (section 1.1.4) they establish a relation between the time-dependent potential and the electron density.

1. *Given a single-particle time-dependent potential expandable in Taylor series at time t_0 and having fixed an initial wavefunction $\Psi(\mathbf{r}, t_0) = \Psi_0(\mathbf{r})$, an invertible relation exists between the potential and the density $n(\mathbf{r}, t)$ up to an additive time-dependent function in the potential.*[15]

2. *The action integral can be represented as a function of the density, $A[n] = B[n] - \int_{t_0}^{t_1} \int n(\mathbf{r}, t) V_{ext}(\mathbf{r}, t) \mathrm{d}\mathbf{r} \mathrm{d}t$ where $B[n]$ is a universal function of the density. The stationary point of action $A[n]$ corresponds to the exact system density.*[15]

The proof to the first theorem consists of taking two different time-dependent potentials V and V' that differ by more than an additive time-dependent function ($V(\mathbf{r}, t) \neq V'(\mathbf{r}, t) + C(t)$) and makes use of the equation of motion so that we can connect the current density $\vec{j}(\mathbf{r}, t)$ with the external potential[15]

$$\left(\frac{i\partial}{\partial t}\right)^{k+1} [\vec{j}(\mathbf{r}, t) - \vec{j}'(\mathbf{r}, t)]\bigg|_{t=t_0} = in(\mathbf{r}, t_0)\nabla\left\{\left(\frac{i\partial}{\partial t}\right)^k [V(\mathbf{r}, t) - V'(\mathbf{r}, t)]\bigg|_{t=t_0}\right\} \neq 0 .$$
(1.44)

In Equation 1.44 j and j' are the current densities that become different at times later than t_0 if $(\frac{i\partial}{\partial t})^k [V(\mathbf{r}, t) - V'(\mathbf{r}, t)]|_{t=t_0}$ is not a constant. By using the continuity equation it is possible then to go one step further and connect the current density $\vec{J}(\mathbf{r}, t)$ with the density $n(\mathbf{r}, t)$ to obtain from Equation 1.44 the following relation

$$\frac{\partial^{k+2}}{\partial t^{k+2}} [n(\mathbf{r}, t) - n'(\mathbf{r}, t)]\bigg|_{t=t_0} = -\mathrm{div}\left\{n(\mathbf{r}, t_0) \cdot \nabla\left[\frac{\partial^k}{\partial t^k}[V(\mathbf{r}, t) - V'(\mathbf{r}, t)]\bigg|_{t=t_0}\right]\right\} .$$
(1.45)

A *reductio ad absurdum* proof finally shows that the right side of Equation 1.45 cannot vanish if the two potentials differ by more than an additive time-dependent function when the two densities $n(\mathbf{r}, t)$ and $n'(\mathbf{r}, t)$ become different infinitesimally after t_0. This theorem proves that the time-dependent potential, up to an additive time-dependent function, indeed is determined by the electron density. Thus, we can conclude that the energy is a functional of the time-dependent density $E[n(\mathbf{r}, t)]$.

Furthermore, let us consider two time-dependent potentials $V(\mathbf{r}, t)$ and $V'(\mathbf{r}, t)$ where

$$V'(\mathbf{r}, t) = V(\mathbf{r}, t) + C(t)$$
(1.46)

and $C(t)$ is a time-dependent scalar function. The potentials $V(\mathbf{r}, t)$ and $V'(\mathbf{r}, t)$ provide the same density (1.45) however, the corresponding wavefunctions will differ by a time-dependent phase

$$\Psi'(\mathbf{r}, t) = e^{-i\alpha(t)}\Psi(\mathbf{r}, t) ,$$
(1.47)

where $\partial\alpha(t)/\partial t = C(t)$. This additional phase cancels out when calculating the density $n(\mathbf{r}, t)$ and the expectation value of any time-dependent operator.

1.2.2 TIME-DEPENDENT KOHN-SHAM EQUATIONS

For time-dependent systems no minimum energy principle is available. Rather, a stationary action principle will provide the exact density of the system. Following the Runge-Gross 2nd theorem, the action is a unique functional of the density $A[n]$ so that the stationary points condition can be found using the Euler–Lagrange equation

$$\frac{\delta A[n]}{\delta n(\mathbf{r}, t)} = 0 \ . \tag{1.48}$$

The proof resides on the fact that the action is defined as

$$\delta A = \int_{t0}^{t1} \langle \Psi(t)| \, i\frac{\partial}{\partial t} - \hat{H} \, |\Psi(t)\rangle \tag{1.49}$$

where $\hat{H} = \hat{T} + \hat{V}_{ee} + \hat{V}_{ext}(t)$ and $\hat{V}_{ext}(t) = \hat{V}_{ne} + \hat{V}(t)$. $V(t)$ being the external time-dependent potential. The actions calculated with two potentials $V(t)$ and $V'(t)$ connected by the equation 1.46 turn out to be the same, as the factor $C(t)$ included in $V'(t)$ cancels out when performing the time derivative on the wavefunction $\Psi'(\mathbf{r}, t)$ (Equation 1.47). Thus, the action is a unique functional of the density.

Analogously to the time-independent universal functional, Eq. 1.20 , we can define a universal functional $S[n]$ as

$$S[n] = \int_{t_0}^{t_1} \langle \Psi[n]| \, i\partial/\partial t - \hat{T} - \hat{V}_{ee} \, |\Psi[n]\rangle \, \mathrm{d}t \ . \tag{1.50}$$

In general, two functionals S refer to two different choices for the electron-electron interaction term $\hat{V}_{ee}$. More specifically, let us define S_0 as the universal functional for non-interacting particles, i.e. $\hat{V}_{ee} = 0$, and $S_{V_{ee}}$, the functional for the system with full electron-electron interaction switched on. The Euler–Lagrange Equation 1.48 for the interacting system becomes

$$
\begin{aligned}
\frac{\delta A[n]}{\delta n(\mathbf{r}, t)} &= \frac{\delta \int_{t0}^{t1} \langle \Psi(t)| \, i\frac{\partial}{\partial t} - \hat{T} - \hat{V}_{ee} \, |\Psi(t)\rangle \, \mathrm{d}t - \int_{t0}^{t1} \int n(\mathbf{r}, t) V_{ext}(\mathbf{r}, t) \mathrm{d}\mathbf{r}\mathrm{d}t}{\delta n(\mathbf{r}, t)} \\
&= \frac{\delta S_0[n]}{\delta n(\mathbf{r}, t)} - \frac{\delta \int_{t0}^{t1} \langle \Psi(t)| \, \hat{V}_{ee} \, |\Psi(t)\rangle \, \mathrm{d}t}{\delta n(\mathbf{r}, t)} + \int v(\mathbf{r}, \mathbf{r}') n(\mathbf{r}', t) \mathrm{d}\mathbf{r}' \\
&\quad - \int v(\mathbf{r}, \mathbf{r}') n(\mathbf{r}', t) \mathrm{d}\mathbf{r}' - V_{ext}(\mathbf{r}, t) \\
&= \frac{\delta S_0[n]}{\delta n(\mathbf{r}, t)} - V_{xc}(\mathbf{r}, t) - \int v(\mathbf{r}, \mathbf{r}') n(\mathbf{r}', t) \mathrm{d}\mathbf{r}' - V_{ext}(\mathbf{r}, t) \\
&= \frac{\delta S_0[n]}{\delta n(\mathbf{r}, t)} - V_{eff}(\mathbf{r}, t) = 0 \ ,
\end{aligned}
\tag{1.51}
$$

where

$$V_{eff}(\mathbf{r}, t) = \int v(\mathbf{r}, \mathbf{r}') n(\mathbf{r}', t) \mathrm{d}\mathbf{r}' + V_{ext}(\mathbf{r}, t) + V_{xc}(\mathbf{r}, t) \ , \tag{1.52}$$

$$V_{xc}(\mathbf{r}, t) = - \int v(\mathbf{r}, \mathbf{r}') n(\mathbf{r}', t) \mathrm{d}\mathbf{r}' + \frac{\delta \int_{t0}^{t1} \langle \Psi(t)| \, \hat{V}_{ee} \, |\Psi(t)\rangle \, \mathrm{d}t}{\delta n(\mathbf{r}, t)} \ . \tag{1.53}$$

Here we defined the *effective* potential (V_{eff}) and the *exchange-correlation* potential (V_{xc}). Finally, we note that Eq. 1.51 is the Euler-Lagrange equation for a system of independent particles moving in an effective potential defined in Eq. 1.52.[15] Consequently, for v-representable density, we can write the time-dependent equivalent of the KS equations,

$$i\frac{\partial}{\partial t}\psi_i(\mathbf{r}, t) = \left[-\frac{1}{2}\nabla^2 + V_{eff}(\mathbf{r}, t)\right]\psi_i(\mathbf{r}, t) , \tag{1.54}$$

where ψ_i are the single-particle orbital wavefunctions. Equation 1.54 is the time-dependent Kohn-Sham equation. Similarly to what has been done to derive the DFT Kohn-Sham equations, a fictitious system of non-interacting particles can be defined where the electron-electron interactions are included through the so-called *Hartree* potential

$$V_H(\mathbf{r}, t) = \int v(\mathbf{r}, \mathbf{r}')n(\mathbf{r}', t)\mathrm{d}\mathbf{r}' \tag{1.55}$$

and the *exchange-correlation* potential (V_{xc}), see equation 1.53. The two potentials sum up with the external time-dependent perturbation to form the one-particle effective potential V_{eff}. The consequences of these theorems will be clear in section 1.3 when describing a linear response approach to the time-dependent KS equation 1.54.

1.3 LINEAR RESPONSE FORMALISM

In this thesis we employed the linear response formalism to calculate the optical properties of different molecules. The response of a system at equilibrium in the linear regime describes the behavior of the system when it weakly interacts with a time-dependent potential. As long as the external stimuli magnitude is *small enough* we can consider the system to respond linearly to the applied perturbation. The *linear response function* $\chi(\mathbf{r}, \mathbf{r}', \omega)$ (in real-space domain and frequency domain), see appendix A, connects the time-dependent external perturbing potential $V_{ext}(\mathbf{r}, t)$ to induced electron density $\delta n(\mathbf{r}, t)$, which represents the change in the electronic density caused by the external perturbation $\delta V_{ext}(\mathbf{r}, t)$. The induced density is given by

$$\delta n(\mathbf{r}, \omega) = \int \chi(\mathbf{r}, \mathbf{r}', \omega)\delta V_{ext}(\mathbf{r}', \omega)\mathrm{d}\mathbf{r}' . \tag{1.56}$$

The response function χ is defined as the functional derivative of the time-dependent density with respect to the external potential, i.e.

$$\chi(\mathbf{r}, \mathbf{r}', \omega) = \left.\frac{\delta n[V_{ext}](\mathbf{r}, \omega)}{\delta V_{ext}(\mathbf{r}, \omega)}\right|_{V_{ext}[n_0]}, \tag{1.57}$$

where n_0 is the unperturbed electron density. In this work we are interested to study the *optical* response of small finite systems, For such small systems if the spatial extend of the electron density is smaller than the wave-length of the driving electromagnetic wave, then the electrical field of the electromagnetic wave can be assumed homogeneous and the magnetic component is neglected. This is the so-called dipole approximation, in this approximation the external potentials is written as

$$V_{ext} = \mathbf{r} \cdot \mathbf{E}_0\cos(\omega t) . \tag{1.58}$$

1.3.1 REAL AND IMAGINARY RESPONSE FUNCTION

The linear response in the time domain is a real quantity, however, its Fourier transform to the frequency domain is a complex quantity

$$\chi(\omega) = \chi'(\omega) + i\chi''(\omega) , \tag{1.59}$$

where χ' and χ'' are, respectively, the real and imaginary parts. For the sake of clarity, we dropped the dependence on the spatial argument $\mathbf{r}$ as it is not important for the purpose of the following sections.

In the following sections we will discuss the symmetry properties of the real and imaginary parts of the response function, the relation between them and also how the imaginary part $\chi''(\omega)$ is related to the energy absorbed by the system.

1.3.2 SYMMETRY OF $\chi(\omega)$

The real and imaginary parts of the response function in the frequency domain have an even and an odd character, respectively. This can be seen when we write the real and imaginary parts as

$$
\begin{aligned}
\chi'(\omega) &= \frac{1}{2}\big(\chi(\omega) + \chi^*(\omega)\big) = \frac{1}{2}\int \chi(t)e^{-i\omega t}\mathrm{d}t + \frac{1}{2}\int \chi(t)e^{i\omega t}\mathrm{d}t \\
&= \frac{1}{2}\int \big(\chi(t) + \chi(-t)\big)e^{-i\omega t}\mathrm{d}t
\end{aligned}
\tag{1.60}
$$

$$
\begin{aligned}
\chi''(\omega) &= -\frac{i}{2}\big(\chi(\omega) - \chi^*(\omega)\big) = -\frac{i}{2}\int \chi(t)e^{-i\omega t}\mathrm{d}t + \frac{i}{2}\int \chi(t)e^{i\omega t}\mathrm{d}t \\
&= -\frac{i}{2}\int \big(\chi(t) - \chi(-t)\big)e^{-i\omega t}\mathrm{d}t ,
\end{aligned}
\tag{1.61}
$$

where we used the fact that $\chi^*(t) = \chi(t)$, i.e. $\chi(t)$ is a real function. The integrand in 1.60 is invariant under time reversal $t \to -t$ while the integrand in 1.61 is not. Therefore, for $\omega \to -\omega$ we have

$$\chi'(-\omega) = \chi'(\omega) , \tag{1.62}$$
$$\chi''(-\omega) = -\chi''(\omega) . \tag{1.63}$$

The real part $\chi'(\omega)$ is an even function in the frequency domain while the imaginary part $\chi''(\omega)$ is an odd function.

1.3.3 ENERGY ABSORBED BY THE SYSTEM

The imaginary part of the linear response function is connected to the average energy absorbed by the system. We will calculate the absorption of the system in terms of the work W done by the system over time in order to show the connection.

The work exerted by an electric field is obtained from the *energy absorption rate*

calculated as the variation in time of the total energy, i.e.

$$\begin{aligned}
\frac{\mathrm{d}E}{\mathrm{d}t} &= \frac{\mathrm{d}}{\mathrm{d}t} \langle \Psi(t)| \hat{H}(t) |\Psi(t)\rangle \\
&= i \langle \dot{\Psi}(t)|\dot{\Psi}(t)\rangle + \langle \Psi(t)| \left[\frac{\mathrm{d}}{\mathrm{d}t}\hat{H}(t)\right] |\Psi(t)\rangle - i \langle \dot{\Psi}(t)|\dot{\Psi}(t)\rangle = \left\langle \frac{\mathrm{d}}{\mathrm{d}t}\hat{H}(t)\right\rangle .
\end{aligned}$$

(1.64)

Here we used the time-dependent Schrödinger equation $\frac{\mathrm{d}}{\mathrm{d}t}|\Psi(t)\rangle = i\hat{H}|\Psi(t)\rangle$. Defining $\hat{H}(t) = \hat{H}_0 + \hat{V}_{ext}(t)$ and $V_{ext}(t) = \mathbf{r} \cdot \mathbf{E}_0 \cos(\omega t)$ we can write

$$\begin{aligned}
\frac{\mathrm{d}E}{\mathrm{d}t} &= \int \Psi^*(\mathbf{r},t)\frac{\partial}{\partial t}V_{ext}(\mathbf{r},t)\Psi(\mathbf{r},t)\mathrm{d}\mathbf{r} \\
&= \int n(\mathbf{r},0)\frac{\partial V_{ext}(\mathbf{r},t)}{\partial t}\mathrm{d}\mathbf{r} + \frac{i\omega}{2}\int \delta n(\mathbf{r},t)\mathbf{r}\cdot \mathbf{E}_0\big(e^{i\omega t} - e^{-i\omega t}\big)\mathrm{d}\mathbf{r} \\
&= \textcircled{1} + \frac{i\omega E_{0\hat{r}}}{2}\iiint \mathbf{r}\chi(\mathbf{r},\mathbf{r}',t-t')V_{ext}(\mathbf{r}',t')\mathrm{d}\mathbf{r}'\mathrm{d}t'\big(e^{i\omega t} - e^{-i\omega t}\big)\mathrm{d}\mathbf{r} \\
&= \textcircled{1} + \frac{i\omega E_{0\hat{r}}^2}{4}\iint \left[\mathbf{r}\chi(\mathbf{r},\mathbf{r}',\omega)e^{i\omega t}\mathbf{r}' + \mathbf{r}\chi(\mathbf{r},\mathbf{r}',-\omega)e^{-i\omega t}\mathbf{r}'\right]\mathrm{d}\mathbf{r}\mathrm{d}\mathbf{r}'\big(e^{i\omega t} - e^{-i\omega t}\big) \\
&= \textcircled{1} + \frac{i\omega E_{0\hat{r}}^2}{4}\left[\alpha(\omega)e^{i\omega t} + \alpha(-\omega)e^{-i\omega t}\right]\big(e^{i\omega t} - e^{-i\omega t}\big) \\
&= n(\mathbf{r},0)\int \frac{\mathrm{d}V_{ext}(\mathbf{r},t)}{\mathrm{d}t}\mathrm{d}\mathbf{r} - \frac{\omega E_{0\hat{r}}^2}{2}\alpha''(\omega)\big[e^{-2i\omega t} - 1\big]
\end{aligned}$$

(1.65)

where $\textcircled{1} = n(\mathbf{r},0)\int \frac{\mathrm{d}V_{ext}(\mathbf{r},t)}{\mathrm{d}t}\mathrm{d}\mathbf{r}$. α defined as $\iint \mathbf{r}\chi(\mathbf{r},\mathbf{r}',\omega)\mathbf{r}'\mathrm{d}\mathbf{r}\mathrm{d}\mathbf{r}'$ is the so-called polarizability and it is discussed in detail in Section 1.3.7. The average energy absorbed by the system per unit of time $\overline{W}$ is given by the integral over T of $\frac{\mathrm{d}E}{\mathrm{d}t}$,

$$\begin{aligned}
\overline{W} &= \frac{1}{T}\int_T \frac{\mathrm{d}E}{\mathrm{d}t}\mathrm{d}t = \int n(\mathbf{r},0)\frac{1}{T}\int_T \frac{\mathrm{d}V_{ext}(\mathbf{r},t)}{\mathrm{d}t}\mathrm{d}t\mathrm{d}\mathbf{r} - \frac{\omega E_0^2}{2}\frac{1}{T}\int_T \alpha''(\omega)\big[e^{-2i\omega t} - 1\big]\mathrm{d}t \\
&= \int n(\mathbf{r},0)\frac{1}{T}\big[V_{ext}(\mathbf{r},T) - V_{ext}(\mathbf{r},0)\big]\mathrm{d}\mathbf{r} - \frac{\omega E_0^2}{2}\alpha''(\omega)\left[\frac{e^{-2i\omega T} - 1}{-i2\omega T} - 1\right].
\end{aligned}$$

(1.66)

For $T \to \infty$ we get

$$\overline{W} = \frac{\omega E_0^2}{2}\alpha''(\omega) .$$

(1.67)

The term $\int n(\mathbf{r},0)\frac{1}{T}\big[V_{ext}(\mathbf{r},T) - V_{ext}(\mathbf{r},0)\big]\mathrm{d}\mathbf{r}$ is 0 because we assumed $V_{ext}(\mathbf{r},t)$ is bound. Thus, when $T \to \infty$, this term goes to zero. Eq. 1.67 shows that the work done by the field on the system, i.e. the optical absorption, is proportional to the imaginary part of the polarizability α''. Thus, it is legitimate to look at the imaginary part of the response function and its related quantities when investigating the excitation energies and properties of excitations.

1.3.4 Causality and Kramers-Kronig relations

The Heaviside function in the Kubo formula (Eq. A.14) ensures causality, meaning that future events cannot influence the past,

$$\chi(t - t') = 0 \quad t' > t \tag{1.68}$$

and

$$\delta n(t) = \int \chi(t - t')V(t')\mathrm{d}t' \tag{1.69}$$

Causality in the time domain leads to the Kramers-Kronig relations in the frequency domain, and connects the real part to the imaginary part of the linear response function. Let us start considering the Fourier transform of the linear response $\chi(t)$,

$$\chi(\omega) = \int \chi(t)e^{-i\omega t}\mathrm{d}t = \int \chi(t)\sigma(t)e^{-i\omega t}\mathrm{d}t = \frac{1}{2\pi} \int \chi(\omega')\sigma(\omega - \omega')\mathrm{d}\omega' \,, \tag{1.70}$$

where $\sigma(t)$ is the Heaviside function. For the last step in Eq. 1.70 we used the convolution theorem. The Fourier transform of the Heaviside function can be shown to be

$$\sigma(\omega - \omega') = \pi\delta(\omega - \omega') - \frac{i}{\omega - \omega'} \,. \tag{1.71}$$

Consequently

$$\chi(\omega) = \frac{1}{2}\chi(\omega) - \frac{i}{2\pi}\mathrm{P} \int \frac{\chi(\omega')}{\omega - \omega'}\mathrm{d}\omega' \,, \tag{1.72}$$

which leads to

$$\mathrm{P} \int_{-\infty}^{+\infty} \frac{\chi(\omega')}{\omega' - \omega}\mathrm{d}\omega' = i\pi\chi(\omega) \,. \tag{1.73}$$

"P $\int$" denotes the *Cauchy principal value* integral. From 1.73 and writing $\chi = \chi' + i\chi''$ we obtain the Kramers-Kronig relations

$$\chi'(\omega) = \frac{1}{\pi}\mathrm{P} \int_{-\infty}^{+\infty} \frac{\chi''(\omega')}{\omega' - \omega} \tag{1.74}$$

$$\chi''(\omega) = -\frac{1}{\pi}\mathrm{P} \int_{-\infty}^{+\infty} \frac{\chi'(\omega')}{\omega' - \omega} \tag{1.75}$$

which connect the imaginary and the real parts of the response function χ. We can re-write 1.74 and 1.75 multiplying both equations at the numerator and denominator by $(\omega' + \omega)$, and using the symmetric properties of the linear response function that are shown in 1.62 and 1.63 we get

$$\chi'(\omega) = \frac{2}{\pi}\mathrm{P} \int_0^\infty \frac{\chi''(\omega')\omega'}{\omega'^2 - \omega^2} \tag{1.76}$$

$$\chi''(\omega) = -\frac{2\omega}{\pi}\mathrm{P} \int_0^\infty \frac{\chi'(\omega')}{\omega'^2 - \omega^2} \,. \tag{1.77}$$

Thanks to these relations the real/imaginary part of the linear response can be calculated from the imaginary/real part of the linear response. Usually, it is easier to compute the imaginary part and then obtain the real part using 1.76 rather than the other way around due to the structure of the function.

1.3.5 NON-INTERACTING AND INTERACTING RESPONSE FUNCTION

So far we have dealt with the generic concept of the linear response function. Our goal is to find the linear response function χ for a system of *interacting* electrons. In practice, in order to do so, it is convenient to define the so-called *non-interacting* response function χ_0 (see appendix A for derivation),

$$\chi_0(\mathbf{r}, \mathbf{r}', \omega) = \frac{\delta n[V_{eff}](\mathbf{r}, \omega)}{\delta V_{eff}(\mathbf{r}', \omega)}\bigg|_{V_{eff}[n_0]} = \sum_{n,m} \frac{(f_m - f_n)\psi_m^*(\mathbf{r})\psi_n(\mathbf{r})\psi_n^*(\mathbf{r}')\psi_m(\mathbf{r}')}{\omega - E_{mn} + i\eta} .$$

(1.78)

Here ψ_m are the one-particle KS orbitals, E_{mn} is the energy difference between the KS states m and n, i.e. $E_{mn} = E_m - E_n$. The η constant represents the Half-Width at Half-Maximum (HWHM) of the Lorentzian peak described by Equation 1.81 and it is the inverse of the excitation lifetime.[45] The occupations of KS levels f_m are typically given by the the Fermi-Dirac (F-D) distribution multiplied by 2, where the 2 arises from spin degeneracy, which is assumed throughout this thesis.[(1)] At zero temperature f_m can be either 0 or 2. As discussed in the foundations of TDDFT (see section 1.2.2) the non-interacting response function χ_0 describes a system of independent particles that generates the same density δn as the "real" system constituted of interacting particles, under the effects of an effective perturbing potential δV_{eff} defined in Eq. 1.52, i.e. $n[V_{ext}]$ and $V_{eff}[n[V_{ext}]]$.[16] The induced density is

$$\delta n(\mathbf{r}, \omega) = \int \chi_0(\mathbf{r}, \mathbf{r}', \omega)\delta V_{eff} \mathrm{d}\mathbf{r} .$$

(1.79)

The electron-electron interactions are included in the KS scheme by means of the potential V_{eff}. Furthermore, from 1.78 we can easily obtain the real χ_0' and the imaginary χ_0'' part of the non-interacting response function,

$$\chi_0'(\mathbf{r}, \mathbf{r}', \omega) = \sum_{n,m}(f_m - f_n)\psi_m^*(\mathbf{r})\psi_n(\mathbf{r})\psi_n^*(\mathbf{r}')\psi_m(\mathbf{r}')\frac{\omega - E_{mn}}{(\omega - E_{mn})^2 + \eta^2}$$

(1.80)

$$\chi_0''(\mathbf{r}, \mathbf{r}', \omega) = -\sum_{n,m}(f_m - f_n)\psi_m^*(\mathbf{r})\psi_n(\mathbf{r})\psi_n^*(\mathbf{r}')\psi_m(\mathbf{r}')\frac{\eta}{(\omega - E_{mn})^2 + \eta^2} .$$

(1.81)

We can relate the interacting response (Eq. 1.58) with non-interacting response function (Eq. 1.78) using the chain rule for variational derivatives and the definition of KS effective potential (Eq. 1.52). Following the procedure from the paper by Petersilka,

---

[(1)]The Fermi-Dirac distribution function is $\frac{1}{1+e^{(\epsilon_m - \mu)/kT}}$, where μ is the chemical potential, k is Boltzmann constant and T is the temperature.

Gossmann and Gross[16] we get the Dyson-like equation

$$
\begin{aligned}
\chi(\mathbf{r}, \mathbf{r}', \omega) &= \int \frac{\delta n(\mathbf{r}, \omega)}{\delta V_{eff}(\mathbf{r}'', \omega)} \frac{\delta V_{eff}(\mathbf{r}'', \omega)}{\delta V_{ext}(\mathbf{r}', \omega)} \bigg|_{V_{ext}[n_0]} \mathrm{d}\mathbf{r}'' \\
&= \int \chi_0(\mathbf{r}, \mathbf{r}', \omega) \left(\frac{\delta V_{ext}(\mathbf{r}'', \omega)}{\delta V_{ext}(\mathbf{r}', \omega)} + \frac{\delta V_H(\mathbf{r}'', \omega)}{\delta V_{ext}(\mathbf{r}', \omega)} + \frac{\delta V_{xc}(\mathbf{r}'', \omega)}{\delta V_{ext}(\mathbf{r}', \omega)} \right) \mathrm{d}\mathbf{r}'' \\
&= \chi_0(\mathbf{r}, \mathbf{r}', \omega) + \iint \chi_0(\mathbf{r}, \mathbf{r}', \omega) \left(\frac{\delta V_H(\mathbf{r}'', \omega)}{\delta n(\mathbf{r}''', \omega)} + \frac{\delta V_{xc}(\mathbf{r}'', \omega)}{\delta n(\mathbf{r}''', \omega)} \right) \frac{\delta n(\mathbf{r}''', \omega)}{\delta V_{ext}(\mathbf{r}', \omega)} \mathrm{d}\mathbf{r}'' \mathrm{d}\mathbf{r}''' \\
&= \chi_0(\mathbf{r}, \mathbf{r}', \omega) + \iint \chi_0(\mathbf{r}, \mathbf{r}'', \omega) f_{Hxc}(\mathbf{r}'', \mathbf{r}''', \omega) \chi(\mathbf{r}''', \mathbf{r}', \omega) \mathrm{d}\mathbf{r}'' \mathrm{d}\mathbf{r}''' .
\end{aligned}
\tag{1.82}
$$

Here the *interaction* kernel $f_{Hxc} = f_H + f_{xc}$ is decomposed into the *Hartree* and *exchange-correlation* kernels

$$
f_H(\mathbf{r}, \mathbf{r}', \omega) = \frac{\delta V_H[n](\mathbf{r}, \omega)}{\delta n(\mathbf{r}', \omega)} = \frac{\int v(\mathbf{r}, \mathbf{r}'') n(\mathbf{r}'', \omega) \mathrm{d}\mathbf{r}''}{\delta n(\mathbf{r}', \omega)} = v(\mathbf{r}, \mathbf{r}')
\tag{1.83}
$$

$$
f_{xc}(\mathbf{r}, \mathbf{r}', \omega) = \frac{\delta V_{xc}[n](\mathbf{r}, \omega)}{\delta n(\mathbf{r}', \omega)} ,
\tag{1.84}
$$

with $v(\mathbf{r}, \mathbf{r}') = 1/|\mathbf{r} - \mathbf{r}'|$.

1.3.6 Exchange-Correlation Potential and Kernel

When previously in section 1.2.2 we introduced the time-dependent KS equations we defined a quantity called the *effective potential* (V_{eff}, see Equation 1.52) that is a functional of the density and it is formed by the *Hartree* (V_H) potential and the *exchange-correlation* (V_{xc}) potential plus the *external* potential (V_{ext}). Electron-electron interactions and nuclear-electron interactions are included in V_{eff} (KS) potential.

When introducing the effective potential concept we omitted to mention that, in the general case, V_{eff} depends on the whole history of the density and on the initial interacting and KS wavefunctions, $\psi_{0,I}$ and ψ_0, respectively,

$$
V_{xc}[n, \psi_{0,I}, \psi_0](\mathbf{r}, t) = V_{eff}[n, \psi_{0,I}, \psi_0](\mathbf{r}, t) - V_{ext}(\mathbf{r}, t) - V_H[n](\mathbf{r}, t) .
\tag{1.85}
$$

However, for non-degenerate ground states in both interacting and non-interacting systems the dependence on the wavefunctions drops due to the fact that the wavefunctions are themselves functionals of the density.[46] Runge-Gross theorems (section 1.2.1) ensure a one-to-one correspondence between the time-dependent external potential and the time-dependent density change, thus, if the analytic form of the functional $V_{eff}[n]$ was known, we could, in principle, obtain an exact result for all the time-dependent problems with Coulomb interactions.[46] In particular, the exchange-correlation term $V_{xc}[n]$ (see equation 1.53) is the problematic term and the real challenge. Thus, for practical purposes an approximated form of $V_{xc}[n]$ has to be used.

In linear response theory, as we have seen in Section 1.3.5, the kernel (f_{Hxc}) connects χ_0 with χ. In particular, in this section, we are interested in the *exchange-correlation* part of the kernel (f_{xc}), which is defined as the functional derivative of $V_{eff}[n]$ with respect to

the density (Equation 1.84), The kernel is a functional only of the ground-state and it is the linear term in the expansion of the potential in the time domain for a weak perturbing field[46]

$$V_{xc}[n_0 + \delta n](\mathbf{r}, t) = V_{xc}[n](\mathbf{r}) + \iint f_{xc}[n_0](\mathbf{r}, \mathbf{r}', t - t')\delta n(\mathbf{r}', t')\mathrm{d}\mathbf{r}\mathrm{d}t' \ . \qquad (1.86)$$

Physicists and chemists have tried to improve f_{xc} over the years. The crudest approximation neglects completely the exchange-correlation term. Such approximation is called *Random Phase Approximation* (RPA) and it only considers V_H. The origin of this name can be understood considering the equation of motion for the density operator, i.e. $\frac{\mathrm{d}}{\mathrm{d}t}\hat{n}(t) = -i[\hat{H}, \hat{n}(t)]$.[47]

A more complete functional is the *Adiabatic Local Density Approximation* (ALDA) that is one of the most common and widely used approximations for f_{xc}. In ALDA the energy functional E is a functional only of the density at each instant of time. From the energy is then possible to obtain the potential and kernel thanks to the following relations

$$V_{xc}(\mathbf{r}) \equiv \frac{\delta E_{xc}}{\delta n(\mathbf{r})} \ , \qquad (1.87)$$

$$f_{xc}(\mathbf{r}, \mathbf{r}') \equiv \frac{\delta V_{xc}(\mathbf{r})}{\delta n(\mathbf{r}')} \ . \qquad (1.88)$$

In ALDA the f_{xc} kernel becomes local in space and time. The locality in space means that the potential is a functional only of the density at each point in space. While the locality in time ignores the dependence on past events, that is, V_{xc} is only a functional of the density on time t and not on all previous times t'

$$V_{xc}^{adiab}[n](t) = V_{xc}^{adiab}[n(t)] \ . \qquad (1.89)$$

Thus, finally the ALDA kernel can be written in the time domain in the following form

$$f_{xc}(\mathbf{r}, \mathbf{r}', t - t') = \delta(\mathbf{r} - \mathbf{r}')\frac{\delta V_{xc}^{LDA}[n](t)}{\delta n(\mathbf{r}', t')}\delta(t - t') \qquad (1.90)$$

In the frequency domain f_{xc}^{LDA} is a simple function depending on the spatial coordinate $\mathbf{r}$ through the electron density $n(\mathbf{r})$ and it is *frequency independent*. The assumption of locality in time holds better if we consider a potential that varies slowly with time (adiabatically).[46] The space locality requirement works better for systems with very small density gradients. In the frequency domain the *Hartree-exchange-correlation* (Hxc) kernel becomes

$$f_{Hxc}(\mathbf{r}, \mathbf{r}') = \frac{1}{|\mathbf{r} - \mathbf{r}'|} + f_{xc}^{LDA}(\mathbf{r})\delta(\mathbf{r} - \mathbf{r}') \ . \qquad (1.91)$$

There are many LDA functionals. Some of the most common LDA functionals are the Perdew-Zunger (PZ)[48] and the Perdew-Wang-92 (PW92).[49]

A more advanced approximation for the potential and kernel is the so-called *Generalized Gradient Approximation* (GGA), in which the energy functional depends upon the density and its gradient in order to account for corrections coming from a spatial inhomogeneity

of the electron density. Many different functionals belonging to the GGA class have been developed, some of the most commonly used are the Perdew-Burke-Ernzerhof (PBE),[50] Revised Perdew-Burke-Ernzerhof (revPBE),[51] Wu-Cohen (WC),[52] Revised Perdew-Burke-Ernzerhof (RPBE)[53] and Perdew-Burke-Ernzerhof for solids (PBEsol).[54]

More advanced approximations include *hybrid functionals* and *meta-GGA*s. The former use an exact exchange functional combined with an approximated form of the correlation term. This is often combined with a spatial cut-off to decide when the exact-exchange term sets in, and/or how this exchange interaction is screened. In meta-GGA, the energy is a functional of the density, its gradient, the gradient of the gradient of the density and of the kinetic energy.

Within GGA, the calculation of the KS potential is widely discussed in the literature,[55–57] however, the TDDFT kernel 1.88 is less commonly discussed[58,59] and more difficult to implement. In Section 2.3.3 the description of the theoretical implementation of a general (LDA and GGA) potential and kernel adapted to our iterative TDDFT code is presented. In this particular thesis, as we will specify in the result sections, at the DFT level both LDA-PZ and GGA-PBE approximations have been used. However, for the TDDFT calculations we have used the LDA-PZ kernel. In fact, the differences between LDA and GGA kernels for the system discussed here is minimal as discussed in a recent publication.[20]

1.3.7 NON-INTERACTING AND INTERACTING POLARIZABILITY

Since χ_0 and χ have been defined we can look in detail at the observables that we can calculate in TDDFT. In particular, we focus on the polarizability which, as shown in section 1.3.3, characterizes the energy absorption of the system as a function of the frequency of the incoming external field. The polarizability connects the external electric field with the induced dipole moment $\mathbf{p} = \alpha \mathbf{E}$, where $\mathbf{p}$ is the dipole moment, $\mathbf{E}$ the electric field and α the polarizability. The polarizability has the units of Bohr^3 in atomic units and it measures the tendency of a system to get polarized under the action of an external perturbing electric field. In particular, in our microscopic system the polarizability in the frequency domain is a complex number whose imaginary part is closely related to the imaginary part of the linear response.

DIPOLE APPROXIMATION

The dipole approximation can be used whenever the external electric perturbing field $\mathbf{E}_{ext}$ does not vary significantly over the size of the system, i.e. we can assume homogeneous electric field given by the electrical potential $V_{ext} = \mathbf{E}_0 \mathbf{r}$. If we consider an external oscillating field $E_{ext}(t) = E_0 \cos(\omega_{ext} t)$ then, we can write the electric potential in the frequency domain as

$$V_{ext}(\mathbf{r}, \omega) = \pi \mathbf{E_0} \cdot \mathbf{r}[\delta(\omega - \omega_{ext}) + \delta(\omega + \omega_{ext})] \tag{1.92}$$

Thus, Equation 1.56 connecting the induced density with the external potential can be written as

$$\delta n(\mathbf{r}, \omega_{ext}) = \pi E_0 \int \chi(\mathbf{r}, \mathbf{r}', \omega_{ext}) \mathbf{r}' \mathrm{d}\mathbf{r}' \, . \tag{1.93}$$

The far-field response is given by the polarizability tensor defined as

$$\alpha_{ij}(\omega) = \iint r_i' \chi(\mathbf{r}', \mathbf{r}, \omega) r_j \mathrm{d}\mathbf{r}\mathrm{d}\mathbf{r}' \tag{1.94}$$

In Equation 1.94 we have introduced the vectorial components for the position vector, the subscripts i and j indicate the directions of the external electric field and the direction along which the dipole is calculated. The α_{ij} tensor is symmetric and its elements are complex numbers. The orientation-averaged polarizability is given by the $1/3$ of the tensor trace

$$\alpha = \frac{1}{3}\sum_{i=1}^{3}(\alpha_{xx} + \alpha_{yy} + \alpha_{zz}) \, . \tag{1.95}$$

The average polarizability α becomes meaningful when we want to compare our results with experimental results obtained for samples with randomly oriented molecules. In experiments usually the optical cross section is the direct result of the measurement. Together with the polarizability, we can define the optical cross section. The cross section is connected to the polarizability by[60, 61]

$$\sigma(\omega) = \frac{4\pi}{c}\omega\alpha(\omega) \, , \tag{1.96}$$

where c is the speed of light.

As a simple approximation to 1.94 the so-called non-interacting polarizability α_0 can be used. It is defined as

$$\alpha_{ij}^0 = \iint r_i' \chi_0(\mathbf{r}', \mathbf{r}, \omega) r_j \mathrm{d}\mathbf{r}\mathrm{d}\mathbf{r}' \, . \tag{1.97}$$

The interacting polarizability is calculated as in 1.94.

f-Sum Rule

The f-sum rule or Thomas-Reiche-Kuhn (TRK) sum rule allows us to connect the imaginary part of the polarizability (cross section) with the total number of electrons in the calculation. This is a useful check for optical calculations. Starting from the relation $\hat{\mathbf{p}} = i[\hat{H}, \hat{\mathbf{r}}]$ and the fact that $\sum_n |n\rangle\langle n| = \mathbb{1}$ where $|n\rangle$ are all the eigenfunctions of $\hat{H}$, we can write (see appendix D.2)

$$-i\langle 0|[\hat{r}, \hat{p}]|0\rangle = N_e = \sum_n 2(\omega_n - \omega_0)|\langle n|\hat{r}|0\rangle|^2 \, , \tag{1.98}$$

where N_e is the total number of electrons in the system. If we consider the single-particle levels ψ_i then 1.98 becomes

$$\sum_{i,j}(f_i - f_j)(E_i - E_j)|\langle\psi_i|\hat{r}|\psi_j\rangle|^2 = N_e \, . \tag{1.99}$$

If now we make use of Sokhotski–Plemelj theorem[62] that states that

$$\lim_{\eta \to 0} \int \frac{1}{\omega' - \omega + i\eta} d\omega = P \int \frac{1}{\omega' - \omega} d\omega - i\pi\delta(\omega' - \omega) , \qquad (1.100)$$

then we can write the polarizability as

$$\alpha_0(\omega) = \int \frac{S(\omega')}{\omega - \omega' + i\eta} d\omega' \qquad (1.101)$$

where the so-called spectral function $S(\omega')$ is defined as

$$S(\omega') = \sum_i^3 \frac{1}{3} \sum_{nm} (f_n - f_m)| \langle \psi_n | \hat{r}_i | \psi_m \rangle |^2 \delta(\omega' - E_{nm}) . \qquad (1.102)$$

Finally, we can write

$$\int_0^\infty \text{Im}\{\alpha_0(\omega)\}\omega d\omega = -\pi \int_0^\infty\!\!\!\int S(\omega')\delta(\omega - \omega')d\omega'\omega d\omega$$

$$= -\pi \int_0^\infty\!\!\!\int \sum_{nm}(f_n - f_m)| \langle \psi_n | \hat{r} | \psi_m \rangle |^2\delta(\omega' - E_{nm})\delta(\omega' - \omega)d\omega'\omega d\omega$$

$$= -\frac{\pi}{3} \sum_{nm}(f_n - f_m)| \langle \psi_n | \hat{r}_i | \psi_m \rangle |^2 E_{nm}. \qquad (1.103)$$

By comparing 1.99 and 1.103 we conclude

$$\frac{1}{\pi} \int_0^\infty \text{Im}\{\alpha_0(\omega)\}\omega d\omega = N_e. \qquad (1.104)$$

The f-sum rule provides an easy way to check if the spectrum area is in agreement with the total number of electrons in the system. Although, here the f-sum rule has been derived for a nonineracting system its validity is general and holds also for interacting systems.

Oscillator Strength

The oscillator strength is a dimensionless quantity that characterizes the transition intensity between two states. It is defined as[63]

$$f_{nm} = \frac{1}{3}(f_n - f_m)\omega_{nm} \sum_{i=1}^3 | \langle \psi_n | r_i | \psi_m \rangle |^2 . \qquad (1.105)$$

It is possible to define the polarizability in terms of oscillator strengths

$$\alpha(\omega) = \sum_{n,m} \int \frac{1}{\omega_{nm}} \frac{f_{nm}}{\omega - \omega' + i\eta} d\omega' . \qquad (1.106)$$

Using 1.105 and 1.104 the f-sum rule becomes simply

$$\sum_{n,m} f_{nm} = N_e . \qquad (1.107)$$

FINITE TEMPERATURE

Most of the TDDFT calculations performed in this thesis the temperature is set to 0. For non-metallic systems most of the time the temperature dependence can be omitted, i.e. an electronic level is fully occupied or unoccupied. However, including a finite temperature in the calculations can be important in certain circumstances, see chapter 4. Considering a finite temperature allows to account for excitations from and to half-filled levels. In particular, this is important for molecules with almost degenerate levels around the Fermi energy. Practically, this consists of inserting a $T \neq 0$ in the Fermi-Dirac distribution. Thus, the occupations f_m become fractional and can vary from 0 to 2. In Fig. 1.5, the Fermi-Dirac (F-D) distribution and KS eigenenergies are plotted for a system consisting of a big graphene nanoflake with $\sim$1000 Carbon atoms, for T=300K. Including the temperature in this particular case, as in most of the cases analyzed in this thesis, would lead to negligible changes in the polarizability.
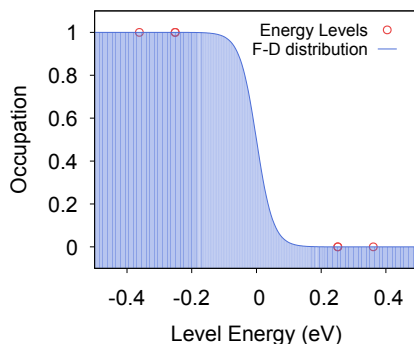

Figure 1.5: The molecular levels of the flake $C_{1014}H_{90}$ are shown as red dots. In blue the Fermi-Dirac (F-D) distribution is shown. An electron temperature of 300 K is assumed.

1.3.8 DENSITY CHANGE

Equation 1.56 describes the change in electron density due to the external time-dependent perturbation. In the frequency domain the electron density change is a complex quantity. The imaginary part is of particular interest because its spatial distribution indicates the parts of a system that are responsible for the absorption at a given resonant-mode frequency, see Section 1.3.3. Moreover, the combined information provided by the real and imaginary parts can be used to describe the real-time evolution of the induced density in real space, see chapter 1.3.9.

Plotting the density change pattern in real space can point to interesting qualitative applications as it gives a visual idea about the contribution to the optical absorption of different parts of molecules or solids such as atomic-size necks (section 5.2.10), impurities, absorbed atoms, molecule tailoring (section 3.7), dangling bond saturation (section 3.8), edges (3.5), etc..

Throughout the thesis, in many occasions, the induced density in real-space is plotted and analyzed in order to characterize or simply visualize a particular resonant mode. This

tool is of particular interest for the identification of plasmons. As it will be shown the density change is able to capture the expected pattern typical of collective excitations such as plasmons and can help to determine the nature of an excitation.

1.3.9 REAL TIME DENSITY CHANGE

In the previous sections, we have introduced the induced density in the frequency domain as a straightforward outcome of the linear response theory. The Fourier transform of $\delta n(\omega)$ is

$$\delta n(\mathbf{r}, t) = \frac{1}{2\pi} \int_{-\infty}^{+\infty} \delta n(\mathbf{r}, \omega) e^{i\omega t} \mathrm{d}\omega \tag{1.108}$$

If we consider an external perturbing electric field such as $E = E_0 \cos(\omega t)$ and making use of 1.56 and 1.92 we can write

$$\begin{aligned}
\delta n(\mathbf{r}, t; \omega_0) &= \frac{E_0}{2} \int \chi(\mathbf{r}, \mathbf{r}', \omega) \mathbf{r}' [\delta(\omega - \omega_0) + \delta(\omega + \omega_0)] e^{i\omega t} \mathrm{d}\mathbf{r}' \mathrm{d}\omega \\
&= E_0 \left[\delta n'(\mathbf{r}, \omega_0) \cos(\omega_0 t) - \delta n''(\mathbf{r}, \omega_0) \sin(\omega_0 t) \right] ,
\end{aligned} \tag{1.109}$$

where we use the symmetry relations of the real $\delta n'$ and imaginary $\delta n''$ parts of the density change, see Section 1.3.1. The indices in $n(\mathbf{r}, t; \omega_0)$ indicate that the density change is a function of time given a perturbing field of frequency ω_0.

The real and imaginary parts of the density change in the frequency domain are (see Equations 1.80 and 1.81)

$$\delta n'(\omega) \propto \frac{\omega - \omega_0}{(\omega - \omega_0)^2 + \eta^2} \tag{1.110}$$

$$\delta n''(\omega) \propto \frac{\eta}{(\omega - \omega_0)^2 + \eta^2} , \tag{1.111}$$

where ω_0 corresponds to one of the resonant frequencies of the system. The plots in Fig. 1.6 show the behavior of the real and imaginary parts of the polarizability which in the frequency domain is the same as the one described by the Equations 1.110 and 1.111. In particular, Fig. 1.6(a) pictures a system presenting a single excitation while 1.6(b) represents a three resonance system. When the excitation is isolated (Fig. 1.6(a)) the imaginary part always shows a maximum when the real part crosses the x-axis. Following 1.109, this leads to a real-time density change that at the resonant frequency is described exclusively by the imaginary part and, thus, it is out of phase with respect to the exciting perturbation. However, see Fig 1.6(b), when the resonances are overlapping, depending on their width, it is possible for the real part to have a value different from 0 at the resonant frequency (green dotted vertical line). This leads to a more complex density-change-pattern oscillation in real time, where the overall oscillation does not just follow the imaginary density change pattern at resonance. In this case, following 1.109, we find a real part that oscillates in phase with the external perturbing field. An example is shown in section 5.3. The real part oscillates in phase with the external perturbation while, the imaginary part is delayed, oscillating out of phase with respect to the electric field.
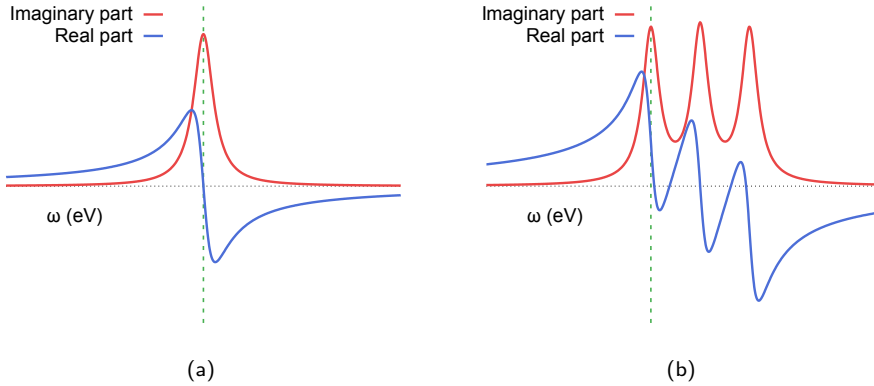
Figure 1.6: Example of the real and imaginary polarizability in the frequency domain. (a) single-resonance system. (b) multi-resonance system.

1.3.10 ELECTRIC CURRENT

The electric density change discussed above is intimately connected to the electron current. In fact, we can compute (calculate) the total charge inside a given volume Ω as $\delta Q(\mathbf{r}, t) = \int_\Omega \delta n(\mathbf{r}, t)\mathrm{d}\mathbf{r}$ and the current flowing through the surface S defining the volume Ω as $I = \mathrm{d}Q/\mathrm{d}t$. Using the continuity equation the current can be calculated as the surface integral of the current density flowing through the boundaries of the volume Ω, i.e. $\mathrm{d}Q/\mathrm{d}t = \int_S \mathbf{j}\cdot\mathrm{d}\mathbf{s}$. Averaged and maximal currents both involve the real and the imaginary parts of the total charge $Q(\omega)$:

$$I_{RMS}(\omega_0) = \frac{\omega_0}{\sqrt{2}}\sqrt{\delta Q'(\omega_0)^2 + \delta Q''(\omega_0)^2} \tag{1.112}$$

$$|I_{max}(\omega_0)| = \omega_0\sqrt{\delta Q'(\omega_0)^2 + \delta Q''(\omega_0)^2} \ . \tag{1.113}$$

I_{RMS} is the Root Mean Square value (RMS) of I while $|I_{max}(\omega_0)|$ is the modulus of the maximal current. The details of the derivation of Equations 1.112 and 1.113 are presented in Appendix E.

The two quantities are related by $\sqrt{2}$ factor, i.e. $I_{RMS} = \frac{|I_{max}|}{\sqrt{2}}$. The choice of the integration volume Ω determines a plane through which the flowing current is calculated. By defining the volume $\Omega < \Omega_{tot}$ where Ω_{tot} is the total volume of the box/cell where the molecule is placed we consequently define a plane between the two volumes Ω and Ω', where $\Omega' = \Omega_{tot} - \Omega$. see Fig. 1.7. The current calculated with this method describes the amount of charge displaced from the volume Ω to the volume Ω' and vice versa.
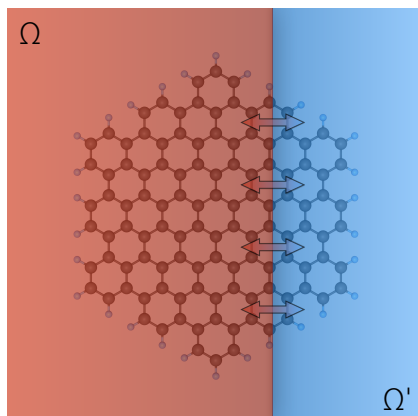
Figure 1.7: The volume Ω can be specially chosen. For instance, defining the volume semi-infinite and limited with a plane at a given orientation, we can compute the current through this plane The calculated current corresponds to the current flowing through the plane dividing Ω by Ω'.

This method is particularly useful when we want to calculate the time-dependent current passing through molecular junctions using a finite model for the electrodes or between acceptors and donors in molecules or again to calculate the amount of charge transfer. In sections 5.2.9 and 5.2.7 this method is applied to calculate the current flowing through an atomic-size neck connecting two metallic nanoparticles at the plasmonic resonance.

1.3.11 CASIDA'S EQUATION

Another approach, that I implemented in the MBPT-LCAO code, used to obtain the optical cross section for a system within the TDDFT framework makes use of the so-called Casida's equation,[64] (the full derivation can be found in Appendix J)

$$\Omega \mathbf{F}_I = \omega_I^2 \mathbf{F}_I .\tag{1.114}$$

This kind of approach consists in solving the eigenvalue Equation 1.114 to obtain the optical spectrum of the system. The method presented previously in Section 1.3.5, in which we calculated the polarizability $\alpha(\omega)$ from χ_0 without computing explicitly χ, does not provide any information about the eigenstates of the modes of the perturbed system. Furthermore, the modes with an even nature (dark modes) are not visible in the polarizability/cross section spectrum and so cannot be analyzed. It is, in fact, not possible to detect any mode corresponding to an even distribution of induced density with respect to the direction where the dipole is calculated. Such modes correspond to optically forbidden transitions. With the Casida approach we can calculate all the excitations of the system, including the dark ones. Moreover, we can calculate the eigenvectors of each mode in the KS electron-hole space. The resulting information can be used, to analyze the nature of the different modes, see chapter 6.

In Eq. 1.114, F_I are the eigenvectors of the system and ω_I represent the energy of the

modes. The matrix Ω is defined as

$$\begin{aligned}
\Omega_{EF,E'F'} &= \delta_{EF,E'F'}(\epsilon_E - \epsilon_F)^2 \\
&+ 2\sqrt{(f_E - f_F)(\epsilon_F - \epsilon_E)}f_{Hxc}\sqrt{(f'_E - f'_F)(\epsilon_{F'} - \epsilon_{E'})}\,.
\end{aligned} \tag{1.115}$$

The indexes E and F label the occupied and unoccupied states respectively. ω_E and ω_F are the energies of occupied and unoccupied states respectively. f_E and f_F are the Fermi-Dirac distributions for occupied and unoccupied levels respectively. When the temperature is taken to be 0 then f becomes the Heaviside function, see Section 1.3.7. f_{Hxc} is the kernel as introduced in Equation 1.91.

For a system of non-interacting particles the Ω matrix becomes diagonal and the elements of the diagonal are the squared energy difference of the KS states, i.e. $(\omega_E - \omega_F)^2$. Once the eigenvalues ω_I and eigenvectors $\mathbf{F}_I$ are found via matrix diagonalization, the cross section can be calculated as

$$\sigma(\omega) = \sum_I f_I \left[\frac{\eta}{(\omega - \omega_I)^2 + \eta^2} - \frac{\eta}{(\omega + \omega_I)^2 + \eta^2}\right] \tag{1.116}$$

where the oscillator strengths f_I are given by

$$f_I = \frac{2}{3}\sum_{i=1}^3 \left|d_i^{EF}\widetilde{S}_{EF,E'F'}^{-1/2}F_I^{E'F'}\right|^2, \tag{1.117}$$

with

$$\widetilde{S}_{EF,E'F'}^{-1/2} = \left(\delta_{EF,E'F'}\sqrt{\epsilon_F - \epsilon_E}\right)_{EF,E'F'}. \tag{1.118}$$

The dipole, $\mathbf{d}^{EF}$, is given by

$$d_i^{EF} = \int \psi^{E*}(\mathbf{r})\psi^F(\mathbf{r})r_i\mathrm{d}\mathbf{r} \tag{1.119}$$

and

$$\sum_{EF} d_i^{EF} c_{I,EF} = \sum_{EF} c_{I,EF} \langle\psi^E|\,\mathbf{r}\,|\psi^F\rangle = \langle\psi_I|\,\mathbf{r}\,|\psi_I\rangle\,, \tag{1.120}$$

where $|\psi_I\rangle$ are the natural orbitals. $c_{I,EF}$ are the transition matrix elements defined as

$$c_{I,EF} = \sum_{E'F'} \widetilde{S}_{EF,E'F'}^{-1/2}F_I^{E'F'}\,. \tag{1.121}$$

From the matrix elements $c_{I,EF}$ we can extract important information regarding the composition of each interacting mode in terms of Kohn-Sham wave functions $|\psi\rangle$ participating in the transition.

1.3.12 TDDFT Momentum Transfer

The transition matrix elements defined in 1.121 can be used to defined the interacting transition density $\phi^I(\mathbf{r})$ as

$$\phi^I(\mathbf{r}) = \sum_{EF} c_{I,EF} \psi^E(\mathbf{r}) \psi^F(\mathbf{r}) . \tag{1.122}$$

The quantity $\phi^I(\mathbf{r})$ contains information about the momentum transfer during the excitation. In order to find the corresponding quantity in momentum space $\phi^I(\mathbf{q}_i)$ a Fast Fourier Transform (FFT) has to be performed, see Appendix G. $\phi^I(\mathbf{q}_i)$ is a discrete quantity and the fineness of the grid in momentum space is $(\mathbf{q}_i - \mathbf{q}_{i+1})$. The function $\phi^I(\mathbf{q}_i)$ has a complex behavior with nonzero value for many different values of $\mathbf{q}_i$, therefore, it is not possible to have a single wave of momentum $\mathbf{q}$ contributing to $\phi^I(\mathbf{r})$. However, in Chapter 6 we show that it is possible to assign for a particular finite system a wavevector to each $\phi^I(\mathbf{r})$. The assignment is done by selecting the $\mathbf{q}_i$ that contributes the most in the momentum domain. The results of such an analysis on a sodium chain system are shown in Chapter 6.

1.3.13 Electron Energy Loss Spectroscopy

It is interesting to note that it is possible to analyze electron transitions and extract information about the momentum transfer from the TDDFT linear response theory developed in section 1.2.[65]

Fluctuation-Dissipation Theorem

The *dynamical structural factor*[66–68] is defined as, see appendix I,

$$S(\mathbf{q}, \omega) = \frac{1}{2\pi} \int \langle n_\mathbf{q}(t) n_\mathbf{q}^\dagger(0) \rangle e^{-i\omega t} \mathrm{d}t = Z^{-1} \sum_{mn} e^{-\beta E_m} |\langle \psi_n | n_\mathbf{q}^\dagger | \psi_m \rangle|^2 \delta(\omega + \omega_{nm}) , \tag{1.123}$$

where Z is the *partition function*, i.e. $Z = \sum_i e^{-\beta E_i}$, with $\beta = 1/K_B T$. If we invert the indexes we get[68]

$$S(\mathbf{q}, \omega) = Z^{-1} \sum_{mn} e^{-\beta E_n} |\langle \psi_m | n_\mathbf{q}^\dagger | \psi_n \rangle|^2 \delta(\omega + \omega_{mn}) \tag{1.124}$$

$$= Z^{-1} \sum_{mn} e^{-\beta E_n} |\langle \psi_n | n_\mathbf{q} | \psi_m \rangle|^2 \delta(\omega - \omega_{nm}) \tag{1.125}$$

$$= Z^{-1} \sum_{mn} e^{-\beta E_n} e^{+\beta E_m} e^{-\beta E_m} |\langle \psi_n | n_\mathbf{q} | \psi_m \rangle|^2 \delta(\omega - \omega_{nm}) \tag{1.126}$$

$$= e^{-\beta \omega} S(-\mathbf{q}, -\omega). \tag{1.127}$$

Because $S(-\mathbf{q}, -\omega) = S(\mathbf{q}, -\omega)$ we can write the

$$S(\mathbf{q}, \omega) = e^{-\beta \omega} S(\mathbf{q}, -\omega). \tag{1.128}$$

which is a way of expressing the *detailed balance principle*. The *detailed balance principle* at thermal equilibrium describes the dynamics of a two-state system and regulate a process and its inverse. The probability of a given process $\mathcal{P}_A$ is equal to the probability of the inverse process $\mathcal{P}_A^{-1}$.[69]

LINEAR RESPONSE AND DYNAMICAL STRUCTURAL FACTOR

Using 1.123 and 1.128 we can then connect the *dynamical structural factor* with the imaginary part of the linear response function in the momentum domain, see Appendix H,

$$
\begin{aligned}
\operatorname{Im}\{\chi(\mathbf{q}, \omega)\} &= \operatorname{Im}\left\{ \sum_n |\langle [n_{\mathbf{q}}(t) n_{\mathbf{q}}^\dagger(0)] \rangle \right\} \\
&= -\pi Z^{-1} \sum_{mn} |\langle \psi_n | n_{\mathbf{q}}^\dagger | \psi_m \rangle|^2 [\delta(\omega - \omega_{nm}) - \delta(\omega + \omega_{nm})] \qquad (1.129) \\
&= -\pi [1 - e^{-\beta\omega}] S(\mathbf{q}, \omega)
\end{aligned}
$$

In 1.130 we used the linear response function χ as in equation A.19 in momentum space, i.e. $\chi(\mathbf{q}) = \sum_n |\langle \psi_n | n_{\mathbf{q}}^\dagger | \psi_0 \rangle|^2$. For the temperature $T \to 0$ we obtain,

$$
-\frac{1}{\pi} \operatorname{Im}\{\chi(\mathbf{q}, \omega)\} = S(\mathbf{q}, \omega), \qquad (1.130)
$$

the *fluctuation-dissipation theorem*. This theorem connects the fluctuations in thermal equilibrium described by the dynamical structural factor (S) and the dissipated system energy which is described by the imaginary part of the response function $(\chi.)$ The response of the system to a small perturbation is equal to the response of the system to statistical fluctuations at the thermal equilibrium.

1.4 PLASMONS

A plasmon can be pictured as a collective electronic oscillation inside a metal. The electrons in the metal are considered free to move and oscillate in response to an external electric stimulus. Eventually, if the frequency of the external field matches the plasmon frequency of the system, a self-sustained mode called plasmon is generated. In our ab-initio approach, we would like to go even further, and define more precisely what "collective" means and how plasmon modes could be distinguished from other types of excitations even for small (nano) objects. In the next sections we are going to have a look at the microscopic approach to try to find a definition of plasmons in ab-initio TDDFT.

1.4.1 DIELECTRIC FUNCTION

In this section we discuss the plasmon dispersion in solids. In order to do so, first, it is convenient to define the microscopic dielectric function ϵ. The dielectric function connects the effective electric potential V_{tot} – total electric potential – with the external electric potential V_{ext}.

When subjected to an external scalar potential, an induced density $\delta n(\mathbf{r}, \omega)$ is created in the media. The response function connects the external perturbing potential and the

density change, $\delta n(\mathbf{r}, \omega) = \int \chi(\mathbf{r}, \mathbf{r}', \omega) V_{ext}(\mathbf{r}', \omega) \mathrm{d}\mathbf{r}'$, and the poles of χ correspond to the electronic excitations of the system. In turn, the created induced density generates an electric field opposed to the external one and, the corresponding induced potential can be approximated by

$$V_{ind}(\mathbf{r}, \omega) = \int v(\mathbf{r}, \mathbf{r}') \delta n(\mathbf{r}', \omega) \mathrm{d}\mathbf{r}'. \tag{1.131}$$

where $v(\mathbf{r}, \mathbf{r}') = f_H = 1/|\mathbf{r} - \mathbf{r}'|$. Here, for convenience, we restrict ourselves to the Random Phase Approximation (RPA), i.e. we consider only the Hartree term in the kernel, see Section 1.3.6. Thus, we can define the effective potential as the sum of the external and the induced potential (Eq. 1.52)

$$V_{tot}(\mathbf{r}, \omega) = V_{ext}(\mathbf{r}, \omega) + V_{ind}(\mathbf{r}, \omega) . \tag{1.132}$$

By combining the equations 1.131, 1.132 and 1.79 we obtain

$$V_{ext}(\mathbf{r}, \omega) = V_{tot}(\mathbf{r}, \omega) - \int v(\mathbf{r} - \mathbf{r}') \int \chi_0(\mathbf{r}', \mathbf{r}'', \omega) V_{tot}(\mathbf{r}'', \omega) \mathrm{d}\mathbf{r}' \mathrm{d}\mathbf{r}'' \tag{1.133}$$

$$= \int \left(\delta(\mathbf{r} - \mathbf{r}'') - \int v(\mathbf{r} - \mathbf{r}') \chi_0(\mathbf{r}', \mathbf{r}'', \omega) \mathrm{d}\mathbf{r}' \right) V_{tot}(\mathbf{r}'', \omega) \mathrm{d}\mathbf{r}''. \tag{1.134}$$

The quantity connecting the total potential with the external potential is called *dielectric function*

$$\epsilon(\mathbf{r}, \mathbf{r}', \omega) = \delta(\mathbf{r} - \mathbf{r}') - \int f_H(\mathbf{r} - \mathbf{r}'') \chi_0(\mathbf{r}'', \mathbf{r}', \omega) \mathrm{d}\mathbf{r}'' . \tag{1.135}$$

In order to understand the origin of resonant frequencies in the interacting absorption spectrum, we have to relate the non-interacting response function with the interacting response function in a convenient way. To do so we can write

$$\delta n(\mathbf{r}, \omega) = \int \chi(\mathbf{r}, \mathbf{r}') V_{ext}(\mathbf{r}', \omega) \mathrm{d}\mathbf{r}' = \int \int \chi(\mathbf{r}, \mathbf{r}') \epsilon(\mathbf{r}', \mathbf{r}'', \omega) V_{tot}(\mathbf{r}'', \omega) \mathrm{d}\mathbf{r}'' \mathrm{d}\mathbf{r}'$$
$$= \int \chi_0(\mathbf{r}, \mathbf{r}') V_{tot}(\mathbf{r}', \omega) \mathrm{d}\mathbf{r}' \tag{1.136}$$

which leads to

$$\chi_0(\mathbf{r}, \mathbf{r}', \omega) = \int \chi(\mathbf{r}, \mathbf{r}'', \omega) \epsilon(\mathbf{r}'', \mathbf{r}', \omega) \mathrm{d}\mathbf{r}'' . \tag{1.137}$$

Defining the inverse dielectric function ϵ^{-1} as

$$\int \epsilon^{-1}(\mathbf{r}, \mathbf{r}'', \omega) \epsilon(\mathbf{r}'', \mathbf{r}', \omega) \mathrm{d}\mathbf{r}'' = \delta(\mathbf{r}' - \mathbf{r}) \tag{1.138}$$

finally, we obtain

$$\chi(\mathbf{r}, \mathbf{r}', \omega) = \int \chi_0(\mathbf{r}, \mathbf{r}'') \epsilon^{-1}(\mathbf{r}'', \mathbf{r}', \omega) \mathrm{d}\mathbf{r}''. \tag{1.139}$$

The excitation energies in the interacting spectrum are the poles of the interacting linear response χ. Equation 1.139 shows that these poles can originate from poles in the non-interacting response function χ_0 or from the zeros of the dielectric function ϵ. At this point it is tempting to think that the zeros in the dielectric function are related to plasmonic modes while, peaks in χ that are originating from χ_0 can be connected to single e-h excitations. The "new" peaks in the spectrum arising from the zeros of the dielectric function are due to electron-electron Coulomb interactions that describe the interacting electrons in the external electric field. However, ϵ itself depends on χ_0 so that even when we hit the frequency of a pole of χ_0, the related pole in χ will undergo a small shift compared to the initial non-interacting resonant frequency.[26] Moreover, if a zero of ϵ is found for a frequency really close to a pole of χ_0 then the two excitation types mix if they have the same symmetry.[26] However, this way of describing and analysing the different nature of the absorption modes seems to be not completely appropriate. First of all, we assumed to be in the RPA and so we discarded the exchange-correlation term in the kernel defining χ from χ_0. However, even when using RPA the nature of the peak cannot be easily understood in terms of the relative shift of the peaks with respect to the non-interacting peaks as we shall see in chapter 6. Moreover, the information contained in the dielectric function goes beyond the plasmonic character of the excitations. Excitons or charge-transfer excitations can give rise to zeros in the dielectric function.

1.4.2 FREE ELECTRON GAS

If we consider a 3D gas made of non-interacting particles the Hamiltonian of the system is given by the kinetic energy

$$-\frac{\nabla^2}{2}\phi_k(\mathbf{r},\omega) = E\phi_k(\mathbf{r},\omega). \tag{1.140}$$

The single-particle state becomes

$$\phi_k(\mathbf{r},\omega) = \frac{1}{\sqrt{V}}e^{i\mathbf{k}\cdot\mathbf{r}} \tag{1.141}$$

$$E(k) = \frac{k^2}{2}, \tag{1.142}$$

where $\mathbf{k}$ is a good quantum number due to the system translational invariance. In such a system an external excitation can promote an electron from below the Fermi energy (E_F) to above E_F. Given 1.142 we can write the difference in energy between levels as

$$\Delta E(\mathbf{k},\mathbf{q}) = E(\mathbf{k}+\mathbf{q}) - E(\mathbf{k}) = \frac{(\mathbf{k}+\mathbf{q})^2}{2} - \frac{\mathbf{k}^2}{2} \tag{1.143}$$

$$= \frac{\mathbf{k}^2 + \mathbf{q}^2 + 2\mathbf{k}\cdot\mathbf{q}}{2} - \frac{(\mathbf{k})^2}{2} = \frac{\mathbf{q}^2}{2} + \mathbf{k}\cdot\mathbf{q}. \tag{1.144}$$

The defining conditions for electron-hole excitations are $|\mathbf{k}| \leq |\mathbf{k}_F|$ and $|\mathbf{k}+\mathbf{q}| \geq |\mathbf{k}_F|$. With this boundary conditions the range of energy allowed becomes,

$$\begin{aligned} \Delta E(q) &\leq k_F q + \frac{q^2}{2} \\ \Delta E(q) &\geq -k_F q + \frac{q^2}{2} \qquad \text{if} \quad q \geq 2k_F \end{aligned} \tag{1.145}$$

Starting from the definition of the non-interacting dielectric function and using the relation 1.135 with the Hartree kernel it can be shown that that condition the dielectric function to vanish is

$$\omega_p^2(q) = 4\pi n_0 + \frac{3}{5}k_F^2 q^2 \ , \tag{1.146}$$

where ω_p is the plasmon frequency of the electron gas, n_0 is the initial density, k_F is the Fermi wavevector and q is the momentum change. When the momentum transferred $\mathbf{q} = 0$ then from 1.146 we obtain the standard classical formula for the plasma frequency, in SI units

$$\omega_{plasma}^2 = \frac{4\pi e^2 n_0}{m} \ . \tag{1.147}$$
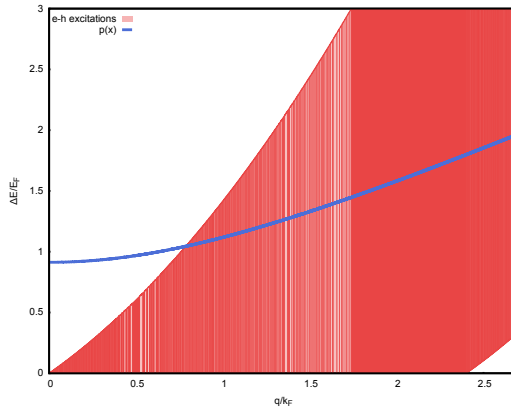
Graphically the results are shown in fig. 1.8,

Figure 1.8: Dispersion relation for electron excitations of the 3D free electron gas. Allowed e-h excitations are represented with red filling, and the solid blue curve represents the plasmon.

The plasmon is clearly visible where no e-h excitations are allowed. Once plasmon and e-h excitations coexist for a given momentum and energy, then they mix and it is difficult to distinguish unambiguously between the two.

The same type of analysis for a 1D system leads to[26]

$$\omega_p^2(q) = \frac{4}{\pi}k_F K_0(lq)q^2 + v_F^2 q^2 \ , \tag{1.148}$$

where K is the zeroth modified Bessel function of second kind and l is a length parameter modeling the width of the wire.[26] An example of a 1D electron gas is given in chapter 6.

2 | Methods and Codes

```
01000100 01101111 00100000 01100101 01101100
01100101 01100011 01110100 01110010 01101111
01101110 01110011 00100000 01101000 01100001
01110110 01100101 00100000 01101101 01100001
01110011 01110011 00111111 00100000 01001001
00100000 01100100 01101001 01100100 01101110
00100111 01110100 00100000 01100101 01110110
01100101 01101110 00100000 01101011 01101110
01101111 01110111 00100000 01110100 01101000
01100101 01111001 00100000 01110111 01100101
01110010 01100101 00100000 01100011 01100001
01110100 01101000 01101111 01101100 01101001
```

2.1 Density Functional Theory

For this work the MBPT-LCAO (Many Body Perturbation Theory with Linear Combination Atomic Orbitals)[17,18,20] code in conjunction with the SIESTA (Spanish Initiative for Electronic Simulations with Thousands of Atoms)[6,7] code have been employed. SIESTA is a GPL (General Public Licence) DFT package. It is used for calculating the ground-state properties for periodic and finite systems: energy-momentum dispersion bands for periodic systems, energy of electronic levels in molecules, total energy of the system, equilibrium geometry, etc. Whilst, the TDDFT calculations are performed using the MBPT-LCAO code. MBPT-LCAO is a non-commercialized code, and it can be viewed as a branch of the code FAST, developed within the NOSSI project funded by the French research agency ANR. MBPT-LCAO has been developed further mainly in San Sebastian - Donostia and used in several national and international projects: ORGAVOLT[(1)] ANR (France), SFB1083 (Germany, Spain), two projects funded by MINECO (Superhybrid 2014-2016, FUNMOLDEV 2017-2019) (Spain), PAMS (FET-EU project, 8 partners from all over europe). The code is composed of three blocks: GW approximation (GWA) block, Bethe-Salpeter (BSE) block and the TDDFT block. Although the basic idea foresees the use of the code in conjunction with SIESTA, by applying many-body perturbation theory, the code enables to calculate the

---

[(1)]ORGAVOLT is an international project involving groups from Spain and France focused on deriving and implementing a software for modeling organic solar cells, and funded by the French Research Agency under the ANR project.

corrected band gap, excitation energies, induced density, induced potential field, induced current, etc. in finite and extended atomistic systems. For this thesis in particular, I worked with the TDDFT block of the code, which have been used to calculate the polarizability, the optical cross-section, the density change and the induced current in different finite systems and molecules. The linear response theory is implemented in MBPT-LCAO using an iterative approach[17] and the so-called Casida's approach.[64] The details regarding the two implemented methods, as well as some other features characterizing the two approaches, are discussed throughout this chapter in the next sections.

2.2 SIESTA

SIESTA is a method and a computing code started at the end of the '90s inspired by the ab-initio Tight-Binding (TB) technique developed by Sankey and Niklewski[70] became a popular ab-initio code for electronic structure calculations. It is an $ab\text{-}initio$ DFT code designed in order to perform electronic ground-state calculations for periodic and finite systems. The use of localized basis sets and linear-scaling algorithms provides the user with a highly efficient code for electronic structure and molecular dynamics simulations.[71] Until recently, SIESTA was distributed free of charge to academic users. Starting with version 4.0 in spring 2016 the SIESTA package became GPL (General Public Licence) and also adopted a modern approach for developing of open-source software.[72]

In this section, as an introduction to the code, we will show two examples of SIESTA input files and explain the different lines in them. Moreover, two of the most important parameters that can be tuned in the input file will be discussed more in detail,

- Basis Set Multiplicity (2.2.2)
- Energy Shift (2.2.3)

Although the main goal of the thesis is the calculation and study of the optical properties, quality of the ground-state SIESTA calculations are of fundamental importance as it is shown in the following chapters. the chapters where the results will be presented. Thus, a convergence study of the ground-state calculations has to be performed in order to obtain reliable optical spectra. In particular, in Section 3.2 a convergence study is presented in detail for the case of graphene flakes.

2.2.1 SIESTA INPUT FILE

In the following section we will describe the most important parameters to set up for a calculation in the SIESTA input file. SIESTA uses its own Flexible Data Format (FDF) to define the physical and calculation parameters of the atomistic systems. In Appendix K, we show two examples of .fdf input files provided with comments. Prescriptions for the discussed options and many others, can be found in the SIESTA manual.[73] In particular, in the following sections we will describe in more detail the meaning of the $PAO.BasisSet$ (2.2.2) and $PAO.EnergyShift$ (2.2.3) parameters. Moreover, the different effects of $PAO.BasisSet$ and $PAO.EnergyShift$ parameters are studied in detail in Sections 3.2.1 and 3.2.2.

2.2.2 Basis Set Multiplicity

SIESTA uses LCAO (Linear Combinations of Atomic Orbitals) for constructing molecular orbitals (ψ_n),[7]

$$\psi_n(\mathbf{r}) = \sum_a X_a^n f^a(\mathbf{r}) . \qquad (2.1)$$

The expansion coefficients X_n^a are determined in a diagonalization procedure. The atomic orbitals $f^a(r)$ are given by a product of radial functions and spherical harmonics. The eigenfunctions in (2.1) are obtained within DFT.[6,74] The size of the basis, i.e. the number of orbitals per atom included in the calculation can be tuned by the user. However, to facilitate the use, a parameter sets the number of AO (Atomic Orbital) generated by the program. Different types of basis sets can be easily chosen by the user: *Single-ζ* (SZ), *Double-ζ* (DZ), *Triple-ζ* (TZ), *Single-ζ Polarized* (SZP) basis sets, *Double-ζ Polarized* (DZP) basis sets, *Triple-ζ Polarized* (TZP) basis sets, *Triple-ζ Double-Polarized* (TZDP) basis sets. However, there is the possibility for the user to define and add manually *ad-hoc* orbitals.

The SZ basis set is the minimal basis set available. It has one single radial function per angular momentum channel, i.e. carbon atom's valence orbitals 2s2p is described by 4 functions, 1 for the s-type orbital and 3 for the p-type orbitals. By adding a second function per channel the DZ basis set is obtained, in this case a carbon atom is described with 8 atomic functions. The default basis set in SIESTA is the DZP basis set, which adds polarization orbitals, i.e. orbitals with a higher angular momentum component. For instance, in case of the carbon atom described by a DZP basis 5 d-type extra-orbitals are added to the DZ basis set. Thus, valence electrons are described with a total of 13 functions per carbon atom when using the DZP basis set.

As we add orbitals, the basis set becomes more accurate. A larger basis set is usually providing a more accurate, reliable result. A more complete basis set is in principle a more precise basis set and is able to provide more reliable results. Furthermore, the choice of the basis set is related to the range of energy that we are interested in. In order to describe properly high-energy absorption-spectrum features a more complete set is needed, as shown in Section 3.2.1.

2.2.3 Energy Shift

PAOs in SIESTA are generated by imposing a cutoff radius beyond which the orbitals are set to 0. Such orbital confinement is controlled by the *PAO.EnergyShift* parameter rather than by the value of the cutoff radius itself. Solving the radial part of the Schödinger equation by adding an energy shift to the energy is equivalent to define a spherical box with infinite walls, the wavefunction is defined to be zero outside that sphere.[6] Usually, a common energy shift is fixed for all the chemical species avoiding the task to define different cutoff radii for different atoms and different angular momenta. The energy shift is given in units of Ry or meV and the default value is 0.02 Ry. The higher is the energy shift value the more contracted are the generated orbitals. Obviously, the extension of the orbitals affects the outcome of the calculation. More extended orbitals (small energy shift) provide in principle more accurate results however, it is more computationally costly. Thus,

it is important to perform convergence studies in order to make sure reasonable values of the $PAO.EnergyShift$ parameter are used. A convergence study for graphene nanoflakes is presented in Section 3.2.2.

In Fig. 2.1(a) we show 2p carbon orbitals generated using an energyshift of 50 meV and 100 meV. In Fig. 2.1(b) the same comparison is done for the polarization orbital with d-symmetry.
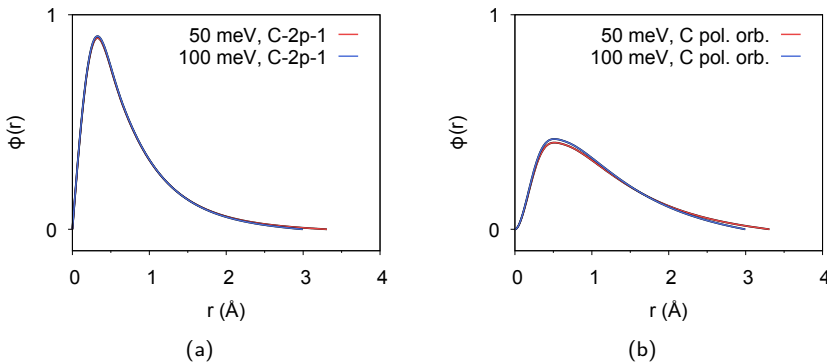

(a)

(b)

Figure 2.1: The effect of the energy shift parameter on the shape of the radial orbitals. Smaller energy shift leads to more extended orbitals.

2.3 MBPT-LCAO

Details about the MBPT-LCAO code can be found at http://mbpt-domiprod.wikidot.com and in the papers by P. Koval et al.,[17, 18, 20] where the methodology employed in the code is carefully explained.

GWA block, Bethe-Salpeter (BS) block and TDDFT block. The flexibility of the code structure allows the user to use each block independently. In particular, it is worth to notice that all electron calculations can be performed, although the code was designed to work in conjunction with the SIESTA code. In the later case, SIESTA calculations provide the input data that are used as starting point to perform ΔSCF, GWA or TDDFT calculations. In the following sections we present a detailed description of the most important features of the code.

2.3.1 Product Basis

MBPT-LCAO makes use of an *ad-hoc* basis set constructed inside the code to represent the products of atomic orbitals. The eigenstates entering the response function (1.78) are expressed using a Local Combination Atomic Orbitals (LCAO). Using an LCAO ansatz (Eq. 2.1) in expression 1.78 for the non-interacting response function, we arrive to expressions similar to that in 2.2. Unfortunately, a product of two atomic functions is generally not another atomic function and we need an additional basis set to express the response functions. This situation is different in using other basis sets as PW or real space grids. In

this case, it is frequently possible to express the product of two functions using the same expansion (PW cut-off) as used for the original functions. In Equation 1.78 for the linear response of a non-interacting system, the product of eigenfunctions $\psi_n^* \psi_m$ leads to a sum of products of atomic orbitals $f_a^* f_b$,

$$\psi_m^*(\mathbf{r})\psi_n(\mathbf{r}) = \sum_{ab} X_b^m X_a^n f^{b*}(\mathbf{r}) f^a(\mathbf{r}) . \tag{2.2}$$

In order to express the product $\psi_m^*(\mathbf{r})\psi_n(\mathbf{r})$ is useful to introduce a set of basis functions capable to span the space of atomic-orbital products. The set has to be as small as possible and contain preferably localized functions. There are several options to construct such set of functions, hereafter *product basis*.[20] The most widely known is probably the auxiliary functions for Gaussian basis sets.[75,76] However, the SIESTA method is based on the so-called Numerical Atomic Orbitals (NAO), that can be more flexible and economic than Gaussian basis sets. There are methods to construct the product basis sets for numerical orbitals.[77,78] In our MBPT-LCAO code we use the so-called *dominant products*.[79,80] The dominant product basis can be very accurate but requires a large number of functions that becomes prohibitive for large systems. Precisely for this reason, we have recently implemented the so-called atom-centered basis set. This is a more economical basis set as compared to the dominant products basis set and it increases the range of applicability and efficiency of the code without losing accuracy.

Dominant Products

The dominant products basis set[80] is formed by atomic-centered functions, *local products*, and by functions that are centered at the midpoint between the two atoms that form each pair, *bilocal products*. By construction the set of products of the orbitals belonging to two atoms contains collinear or nearly collinear elements, thus, a proper strategy consists in identifying the "dominant products" as special linear combinations in the space of products of orbitals such that the linear dependencies are minimized. In detail, we define

$$f^a(\mathbf{r})f^b(\mathbf{r}) = \sum_{\mu} V_\mu^{ab} F^\mu(\mathbf{r}) \tag{2.3}$$

$$F^\mu(\mathbf{r}) = \sum_{ab} \Lambda_{ab}^\mu f^a(\mathbf{r})f^b(\mathbf{r}) \tag{2.4}$$

$$\mathbf{V}^{-1} = \mathbf{\Lambda} , \tag{2.5}$$

where F^μ are the so-called *dominant product* while V_μ^{ab}, the vertex matrix, connects the "new" with the "old" basis set. The coefficients Λ_{ab}^μ are the elements of the eigenvectors of the metric in the space of orbital products, here the metric is defined using the Coulomb interaction,

$$g_{ab}^{a'b'} = \int f^a(\mathbf{r})f^b(\mathbf{r}) \frac{1}{|\mathbf{r} - \mathbf{r}'|} f^{a'}(\mathbf{r}')f^{b'}(\mathbf{r}') d\mathbf{r}d\mathbf{r}'. \tag{2.6}$$

Those initial atomic-orbital products associated with the pairs $(ab, a'b')$ that are orthogonal with respect to the Coulomb metric will provides null elements $g_{ab}^{a'b'}$. The solution of the

eigenvalue equation

$$g_{ab}^{a'b'} \Lambda_{a',b'}^{\mu} = \lambda^{\mu} \Lambda_{a,b}^{\mu} \qquad (2.7)$$

allows us to identify the "most important" dominant products. In practice, the eigenvalues λ^{μ} are used as indicators to determine the importance of a particular dominant product $F^{\mu}(\mathbf{r})$ to the completeness of the basis $\{F^{\mu}(\mathbf{r})\}$. By ignoring those eigenvectors correspondent to λ^{μ} lower that a chosen eigenvalue threshold we remove non-essential dominant products. The procedure is applied to each atom-pair individually keeping the operation count at $O(N)$ scaling where N is the number of atoms in the system. A dominant product index μ is connected to orbital indices a and b of one atom (local pairs) or two atoms (bilocal pair) rather than to all orbital indices in the molecule. The dominant products here described have been used in TDDFT, Hedin's GW approximation and for solving the Bethe-Salpeter equation.[17, 20–22, 81]

ATOM-CENTERED BASIS SET

The construction of dominant products has the important disadvantage of generating a large number of functions. This disadvantage stems from the construction procedure which is repeated independently for each atom pair. It is easy to see that the dominant products $F^{\mu}(\mathbf{r})$ can strongly overlap because different atom pairs can have the same or close centers at which the products have their maximal values. This fact results in a redundant description of the orbital products by the dominant product basis set when looking from the perspective of the whole system. In order to correct for this, we use an ansatz for the auxiliary basis set that is widely known in quantum chemistry,[75, 76] and also in more "physics-oriented" proposals.[77, 78, 82] The possibility to work with only *atom-centered* functions allows to reduce the linear dependencies in a product basis set because atom centers are separated from each other at least by a bonding distance, which prevents strong overlaps of the resulting functions. The local dominant products, defined as the dominant products obtained from the analysis of orbitals products belonging to the same atom, are taken as the atomic-centered functions $A^{\mu}(\mathbf{r})$. We, thus make the expansion

$$f^a(\mathbf{r})f^b(\mathbf{r}) = P_{\mu}^{ab} A^{\mu}(\mathbf{r}) . \qquad (2.8)$$

The procedure to find the new vertex P_{μ}^{ab} is based on the proposal of drawing a sphere around a given atom pair (a,b) with a radius corresponding to the maximal spatial extension of its orbital products, and consider all the atom centers within that sphere as contributing to the expansion of products of orbitals in that atom pair. The vertex is obtained as $P_{\mu}^{ab} = T^{ab,\nu}[v^{\nu,\mu}]^{-1}$ where $T^{ab,\nu} = \iint f^a(\mathbf{r})f^b(\mathbf{r})\frac{1}{|\mathbf{r}-\mathbf{r}'|}A^{\nu}(\mathbf{r}')\mathrm{d}\mathbf{r}\mathrm{d}\mathbf{r}'$ and $v^{\nu,\mu}$ is the Coulomb matrix element between the functions $A^{\nu}(\mathbf{r})$ and $A^{\mu}(\mathbf{r})$, i.e. $v^{\nu,\mu} = \iint A^{\nu}(\mathbf{r})\frac{1}{|\mathbf{r}-\mathbf{r}'|}A^{\mu}(\mathbf{r}')\mathrm{d}\mathbf{r}\mathrm{d}\mathbf{r}'$. Unfortunately, there is a limiting practical reason in using this strategy, the number of non-zero vertex elements P_{μ}^{ab} can be an order of magnitude bigger that the number of non-zero dominant products vertex elements V_{μ}^{ab}. This is due to distant bilocal atom pairs for which we have very few dominant products $F^{\mu}(\mathbf{r})$ but many atom-centered functions $A^{\mu}(\mathbf{r})$ contributing to such pairs.

A better strategy consists in re-expressing the bilocal dominant products in terms of functions centered on different atom centers,

$$F^\mu(\mathbf{r}) = c_\nu^\mu A^\nu(\mathbf{r}) \tag{2.9}$$

where

$$c_\nu^\mu = M^{\mu\nu'}[v^{\nu\nu'}]^{-1}. \tag{2.10}$$

$M^{\mu\nu'}$ and $v^{\nu'\nu}$ are the matrix elements of Coulomb operator,

$$M^{\mu\nu'} = \int F^\mu(\mathbf{r}) \frac{1}{|\mathbf{r}-\mathbf{r}'|} A^{\nu'}(\mathbf{r}') \mathrm{d}\mathbf{r}\mathrm{d}\mathbf{r}' \tag{2.11}$$

$$v^{\nu\nu'} = \int A^\nu(\mathbf{r}) \frac{1}{|\mathbf{r}-\mathbf{r}'|} A^{\nu'}(\mathbf{r}') \mathrm{d}\mathbf{r}\mathrm{d}\mathbf{r}' \tag{2.12}$$

The number of atom centers included in the description of a bilocal dominant product is defined by choosing those centers inside a sphere of a radius determined by the bilocal product. The projection 2.9 is useful because it is computationally very fast to pass from the dominant product set to the atom-centered product set and viceversa, depending on the quantity that needs to be computed. Actually, we found that it is faster to apply the non-interacting response in the basis of dominant products and, on the other hand, it is faster to compute and easier to store the TDDFT kernel in the basis of atom-centered functions.

2.3.2 ITERATIVE APPROACH

We can write the non-interacting linear response 1.78 in terms of dominant products using 2.2 and 2.3

$$\chi_0(\mathbf{r}) = \sum_{\mu,\nu} F^\mu(\mathbf{r}) \chi_{\mu\nu}^0(\omega) F^\nu(\mathbf{r}') \tag{2.13}$$

$$\chi_{\mu\nu}^0(\omega) = \sum_{\substack{n,m \\ a,b \\ c,d}} (f_m - f_n) \frac{\left(X_a^m V_\mu^{ab} X_b^n\right)\left(X_c^n V_\nu^{cd} X_d^m\right)}{\omega - E_{mn} + i\eta} . \tag{2.14}$$

If we assume the interacting response function to be written in the same fashion we can write the Petersilka-Gossmann-Gross equation 1.82, in matrix form as

$$\chi_{\mu\nu}(\omega) = \chi_{\mu\nu}^0(\omega) + \sum_{\mu'\nu'} \chi_{\mu\mu'}^0(\omega) f_{Hxc}^{\mu'\nu'} \chi_{\nu'\nu}(\omega) . \tag{2.15}$$

or, suppressing the indices we obtain for the response matrix

$$\chi = \left[\mathbb{1} - \chi^0 f_{Hxc}\right]^{-1} \chi^0 . \tag{2.16}$$

Consequently, the polarizability tensor becomes

$$P = d\left[\mathbb{1} - \chi^0 f_{Hxc}\right]^{-1} \chi^0 d \tag{2.17}$$

where $d_i^\mu = \int F^\mu(\mathbf{r})r_i \mathrm{d}\mathbf{r}$ are the dipole moments of the product functions. Apart from polarizability also the induced density δn will be computed $\delta n(\omega) = [\mathbb{1} - \chi^0(\omega)f]^{-1}\chi^0(\omega)d$ so that

$$[\mathbb{1} - \chi^0(\omega)f]\delta n(\omega) = \chi^0(\omega)d. \tag{2.18}$$

THE GMRES METHOD

Instead of solving 2.18 by inverting $[\mathbb{1} - \chi^0(\omega)f]$ a Generalized Minimal RESidue (GM-RES)[83, 84] method is used to calculate δn. An iterative approach[17] similar to the Arnoldi method and optimized for providing directly the polarizability P rather than the density change $\delta n(\omega)$ is adopted. GMRES belongs to the Krylov-type methods[83, 85] and it is used to solve linear system of equations of the form $A\vec{X} = \vec{b}$. In this method a Krylov-type basis is iteratively constructed. Starting from the matrix-vector multiplication between A and a trial initial vector $|v_1\rangle$, it is possible to build up the subspace; after each iteration a new vector is added to the Krylov space. The first vector $|v_1\rangle$ is chosen equal to $|b\rangle$. The new vectors are computed recursively and orthonormalized using the Gram-Schmidt procedure,

$$|v_i\rangle = A|v_{i-1}\rangle - \sum_{j=1}^{i-1} \frac{\langle v_j| A |v_i\rangle}{\langle v_j|v_j\rangle} |v_j\rangle. \tag{2.19}$$

The orthonormal basis $\{v\}$ built in this way is used in the GMRES method to approximately solve the original system of equations by minimizing the residue $|r_m\rangle = A|X_m\rangle - b$. The process is iterated until a reasonable value of the residue is found. Then, the approximate solution is found as $|X\rangle = \sum_i \langle v_i|x\rangle |v_i\rangle$. Moreover, in the specific case we are considering in Eq. 2.19, in order to avoid matrix multiplications, the application of the matrix A to a vector $|z\rangle$ is done sequentially by computing first $|z'\rangle = f_{Hxc}|z\rangle$ and then $A|z\rangle = |z\rangle - \chi^0(\omega)|z'\rangle$. The kernel matrix is computed before the iterative procedure. It can be easily stored and reused since it is frequency-independent with the standard "adiabatic" DFT functionals, while the procedure for matrix-vector product $\chi^0(\omega)\mathbf{z}$ is detailed in the next section.

KOHN-SHAM RESPONSE FUNCTION, $\chi^0(\omega)$

The iterative procedure outlined above uses a matrix-vector product $\chi^0(\omega)\mathbf{z}$ in order to construct a Krylov space and computes the density change $\delta n(\mathbf{r}, \omega)$ and the polarizability. The matrix-vector product will be split into a series of matrix-vector and matrix-matrix operations according to the explicit expression for non-interacting response function 2.14. Namely, the action of χ^0 to a given vector $\mathbf{z}$ is given by

$$\delta n_\mu^0(\omega) = \sum_{\substack{n,m \\ a,b \\ c,d}} (f_m - f_n)\frac{\left(X_a^m V_\mu^{ab} X_b^n\right)\left(X_c^n V_\nu^{cd} X_d^m\right)}{\omega - E_{mn} + i\eta}\vec{d}_j^\nu \tag{2.20}$$

and can be split into the following sequence of operations,

$$\sum_d V_\nu^{cd} X_d^m = \alpha_\nu^{cm} \qquad \text{index } m \text{ runs over the occupied KS orbitals}$$

$$\downarrow$$

$$\sum_\nu \alpha_\nu^{cm} d_j^\nu = \beta_j^{cm}$$

$$\downarrow$$

$$\sum_c X_c^n \beta_j^{cm} = \gamma^{nm} \qquad \text{index } n \text{ runs over the unoccupied KS orbitals}$$

$$\downarrow$$

$$\gamma_j^{nm}(f_m - f_n)\left(\frac{1}{\omega - E_{mn} + i\eta}\frac{1}{\omega + E_{mn} + i\eta}\right) = \tilde{\gamma}_j^{nm}$$

$$\downarrow$$

$$X_b^n \tilde{\gamma}_j^{nm} = \tilde{\beta}_j^{mb}$$

$$\downarrow$$

$$\delta n_\mu^0 = \alpha_\mu^{mb} \tilde{\beta}_j^{mb}.$$

α_ν^{cm} is stored in a block-sparse storage that uses $O(N^2)$ elements of the random access memory (RAM). The sequence of matrix operations detailed above enables a relatively fast calculation of interacting polarizability in plasmonic systems, i.e. in systems that have many nearly-degenerated transitions. This allows us to perform calculations for system sizes containing hundreds of atoms, despite the fact that our implementation uses only OpenMP parallelization, i.e. can use only relatively small number of processors through the OpenMP parallelization scheme.

2.3.3 TDDFT Kernel and LIBXC Library

The kernel, defined as in Equation 1.88, is necessary in order to solve Equation 1.82 and to calculate the linear response function χ. It is interesting to derive the exchange-correlation kernel f_{xc} starting from the exchange-correlation energy functional ϵ_{xc} in Generalized Gradient Approximation (GGA). We shall calculate before the exchange-correlation potential V_{xc} defined as $\frac{\delta \epsilon_{xc}}{\delta n}$ and eventually the exchange-correlation kernel $f_{xc} = \frac{\delta V_{xc}}{\delta n}$.

Let us consider an exchange-correlation energy functional of the density n and of its gradient $\vec{\nabla} n$. In case of GGA we can generally write

$$E_{xc} = \int \epsilon_{xc}(n(\mathbf{r}), \nabla n(\mathbf{r})) \mathrm{d}\mathbf{r} \tag{2.21}$$

where ϵ_{xc} is the energy per unit of volume. Using equation F.7 in Appendix F we can write the potential as

$$V_{xc}(\mathbf{r}) = \frac{\partial \epsilon_{xc}}{\partial n(\mathbf{r})} - \nabla \cdot \frac{\partial \epsilon_{xc}}{\partial \nabla n(\mathbf{r})} \ . \tag{2.22}$$

Finally, the exchange-correlation kernel f_{xc} needed in TDDFT can be found by performing a further functional derivative to the expression 2.22, i.e. $f_{xc} = \delta V_{xc}/\delta n = \delta^2 \epsilon_{xc}/\delta n^2$. In order to calculate the kernel in practice it is convenient to write the potential in an integral

form, $V_{xc}(\mathbf{r}) = \int V_{xc}(\mathbf{r}')\delta(\mathbf{r} - \mathbf{r}')\mathrm{d}\mathbf{r}'$. Thus, we can write

$$
\begin{aligned}
\delta V_{xc}(\mathbf{r}) &= \frac{\delta V_{xc}(\mathbf{r})}{\delta n(\mathbf{r})}\delta n(\mathbf{r}) + \frac{\delta V_{xc}(\mathbf{r})}{\delta \nabla n(\mathbf{r})}\delta \nabla n(\mathbf{r}) \\
&= \frac{\delta}{\delta n(\mathbf{r})}\left[\frac{\partial \epsilon_{xc}}{\partial n(\mathbf{r})} - \nabla \cdot \frac{\partial \epsilon_{xc}}{\partial \nabla n(\mathbf{r})}\right]\delta n(\mathbf{r}) + \frac{\delta}{\delta \nabla n(\mathbf{r})}\left[\frac{\partial \epsilon_{xc}}{\partial n(\mathbf{r})} - \nabla \cdot \frac{\partial \epsilon_{xc}}{\partial \nabla n(\mathbf{r})}\right]\delta \nabla n(\mathbf{r}) \\
&= \frac{\partial^2 \epsilon_{xc}}{\partial n^2}\delta n(\mathbf{r}) + \frac{\partial^2 \epsilon_{xc}}{\partial \nabla n \partial n}\delta \nabla n(\mathbf{r}) - \nabla \cdot \left[\frac{\partial^2 \epsilon_{xc}}{\partial n \partial \nabla n}\delta n(\mathbf{r}) + \frac{\partial^2 \epsilon_{xc}}{\partial \nabla n \partial \nabla n}\delta \nabla n(\mathbf{r})\right]
\end{aligned}
\tag{2.23}
$$

In order to "convert" the variations density of the density gradient $\delta \vec{\nabla} n$ into variations of the density δn we use the identity $f(x) = \int f(x')\delta(x - x')\mathrm{d}x'$,

$$
\begin{aligned}
\delta V_{xc}(\mathbf{r}) &= \int \delta(\mathbf{r} - \mathbf{r}')\left\{\frac{\partial^2 \epsilon_{xc}}{\partial n^2(\mathbf{r}')}\delta n(\mathbf{r}') + \frac{\partial^2 \epsilon_{xc}}{\partial \nabla n(\mathbf{r}')\partial n(\mathbf{r}')}\delta \nabla n(\mathbf{r}')\right. \\
&\quad \left. - \nabla \cdot \left[\frac{\partial^2 \epsilon_{xc}}{\partial n(\mathbf{r}')\partial \nabla n(\mathbf{r}')}\delta n(\mathbf{r}') + \frac{\partial^2 \epsilon_{xc}}{\partial \nabla n(\mathbf{r}')\partial \nabla n(\mathbf{r}')}\delta \nabla n(\mathbf{r}')\right]\right\}\mathrm{d}\mathbf{r}' \\
&= \int \delta(\mathbf{r} - \mathbf{r}')\frac{\partial^2 \epsilon_{xc}}{\partial n^2(\mathbf{r}')}\delta n(\mathbf{r}')\mathrm{d}\mathbf{r}' - \int \nabla \left[\frac{\partial^2 \epsilon_{xc}}{\partial \nabla n(\mathbf{r}')\partial n(\mathbf{r}')}\delta(\mathbf{r} - \mathbf{r}')\right]\delta n(\mathbf{r}')\mathrm{d}\mathbf{r}' \\
&\quad + \int \left[\nabla \delta(\mathbf{r} - \mathbf{r}')\right]\frac{\partial^2 \epsilon_{xc}}{\partial n(\mathbf{r}')\partial \nabla n(\mathbf{r}')}\delta n(\mathbf{r}')\mathrm{d}\mathbf{r} \\
&\quad - \int \nabla \left\{\left[\nabla \delta(\mathbf{r} - \mathbf{r}')\right]\frac{\partial^2 \epsilon_{xc}}{\partial \nabla n(\mathbf{r}')\partial \nabla n(\mathbf{r}')}\right\}\delta n(\mathbf{r}')\mathrm{d}\mathbf{r}' \\
&= \int \left\{\delta(\mathbf{r} - \mathbf{r}')\frac{\partial^2 \epsilon_{xc}}{\partial n^2(\mathbf{r}')} - \delta(\mathbf{r} - \mathbf{r}')\nabla \left[\frac{\partial^2 \epsilon_{xc}}{\partial \nabla n(\mathbf{r}')\partial n(\mathbf{r}')}\right]\right. \\
&\quad \left. - \nabla \left[\left[\nabla \delta(\mathbf{r} - \mathbf{r}')\right]\frac{\partial^2 \epsilon_{xc}}{\partial \nabla n(\mathbf{r}')\partial \nabla n(\mathbf{r}')}\right]\right\}\delta n(\mathbf{r}')\mathrm{d}\mathbf{r}' \ .
\end{aligned}
\tag{2.24}
$$

Using the fact that by definition $\delta V_{xc} = \int \frac{\delta V_{xc}}{\delta n}\delta n(\mathbf{r})\mathrm{d}\mathbf{r}$ we get

$$
\begin{aligned}
f_{xc}(\mathbf{r} - \mathbf{r}') &= \delta(\mathbf{r} - \mathbf{r}')\frac{\partial^2 \epsilon_{xc}}{\partial n^2(\mathbf{r}')} - \delta(\mathbf{r} - \mathbf{r}')\nabla_i \left[\frac{\partial \epsilon_{xc}}{\partial \nabla_i n(\mathbf{r}')\partial n(\mathbf{r}')}\right] \\
&\quad - \nabla_k \left[\left[\nabla_i \delta(\mathbf{r} - \mathbf{r}')\right]\frac{\partial^2 \epsilon_{xc}}{\partial \nabla_k n(\mathbf{r}')\partial \nabla_i n(\mathbf{r}')}\right] \ .
\end{aligned}
\tag{2.25}
$$

In the last equation the subscripts in ∇_i and ∇_k indicate the direction.

LIBXC OUTPUTS

Recently, we have coupled the LIBXC library[86] to the MBPT-LCAO code. LIBXC is a powerful library that allows to access many different types of functionals. In practice, the library provides several outputs that have to be put together carefully in order to build the potential and/or the kernel. The different outputs provided by LIBXC in case of GGA functionals are:

- $\frac{\partial \epsilon}{\partial n}$ (first partial derivative of the energy per unit volume in terms of the density).
- $\frac{\partial \epsilon}{\partial \sigma}$ (first partial derivative of the energy per unit volume in terms of sigma).
- $\frac{\partial^2 \epsilon}{\partial n \partial n}$ (second partial derivative of the energy per unit volume in terms of the density).
- $\frac{\partial \epsilon}{\partial n \partial \sigma}$ (second partial derivative of the energy per unit volume in terms of the density and sigma).
- $\frac{\partial^2 \epsilon}{\partial \sigma \partial \sigma}$ (second partial derivative of the energy per unit volume in terms of the density and sigma).

Where σ is the so-called contracted gradients of the density $\sigma = (\nabla n)^2$. With the provided outputs the user has to build up the correct exchange-correlation potential and kernel. Equation 2.22 becomes

$$V_{xc}[n] = \frac{\partial \epsilon_{xc}[n, \nabla n]}{\partial n} - 2\nabla \cdot \left[\frac{\partial \epsilon_{xc}[n, \nabla n]}{\partial \sigma} \nabla n \right] . \tag{2.26}$$

While Equation 2.25 becomes

$$f_{xc}[n] = \delta(\mathbf{r} - \mathbf{r}') \frac{\partial^2 \epsilon_{xc}[n, \nabla n]}{\partial n^2} - 2\delta(\mathbf{r} - \mathbf{r}')\nabla \left[\frac{\partial \epsilon_{xc}[n, \nabla n]}{\partial \sigma \partial n} \right] \tag{2.27}$$

$$- 4\nabla \left[[\nabla \delta(\mathbf{r} - \mathbf{r}')] \frac{\partial^2 \epsilon_{xc}[n, \nabla n]}{\partial \sigma^2} \right] . \tag{2.28}$$

The computation of the matrix elements $f_{xc}^{\mu\nu}[n]$ between atomic-orbital-like functions $F^{\mu}(\mathbf{r})$ can be written in terms of integrals involving the gradient of the functions as described in our paper P. Koval et al.[20]

3 | Optical Properties of Graphene-like Material

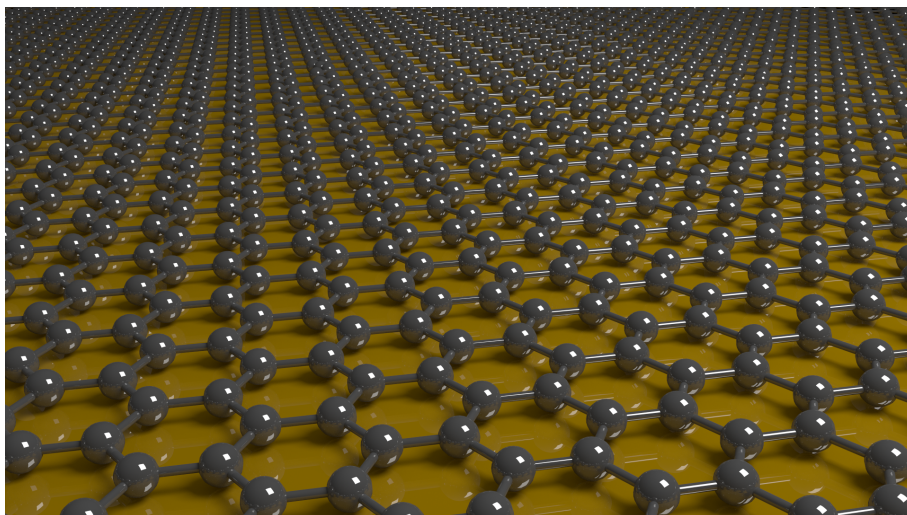Figure 3.1: 3D visualization of the honeycomb lattice structure of a graphene layer.

The recent discovery of graphene in 2004[23,24] prompted intensive investigations[87] mainly because of the perspectives for many potential applications, Although, we are still far from the moment when it will become a commercial reality. At first, graphene was produced by mechanically exfoliating a piece of graphite.[23] Nowadays, and depending on the application, graphene can be produced in mainly two formats: films and platelets. While films are mainly manufactured by Chemical Vapour Deposition (CVD) on different substrates, liquid phase exfoliation techniques are the preferred for making platelets which consists of micro graphene-flakes in form of powder. The peculiar graphene structure and electronic configuration provide the material with new unseen properties useful for many possible industrial applications such as its high electronic mobility which is reported to be higher than 200000 $cm^2V^{-1}s^{-1}$,[25] high flexibility, high transparency,[88] high mechanical strength, good thermal conductivity,[89] etc., with potential applications in many different fields such as

plasmonics,[90] photonics,[91] energy storage,[91] flexible electronics,[91] aerospace, optical signal processing,[92] etc. Possible applications include the use of graphene for optical waveguides in nanocircuits capable to confine light to the nanometer scale and transmit optical signals. Moreover, its transparency makes it a suitable candidate for electrodes in new photovoltaic cells. The characterization of graphene's optical properties is based on the analysis of the material as it interacts with an electric time-dependent field, that represents the light field, via quantities such as density change, polarizability and cross-section.

Main objective of this work is to study the 0-dimensional homologous of graphene, i.e. *graphene nanoflakes*. Graphene nanoflakes have even more versatile properties than an infinite sheet of graphene. However, to better interpret the electronic and optical properties of the graphene flakes it is useful to compare them with the infinite graphene.

3.0.1 GRAPHENE STRUCTURE

The theory of graphene and its derivatives has anticipated their experimental realization. The band structure of the graphene's honey-comb lattice was first analyzed in 1947.[93] Graphene is characterized by a honeycomb lattice formed by carbon atoms, Fig. 3.1. The carbon-carbon distance in graphene is 1.42 Å,[94] although the carbon-carbon bond is highly flexible.[95] Due to the hexagonal structure formed by the carbon atoms, graphene shows a typical linear dispersion at the so-called Dirac points K and K' (Dirac fermion).[96] At the K point in neutral graphene the Fermi energy (E_F) crosses exactly the Dirac point yielding zero Density Of the States (DOS) at E_F. The calculated SIESTA DFT band structure for an infinite graphene sheet is shown in Fig. 3.2(a). On the y-axis I plot the energy of the KS bands with subtracted Fermi Energy, while the momentum is displayed along the x-axis. The symmetry points K, M and Γ are highlighted on the x-axis and by vertical lines. The valence and conduction bands meet at the corners of the Brillouin Zone (BZ) (K points) at the Fermi energy, which has been set to 0 eV. In Fig. 3.2(b), I show in the reciprocal space the path chosen for the band structure plot of Fig. 3.2(a). b_1 and b_2 are the unit vectors in the reciprocal space.
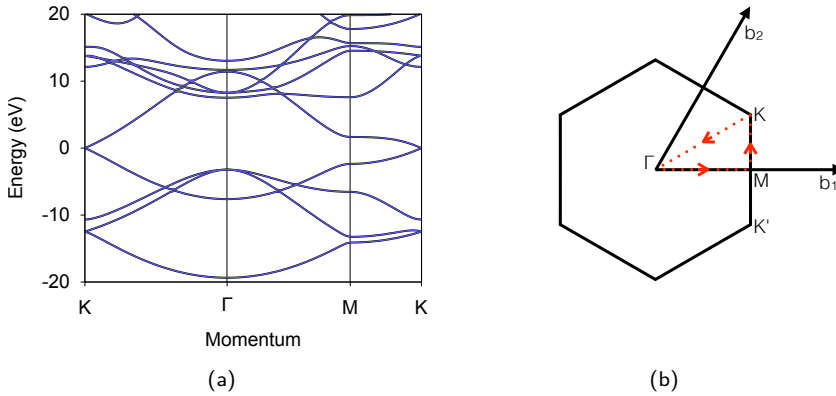
Figure 3.2: Graphene band structure in panel (a). In panel (b) the red dotted line shows the path in the Brillouin Zone (BZ) along which the bands in panel (a) are calculated.

The hexagonal lattice provides graphene with a trigonal structure characterized by the in-plane orbitals forming the σ bonds, which connect each carbon atom with its closest neighboring atom. The σ bond is the outcome of a sp^2 hybridization, see Fig.3.3, involving the s, p_x and p_y orbitals, xy-plane being parallel to the graphene sheet. The so-called π bands are formed by the out-of-plane p_z orbitals.[95]
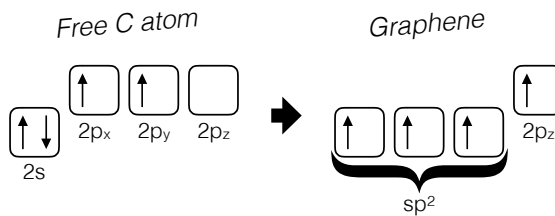
Figure 3.3: Graphene hybridization scheme.

Graphene's electronic and optical properties are determined by the π bonding (valence band) and π^* anti-bonding (conduction band) orbitals. Although the conductivity of the neutral graphene is quite low due to the zero DOS at the K point (see fig.3.2(a)), it can be enhanced by tuning the Fermi level via doping the material. Analogously, the control of the optically active electronic excitations can be reached by doping the material. In nutshell, by changing the E_F of graphene we introduce a range in energy equal to twice the shift of the E_F in which no interband optical transitions are allowed, as shown in Fig.3.4. In a dispersion plot for energies below $2\Delta E_F$ no interband transitions are allowed, resulting in the appearance of well-defined low energy electronic excitations (same as in Capture 3.4).
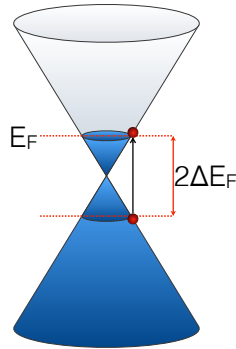
Figure 3.4: At the Dirac cone, for doped graphene, the Fermi energy is shifted (in this case electrons have been added to the system). A minimum amount of energy of twice the shift of Fermi energy compared to the undoped graphene is needed to allow optically driven electronic excitations.

The electronic and optical properties of graphene flakes are even more versatile than these of infinite graphene sheets. Such properties characteristic of graphene nanoflakes are discussed in the next section.

3.1 GRAPHENE NANOFLAKES

As nanotechnology evolved, it became possible to "cut" two-dimensional graphene and produce one-dimensional (nanoribbons) and zero-dimensional (nanodots) planar structures.[97, 98] Due advance in technology allowing the fabrication of graphene nanodots[94] a new wave of theoretical studies of nanodots and nanoflakes has been triggered. Remarkably, the reduction of dimension opens additional ways to control the electronic properties of these graphene derivatives. For instance, it is experimentally found that the width of nanoribbons affects its magneto-resistance[99] and their electron-transfer characteristics.[100] Graphene nanoribbons are currently produced with high accuracy using "on-surface" chemistry techniques,[101] a variant of CVD technique. Moreover, it is experimentally confirmed that the type of edges created by cutting the sheet in different directions determines the resistance of thin nanoribbons[102] and the edge's functionalization modifies their optical properties.[103] Furthermore, zero-dimensional derivatives should exhibit an additional versatility, compared to one-dimensional nanoribbons, due to the multitude of possible shapes. Several groups actually fabricated 0D graphene islands either via a top-down or bottom-up approaches.[2, 94, 104–106] There is experimental evidence that the size of graphene nanoislands can be controlled,[107, 108] nanoislands can also be chemically functionalized[104, 109, 110] and electrically doped.[111] Graphene nanoislands are also being produced by CVDs methods, like graphene on Ni(111),[112] although it is difficult to desorb the islands from the surface. Recently, nanotube transistors have shown size-independent resistance, this result opens the way to the fabrication of new graphene-based nano-transistors smaller that the actual silicon-based transistors allowing scaled device technologies.[113]

In this work we focus on graphene nanoflakes with the goal to theoretically model the

effects of shape, size and, edge functionalization. Nanoflakes can be regarded as poly-cyclic aromatic hydrocarbons which also received a considerable theoretical attention.[60,114] Several authors employed tight-binding (TB) models to characterize energy levels and optical excitation spectra of hexagonal, rectangular and triangular flakes.[115–117] Despite their simplicity, TB models describe the dependence of the low-energy spectra of the graphene nanoislands on size, shape, type of edges, external mechanical strains, magnetical and electrical fields.[111,118–120] Many first-principles calculations have been performed to characterize graphene nanoislands. DFT and TDDFT have been extensively used to study all the above mentioned properties of nanoislands.[94,121–123] Additionally to the problems accounted by TB models, first-principles calculations can naturally tackle the problem of chemical functionalization.[123–125] For instance, Zheng and Duley[124,125] studied small rectangular flakes with B3LYP functional and found that the density of states of these flakes dramatically changes upon application of external electrical field across zigzag edges and upon chemical doping with boron and nitrogen. Another comprehensive (molecular dynamics, DFT, TDDFT) study[121] revealed the thermo-stability properties, size and shape dependence of transport- and optical gaps of the rectangular, triangular and hexagonal flakes that contain up to 240 carbon atoms. It is interesting to note that such small flakes (240 carbon atoms, 2.4 nm edge length) can be already fabricated.[105] This fact makes theory and experiment overlap. However, much larger graphene nanodots (measuring a few dozens nm) will always be relevant for *plasmonic* applications due to their better coupling to external optical fields. Therefore, the advancing of theoretical methods is required in order to allow for an efficient ab-initio description of large nanodots.

In this chapter, we perform TDDFT calculations of graphene nanoflakes of considerable larger sizes, relevant for plasmonic field-enhancement applications.[90,111,126] Moreover, we aim at preserving the ab-initio merits of our theoretical framework, in order to credibly describe realistic *chemical modifications* of graphene nanoflakes and nanodots.

In the Section 3.2 we justify the calculational parameters, and then, in Section 3.3 and 3.4 we perform an analysis of the optical spectrum in terms of involved symmetries of atomic orbitals. The size dependence will be discussed in Section 3.5. In Section 3.6 we discuss the spatially resolved representation of electronic excitations given by the induced density change. Finally, in Section 3.7 we analyse the effect of graphene tailoring and graphene passivation. Depending on the way the graphene is cut, graphene flakes can have two different types of edges: ArmChair (AC) and ZigZag (ZZ). For this study we considered three different geometries of graphene flakes: HEXagonal (HEX) with AC edges, hexagonal with ZZ edges, and (nearly) SQuare flakes (SQ) in which are present both AC and ZZ edges. For the square flakes the length of edges can be equal only approximately. Examples of the different geometries are shown in Fig.3.5(a), 3.5(b) and 3.5(c) for hexagonal and square flakes. The flakes in Fig.3.5 are medium/small having a lateral dimension between ~17 Å and ~22 Å. The flake sizes considered in this study go from a minimum of ~10 Å to a maximum of ~60 Å, in lateral dimensions. For hydrogen saturated graphene nanoflakes ideal geometries are used. Namely, the structures are strictly planar and the carbon-carbon distance is held fixed to its experimental value 1.42 Å.[94] The edges of the flakes are saturated by hydrogen with a carbon-hydrogen distance of 1.09 Å.[124,127]
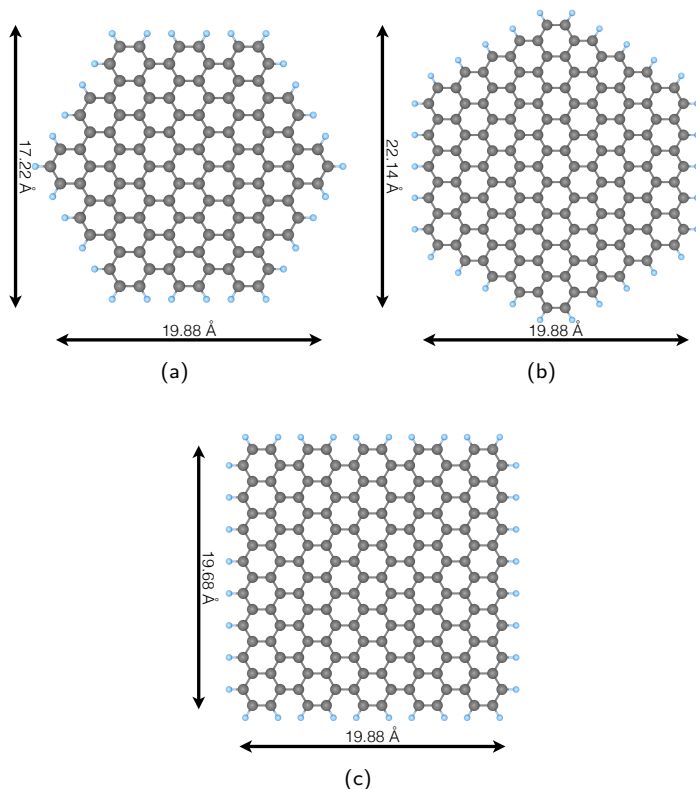
Figure 3.5: The geometries of the armchair hexagonal $C_{114}H_{30}$ and zigzag hexagonal $C_{150}H_{30}$ are shown in panel (a) and (b), respectively. The geometry of the nearly "square" flake $C_{170}H_{36}$ is shown in panel (c). Both types of edges are necessarily present in the square flakes. VMD is used to produce the pictures of the molecular geometries.[128, 129]

Finally, in section 3.7 we analyze the effects of different passivations of the carbon dangling bond on the absorption properties. In particular, fluorine (F), oxygen (O) and hydroxyl group (OH) passivation are covered in this study. In this case, atomic relaxation has to be taken into account in order to provide reasonable values of the bond-length for the different types of passivation.

3.2 CONVERGENCE STUDIES OF COMPUTATIONAL DETAILS

In section 2 we have seen how the DFT SIESTA code and the MBPT-LCAO TDDFT code are thought to work together. The SIESTA calculation provides the necessary inputs, namely, ground state KS orbitals, that are going to be used in MBPT-LCAO. Because many parameters either at the DFT stage and at the eventual TDDFT stage can affect the outcome of the calculations a thorough convergence procedure needs to be done in

order to obtain reliable results. Thus, for this purpose, we compared the optical properties of graphene flakes up to ∼6-7 nm size of hexagonal shape using a range of values for different calculational parameters. It is important to know that the convergence study has to be performed in relation to the quantities that we want to estimate. For instance, the convergence of DFT eigenenergies can be rather different from the convergence of their *differences* that are more relevant for TDDFT.

In SIESTA, the spatial support of radial orbitals as well as several other parameters can be either automatically chosen or controlled manually, see 2.2. In the following paragraphs we compare the resulting TDDFT absorption spectra with respect to the properties of the used basis set and we show that is possible obtain reasonable spectrum with a "cheap" set up. We rely on automatic choice of all parameters except the Basis Set's Multiplicity[6] (Section 2.2.2) and the Spatial extension of atomic orbitals[6] (Section 2.2.3).

3.2.1 Basis Set Multiplicity

As described previously in section 2.2, SIESTA makes use of LCAO for constructing molecular orbitals. General applicability of the SIESTA's basis sets to TDDFT calculations of low energy optical excitations has been shown by a direct comparison with a plane-wave-based calculation.[17] Here, we question to which extend small, computationally inexpensive basis sets reproduce the absorption spectra of carbon flakes. The user can choose among Single-ζ (SZ), Double-ζ (DZ), Triple-ζ (TZ), Single-ζ Polarized (SZP) basis sets, Double-ζ Polarized (DZP), Triple-ζ Polarized (TZP) basis sets and Triple-ζ Double-Polarized (TZDP) basis sets, as described in Section 2.2.2. The more complete basis set is the DZP, however, in order to address very large finite systems a smaller basis is used. Here we discuss the validity of calculations employing minimal basis set. The analysis on the data collected helps to define how well the smaller sets reproduce the features of quantities relevant for the modelling of optical absorption spectrum.

The simplest quantity to analyze is the spectrum of the DFT eigenenergies. It is a necessary check for a credible simulation of excitation properties because TDDFT calculations are based on DFT results. The table 3.1 shows the energy difference between the Highest Occupied Molecular Orbital (HOMO) and the Lowest Unoccupied Molecular Orbital (LUMO) for the two basis sets DZP and SZ and for several flakes. In the last column the differences DZP and SZ data are shown. The table shows that although the absolute HOMO and LUMO levels are affected by the multiplicity of the basis set rather strongly, the energy differences are influenced to a lesser extend. Moreover, the influence of the basis set incompleteness is diminishing with the size of the flake.

HOMO-LUMO, eV

	System	DZP	SZ	|DZP - SZ|
Armchair	$C_{42}H_{18}$	2.31	2.37	0.06
	$C_{114}H_{30}$	1.45	1.47	0.02
	$C_{222}H_{42}$	1.03	1.06	0.03
	$C_{366}H_{54}$	0.82	0.83	0.01
	$C_{546}H_{66}$	0.68	0.68	0.00
	$C_{762}H_{78}$	0.57	0.58	0.01
Zigzag	$C_{54}H_{18}$	1.77	1.79	0.02
	$C_{96}H_{24}$	1.22	1.23	0.01
	$C_{150}H_{30}$	0.87	0.86	0.01
	$C_{216}H_{36}$	0.62	0.61	0.01
	$C_{294}H_{42}$	0.45	0.43	0.02
	$C_{384}H_{48}$	0.32	0.31	0.01
	$C_{486}H_{54}$	0.21	0.21	0.00

Table 3.1: HOMO-LUMO gap calculated with DZP and SZ basis sets. In the last column the difference between HOMO-LUMO gap for DZP and SZ is shown.

Approximately, the optical properties depend on the difference of eigenenergies, see expression for the non-interacting linear response function 1.78. Therefore, one could expect that also the true optical gaps will be less affected by the incompleteness of the used basis sets. In order to check this conjecture we perform some TDDFT calculations for the first hexagonal flakes from the table 3.1 using SZ and DZP basis sets and compare the optical gaps. First, the optical gap is extracted from the polarizability as the energy of the first peak. The Table 3.2 shows that the maximal difference of the optical gaps computed with SZ and DZP basis sets does not exceed 0.13 eV. This result is a first indication that even SZ basis set is capable to reproduce the optical properties, at least in a low frequency range, for the flakes.

HOMO-LUMO, eV

System		DZP	SZ	$|DZP - SZ|$
AC	$C_{42}H_{18}$	2.79	2.92	0.13
	$C_{114}H_{30}$	1.77	1.84	0.07
	$C_{222}H_{42}$	1.30	1.34	0.04
ZZ	$C_{54}H_{18}$	2.36	2.44	0.08
	$C_{96}H_{24}$	1.67	1.71	0.04
	$C_{150}H_{30}$	1.22	1.23	0.01
	$C_{216}H_{36}$	0.91	0.91	0.00

Table 3.2: Optical gaps from TDDFT calculations with SZ and DZP basis sets.

In a next test, we compare the optical cross section, given by Equation 1.96, computed with SZ, DZ and DZP basis sets for the $C_{42}H_{18}$-AC flake, which shows the largest difference for the optical gap (see Table 3.2). The optical cross sections are shown in Figure 3.6. In Fig.3.6(a) and 3.6(b) the spectrum in a low-frequency range 0–10 eV is qualitatively similar for all basis sets, i.e., in this energy range we find peaks corresponding to the so-called π-plasmon at roughly the same energies and carrying similar spectral weights for all the basis sets used. At higher frequencies, above 10 eV one also recognizes similar features, see Figure 3.6(b). Namely, we always observe a σ plasmonic resonance around 16 eV, although it is not possible to make a one-to-one correspondence between the peaks obtained in the calculations using different basis sets. In Figure 3.6(c) the cross section is plotted by convoluting the spectra with a Lorentzian with a width $\epsilon = 0.5$ eV. This additional broadening has to be compared with an initial small broadening of 0.073 eV and can be understood as a model of low-resolution spectra. At low resolution, the spectra in the low-frequency range are practically coinciding, which is a further prove that the main features of the spectra are preserved in all cases, with good agreement at low energies. In the low-frequency range 0-10 eV, the optical cross section is qualitatively similar for all three basis sets (see Figure 3.6(a)). At frequencies above 30 eV, DZP basis shows resonances which are totally absent in the calculations with SZ and DZ basis sets. These resonances are caused by polarization orbitals of d symmetry that are present in DZP basis set and absent in the other basis sets.
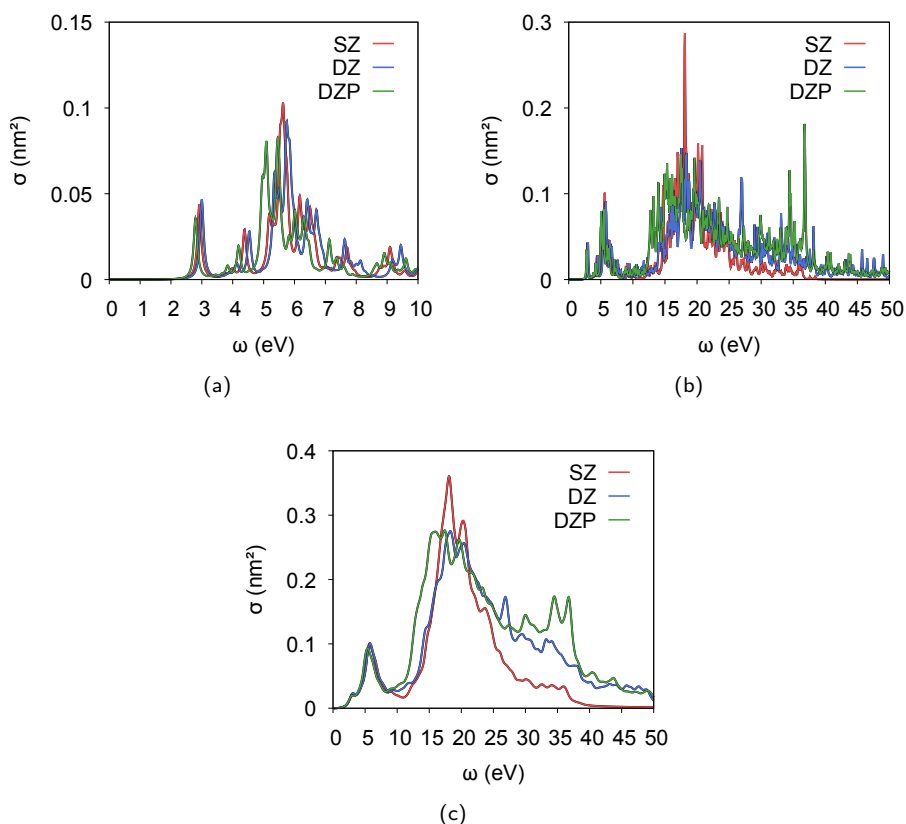
Figure 3.6: Optical absorption cross section of the $C_{42}H_{18}$-AC flake. Calculations with SZ, DZ, and DZP basis sets are presented in the frequency ranges 0–10 eV (a) and 0–50 eV (b). Panel (c) shows the same data presented in panel (b) but convoluted with Lorentzian of width $\epsilon = 0.5$ eV.

Similarly to the discussed case of $C_{42}H_{18}$-AC flake, for all studied flakes in the low frequency range, there is good agreement of the optical spectra computed with different basis sets. Moreover, the agreement improves for larger flakes. The usage of SZ basis allows us to perform calculations for very rather flakes, which would be impossible with DZP basis.

3.2.2 Spatial Extension of Atomic Orbitals: Energy Shift

The shape of basis set functions obviously affects DFT and TDDFT calculations. The spatial extend of the basis set functions is an important characteristic of the function's shape and can be controlled simultaneously for all orbitals with a single parameter called *energy shift*[73, 130] and described in paragraph 2.2.3. The energy shift is a mismatch of the eigenenergy in the radial KS equation causing the orbital to cross the x axis prematurely. The crossing point is used as cutoff radius. Therefore, the larger the energy shift the

smaller is the basis function extend. The default value of the energy shift is 0.02 Ry, which results in rather contacted orbitals while a small energy shift leads to the generation of more a extended basis set. Larger support orbitals produce in principle more credible results, although at a higher computational cost. Therefore, it is important to verify to which extend the contraction of orbitals affects the optical properties of graphene flakes.

We performed calculations of the cross section with different energy shifts and basis multiplicities (SZ, DZP) for the flakes mentioned in the Table 3.6. The spectra of the smallest flakes are the most affected by the energy shift. In Figure 3.7 the cross section of the most affected calculation (SZ $C_{42}H_{18}$-AC flake) is shown. By looking at the cross section we see that the spatial extension of localized orbitals only weakly affects the optical properties of the flakes. According to other calculations not presented here, the extension of the orbitals affects the absorption spectrum of the larger flakes to even a lesser extend.
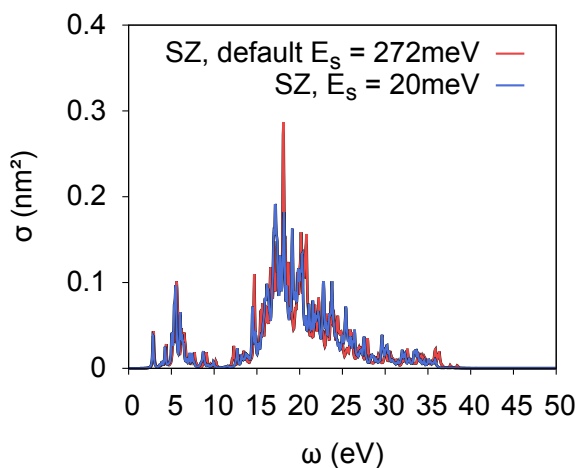
Figure 3.7: Dependence of the cross section on the spatial extension of radial orbitals in the frequency range 0–50 eV. The cross section is calculated with energy shifts 20 meV and 272 meV (SIESTA's default) for $C_{42}H_{18}$-AC flake.

The results in Fig.3.7 together with Table 3.6 show that even the minimal basis set with rather contracted orbitals provides reasonable results in a low frequency range 0–5 eV. In the mid-frequency range 10–30 eV, the use of minimal basis set is sensible if one is interested in the basic features of absorption spectra. The low frequency range is mostly important for applications and the calculations with SZ basis with contracted orbitals are possible for much larger flakes. Therefore, we continue to use SZ basis set with rather short orbitals in the other calculations in this chapter if not stated otherwise. The usage of SZ basis allowed us to perform simulations for flakes involving more than 4000 valence electrons, while the upper limit for the DZP basis set was around 250 valence electrons (each carbon atom contributes with 4 valence electrons while hydrogen with 1). [1]

---

[1]In this chapter of the thesis, we used only the basis of so-called dominant products, which is turned out to be not optimal, as we established in later works.[20]

3.3 π AND σ PLASMONS

As mentioned above, the polarizability, equation 1.94, of graphene flakes depends in a complex manner on the size and on the shape of the flakes. However, before analyzing in detail the relation between graphene flakes' size and shape and its optical properties, it is worth to analyze the origin of the main features, which are present in the optical spectra of all the calculated flakes. Graphene flakes present two intense broad peaks. The low frequency peak is the so-called π plasmon peak.[131] It is located in a range of frequencies between 4.7 and 6.4 eV depending on the size of the flake (see section 3.5). In contrast, the so-called σ plasmon peak[131] is found between 17.5 and 18.8 eV, even if also in this case the size and the shape of the flake determines the exact frequency of the plasmon. The plasmon peaks are called π and σ due to their angular momentum of orbitals contributing to the corresponding electronic excitations. $\pi \to \pi^*$ orbital transitions build up the π plasmon while $\sigma \to \sigma^*$ orbital transitions build up the σ plasmon as shown in section 3.4. There is also a minor contribution to the σ peak coming from $\pi \leftrightarrow \sigma$ transitions. These excitation peaks are found in the low-energy part of the σ peak, see section 3.4. In Fig. 3.8 panel (b) the results obtained for the $C_{1014}H_{78}$ flake are shown. In panel (b.α) and in panel (b.β) the optical cross section and the geometry of the flake are presented, respectively. Moreover, in panel (b.γ) a cross section with an additional broadening is plotted. The additional broadening allows us to better determine in an unambiguous and consistent way the energy position of the two main peaks for all the flakes considered here, including the smallest ones. π and σ plasmons are also characteristic of the Electron Energy Loss Spectroscopy (EELS) of an infinite graphene sheet, as in experiments.[131] In Fig. 3.8 a comparison between EELS data for graphene[131] and our calculated absorption spectrum for the $C_{1014}H_{78}$ graphene nanoflake is presented. The chosen flake in Fig. 3.8 has a linear dimension of 50-60 Å, however, the frequency position of the plasmonic peaks is already converged with respect to the size of the flake, as shown later on in this chapter. The calculations show good agreement with the experimental results, reproducing the main optical plasmonic features. In particular, the π peak frequency position is described with good accuracy in our calculations, i.e. the calculated value is 4.8 eV while the experimental value is 4.7 eV.[131] However, the calculated position of the σ plasmonic peak is off by 3 eV compared with the experimental value.[131] The difference in the position of the σ can be due, on one hand, to a large momentum transfer which is characteristic of EELS spectroscopy and, on the other hand, to the incompleteness of the used SZ basis set and the deficiencies of the used functional (LDA), which affect the high frequency features of the spectra to a larger extend than the low-frequency ones. It is worth noting, that a flake of only a few nanometers in lateral size already presents features converged to those typical of infinite graphene.
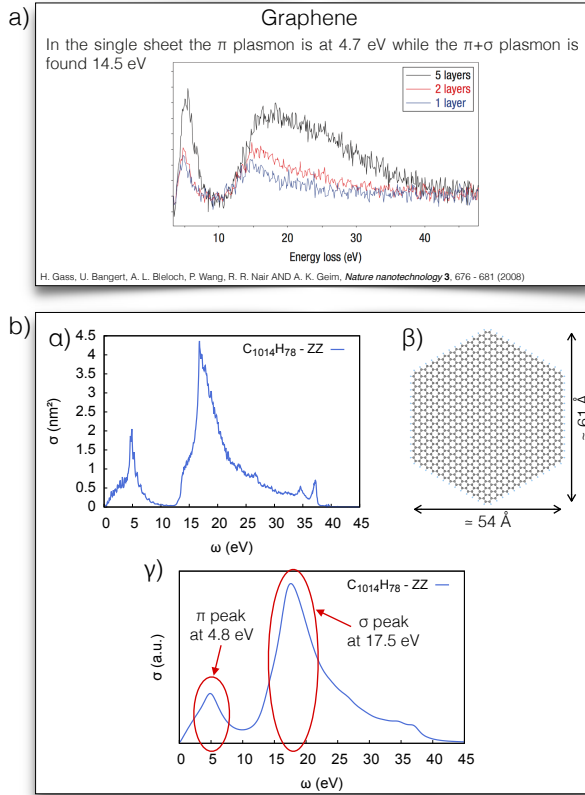
Figure 3.8: Comparison of the experimental frequencies π and σ plasmonic modes with the calculated values. In panel (a) the absorption experimental results for graphene layers are shown.[131] In panel (b) the calculated optical cross-section for the flake $C_{1014}H_{78}$ is shown together with its geometrical structure. In particular, in panel (b.γ) features the same absorption spectrum shown in Figure (b.α) but with a higher broadening parameter.

3.4 SYMMETRY OF ELECTRONIC TRANSITIONS: INTERACTING AND NON-INTERACTING SPECTRUM

σ bonds are the result of the sp^2 hybridization of the s, p_x and p_y orbitals and π bonds are formed by p_z orbitals. These basics of graphene electronic structure must be reflected in the optical absorption of graphene flakes, namely, the two main plasmonic peaks seen in the spectrum (π and σ) should be related to symmetry allowed transitions involving molecular orbitals (π and σ) with different symmetries. A symmetry analysis is straightforward for the non-interacting response function (1.97), but it is obscured by the presence of a TDDFT interaction kernel in the true interacting response function (1.94). However, when comparing the non-interacting and interacting cross sections, we always observe qualitative similarities for these cross sections. In order to exemplify this fact, we plot both cross

sections for the $C_{216}H_{36}$-ZZ flake. In Fig. 3.9(a) we see that the renormalization due to the TDDFT kernel strongly modifies the low-frequency (0–3 eV) cross section, while in the range above 5 eV both interacting and non-interacting cross sections are qualitatively similar. However, this similarity extends to low frequencies if an enlarged broadening constant ε is used (see Fig. 3.9(b)), i.e. if we look at the mean position of the π-peaks, rather than to their distribution. Therefore, we will perform the symmetry-channel analysis with the non-interacting response, and later we will directly demonstrate that the presence of the interaction kernel does not affect the conclusions of such analysis.
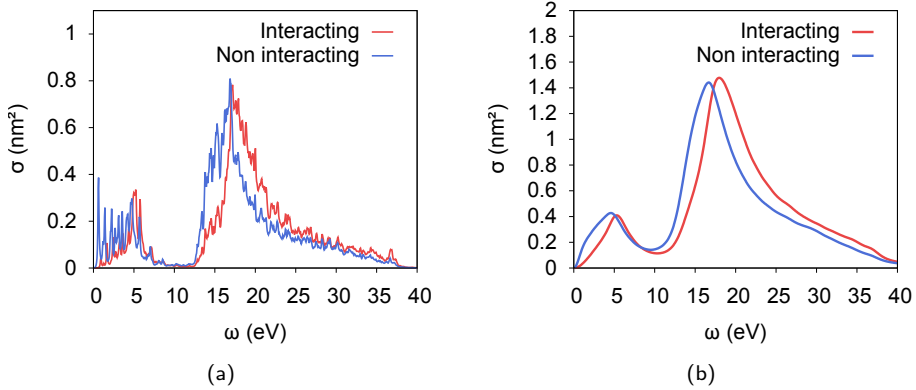
Figure 3.9: Interacting and non interacting cross sections for $C_{216}H_{36}$-ZZ flake is plotted with small ($\epsilon = 0.07$ eV) and large ($\epsilon = 1$ eV) broadening constants, on panels (a) and (b), respectively.

The symmetry-channel analysis of non-interacting response is straightforward because we use basis of atomic orbitals. In the framework of LCAO, a KS eigenstate $\psi_i(\boldsymbol{r})$ reads $\psi_i(\boldsymbol{r}) = \sum_a X_a^i f^a(\boldsymbol{r} - \boldsymbol{R}_a)$, where the sum goes over atomic orbitals $f^a(\boldsymbol{r})$ and the coefficients X_a^i are determined by the diagonalization of the Hamiltonian. The atomic orbitals are centered on atomic nuclei $\boldsymbol{R}_a$, and are chosen to carry a certain spherical symmetry characterized by the orbital l_a and magnetic m_a angular momentum. Using the quantum numbers l_a and m_a of the atomic orbitals and the magnitudes of the coefficients X_a^i one can conditionally nullify some eigenstates $X_a^i = 0$, according to a rule. Such artificial modification affects the absorption cross section and may give rise to useful conclusions. For instance, we can confirm the nature of σ plasmon resonance by removing all eigenstates $\psi_i(\boldsymbol{r})$ which satisfy an inequality (i) $\sqrt{\sum_a (X_a^i)^2}|_{l_a=0} < S_{\text{tol}}$. Here S_{tol} is a switch-off tolerance. A sensible choice of the tolerance does not affect the conclusions. The nature of the π plasmon resonance is confirmed analogously, using a similar switch off condition: (ii) $\sqrt{\sum_a (X_a^i)^2}|_{l_a=1, m_a=0} < S_{\text{tol}}$. The orbital angular momentum $l_a = 1$ correspond to a p shaped orbital and the magnetic moment $m_a = 0$ corresponds to the z direction. This is equivalent to switch off p_z orbitals, which form the π and π^* molecular orbitals. We used a small value of tolerance $S_{\text{tol}} = 0.01$ for the (i) and (ii) switch off conditions.
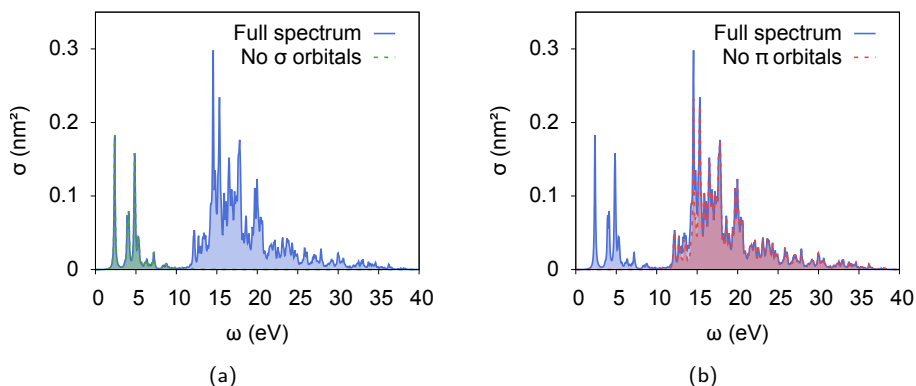
Figure 3.10: Symmetry channel analysis of the non-interacting response. The cross sections of the small hexagonal flake $C_{42}H_{18}$-AC have been artificially altered (see text) to exclude σ and π orbitals on panels (a) and (b), respectively, dashed lines. The unmodified cross sections are shown by solid (blue) curves.

In Figure 3.10 we show the original and artificially altered non-interacting cross sections for the small hexagonal flake $C_{42}H_{18}$-AC. The results obtained with the switch-off criteria (i) and (ii) are presented in Figures 3.10(a) and 3.10(b), respectively. We can see that the removal of eigenstates according to the condition (i) indeed "wipes out" the cross section above 10 eV, while the spectrum below 10 eV remains unaffected. This happens because the σ molecular orbitals do necessarily include contributions from s atomic orbitals and we artificially removed all eigenstates with noticeable weight on the s atomic orbitals. Figure 3.10(a) shows that the low-frequency spectrum features are not given by $\pi \rightarrow \sigma^*$ transitions nor by $\sigma \rightarrow \sigma^*$ transitions. The switch-off criterion (ii) allows to unambiguously clarify the origin of the low-frequency features. Namely, the artificially altered cross section in 3.10(b) is zero below 10 eV and it is almost entirely reconstructed above 10 eV. Therefore, we conclude that solely $\pi \rightarrow \pi^*$ transitions govern the low-frequency optical response. Furthermore, the removal of p_z atomic orbitals gives rise to a noticeable alteration of the absorption in the range 10–25 eV. Particularly, between 10 and 15 eV, a departure of the p_z-removed cross section from the original cross section shows the presence of coexisting $\pi \rightarrow \sigma^*$ and $\sigma \rightarrow \sigma^*$ transitions. Above 15 eV, the $\sigma \rightarrow \sigma^*$ transitions solely determine the absorption cross section. The symmetry-channel analysis of the other flakes AC, ZZ and SQ flakes from Table 3.3 leads to the same conclusions. This fact validates the designation of π and σ labels as the low- and high-frequency plasmons, respectively.
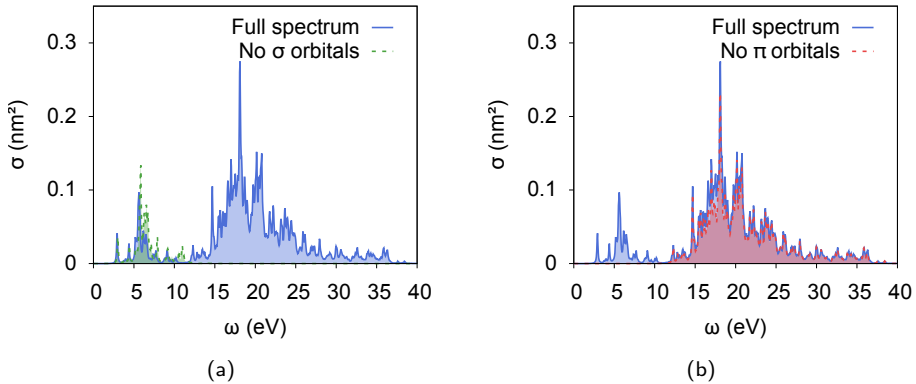
Figure 3.11: Symmetry channel analysis of the interacting response. The cross sections of the small hexagonal flake $C_{42}H_{18}$-AC have been artificially altered (see text) to exclude σ and π orbitals on panels (a) and (b), respectively, solid lines. The unmodified cross sections are shown by dashed (blue) curves.

The same type of analysis is possible also for the interacting cross section. In Figure 3.11 we present the original and modified interacting cross sections for the flake $C_{42}H_{18}$-AC. The conditional removal of eigenstates erases completely either σ or π plasmons, respectively. However, in contrast to the non-interacting cross-section case, the removal of σ molecular orbitals visibly alters the low-frequency spectrum. The mathematical origin of this altering is traced back to the real part of the response function. Namely, the imaginary part of the interacting response function used to calculate the spectrum depends on the real part of the non-interacting response function as can be seen from the Dyson-like equation 1.82. The real part of the non-interacting response function associated to a particular transition is not fully localized in frequency and therefore, contributes to the interacting response function in an ample frequency range. However, despite this complication, we can verify again that the removal of the σ states wipes out the high-frequency part of the interacting spectrum, while the removal of the π states wipes out the low-frequency part of the interacting spectra. These facts confirm once more the designation of π and σ labels as the low- and high-frequency plasmons, respectively.

3.5 Dependence on the Flakes' Size: Zigzag vs Armchair

It is interesting to study the size dependence separately for each geometry type of graphene flakes. Short-ranged orbitals and the minimal basis set (see section 3.2) allow to reach sizes of flakes containing up to 1014 carbon atoms. The geometry of all flakes is kept planar, with experimental bond lengths of 1.42 Å, as mentioned in the section 3.1. In Figures 3.12(a), 3.12(b) and 3.12(c) we show high-resolution cross sections for geometry types, respectively AC, ZZ and SQ. The cross section is computed in a wide frequency range, 0–50 eV, on an equidistant frequency grid of 1024 points. The broadening constant is

connected to the frequency resolution $\Delta\omega$: $\epsilon = 1.5\ \Delta\omega$, $\Delta\omega = 0.07324$ eV. The spectra are normalized in these plots for the sake of comparison. Without normalization the area under cross section curves would be proportional to the number of electrons as the f-sum rule dictates, see equation 1.104.

The maximal size of hexagonal flakes is 1014 carbon atoms for both AC and ZZ hexagonal flakes which correspond to a lateral size of about 60 Å. The number of carbon atoms in AC flakes is $18N(N-1)+6$, while for ZZ flakes it is $6\ N^2$, where N is number of hexagons along the edge of the flakes.

As commented before, in all plots we can see two main groups of peaks. For small flakes, the single-particle excitations can be resolved in the π and σ plasmon frequency range. As the flakes get larger, the density of the excitation spectrum increases and the two peaks become more and more defined. Low-resolution spectra, obtained using a larger broadening parameter, are presented in Figures 3.12(a), 3.12(b) and 3.12(c) respectively for AC, ZZ and SQ flakes. A broadening constant $\epsilon = 1$ eV is used in the plots. In the low-resolution plots, we can clearly identify that the maxima of envelope functions "move" towards lower frequencies as the flakes grow in size. This trend is true for both $-$ π and σ plasmons $-$ and for all the geometries we considered.
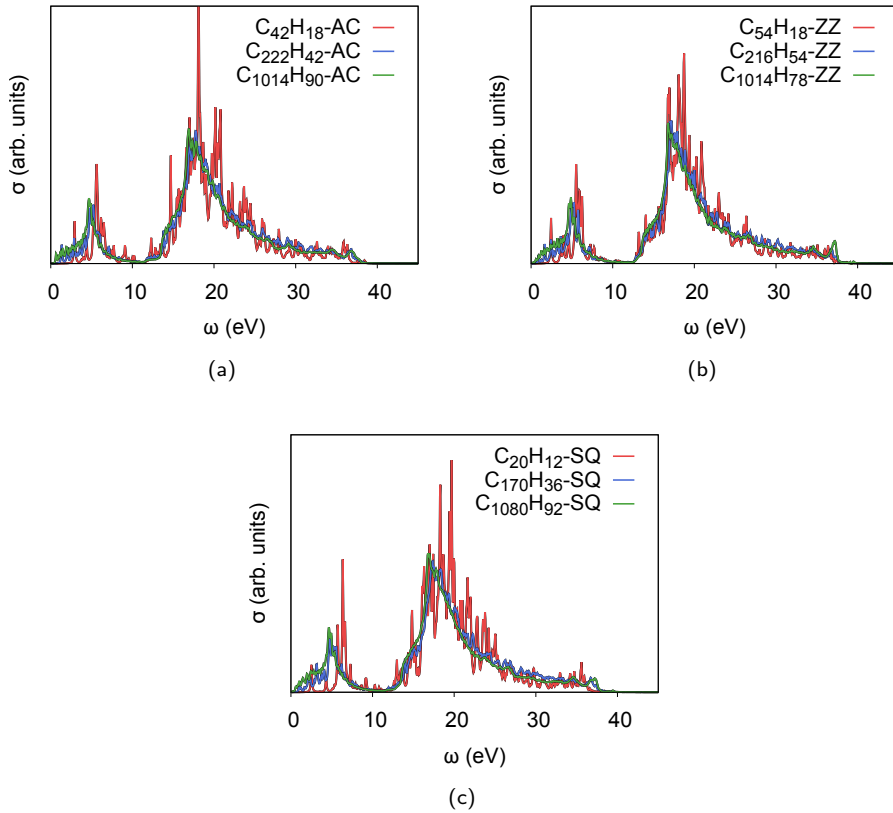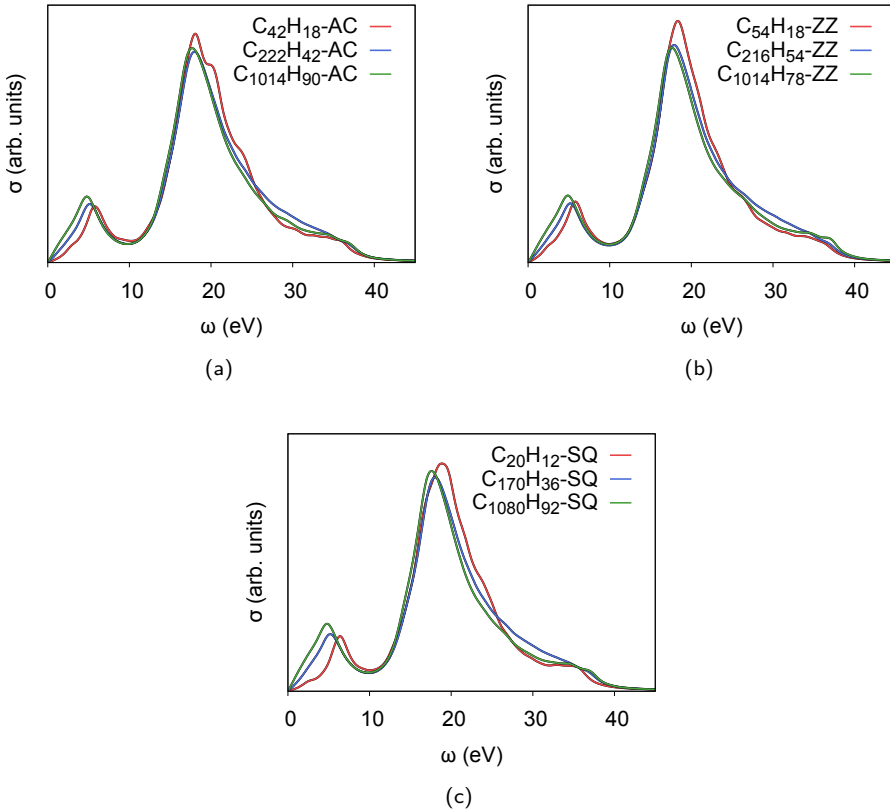
Figure 3.12: High-resolution optical cross section $\sigma(\omega)$. The cross sections for AC, ZZ, and SQ flakes are collected on panels (a), (b) and (c), respectively. The cross sections are normalized to enable a qualitative comparison.

Figure 3.13: Low-resolution optical cross section $\sigma\ (\omega)$. The cross sections for AC, ZZ, and SQ flakes are collected on panels (a), (b) and (c), respectively. The cross sections are normalized to enable a qualitative comparison. A relatively large broadening ($\epsilon = 1$ eV) does not merge π and σ bands, but clearly reveals two envelop functions.

The frequencies of the π and σ resonances can be unambiguously determined from low-resolution spectra. We collected the frequencies in Table 3.3. For all the data we used a broadening constant equal to 1 eV. From the data, one can recognize that the frequencies of neither π or σ plasmonic resonances do strongly depend on flake's shape or edge's type. However, the plasmonic frequencies do depend on the size of flakes. These facts can be understood from the fact that the observed plasmons in the flakes derive from the corresponding ones in the infinite graphene layer, i.e., they derive from "bulk" collective modes. Moreover, it is worth to point out as already described in section 3.3 that the frequencies of the π plasmon shown in Table 3.3 for the big flakes are in good agreement with the experimental value of 4.7 eV[131] found for free standing graphene. If we compare the position of the π plasmon for the biggest of the AC and ZZ flakes we notice that for the AC flake the value is closer to the experimentally obtained even though the difference between the two values is minimal. For the SQ flake the same value as in the AC case is

found.

Shape	Formula	N_e	π peak, eV	σ peak, eV
AC	$C_{42}H_{18}$	186	5.82	18.12
	$C_{114}H_{30}$	486	5.31	18.08
	$C_{222}H_{42}$	930	5.08	17.91
	$C_{366}H_{54}$	1518	4.95	17.83
	$C_{546}H_{66}$	2250	4.85	17.77
	$C_{762}H_{78}$	3126	4.79	17.75
	$C_{1014}H_{90}$	4146	4.74	17.62
ZZ	$C_{54}H_{18}$	234	5.73	18.27
	$C_{96}H_{24}$	408	5.42	17.99
	$C_{150}H_{30}$	630	5.25	17.86
	$C_{216}H_{36}$	900	5.11	17.82
	$C_{294}H_{42}$	1218	5.05	17.77
	$C_{384}H_{48}$	1584	4.99	17.74
	$C_{486}H_{54}$	1998	4.94	17.72
	$C_{600}H_{60}$	2460	4.89	17.71
	$C_{726}H_{66}$	2970	4.86	17.69
	$C_{1014}H_{78}$	4134	4.81	17.54
SQ	$C_{20}H_{12}$	92	6.33	18.79
	$C_{28}H_{14}$	126	5.93	18.76
	$C_{66}H_{22}$	286	5.49	18.09
	$C_{170}H_{36}$	716	5.13	17.96
	$C_{252}H_{44}$	1052	5.04	17.88
	$C_{350}H_{52}$	1452	4.96	17.82
	$C_{464}H_{60}$	1916	4.89	17.77
	$C_{858}H_{82}$	3514	4.78	17.72
	$C_{1080}H_{92}$	4412	4.74	17.53

Table 3.3: Plasmonic frequencies. One can observe that, for large flakes, with a number of electrons $N_e > 500$, the frequencies of neither π or σ plasmonic resonances do strongly depend on flake's shape or edge's type. The size of the flake, however, plays a determinant role. The number of valence electrons N_e is indicated in the third column.

In Fig. 3.14(a) and 3.14(b) the frequencies of π and σ plasmons versus the number of electrons are plotted for the three different types of flakes. The trend of the points representing the positions of the peaks suggest that the plasmonic frequencies almost exclusively depend on the size of flakes, although a minor deviation from this observation is obvious for small flakes. Edges/surface contribution diminishes as the flakes get bigger and bigger. In Fig. 3.14(b) the last group of points when the flakes contains more than 4000 valence electrons is oddly redshifted. The use of SZ for such high energy range could affect the results, although we could not verify this by comparing to a better calculation.

In conclusion we can say that no clear edge effects on π and σ plasmon position are observed. In all the three cases (AC, ZZ and SQ) the position of the plasmons decreases smoothly, reaching the measured experimental value of 4.7 eV[131] for the π plasmon. The

energy of the plasmons seems to be stabilized, so we do not expect very strong shifts even for larger flakes.
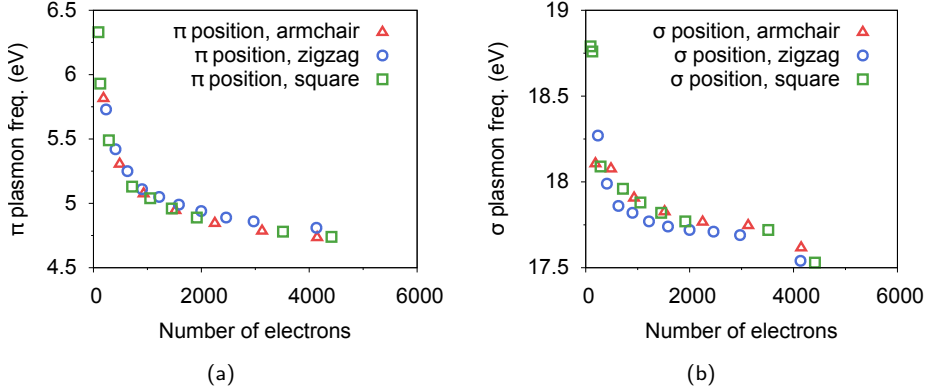

Figure 3.14: Frequencies of confined plasmons. The data from Table 3.3 suggests an approximate independence of plasmon frequencies on the details of the geometry, for both π and σ plasmons (panels (a) and (b), respectively).

3.5.1 POLARIZATION DEPENDENCE OF OPTICAL RESPONSE

So far we have plotted spectra showing the average value of the polarizability or cross section. Namely, the diagonal component of the polarizability tensor were averaged, i.e. $(\alpha_{xx} + \alpha_{yy} + \alpha_{zz})/3$, see paragraph 1.3.7. Where the subscripts indicate the direction of the incident light and the direction along which the dipole is measured. Due to the 2D geometry of the flakes we expect differences in the optical response depending on the different polarization direction of the incident light and the direction of the density dipole created (in-plane and out-of-plane). Measuring experimentally such dependence can be difficult as the samples have to be aligned with respect to the electrical field of the incident light. In our theoretical framework this can be done by analyzing the components of the polarizability tensor. Due to the symmetry of the flakes the off-diagonal components of the polarizability (α_{xy}, α_{xz}, ... α_{zy}) are negligible for AC, ZZ and SQ flakes. In the case of SQ flakes, the α_{xy} (and so α_{yx}) component can be different from zero if mirror symmetries are broken. If z is normal to the flake's plane, and the flake is flat, then α_{xz} (α_{zx}) and α_{yz} (α_{zy}) have to be zero by definition – due to reflection symmetry along the flake's plane. Thus, the remaining diagonal components (α_{xx}, α_{yy} and α_{zz}) characterize the whole optical response. The in-plane components $P_{xx}(\omega)$ and $P_{yy}(\omega)$ are equal in the hexagonal AC and ZZ flakes. This is due to the six-fold symmetry of the AC and ZZ flakes. On the contrary, square and rectangular flakes exhibit different in-plane polarizability components. SQ flakes present both types of edges reducing the symmetry of the flakes. In Fig. 3.15(a) the in-plane components $P_{xx}(\omega)$, $P_{yy}(\omega)$ for the square flake $C_{170}H_{36}$ are shown while the out-of-plane component $P_{zz}(\omega)$ is shown in Fig. 3.15(b). As explained above, the two in-plane components $P_{xx}(\omega)$ and $P_{yy}(\omega)$ slightly differ for square flakes, however, both contribute to the polarizability $\sigma(\omega)$ in a fairly similar way.
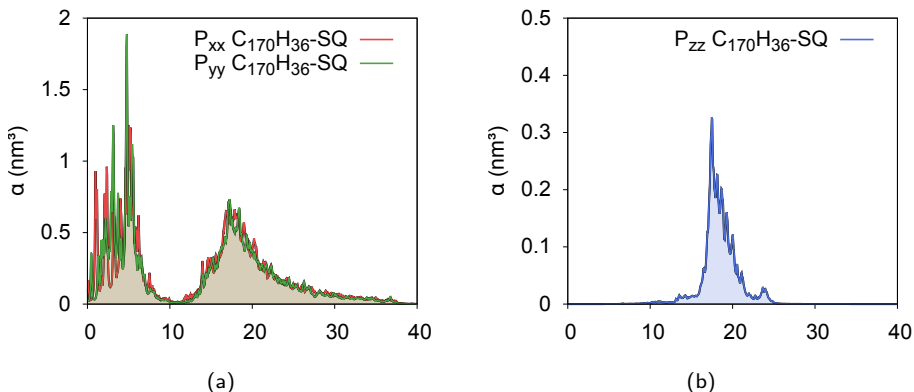
Figure 3.15: Diagonal components of the polarizability tensor $P_{ij}(\omega)$ for the square flake $C_{170}H_{36}$-SQ. The in-plane components $P_{xx}(\omega)$ and $P_{yy}(\omega)$ are shown in panel a), while in panel b) the out-of-plane component $P_{zz}(\omega)$ is shown. The out-of-plane response is non-zero only in the high-frequency range $\sim$12–25 eV.

In plane components of the polarizability contribute over the whole frequency range, giving rise to the π and σ plasmons peaks. In contrast, the out-of-plane component $P_{zz}(\omega)$ has non-negligible values only in the high frequency range, approximately above 12 eV. Recalling the results of the symmetry-channel analysis from section 3.4 we can immediately exclude the $\pi \to \pi^*$ transitions to be responsible for the $P_{zz}(\omega)$ polarizability. Moreover, we performed the symmetry-channel analysis for the out-of-plane component: the component has been wiped out completely whether σ or π molecular orbitals were removed. Therefore, we conclude that solely $\pi \to \sigma^*$, $\sigma \to \pi^*$ transitions are responsible for the $P_{zz}(\omega)$ component of the polarizability. The fact that only $\pi \to \sigma^*$, $\sigma \to \pi^*$ transitions contribute to the $P_{zz}(\omega)$ polarizability can be understood from the selection rule for the dipole matrix elements $\langle \psi_i | z | \psi_j \rangle$. The dipole matrix element is zero if the eigenfunctions ψ_i possess the same mirror symmetry with respect to the xy plane because of the odd character of the dipole operator z. The other flakes (AC and ZZ) considered in this work exhibit a similar behavior, of in-plane versus out-of-plane components, with the only difference that the in-plane component is isotropic.

3.5.2 OPTICAL GAP

In section 3.5 we have shown that plasmons do not strongly depend neither on the shape nor on the details of edge's structure. Indeed, the π and σ plasmons are inherent to the graphene lattice, i.e. they appear in every large-enough carbon flake, and their position depends *solely* on the size of the flake. In contrast to this geometry-insensitive behavior, the *optical gap* depends strongly on the details of the flake's geometry. The optical gap (Δ_{opt}) is defined as the lowest-frequency dipole-allowed transition, i.e. the optical gap is the frequency of the lowest energetic peak in the absorption cross section. For this purpose, the cross sections for AC, ZZ and SQ flakes are analyzed at high resolution, i.e. using a small imaginary factor ϵ. The use of a small ϵ value reflects in the spectra with very sharp

peaks allowing us to extract the value of the maximum of the first optical peak. The results are displayed the Table 3.4 and Figure 3.16(a). The dependence of the optical gap on the number of electrons is smooth. The optical gap decreases monotonically while increasing the size for all hexagonal flakes. Eventually, the optical gap should converge to 0 eV for big flakes, approaching the limit of the infinite graphene sheet. Moreover, for different kind of flakes the optical gap have different dependence on flake's size. Actually, the optical gap approaches zero "faster" in ZZ flakes. Furthermore, it is interesting to compare the optical gap Δ_{opt} with the so-called KS gap Δ_{DFT}, which is the lowest-frequency dipole-allowed transition in the non-interacting picture. For the flakes studied the Δ_{DFT} corresponds to the energy difference between LUMO and HOMO. From Table 3.4 we see that the KS gap shows a similar behavior as the TDLDA optical gap. The two series of data, for Δ_{opt} and for Δ_{DFT}, have the similar dependence with the number of electrons in the system.

KERNEL SHIFT

We define the kernel shift (Δ_{kernel}) as the difference between the Δ_{opt} and the Δ_{DFT}. For AC and ZZ flakes the kernel shift depends on the size of the flake as can be seen from Table 3.4 in 6-th column and in Fig. 3.16(b). As the flakes get bigger and bigger the promotion of only one electron from the HOMO to the LUMO affects the system to a lesser extend, leading to a more moderate absolute shift between Δ_{opt} and Δ_{DFT}. This is a well-known pathology of local and semi-local exchange-correlation kernel. A more sophisticated description of long-range exchange is necessary to get a proper renormalization of delocalized electron-hole pair excitations in very large/infinite systems. However, we notice that if we look at the ratio $R = \Delta_{kernel}/\Delta_{opt}$, qualitative differences are found between AC or ZZ flakes, as illustrated in Fig. 3.16(c). The relative kernel shift R increases linearly with the number of electron ZZ flakes while it remains rather flat for AC flakes. The nature of the edges seems to play a crucial role in this case. The relative renormalization due to the kernel, Fig. 3.16(c), which takes into account electron interactions, is bigger for flakes presenting only zigzag edges. The confinement of the HOMO and LUMO on the edges of the zigzag flake (the HOMO electron density is plotted in Fig. 3.18(b), the corresponding LUMO electron density presents a pattern very similar to the HOMO one) can be traced as the cause of such a difference in the dependence of the kernel shift ratio R versus AC flakes. In armchair flakes, the HOMO as well as the LUMO are well spread all over the flake, this is shown in Fig. 3.18(a). The separation of the electron charge located on the edges of the ZZ flakes makes the screening of the other electrons more difficult leading to a bigger relative blueshift renormalization. This last conjecture is supported by the fact that around the optical-gap energy the density change is located mainly on the edges, see Fig. 3.19(d) and Fig. 3.19(e), and by the fact that, as showed in chapter 6, the plasmonic resonances are build up out of a linear combination of KS orbitals around the energy of the resonance at least at low energies. A more direct estimation of the kernel shift behavior is possible in a simplified calculation of the interacting transition energies using Laurent expansion of the interacting response formulation.

Shape	Formula	N_e	Optical gap (eV)	DFT gap (eV)	Kernel shift (eV)	Relative Kernel shift (eV)
AC	$C_{42}H_{18}$	186	2.916	2.368	0.548	0.188
	$C_{114}H_{30}$	486	1.835	1.472	0.363	0.197
	$C_{222}H_{42}$	930	1.340	1.062	0.278	0.207
	$C_{366}H_{54}$	1518	1.057	0.8311	0.2259	0.2137
	$C_{546}H_{66}$	2250	0.8717	0.6823	0.1894	0.2173
	$C_{762}H_{78}$	3126	0.7432	0.5785	0.1647	0.2216
	$C_{1014}H_{90}$	4146	0.6480	0.5024	0.1456	0.2247
ZZ	$C_{54}H_{18}$	234	2.437	1.788	0.649	0.266
	$C_{96}H_{24}$	408	1.706	1.227	0.479	0.281
	$C_{150}H_{30}$	630	1.238	0.864	0.374	0.302
	$C_{216}H_{36}$	900	0.9109	0.6131	0.2978	0.3269
	$C_{294}H_{42}$	1218	0.6798	0.4347	0.2451	0.3605
	$C_{384}H_{48}$	1584	0.5086	0.3063	0.2023	0.3978
	$C_{486}H_{54}$	1998	0.3805	0.2140	0.1665	0.4376
	$C_{600}H_{60}$	2460	0.2843	0.1485	0.1358	0.4777
	$C_{726}H_{66}$	2970	0.2139	0.1020	0.1119	0.5231
	$C_{864}H_{72}$	3528	0.2013	0.0694	0.1319	0.6552
	$C_{1014}H_{78}$	4134	0.1185	0.0469	0.0716	0.6042

Table 3.4: The optical gap Δ_{opt}, the DFT gap Δ_{DFT}, the kernel shift Δ_{kernel} and relative kernel shift $\Delta_{kernel}/\Delta_{opt}$ are shown for AC and ZZ flakes. The number of valence electrons N_e is also given.
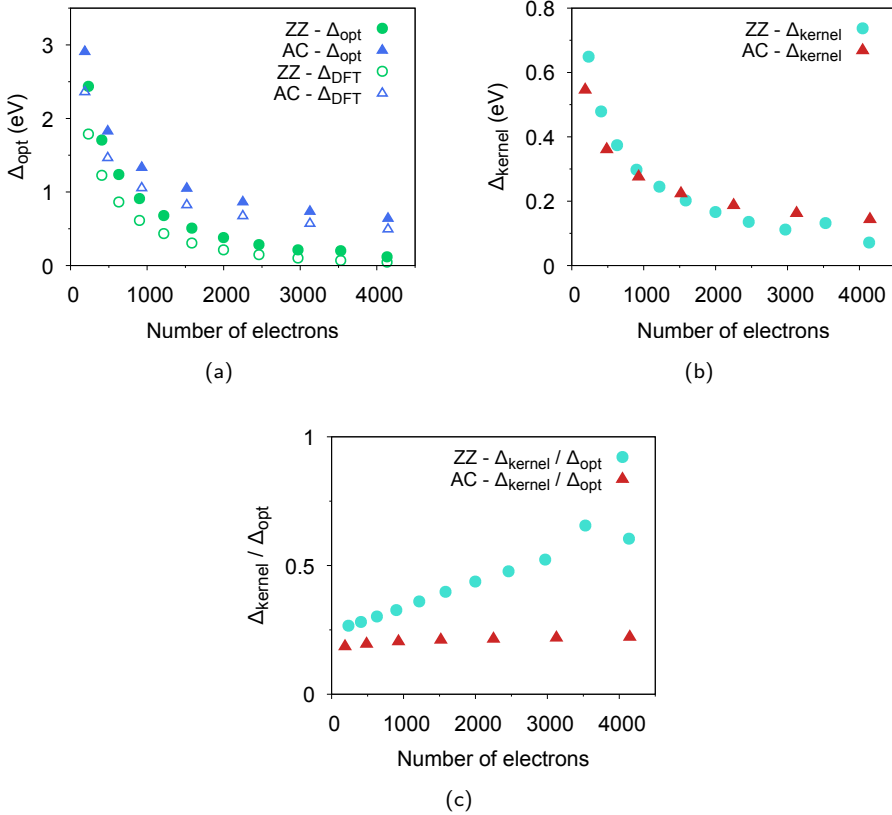
Figure 3.16: The optical and KS gaps are shown in panel (a). In panel (b) the kernel shift ($\Delta_{kernel} = \Delta_{opt} - \Delta_{DFT}$) versus the number of electrons in the flake is shown. The relative kernel shift $\Delta_{kernel}/\Delta_{opt}$ is shown in panel (c).

OPTICAL GAP DEPENDENCE ON NUMBER OF ELECTRONS

The smooth dependence of the optical gap on the number of electrons and the fact that gap should approach the graphene limit, i.e. zero, as the number of electrons goes to infinity (Fig.3.16) facilitate analytical fits which are similar to the scaling rules for graphene nanoribbons.[132, 133] Indeed, the optical gap of AC flakes obeys a two-parameter power fit $G = (N_e/N_0)^{1/a}$ to a high precision. Here N_e is the number of (valence) electrons, N_0 and a are the fit parameters. Parameters must be $N_0 = 1694.0, a = -2.0642$ to obtain the gap in eV, with a maximal deviation from calculated gap 0.006 eV.

In contrast, the optical gap of ZZ flakes does not obey the simple power law to such a high precision. However, it is possible to suggest a tri-parameter formula which permits an analytical solution

$$G = G_0\, N_e^{1/a}\, e^{-N_e/M}. \tag{3.1}$$

The parametric fit formula (3.1) allows to express the parameters G_0, a and M via three

calculated points from the table (3.4). For optical gap of AC flakes we choose points $N_e = 186$, $N_e = 1518$ and $N_e = 3126$, while for ZZ flakes we choose $N_e = 234$, $N_e = 1218$ and $N_e = 2460$. Consequently, we obtain for AC flakes $M = 136739.0$, $a = -2.0908$ and $G_0 = 35.584$ and for ZZ flakes $M = 2860.139$, $a = -1.7740$ and $G_0 = 57.279$. The parameter M for AC flakes is 48 times larger than for ZZ flakes. This ratio tells that even a simple power law fits the optical gap for AC flakes rather accurately. The maximal deviation of tri-parameter fit (3.1) for ZZ flakes is 0.03 eV, while for AC flakes it remains below 0.006 eV. Moreover, the parameter a is close to -2 for both AC and ZZ flakes. This suggests, reasonably, that the optical gap would be inversely proportional to a linear dimension of the flakes, rather than to their surface dimensions (area). The two-parameter fitting curve found for AC flakes and the tri-parameter fitting curves found for AC and ZZ flakes are shown in Fig. 3.17 together with the original data.
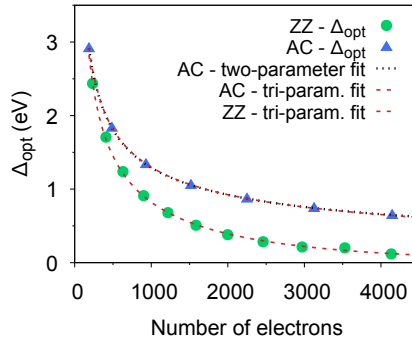
Figure 3.17: Fitting curves are shown together with the original data for hexagonal flakes.

Square flakes show radically different dependence of the optical gap on flake's size. Optical and KS gaps for square flakes are collected in Table 3.5. For square flakes, the optical gap abruptly goes to negligible values already for rather small flakes (66 carbon atoms in our case). In order to understand this behavior, we track down its origin to the underlying DFT calculation. The data in the table shows that the DFT gap behaves qualitatively similar to the true optical gap. In fact, the calculations show that the spectra of DFT eigenstates appear nearly degenerated at the Fermi energy. The number of the states at Fermi energy grows with the size of the flake. However, on the contrary of what it is done in chapter 4 it is not possible to estimate the degeneracy of the Fermi-energy states by means of Lieb's theorem[134] and using triangular bipartition of honey-comb lattice, as it is possible for triangular flakes.[135]

Alternatively, we can explain the gap closure in SQ flakes by a comparison with the band structure of nano ribbons. The zigzag nano ribbons possess edge states that determine the closure of their band gaps in the non spin-polarized case.[136,137] The band structure of a nano ribbon can be used to approximate the KS spectrum of SQ flakes if one takes into account only the k points allowed by the momentum discretization. The valence and conduction bands of zigzag nano ribbons in momentum space meet when k takes values between $2\pi/3$ and π ($2\pi/3 < k < \pi$)[137] if the width of the ribbons exceed certain value (π is the border of the Brillouin Zone (BZ)). Therefore, we should expect a gap closure

in the SQ flakes beyond some critical size, when the now discrete k values start to fill the nano ribbon zero-gap range $2\pi/3 < k < \pi$. In particular, if we take a finite ribbon made of 3 unit cells we obtain the gap closure. We performed additional DFT calculations of rectangular flakes in order to characterize the degeneration of Fermi-energy states. As expected, the calculations indicate that mainly the length of zigzag edge determines the degeneracy, i.e. as the size of the flake increases the sampling of the BZ adds points in the zero-gap range $2\pi/3 < k < \pi$. This observation is also supported by the spatial distribution of the Fermi-energy states, see fig.3.18(b).

Shape	Formula	N_{e}	Optical gap (eV)	DFT gap (eV)
	$C_{20}H_{12}$	92	2.50	1.66
	$C_{28}H_{14}$	126	1.51	0.76
	$C_{66}H_{22}$	286	0.05	0.01127
SQ	$C_{170}H_{36}$	716	0.05	0.01764
	$C_{252}H_{44}$	1052	0.17	0.00291
	$C_{350}H_{52}$	1452	0.02	0.00196
	$C_{464}H_{60}$	1916	0.06	0.00195

Table 3.5: Optical and DFT gaps are shown for SQ flakes.

In Figures 3.18(a), 3.18(b) we plot the isosurfaces of the HOMO electron density for AC, ZZ respectively. While in Figure 3.18(c) the electron density describing the almost degenerated levels around the Fermi energy is plotted. The electron density is distributed almost evenly across the area of AC flakes, while it is localized at zigzag edges in ZZ and SQ flakes. The optical gap of ZZ and SQ flakes depends very differently on the size, although the zigzag edges "attract" the eigenstates close to Fermi energy in both ZZ and SQ flakes. We think that the difference in behavior is caused by the fact that edges in SQ flakes do not interact due to their small overlap, while in ZZ flakes do interact because their terminations are always spatially close to each other, independently on the size.
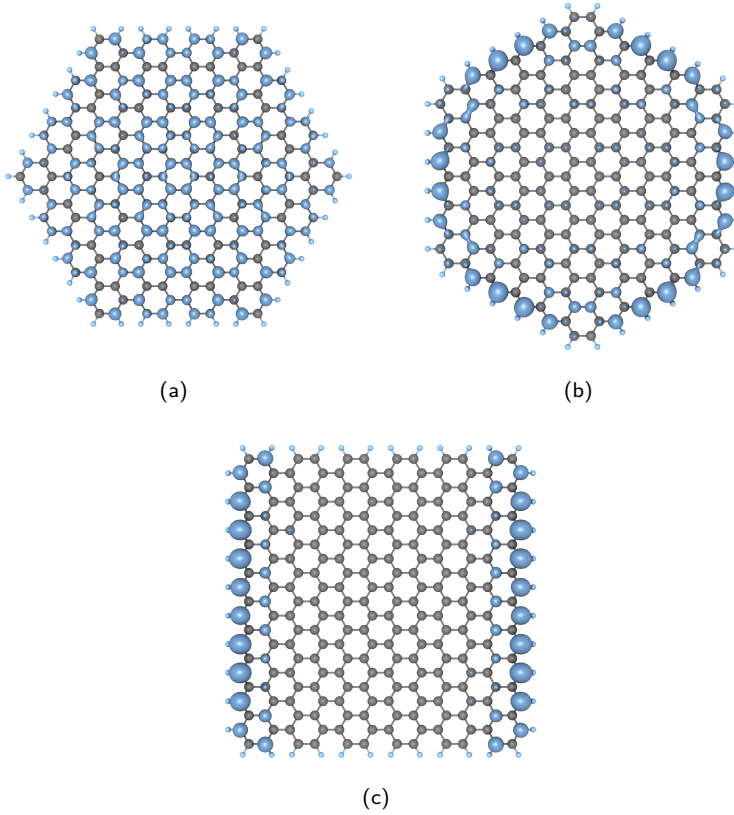
(a)   (b)

(c)

Figure 3.18: Electron density of HOMO levels are plotted for the flakes $C_{222}H_{42}$-AC, $C_{216}H_{36}$-ZZ in panels (a) and (b) respectively. In panel (c) the electron density created by the almost degenerated levels around the Fermi energy is plotted. The plots were done using the molecular visualization software VMD.[128, 129]

3.6 INDUCED DENSITY CHANGE

Another approach to characterize the optical absorption consists in the analysis of the induced density given by Eq.1.56,

$$\delta n(\mathbf{r}, \omega) \propto \int_{\omega_{win}} \int \chi(\mathbf{r}, \mathbf{r}', \omega) \mathbf{r}'_j \mathrm{d}\mathbf{r}' \mathrm{d}\omega.$$

The frequency integration is done over a chosen frequency window (ω_{win}) that can include an entire group of peaks or just the width of a single peak. δn is complex valued quantity. As explained in section 1.3.3 the imaginary part of the polarizability is proportional to the photo-absorption losses of the system. Thus, the imaginary part of the density change gives a graphical idea of the areas where photo-absorption takes place. Moreover, the imaginary part characterizes the resonant oscillating-charge modes in real space. On the other hand,

the real part of the density change is needed in order to calculate the density change in time domain as explained in section 1.3.9. However, for our purposes for the rest of the chapter we focus only on the imaginary part of the density change.

Thanks to the induced density plots it is possible to analyze the spatial distribution of the electron cloud. This opens the possibility to characterize the different oscillating-charge modes as well as the contribution of different atoms to the optical polarizability. Figure 3.19 shows the isosurfaces of electronic density change in three frequency ranges 0–2, 2–10 and 10–30 eV for the flake $C_{222}H_{42}$-AC in panels (a), (b) and (c); for the flake $C_{216}H_{54}$-ZZ in panels (d), (e) and (f); for the flake $C_{170}H_{36}$-SQ in panels (g), (h), (i), (j), (k) and (l), respectively. The direction of the external electrical field is vertical in-plane in panels (a), (b), (c), (d), (e), (f), (g), (h), (i). While, in (j), (k) and (i) the field is horizontal. We can see that the density change is distributed differently for the three frequency windows. In the optical range 0–2 eV, the region dominated by the π plasmon, the density change of AC and square flakes (Figures 3.19(a), 3.19(g) and 3.19(j) respectively) is broadly distributed along the vertical axis, while it resides mainly at the edges (Fig. 3.19(d)) for the ZZ flake. Interestingly, in a mid-UV band 2–10 eV, the density change is induced on the edges for all the flakes (Figures 3.19(b), 3.19(e), 3.19(h) and 3.19(k)). This fact can be surprising for the AC flake. In contrast to the mid-UV band, the density change due to high-frequency excitations (corresponding to the σ plasmon) is distributed evenly among the atoms in the flakes (Figures 3.19(c), 3.19(c), 3.19(i) and 3.19(l)). However, the carpet-like high-frequency density changes are qualitatively different from the broad distribution for AC and SQ flakes in the optical band. Namely, the sign of the density change remains mainly the same over the upper and lower part of the flake at low frequencies and changes from carbon-carbon bond length at high frequencies. Loosely speaking, at low frequencies, the optical response can be represented as a very few dipoles separated by the characteristic length of the flake, while at high frequencies, the generated dipoles are separated by a graphene lattice constant.
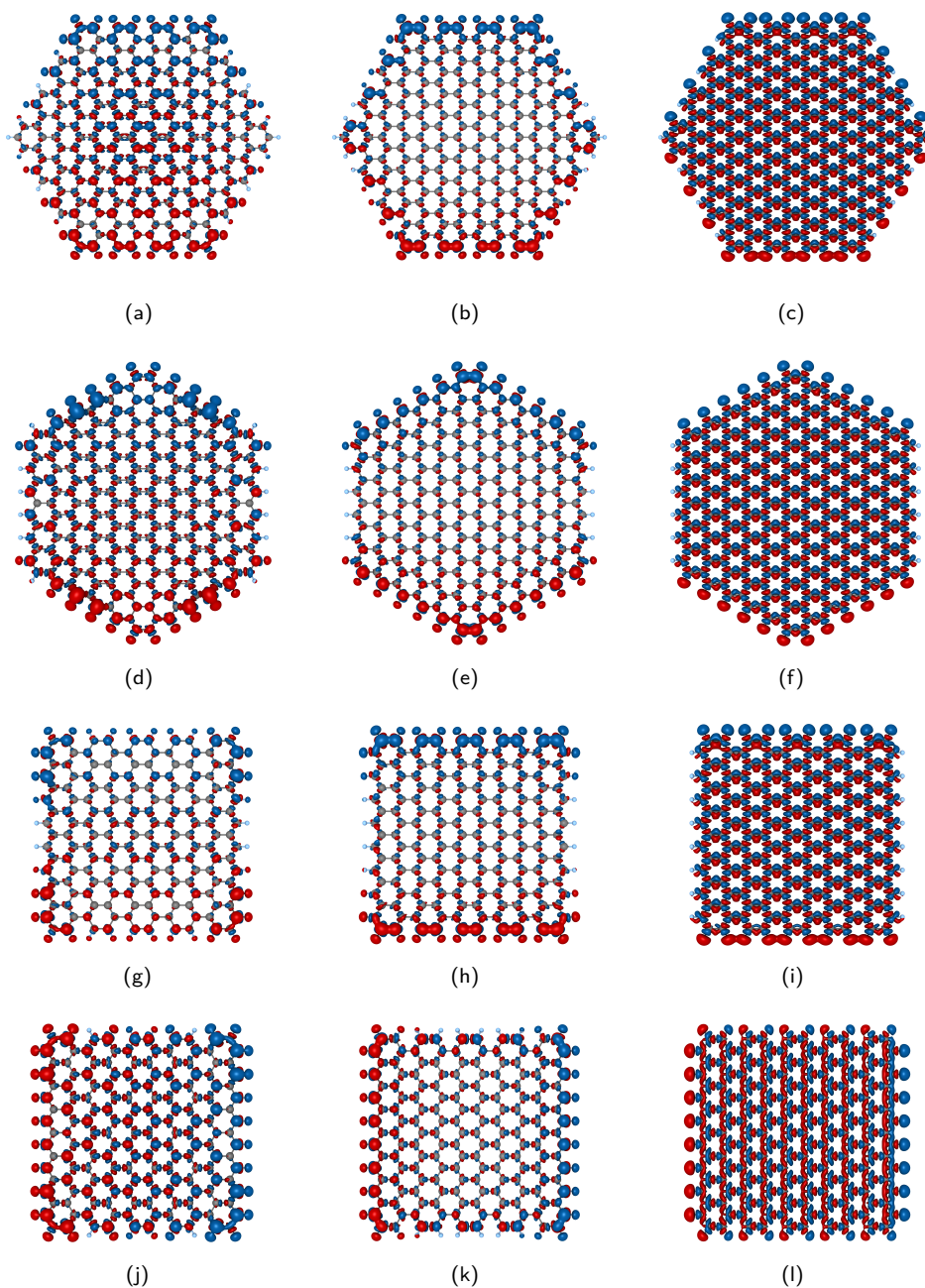
Figure 3.19: Imaginary part of density change in graphene flakes. Frequency bands, optical 0–2, mid-UV 2–10 eV and extreme UV are considered for armchair flake in panels (a), (b) and (c); for zigzag flake on panels (d), (e) and (f); for square flake in panels (g), (h) and (i), respectively. The isolevel value is set to 10% of the maximum intensity for each plot. The plots were done using the molecular structure visualization software XCrySDen.[138]

The maps of the density change like those shown in Fig. 3.19 identify the flake's parts that are mostly responsible for photo-absorption losses giving a hint on how local physical and chemical perturbation e.g. adsorbed atoms on the surface, functionalized edges or an interaction with a tip would affect the optical response. Moreover, the spatial map of density change may be regarded as a tool for constructing new flake's *geometries* with particular optical properties, as it is shown in section 3.7.

3.7 Tailoring and Passivation of Graphene Nanoflakes

Graphene-flake tailoring can give the possibility to select certain desired optical properties, designed new flakes can have very different optical absorption. For example, in the optical range for the rectangular flake (Figures 3.19(i) and 3.19(l)) a significant part of the density change is located at the corners of the flake. Because the density change is symmetric, only diagonal components of the polarizability tensor $P_{ij}(\omega)$ are non-zero. However, we can anticipate that by removing a corner of the flake we can destroy the symmetry of generated dipoles and the polarizability tensor will acquire significant off-diagonal components.
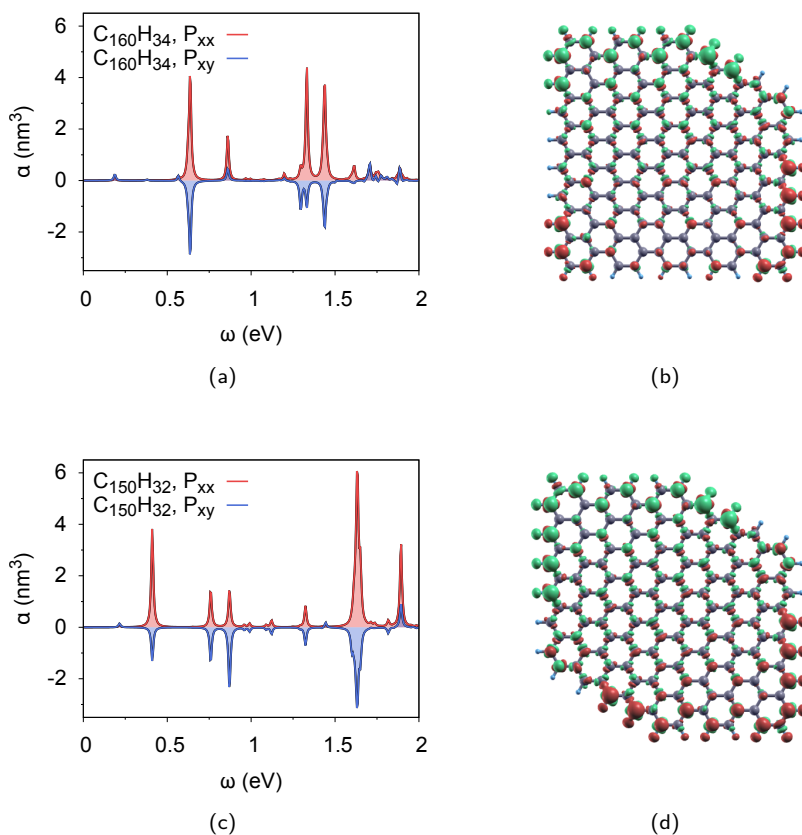
Figure 3.20: Polarizability components of "tailored" flakes. Off-diagonal and diagonal components are compared for flakes with one and two removed corners (RC) on panels (a) and (c). Isosurfaces of corresponding density changes (in the optical range, $0\ldots2$ eV, with electrical field oriented vertically) are plotted on panels (b) and (d).

In order to check this conjecture, we take the flake $C_{170}H_{36}$ and remove one or two corners. The geometries of the flakes with removed corners (RC) $C_{160}H_{34}$-RC and $C_{150}H_{32}$-RC are shown in Fig. 3.20, on panels (b) and (d), respectively. The components of the corresponding polarizability tensors are shown on panels (a) and (c). We can see that the off-diagonal component $P_{xy}(\omega)$ of the flake with one removed corner is not negligible if compared with its own diagonal component $P_{xx}(\omega)$.

3.8 CHEMICAL MODIFICATION OF GRAPHENE FLAKES

So far only hydrogen-saturated flakes have been considered although graphene flakes can covalently bind the other chemical species. Unlike simple tight-binding models, the method

we employ allows to predict, from first principles, how chemical modifications affect its electronic structure and optical properties. As first example, we substitute the edge-saturating atoms in zigzag flakes. This choice is motivated by its simplicity and the observation that edges play an important role for optical absorption of zigzag flakes in the low frequency range (see figure 3.19). We study the saturations with hydrogen, fluorine and oxygen atoms and with hydroxyl (OH) groups because these are among the most relevant for applications.[124]

3.8.1 Edge Saturation with Single-Atoms

Fluorine and oxygen are the chosen atoms used to saturate the graphene dangling bonds. In contrast to hydrogen-saturated flakes, we found that geometry relaxation strongly affects the optical spectra of chemically modified flakes and the minimal basis is not always reliable for this purpose. Consequently, in the calculations presented in this section we used DZP basis with extended orbitals (energy shift of 100 meV). The flakes relaxed with fluorine and oxygen show a planar structure as in the case of hydrogenated flakes. The bond lengths (carbon-terminal atom) are equal to $\simeq$ 1.109, 1.329, 1.222 Å for $C_{54}H_{18}$, $C_{54}F_{18}$ and $C_{54}O_{18}$ flakes respectively and $\simeq$ 1.110, 1.330, 1.235 Å for $C_{216}H_{36}$, $C_{216}F_{36}$ and $C_{216}O_{36}$ flakes respectively. The optical cross section of small $C_{54}A_{18}$ and large $C_{216}A_{36}$ flakes are shown in Fig. 3.21(a) and in Fig. 3.21(b) respectively, where the capital letter A denotes an atom (H, F, O). The optical gap of the fluorinated and oxygenated flakes are lower than that of the hydrogenated flakes. Whereby, the cross sections of fluorinated and hydrogenated flakes are qualitatively similar, while the oxygenated flakes show much richer optical spectra. Hydrogen and fluorine need just one electron to complete the outer shell, this makes them chemically more similar compared to oxygen, which needs two electrons to complete the shell. Therefore, in oxygenated flakes oxygen attracts more electrons and causes a hole doping of the flake. The optical cross section for the small and the large flake gives evidence that the hole doping (due to perimeter modifications) gets weaker as the flake size increases. Namely, the strongest low-frequency resonance occurs approximately at the same frequency in all the large flakes and exhibit approximately the same magnitudes. The additional resonances of $C_{216}O_{36}$ (below the strongest resonance) are much weaker than similar resonances in the $C_{54}O_{18}$ flake. As can be understood, chemical doping of edges turned out to be more significant in smaller flakes. The hole doping of $C_{54}O_{18}$ causes the optical resonances to spread over a larger number of frequencies, although the magnitude of the resonances gets smaller than that of the hydrogenated and fluorinated flakes.
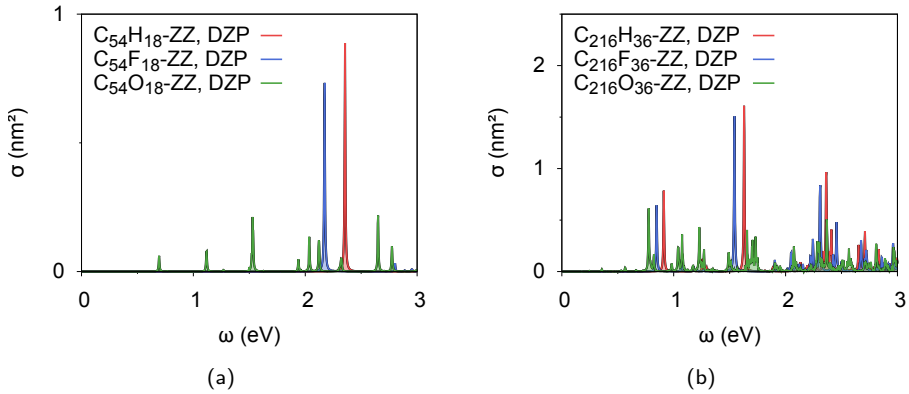
Figure 3.21: Optical cross section of zigzag graphene flakes with chemically alternative edge terminations. The cross sections of small flakes $C_{54}A_{18}$ on the panel (a) can be compared with that of large flakes $C_{216}A_{36}$ on the panel (b).

A further analysis of optical response is provided by the density change. In Figures 3.22(a), 3.22(b) and 3.22(c) the isosurfaces of density change for $C_{54}H_{18}$, $C_{54}F_{18}$, $C_{54}O_{18}$ are shown respectively. The density change is caused by a vertically-polarized (within the plane of the paper) light. The chosen windows of frequency include the optical gaps (2.45, 2.2, 0.7 eV) for $C_{54}H_{18}$, $C_{54}F_{18}$, $C_{54}O_{18}$, respectively. The density change is distributed spatially in a similar way for hydrogenated and fluorinated flakes, while for oxygenated flakes the distribution is qualitatively different. The electron activity of the oxygenated flake locates mainly on the oxygen atoms. The equivalued surface of the density change can be approximated as a set of d-type spherical harmonics $x^2 - y^2$ with principal axis oriented along carbon-oxygen bonds. The shape hints a strong localization of electrons towards oxygen, comparing to a relatively weak attraction by hydrogen and fluorine. As stated above the qualitative difference for the oxygenated flake can be traced to the different electronic structure of the atom's outer shell.
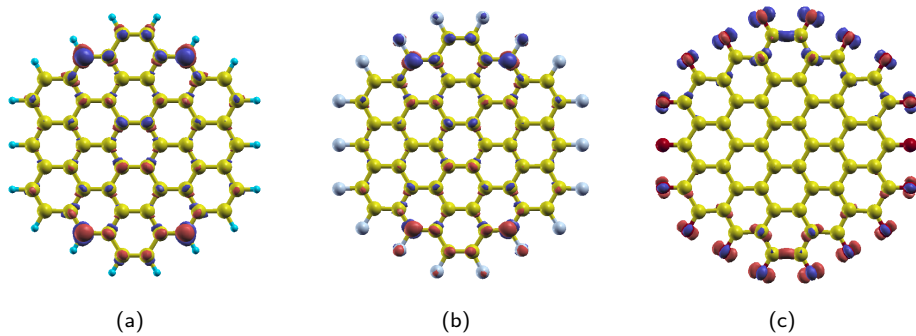
Figure 3.22: Density change for chemically modified flakes $C_{54}A_{18}$-ZZ. The density change is caused by a vertically polarized light at the frequency of the first resonance of the cross section. Panel a), b) and c) show the density change for terminal atoms H, F and O, respectively.

3.8.2 EDGE SATURATION WITH HYDROXYL GROUPS

A richer behavior is caused by saturating graphene dangling bonds with hydroxyl groups. The modification of the flake's edges with hydroxyl groups (OH) is more complex than the single-atom modifications discussed in section 3.8.1. The geometry optimization calculations show many different equilibrium geometries in which the hydrogens in the hydroxyl group can also stick out of the 2D-molecular-plane. Moreover, hydrogen-oxygen bonds of the hydroxyl groups can be oriented differently with respect to the flake plane. In Figure 3.23(a)[138] we show four geometries found by relaxing the flake with SIESTA starting from slightly different initial configurations. The colored enlarged dots indicate hydroxyl groups which are sticking out of the plane. Although the total energy of the flakes increases with the number of out-of-plane groups – see Table 3.6 where the total energy for the smaller flake for 4 different geometries is shown – there is an energy barrier which prevents a relaxation to the lowest-energy in-plane geometry. On average the C-O bond length is found equal to $\simeq 1.365$Å and the O-H bond length equal to $\simeq 1.000$ Å.

Similarly, total energy, the optical cross section also depends on the chosen equilibrium geometry configuration. In Fig. 3.23(b) we show the cross sections for the four considered flakes. The cross section curves are color-coded to create a connection with the corresponding equilibrium geometries. We see that the symmetric geometries (first two of Fig. 3.23(a)) lead to the appearance of single strong resonances in the range 0–2.5 eV, while the asymmetric geometries (last two of Fig. 3.23(a)) lead to the appearance of many weaker resonances. In order to confirm the origin of the resonances, we analyzed the non-interacting optical response functions. The corresponding non-interacting cross sections (shown in the Figure 3.23(c)), are qualitatively similar to the true cross sections, Figure 3.23(b). The analysis of the dipole transitions shows that the strong resonances of symmetrical arrangements are four-fold degenerated, while the asymmetry (introduced by hydroxyl groups) removes this degeneracy. The number of optical resonances is increased due to the symmetry breaking.

System	Total energy, eV
$C_{54}OH_{18}$, Geometry 1	-16478.31
$C_{54}OH_{18}$, Geometry 2	-16473.83
$C_{54}OH_{18}$, Geometry 3	-16476.73
$C_{54}OH_{18}$, Geometry 4	-16477.42

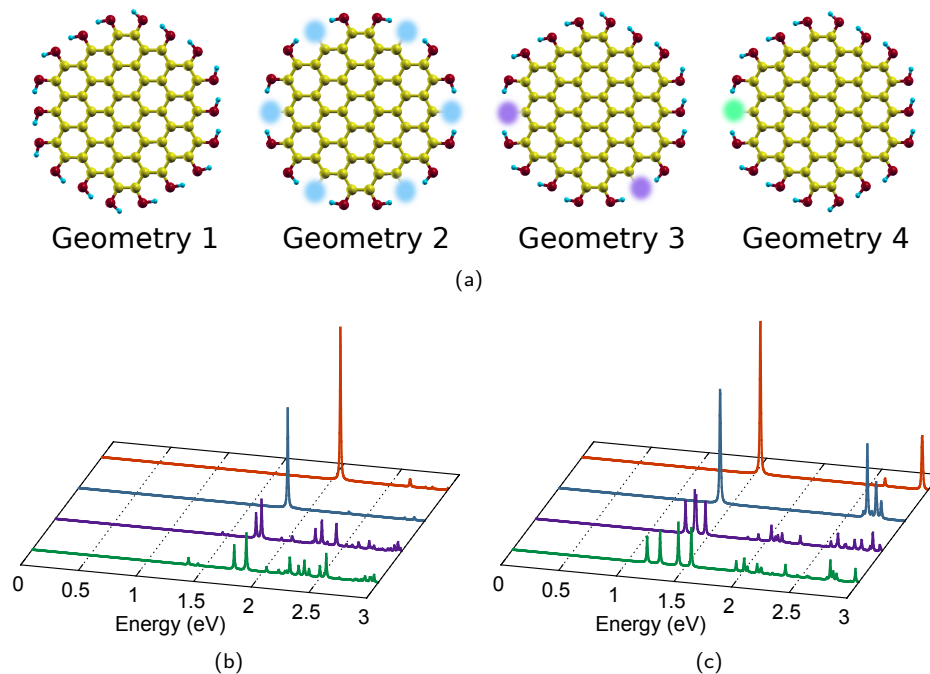Table 3.6: Total energy of the system for different geometry configurations.

Figure 3.23: Hydroxyl-saturated flake $C_{54}OH_{18}$-ZZ. The considered equilibrium geometries are collected on panel (a). True optical cross section is shown on panel (b), while the non-interacting cross section is shown on panel (c). Filled colored circles on panel (a) indicate the out-of-plane OH groups. Spectra on panels (b) and (c) are plotted with the same color as the colored circles on panel (a).

In Fig. 3.24 the calculated density change for the lowest energy isomer of the hydroxyl-saturated flake is shown. Hydrogen binds the spare oxygen electron and OH group becomes chemically similar to hydrogen and fluorine. Similarity between OH group saturated flakes and hydrogenated and fluorinated flakes are evident in the cross section, Fig.3.21, and in the density change plot, Fig. 3.22.
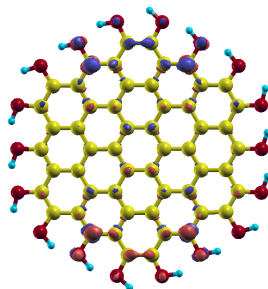
Figure 3.24: Density change for chemically modified flakes $C_{54}A_{18}$-ZZ. The density change is caused by a vertically in-plane polarized light at the frequency of the first resonances of the cross section.

In this section we demonstrated that the optical response of graphene flakes is tunable by chemical modifications. The substitution of edge-saturating hydrogen atoms by fluorine lowers the energy gap. In contrast, the oxygen passivation leads to a hole doping which alters optical absorption of small flakes dramatically. In hydroxyl-saturated flakes many equilibrium geometries can be achieved each of which produces a different optical absorption spectrum, lifting degeneration and thus, enriching the optical optical spectra.

3.9 CONCLUSIONS

The optical absorption of graphene-like nanoflakes has been studied in relation to its shape, size and chemical doping. We have considered flakes of flat hexagonal and rectangular shape. Due to the honeycomb structure typical for graphene-like material, hexagonal flakes can have only one type of edge – ArmChair (AC) or ZigZag (ZZ). In contrast, the rectangular flakes always have both types of edges. The flakes considered in the study contain a minimum of 42 carbon atoms and up to 1080 carbon atoms. This was possible by employing the SZ basis set, a least computationally expensive basis set, which is proven to provide reliable qualitative results as compared with more complete basis sets. We have shown that the overall features of the absorption spectrum are not affected by the use of this small basis set. Moreover, also the general behavior of well-defined excitation peaks in relation to the flakes' size and geometry can be analyzed even employing the minimal SZ basis set available in SIESTA.

The results show that the low-energy features in the spectrum can be largely affected by the edge's type, even for relatively large flakes. In particular, the dependence of the optical gap frequency on the edge type appeared to be evident and it can be traced back to the edge states typical of the ZZ edge type. The presence of both ZZ and AC edges as in the case of square flakes leads to closing the optical gap even for very small nanoflakes. Contrary to the optical gap, the frequency of plasmon excitations almost independent on size (starting from 500 electrons) and the edge type. Moreover, the capacity to plot and analyze the induced density allows us to study in which part of the flake the absorption takes place. Finally, the saturation of the dangling bonds by means of different chemical species has been proven to be a meaningful way to tailor the optical properties of nanoflakes.

4 | TUNABLE MOLECULAR PLASMONS IN POLYCYCLIC AROMATIC HYDROCARBONS
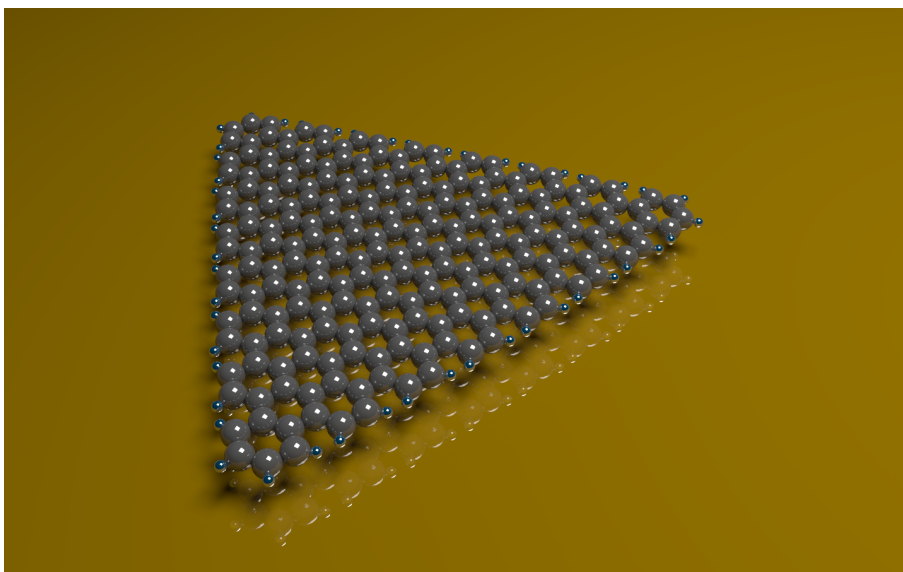
In the work published by Manjavacas et al.[139] we analyzed the effect of electronic doping in Polycyclic Aromatic Hydrocarbons (PAHs). Moreover, in the paper we showed the validity of the Tight-Binding (TB) method for calculating the absorption spectra and study the effect of electronic doping. The TB results were compared to the more sophisticated TDDFT results and they were found to be in good agreement. Both approaches succeeded in capturing the behavior of PAHs under electronic doping. Furthermore, in the manuscript we showed the plasmonic field enhancement when considering an array of PAH molecules placed in proximity. In this Chapter we focus on the results for PAHs molecules obtained with our TDDFT code.

Plasmonics has emerged as a promising path towards nanoscale light circuitry[140, 141] and

optical integration,[142,143] providing significant subwavelength confinement[144] and mechanisms for both spectral and spatial control over light propagation.[140,145,146] The remarkable structural tunability of plasmon resonances, as manifested from their strong dependence on size, composition, and shape of the supporting nanostructure,[147] enables light manipulation at the nanoscale, but demands exquisite fabrication accuracy.

Traditional plasmonic materials are simple and noble metals, which are molded into desired geometries by either chemical or lithographic methods. A vast amount of work has been devoted to producing monodispersive colloids of nanoparticles of these materials with specific morphologies such as spheres, shells, rods, stars, and simple polyhedra.[148] Integration of such nanoparticles into plasmonic systems using chemical self-assembly[149] offers a scalable strategy for high-yield synthesis of complex plasmonic nanostructures, although control over individual particle positions and interparticle gaps is generally poor and severely hampers the performance of the whole system. The alternative approach, based on lithography, provides better control over the relative positions of individual components, but suffers from limited spatial resolution ∼10 nm and contamination from resists in electron and optical lithographies and from spurious atomic species in focused ion-beam milling.

In this Chapter, we demonstrate plasmonic behavior in individual PAHs. Specifically, we predict highly tunable low-energy plasmonic resonances in PAHs using TDDFT. These molecules can be regarded as nanometer-sized forms of graphene, from which they inherit their high electrical tunability. They consist of finite arrangements of aromatic benzene rings and bear a close resemblance to the so-called graphene quantum dots,[150] are readily available through chemical synthesis[106,151–154] and have been extensively investigated in a variety of settings ranging from possible candidates for primitive forms of life[155] to device materials in electronic and optical applications.[152] While the electronic excitations and fluorescence properties of PAHs are well studied and understood,[60,156,157] their collective low-energy resonances and their dependence on the charge state and edge configuration have, to our knowledge, not been addressed previously. Using state-of-the-art theoretical calculations, we show the existence of pronounced collective electronic excitations in small systems consisting of less than 100 carbon atoms, and we find their frequencies to be strongly dependent on the charge state of the molecules. This behavior is reminiscent of the plasmons recently observed in doped graphene.[111,158] Furthermore, both the frequencies and the strengths of these resonances are strongly renormalized with respect to the one-electron transitions obtained in a noninteracting picture. For these reasons, in what follows we refer to these excitations as molecular plasmons.

While the existence of plasmons has been extensively demonstrated in atomic-scale systems such as atomic chains,[159] fullerenes,[160] and carbon nanotubes,[161] we find that the PAH structures provide a more general strategy for nanoscale plasmonics because their molecular plasmons exhibit an exceptional structural and electrical tunability, as we show below. Just like graphene,[111,158,162] these carbon-based planar structures sustain plasmons that can be switched on/off through electrical doping. However, we find that the electrical tunability of PAHs is even greater than for graphene. Quite remarkably, we find that the plasmonic behavior of PAHs can be controlled by the addition or removal of a single electron. For comparison, raising the Fermi level of an individual sheet of graphene by 1 eV, which is an affordable change, requires adding one electron for every 50 carbon atoms, and thus, adding or removing one electron can be simply achieved through electrical gating in molecules of that size. A significant advantage with PAHs over graphene is that

their extreme electrical tunability extends through the visible range of the spectrum, thus emphasizing their potential importance for optoelectronic technologies. This analysis can be straightforwardly extended to very large and coupled systems, in which PAHs can act as tunable integrated plasmonic components. The findings enforce interest on chemically-available structural-imperfection-free molecules for plasmonic devices development.

4.1 Calculation Details

For the ground state DFT calculations the SIESTA method[6] is employed. We used the local-density approximation (LDA)[48] for the exchange and correlation energy and a double-ζ polarized (DZP) basis set, see Section 2.2.2. This yielded nearly identical results to the ones obtained using the generalized gradient approximation (GGA).[163] The DZP basis contains 13 orbitals per C atom and 5 orbitals per H atom. The radii of those orbitals are determined by an energy shift of 100 meV,[6] see Section 2.2.3, and the fineness of the real-space mesh is equivalent to a plane-wave cutoff of 100 Ry, see Section 2.2.1. In all PAH molecules here considered, the carbon atoms along the edges are bound to hydrogen atoms. We take the PAH atomic structures to be planar, with C-C and C-H distances of 0.142 and 0.109 nm, respectively. Note that structural optimized geometries do not show qualitatively different results, the emergence of low-energy optical transitions upon doping is a robust effect, independent of the fine structural details, and it takes place even after the effect of structural relaxation on the optical spectra of the molecules is considered. In our theoretical framework we measure the above mentioned properties by changing the net charge state of the molecules. In particular, in SIESTA via the input-flag $NetCharge$ we can perform DFT ground-state calculations specifying the net charge of the system. This allows us to simulate the presence of an external gate enabling the PAHs to gain or lose extra charge. Negative values of $NetCharge$ correspond to a higher number of electron charges in the system, while positive values of $NetCharge$ lead to a system where electron charges are removed. A value of $NetCharge$ equal to -1 means an electron charge has been added to the system. For the calculations presented in this chapter an electronic temperature equal to $300K$ has been chosen. TDDFT calculations including the temperature effects have been introduced in Section 1.3.7.

The KS orbitals and energies obtained with SIESTA are taken as input to calculate the optical response of the system within TDDFT[46] using the MBPT-LCAO.[17,81] We disregard spin-polarization effects, which we find to produce marginal energy shifts in the electronic energies, and therefore, we expect them to contribute negligibly to the optical response.

4.2 Armchair and Zigzag Triangular PAHs

Let us first consider triangular shaped carbon PAHs. Due to the honey-comb lattice structure typical of graphene-like material the triangular PAHs have either ArmChair (AC) or ZigZag (ZZ) edges. In Fig. 4.1 and Fig. 4.2 the optical cross section results for AC triangular PAHs of different sizes together with the corresponding geometries are shown. In particular, the low-energy cross section is compared for AC flakes with different net charge. In Fig. 4.2 Q indicates the netcharge of the PAH: $Q = 0$ is the neutral system, $Q = -1$

indicates that one negative electronic-charge is added to the system and $Q = 1$ stands for the removal of one electron charge from the system.

The smallest AC flake considered, see Fig. 4.1, is the triphenylene molecule and contains 2 benzene rings along each triangular side. In Figures 4.2(a), 4.2(b) and 4.2(c) we consider AC triangular PAHs with a higher number of benzene rings along the side, respectively with 3, 4, 8 benzene rings. In theirs neutral form (charge state Q = 0), no observable excitation resonances are apparent in the low-energy region of the spectra. However, when an electron is either added or subtracted from the molecules, new strong features emerge in the absorption spectrum.

In particular, for triphenylene (Fig. 4.1), this is in agreement with the measured >4 eV absorption gap.[154] A satellite peak is also discernible to the right (left) of the dominant feature for single electron (hole) doping. Adding a second electron or hole to the molecule results in an increased plasmon strength and a blue shift in energy, as expected from the higher concentration of doping charges.[126] For the triphenylene molecule in Fig. 4.1 panel (b) we plot the induced charge distributions corresponding to the different peaks in the optical cross section. The charge distribution analysis reveals that these modes have a strong dipolar character, similar to those typically observed in coupled plasmonic systems, and support our identification of the absorption features in this PAH as molecular plasmons.

Furthermore, in panels (c) and (d) are shown the density change and the optical cross section for the noninteracting case. Also in this case, new resonances in the cross section rise when we dope the system. This fact is then independent of the renormalizing kernel and, thus, it can be understood by analysing the KS levels before and after doping. The results of this analysis are presented in Section 4.2.1, where we relate the different behavior of AC and ZZ with their KS level degeneracy at the Fermi energy.

In general, we observed that all the AC triangular PAHs show a similar response under doping, with the appearance of new low-frequency resonances as the system is electronically doped. Notable, in AC triangular PAHs, low-frequency resonances can be turned on just by adding or removing *one* electron. As expected, the bigger the flake the richer is the absorption spectrum, with more peaks arising at low frequency once the flake is doped. Completely different is the behavior of ZZ triangular flakes, see Fig. 4.3. No new low-frequency resonances arise after doping the flakes when we add (remove) a single electron, and not even after a second electron is added (removed) from the system we are able to observe new resonances in this energy window. In order to understand why this happens we need to look at the energies of the KS orbitals around the Fermi energy (E_F), see Section 4.2.1.
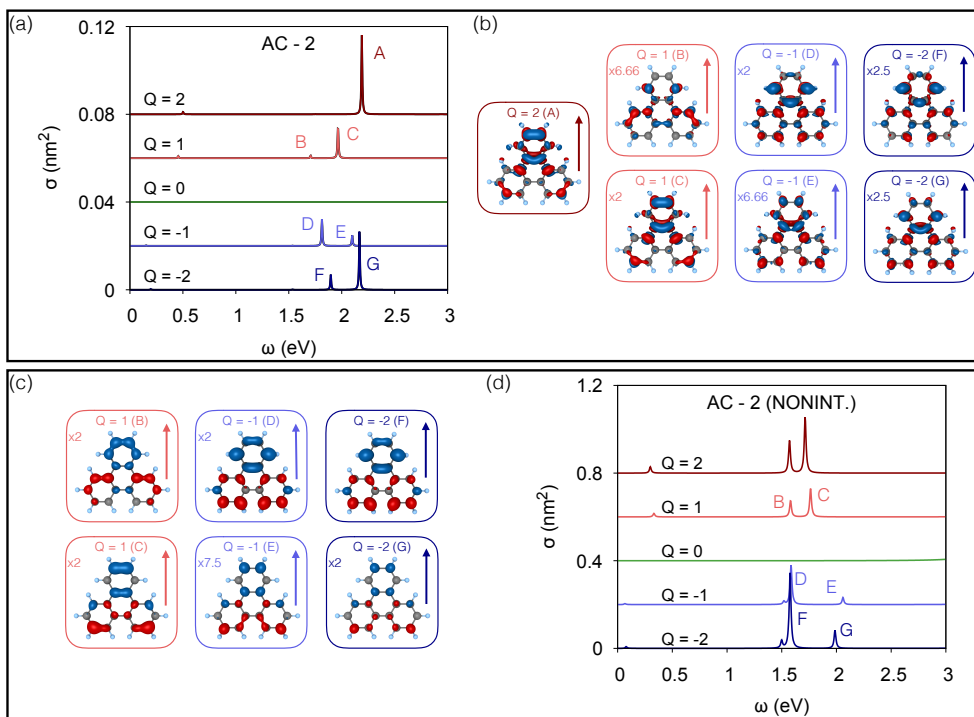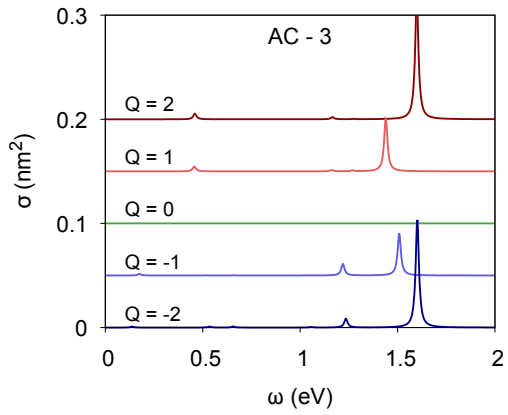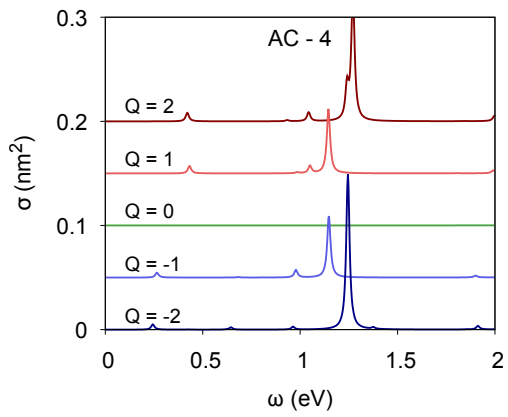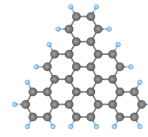
Figure 4.1: Triphenylene molecule. In panel (a) the interacting optical cross section is shown while in panel (b) the corresponding induced density is plotted. Panels (c) and (d) show the noninteracting density change and optical cross section, respectively.
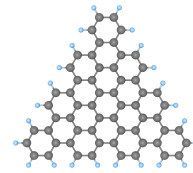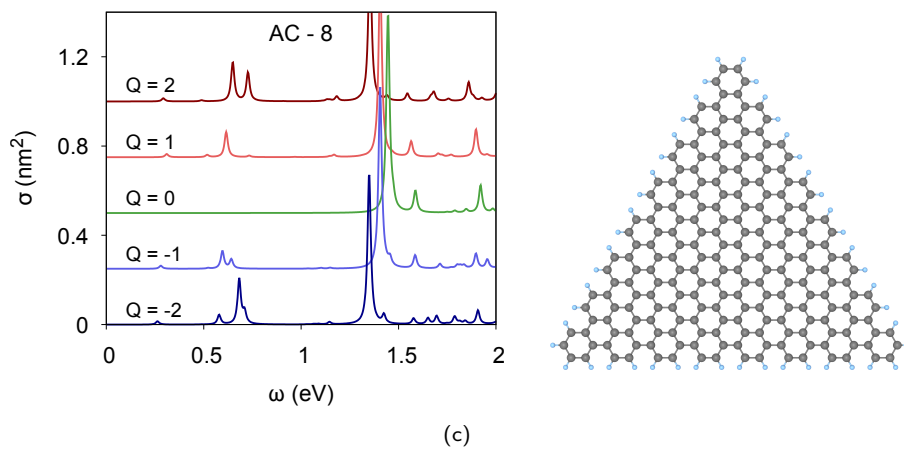
(a)

(b)

(c)

Figure 4.2: Cross section comparison for AC PAHs having different dimension and with different net charge. On x-axis the energy in eV in shown. In each plot Q states the net charge of the system.
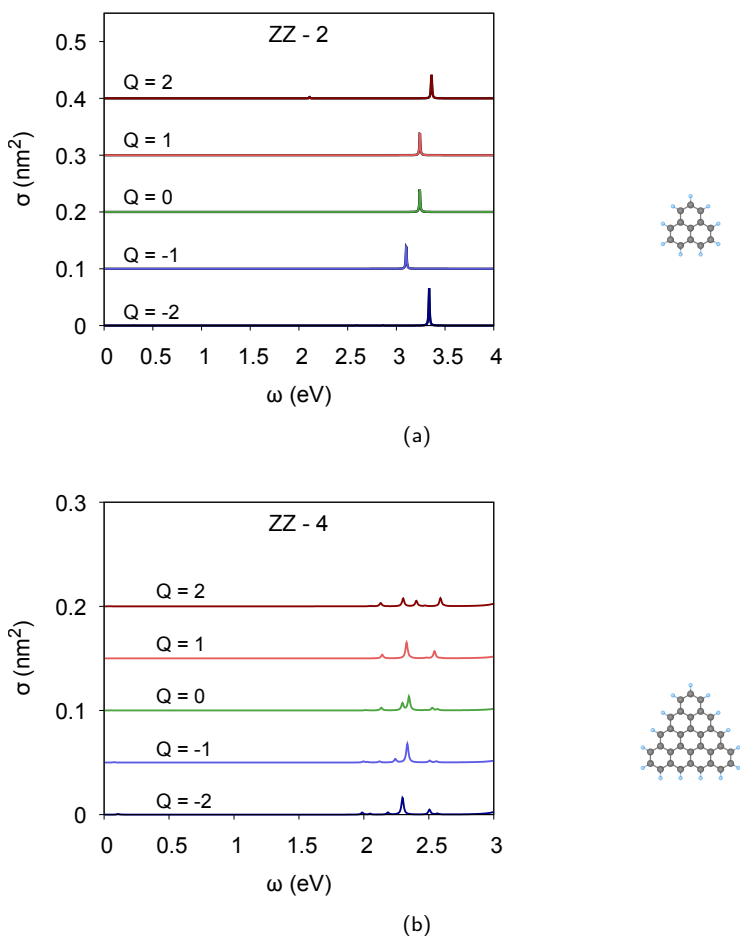
(a)

(b)

Figure 4.3: Cross section comparison for ZZ PAHs having different dimension and with different net charge. On x-axis the energy in eV in shown. In each plot Q states the net charge of the system.

4.2.1 OPENING OF NEW TRANSITIONS

The interacting absorption spectrum undergoes a strong renormalization which leads to a spectrum that differs significantly from the non-interacting one calculated out of the Kohn-Sham DFT orbitals. However, the opening of new transitions at low energy can be tracked using a DFT ground states analysis as we are going to show in this Section.

In Fig. 4.4 we show the Density Of the State (DOS), obtained from the SIESTA DFT calculation, for some triangular AC and triangular ZZ PAHs. In particular, in Fig. 4.4(a) the two smallest undoped flakes of each family (AC and ZZ) are analyzed. On the bottom-x-axis the orbital levels are shown, the HOMO level is highlighted by the vertical green dashed line. The y-axis indicates the energy of the levels, the 0 represents the Fermi energy

(E_F). The Fermi Dirac (F-D) distribution indicated on the top-x-axis is plotted as a green curve. From Fig. 4.4(a) we note that for the AC PAH the E_F lies within the gap while ZZ PAH have degenerate levels at the Fermi energy. This behavior is the same in all AC and ZZ PAHs, independent of the size of the PAH.

In Fig. 4.4(b) and Fig. 4.4(c) the DOS of doped PAHs is presented, respectively, for the AC-4 and the ZZ-4. For the AC-4 we note that the DOS changes once we remove electrons. On the contrary, the DOS of the ZZ-4 system is unchanged. This behavior holds for all the AC and ZZ PAHs and even for doping levels as minimal as one electron. In fact, when we consider for example the AC-4 PAH we see that, even when one single electron is added (removed) it has to occupy the LUMO (leave a vacancy in the HOMO) opening the way for new low-energy electronic transitions, i.e. LUMO→LUMO+n (HOMO-n→HOMO) transition. Degenerate partially-occupied electronic levels are now found at the Fermi energy. By adding (removing) a second electron we observe a less drastic change in the spectra with the possibility of rising new resonances. In general, for all AC PAHs, the KS level configuration guarantees the appearance of new resonances in the optical spectrum after electron doping.

For ZZ flakes the situation is different, ZZ flakes have degenerate orbitals partially occupied around the E_F, before turning on new low-energy transitions all the levels need to be filled or emptied. This does not happen by adding (removing) only one or two extra electronic charges to the system, as can be seen in Fig. 4.4(c) where we compare the pristine ZZ-4 flake with the doped one. Much heavier electron doping is needed to move the Fermi energy and allow new excitations in the optical cross section.

In general, the optical unresponsiveness of ZZ triangular PAHs to light electronic doping can be connected to the presence of degenerate edge states at the Fermi energy. Moreover, we can correlate the size of the flake with the number of degenerate levels. Following Lieb's theorem,[134] it is the different number of atoms belonging to the two graphene intertwined hexagonal carbon sublattices (a and b) that define the number of degenerate orbitals.[135] In Fig. 4.5 the two sublattices a and b are shown for the AC-4 (left) and a ZZ-4 flake (right). The ZZ-4 in Fig. 4.5 has an unbalance between the two sublattice sites equal to 3 and indeed 3 degenerate levels at the Fermi energy are found, see Fig. 4.4(a).
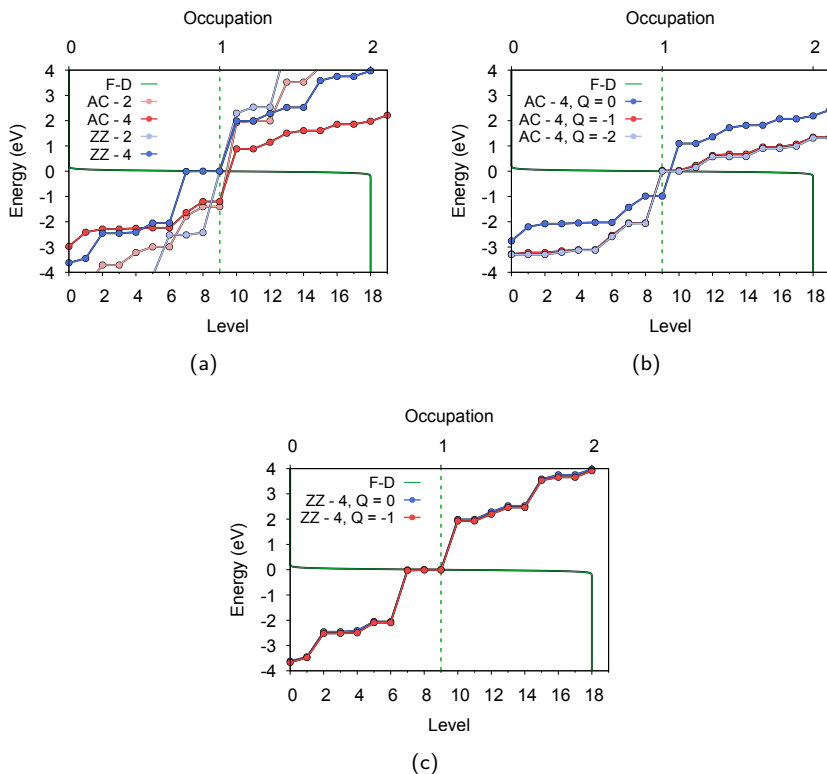
(a)

(b)

(c)

Figure 4.4: In each graph the bottom-x-axis indicates the molecular levels, the vertical dashed green line defines the HOMO level. The energy in eV of the different levels is indicated on the y-axis, 0 is Fermi energy (E_F). The top-x-axis shows the Fermi Dirac (F-D) distribution. In panel (a) a comparison between pristine AC and ZZ flakes for $Q = 0$ is shown. In panel (b) and (c) the levels of AC-4 and ZZ-4 triangular flakes for pristine and doped systems are plotted, respectively.
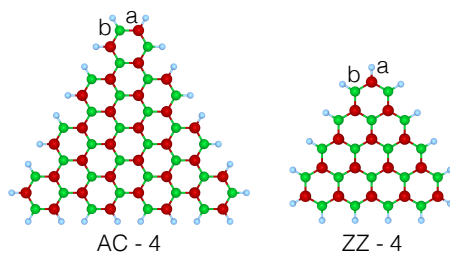

Figure 4.5: The sublattice sites a (red atoms) and b (green atoms) are shown. For the AC-4 flake (left) the a and b sites are balanced. While, for the ZZ-4 flake (right) the unbalance is equal to 3.
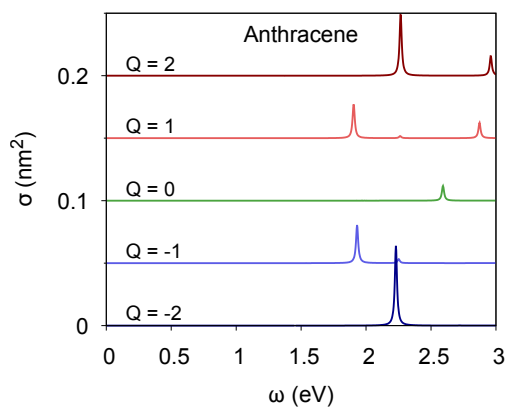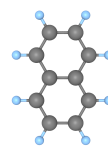
4.3 ONE DIMENSIONAL PAHS

In this section we show the optical response of one-dimensional PAHs. The C-C and C-H distance is taken, as in the previous case, equal to 0.142 and 0.109 nm, respectively. All the structure are planar.

One-dimensional PAHs behave similarly to triangular AC PAHs. Doped PAHs show low-energy resonance peaks that are not present in the undoped systems.
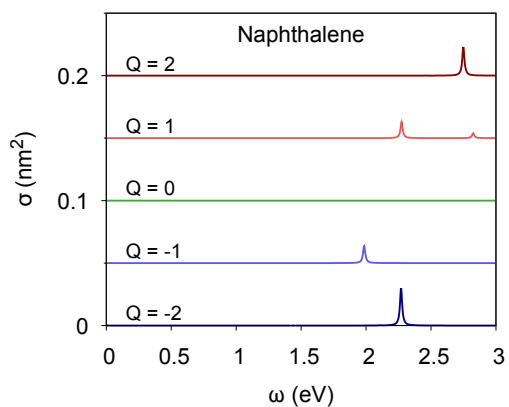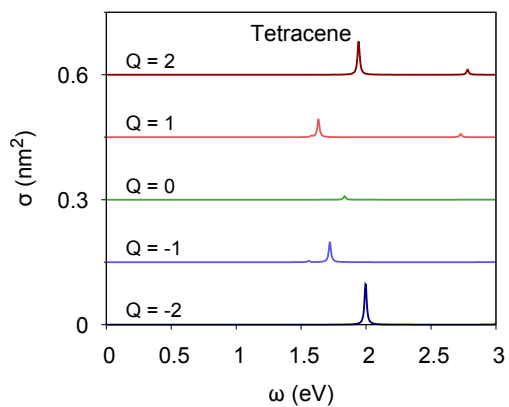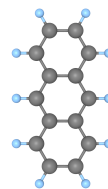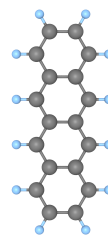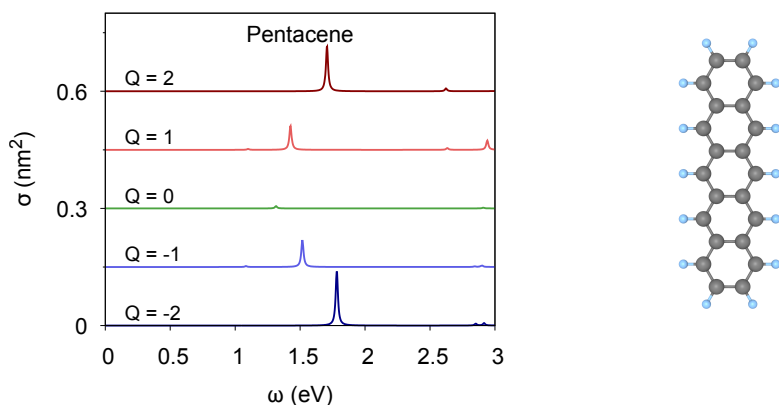
(a)

(b)

(c)

(d)
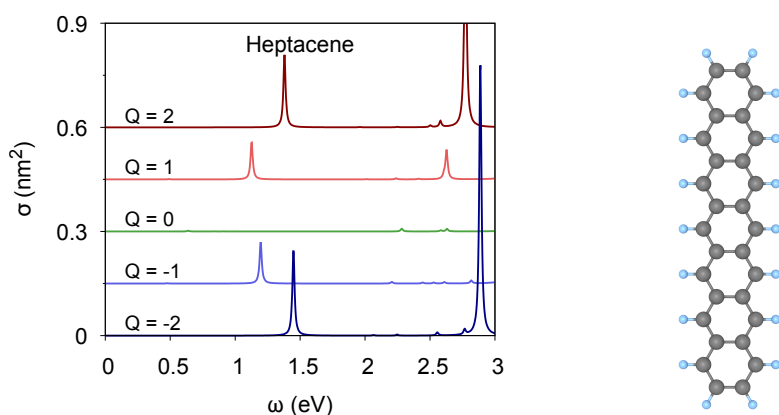
(e)

Figure 4.6: Cross section comparison of one-dimensional PAHs having different dimension and different net charge. On x-axis the energy in eV in shown. In each plot Q states the net charge of the system.

4.4 CONCLUSIONS

We have shown that PAHs with AC edges can sustain optical excitations at visible and near-infrared frequencies and that their energies are strongly dependent on the net charge state of the molecules, to the point that the addition or removal of a single electron can switch on/off the existence of such excitations. The mode frequencies are strongly modified when the effect of electron-electron interactions is taken into account via the kernel. However, we were able to trace back to the KS DOS configuration the reason for such a behavior. The existence of a gap in the AC pristine PAHs implies that, once doped, new transitions are available. These new transitions are renormalized by the kernel but still visible in the

optical response. On the contrary, PAHs with ZZ edges present degenerate KS levels at the Fermi energy and, thus, for such low level of doping, doped systems do not show any new low-energy transitions.

The renormalization due to the action of the kernel is interpreted as a signature of collective electron motion, either in the form of multiply coupled e-h pair excitations or severe renormalization of individual e-h pairs due to efficient polarization of other modes. Because of this incipient collective character, and in analogy to graphene plasmons, we refer to these doping induced optical resonances as molecular plasmons.

The existence of tunable plasmons in molecule-sized graphene structures has to be contrasted with the lack of well-defined plasmons in noble-metal nanoparticles of similar diameter, where nonlocal Landau damping plays a relevant role (i.e., plasmons can directly decay into e-h pairs). Additionally, our study poses new questions, such as how many plasmons can be supported by a molecule with a small number of valence electrons, and how large is the nonlinearity arising from the difference between the energy of a two-plasmon state and twice the energy of one plasmon. These nonlinear effects, which are essentially absent from traditional metallic nanoparticles, could be exploited in nonlinear optical applications.

Other types of unique plasmonic applications of PAH structures include the optical detection of atoms/molecules that act as charge donors or acceptors. Here, new plasmonic features would signal the occurrence of a charge transfer reaction. As already demonstrated for graphene in the infrared,[164, 165] electrical doping in a gated device could be used to maintain a certain fraction of molecules deposited on a transparent gate (e.g., ITO) in a charged state, thus enabling light modulation in the visible through fast electrical gating technology. The magnitudes of the absorption cross sections of the plasmons are comparable with the physical cross-section of the molecules, which could therefore be exploited to produce electrically tunable complete optical absorption[166] (perfect absorbers) in the visible. Finally we note that the plasmon linewidths (which have been fixed to 10 meV in the present calculations to facilitate the visualization of the spectra) are likely to be even narrower in realistic systems. Such sharp plasmons may also provide large field enhancements and be used in plasmonic waveguide applications.

PAH molecules can be regarded as nanometer-sized fragments of Graphene, but exhibit plasmons in the visible rather than in the mid infrared part of the spectrum. An interesting aspect of the molecular plasmons under investigation is that they require quantum mechanics to be properly described, and the interaction with each individual electron of the molecules is important. The TDDFT method here employed provides an efficient and reasonably accurate tool to describe many-electron quantum interactions in PAHs molecules. We believe that our study paves the way for a new area in nanophotonics benefiting from the unique plasmonic properties of molecular plasmons.

5 | Plasmonics at the Atomic-Scale: Near Field Distribution and Influence of Quantized Transport at Interfaces
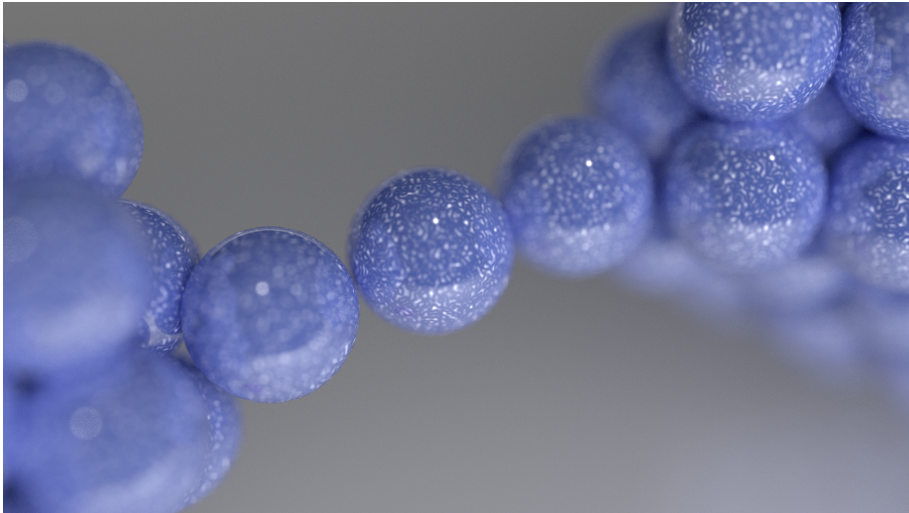
Collective excitations of conduction electrons at the surface of metallic nanostructures, commonly referred to as surface plasmons,[167, 168] provide a means to effectively bring light to the nanometer-scale thanks to the ability of the nanostructures to produce subwavelength field localization and large electro-magnetic enhancement in the proximity of the nanostructures,[4, 5, 169–172] establishing metal nanoantennas and nanoparticles as relevant building blocks in current nanooptics.[29, 173] The ability of light to coherently excite surface

plasmons in nanostructures[174,175] closes the gap between electronics and photonics. Thus, helping us to understand and control the optical response of nanosystems[30] in the search for nano-architectures that combine the current performance of miniaturized silicon-based electronics with the fast control and engineering of optical signals.

As nanotechnology reaches a control of nanoarchitectures at scales of the order of the nanometer and even subnanometer,[176–180] nanooptics is called to face new regimes of interaction, where the atomic scale needs to be considered to correctly determine the optical response of the nanosystem. Optical processes at the atomic scale can be critical in many branches of nanoscience such as in field-enhanced photochemistry,[181–184] in single molecule spectroscopy,[185–189] or in electronics at optical frequencies.[177,190–193] Surface plasmons are central for the development and the high optimization level of many techniques and processes, such as vibrational spectroscopies,,[185,194,195] field-enhanced spectroscopy,[169,195–200] photovoltaics,[201,202] active control of nanodevices,[111,203] thermotherapies,[204] optical sensing,[205–207] optical nanoengineering,[208] or near-field microscopy.[169,188,189,209]

Moreover, it has recently been shown that pushing the limits of nanometric plasmonics down to the realm of the atomic scale, the interaction of metal surfaces in the subnanometric proximity drives new optoelectronic phenomena, where an interplay between the photons, single electron transitions, plasmons, vibrations, and motion of atoms determine the complex outcome of the optical response, including strong quantum effects and nonlinearities.[172,179,210] Strong nonlocal dynamical screening[211] and quantum tunnelling[212–215] have been shown to drastically modify the optical response in a metallic subnanometric gap, establishing the limit of localization and enhancement of the optical fields far below the predictions from simple classical approaches.[170,212,216–220] On the other hand, even if typical surface plasmon excitations localize in the nanometer scale, recent ab initio calculations considering realistic nanoparticle structures have shown that the fine atomistic details of the crystallographic facets and vertices of the metal particle, with the presence of single atomic protrusions and edges, introduce further nonresonant light localization.[170,221] This is analogue to the macroscopic lightning rod effect,[144,222] but brought down to the atomic scale. The work presented in this Chapter covers two subjects related to the exciting lines of research described in the previous paragraph, namely, a study of the localization of the local field and the coupling of quantum transport with the far-field response. This work has resulted in two publications[170,223] In particular, in this chapter in Section 5.2[223] we tackle, among other issues, the problem posed by the "miniaturization" of molecular structures analyzing how structural atomistic details influence the plasmonic response in such nanosize objects. This is done by simulating a nanocavity formed by two metallic nanoparticles whose structures are prone to changes due to their proximity.

5.1 Atomistic Near-Field Nanoplasmonics: Field Localization

In order to study the plasmonic response of nanosystems it is necessary to address the problem theoretically within the framework of electronic structure methods going beyond more commonly used classical approaches which fail in describing the atomic-scale features produced by irregularity at the nanoscale. Classical approaches are often appropriate since the atomic-scale features are typically hidden in far-field optical spectroscopies. Never-

theless, in many physical and chemical processes nanoplasmonic modes are important and depend on the detailed distribution of the near-fields in confined systems.

In a recently published work[170] we have analyzed the evolution of the plasmonic response together with the distribution of the induced-localized-electric field for a system composed of two sodium nanoparticles placed in proximity and perturbed with an external electric field. In this study, the distance between the clusters is changed allowing to analyze the evolution of the optical plasmonic modes. The results for the optical properties showed the important role of atomic-scale structure details for nanoclusters placed few Angstrom apart. The two icosahedral nanoclusters contain 380 sodium atoms each. The single-cluster structure has been optimized in order to find an equilibrium geometry. Starting from an initial separation distance between the particles' inner faces of 20 Å the two clusters are brought together. The optical cross-section and the induced electric field is computed and analyzed as a function of the separation distance.

5.1.1 STRUCTURES AND COMPUTATIONAL DETAILS

The single cluster geometry optimization and the DFT ground state calculations for the dimer were performed with the SIESTA code.[6,7] The resulting Kohn-Sham wavefunctions and energies were used as an input for the MBPT-LCAO TDDFT code.[17] A Double–ζ Polarized (DZP) basis set was used for all the DFT calculations. The extension of the basis is given by an energyshift parameter equal to 100 meV. A MeshCutOff of 150 Ry was used for determining the fineness of the real-space grid used to compute the Hartree and exchange-correlation contributions to the energy and Hamiltonian. A description of the detailed meaning of the above mentioned SIESTA parameter can be found in section 2.2. The icosahedral single-cluster structure containing 380 sodium atoms was optimized starting from a configuration optimized with empirical potentials[224] and available at the Cambridge Cluster Database.[225] The relaxation stopped when the forces acting on the atoms were smaller than 0.03 eV/Å. The obtained structure of the Na_{380} turned out to be very similar to the initial one, showing a slightly higher density due to the well–known underestimation of the sodium lattice parameter by LDA,[226] see paragraph 5.2.1. In particular, the Local Density Approximation Ceperley-Alder (LDA-CA) functional has been adopted here. The geometry of the clusters in all the cases is the same, only the mutual position is changed. Once the optimized geometry is found, the two clusters are placed in proximity and three different configuration (face-to-face, tip-to-face, tip-to-tip) are considered in the calculations, see Fig. 5.1.

The TDDFT calculations were performed employing the Adiabatic Local Density Approximation (ALDA), i.e. using the LDA exchange-correlation kernel. In Fig. 5.1 the three considered configurations are shown. The separation distance (d_{sep}) is defined as the distance between the two cluster inner facets or atom (for the tip-to-tip configuration). A nominal size gap of zero value would correspond to the superposition of the atoms forming the two opposing tips/faces. A change in the separation distance corresponds to a change in the relative position of the clusters. The geometry of the clusters is not relaxed as the distance is changed, but it is assumed to correspond to the of the free-standing clusters.
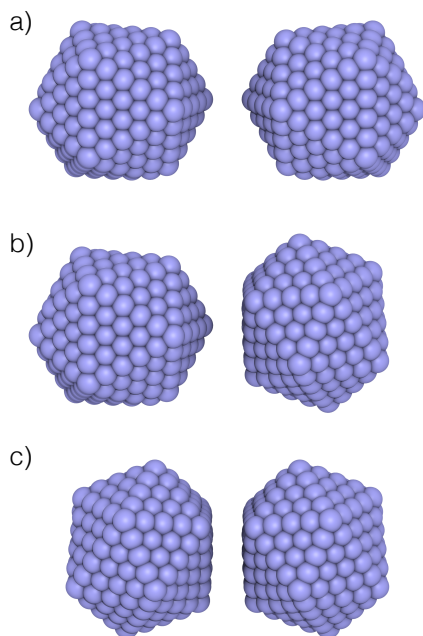
Figure 5.1: The three studied configurations are shown, starting from the top we find the tip-to-tip configuration (a), tip-to-face configuration (b) and face-to-face (c) configuration.

5.1.2 CLASSICAL DIPOLE-DIPOLE INTERACTION

In this section we want to show the polarizability results obtained with a simple classical model in which the two clusters are approximated with two polarizable point particles in an external oscillating electric field. This simple model is able to describe the dispersion of the main plasmonic modes as long as the dipole-dipole distance is larger that the size of the dipoles. For low dipole-dipole distance, this model is not applicable anymore. Depending on the direction of the external field we can have two relevant configurations,
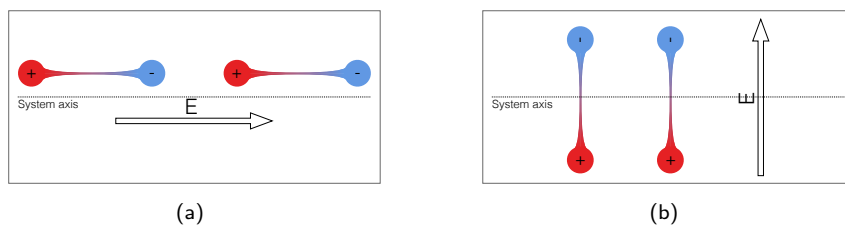

Figure 5.2: Representation of the relevant dipole-dipole configurations in relation with the external electric field. In panel (a) the direction of the electric field is along the two-cluster system axis. In panel (b) the electric field is orthogonal to the two-cluster system axis.

In both cases, when the two dipoles are far apart, the dipole-dipole interaction is negligible and each dipole behaves independently from the other. Once they are brought close enough they interact and the total dipole moment acting on the dipole 1 can be written as

$$\vec{\mu}_1 = \alpha(\vec{E}_2 + \vec{E}_{ext}(\omega)) = \alpha(T_{12}\mu_2 + \vec{E}_{ext}(\omega)) \tag{5.1}$$

where μ_1 and μ_2 are the values of dipole moment 1 and dipole moment 2, respectively, α is the polarizability, $\vec{E}_2$ is the electric field induced by dipole 2 on dipole 1 and $\vec{E}_{ext}(\omega)$ is the external field. T_{12} ($T_{12}^{ij} = (3r_{12,i}r_{12,j} - r_{12}^2\delta_{ij})/r_{12}^5$) is the dipole-dipole interaction matrix. where 1 and 2 indicate the dipoles and i and j the directions x, y, z. In matrix notation T becomes

$$T = \begin{pmatrix} -1/r^3 & 0 & 0 \\ 0 & 2/r^3 & 0 \\ 0 & 0 & -1/r^3 \end{pmatrix} \tag{5.2}$$

where r is the distance between the particles along the y coordinate. As we said if $\vec{E}_2$ is negligible the dipoles act independently on each other and the polarizability of each particle is then given by, where we have assume that the response of the isolated particle is dominated by a single resonance at ω_0 the solution of the driven harmonic oscillator,

$$\alpha \propto \frac{1}{(\omega_0^2 - \omega^2) - i\gamma\omega}. \tag{5.3}$$

If we take an isotropic particle we write the polarizability tensor

$$Re\{\alpha\} = \begin{pmatrix} \frac{\omega_0^2 - \omega^2}{(\omega_0^2 - \omega^2)^2 + \gamma^2\omega^2} & 0 & 0 \\ 0 & \frac{\omega_0^2 - \omega^2}{(\omega_0^2 - \omega^2)^2 + \gamma^2\omega^2} & 0 \\ 0 & 0 & \frac{\omega_0^2 - \omega^2}{(\omega_0^2 - \omega^2)^2 + \gamma^2\omega^2} \end{pmatrix} \tag{5.4}$$

$$Im\{\alpha\} = \begin{pmatrix} \frac{-\omega\gamma}{(\omega_0^2 - \omega^2)^2 + \gamma^2\omega^2} & 0 & 0 \\ 0 & \frac{-\omega\gamma}{(\omega_0^2 - \omega^2)^2 + \gamma^2\omega^2} & 0 \\ 0 & 0 & \frac{-\omega\gamma}{(\omega_0^2 - \omega^2)^2 + \gamma^2\omega^2} \end{pmatrix} \tag{5.5}$$

where $\gamma << 1$ and ω_0 is the natural frequency of the oscillator. Equation 5.1 can be written for dipole 2,

$$\vec{\mu}_2 = \alpha(\vec{E}_1 + \vec{E}_{ext}). \tag{5.6}$$

Combining 5.6 in 5.1 we get

$$\vec{\mu}_1 = (1 - \alpha T\alpha T)^{-1}\alpha(T\alpha + 1)\vec{E}_{ext} \tag{5.7}$$

where we used the fact that $\mu_1 = \mu_2$. In our modelled dipole-dipole interaction we observe a redshift as we decrease the distance between the two dipoles when the two particles are oriented sequentially, see in Fig. 5.2(a). On the contrary they are blueshifted when they are parallel, see Fig. 5.2(b). Our ab-initio simulations, as we will show in the next sections, show the same trend. This is a oversimplified classical model where point particles

and only dipole-dipole interactions were considered. However, in general, even in more advanced classical approaches, they have some limitations and the need of a quantum-correct model[213] or a quantum approach[170, 223] is necessary to correctly describe the system for intercluster distances below few Angstrom. If we compared the results in Fig. 5.3 with the ab-initio results obtained for the nonrelaxed two-cluster system described in Section 5.2 we see, in particular, that the classical approach completely misses the tunneling regime. The results on the absorption spectrum obtained with our ab-initio MBPT-LCAO code are shown and explained in detail in the next sections.

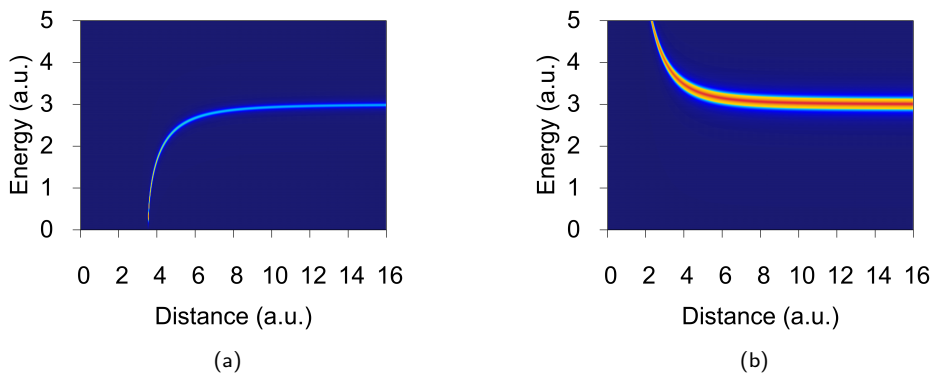(a)   (b)

Figure 5.3: Simple model for the optical response of two point dipoles. The model is not applicable when the interparticle distance starts to be comparable to the dipole size, i.e. the size of the real particle. In panel (a) the electric field is aligned along the line connecting the point dipoles. In panel (b) the electric field is orthogonal to the line connecting the point dipoles.

5.1.3 EVOLUTION OF THE OPTICAL ABSORPTION AND FIELD LOCALIZATION WITH INTER-CLUSTER DISTANCE

The three dimer configurations shown in Fig. 5.1 have very different optical responses. In Fig. 5.4 the absorption cross-section and the induced electric field distribution are plotted. Moreover, in Fig. 5.4 we present the comparison between the ab-initio TDDFT and TDDFT-LDA simulations within the Jellium Model (JM),[210] where the plasmon cavity is formed by a sharp spherical potential (positive background), Fig. 5.4 (d) and (h) panels. In the JM only the valence electrons are treated explicitly, and the ionic cores are represented through an homogeneous positive background potential limited by a spherical boundary (jellium edge). In the comparison, we used JM spheres of radius 15.57 Å and fixed the averaged electron density to that of bulk Na (Wigner-Seitz radius $r_s = 2.12$ Å). The resulting closed-shell JM cluster contains 398 electrons and is similar in size to the Na_{380} cluster tackled in the atomistic calculations.

For distances above $\sim$7 Å all the four spectra present a Bonding Dipolar Plasmon (BDP) at very similar energies, dispersing as the two clusters approach, i.e. the BDP resonance

redshifts as the two clusters get closer and closer.[30, 227, 228] At such spatial separations no significant current can flow from one cluster to the other, since the tunnelling probability for electrons to go from one cluster to the other is small. As we keep approaching the two clusters we eventually enter in the tunnelling regime, the BDP mode slowly disappears leaving the way to the Charge Transfer Plasmon (CTP) and modes with higher angular components, here so-called Quadrupolar Plasmon (QP) mode.

A more intense CTP corresponding to a larger tunnelling current is found for the face-to-face configuration. Moreover, in this configuration a non-negligible tunneling current is first observed at larger separation distance due to the larger contact area in the face-to-face configuration. In the tip-to-tip configuration a smaller separation distance (d_{sep}) is required for the quenching of the BDP and the appearance of the CTP mode.

In Fig. 5.4 (e), (f), (g) and (h) the induced near-field is shown in the plane orthogonal to the dimer axis and passing through the center of the nanoparticles for the face-to-face (e), tip-to-facet (f), tip-to-tip (g), and jellium spherical (h) configurations. The width of the gap is set in all the cases to $d_{sep} = 10$ Å, with the incident light in resonance with the hybridized BDP corresponding to the position marked with a green dot on the spectra to the left. The Coulomb coupling between induced charges of opposite signs across the gap leads to a strong localization and enhancement of the near fields in the gap. Overall, the nanometric near-field distributions obtained in the full atomistic calculations at the BDP frequency show similar gross features to those in the JM calculations. However, the exact atomistic structure of the junction determines the details of the near-field distribution, and in particular the appearance of extremely localized "hot spots". In the face-to-face configuration the field is distributed quite homogeneously in the whole cavity as expected. Less intense atomic-scale hot spots can be also identified at the edges and vertices of the different facets of the nanocrystal surfaces. These are due to an atomic-scale lightning rod effect. Lightning rod effect states that for an electrically charged object the electric field is higher at the sharpest features of the object. In our case, what we observe is an atomic-scale lighting rod effect where the electric field is enhanced by the sharp features (edges and tips) of our nanoparticles. In the configurations with the tip, the tip-induced enhancement produces an extreme localization of the local near-field down to an extension of a few Angstroms. This extreme confinement of the fields is missing in the spherical JM.
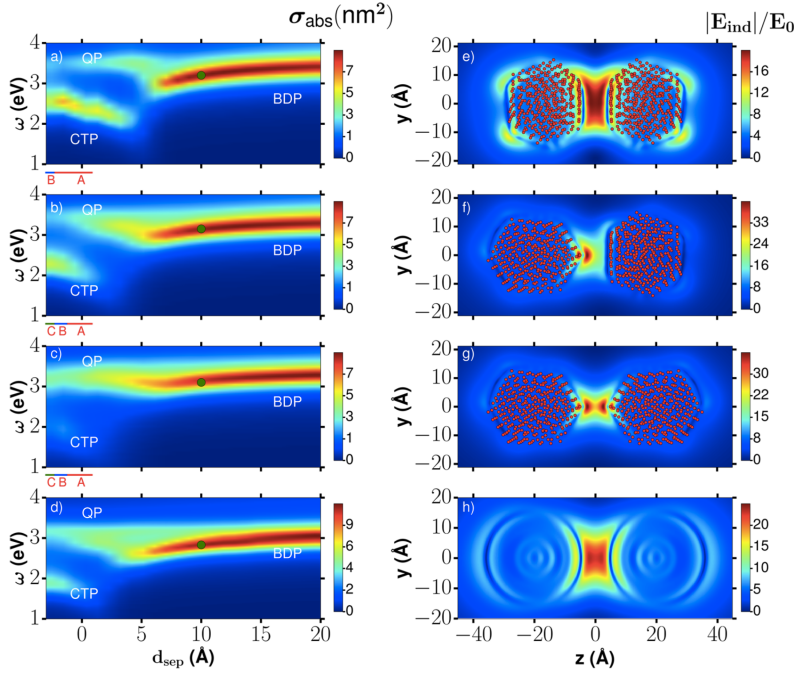
Figure 5.4: Spectral evolution of the absorption cross section of the plasmonic dimers (a), (b) and (c) depicted in (e), (f) and (g) compared with the results obtained from jellium sphere, (d) and (h). The direction of the polarization field is parallel to the dimer axis and d_{sep} is the interparticle distance (see the text for the precise definition). Separation distances lower than 1 Å and negative distances represent overlapping clusters and have been modeled in (a), (b) and (c) by modified geometries in which atomic layers of one of the clusters are subsequently removed (region A, one layer removed; region B, 2 layers; region C, 3 layers). Panels (e), (f) and h) show the distribution of the local induced–field produced in the (y,z) plane containing the axis of the dimer for an energy in resonance with the BDP and for a separation distance of 10 Å: (e) the gap is formed by a face-to-face junction, (f) face-to-tip, and (g) tip-to-tip configurations. In (h) the same situation for a dimer described by the jellium model is displayed.

The evolution of the field confinement in the gap as a function of separation distance, d_{sep}, and the corresponding change of the localization area A is further illustrated in Fig. 5.5, where the field enhancement is shown in the plane orthogonal to the axis dimer in the center of the gap between the two particles for each configuration (face-to-face on the left column, tip-to-face on the middle column, and tip-to-tip on the right column). When the particles are far away from each other ($d_{sep} = 20$ Å) a broad spatial profile of the plasmonic near-field is obtained (top row). For smaller separations, $d_{sep} = 10$ Å, the profile of the near field reflects the atomistic structure of the nanoparticle surfaces across the gap, showing a triangular shape for the face-to-face configuration, a round spot for the tip-to-tip configuration, and a round spot on top of a triangular background for the tip-to-face configuration. The tip-to-tip configuration corresponds to the strongest field

confinement with the smallest spot size reduced to atomic dimensions, i.e. below 1 nm^2 for $d_{sep} \approx 6$ Å. For the face-to-face configuration, the spot profile and size change only slightly when d_{sep} is reduced from 10 to 6 Å, and the tip-to-face configuration is characterized by an intermediate situation.
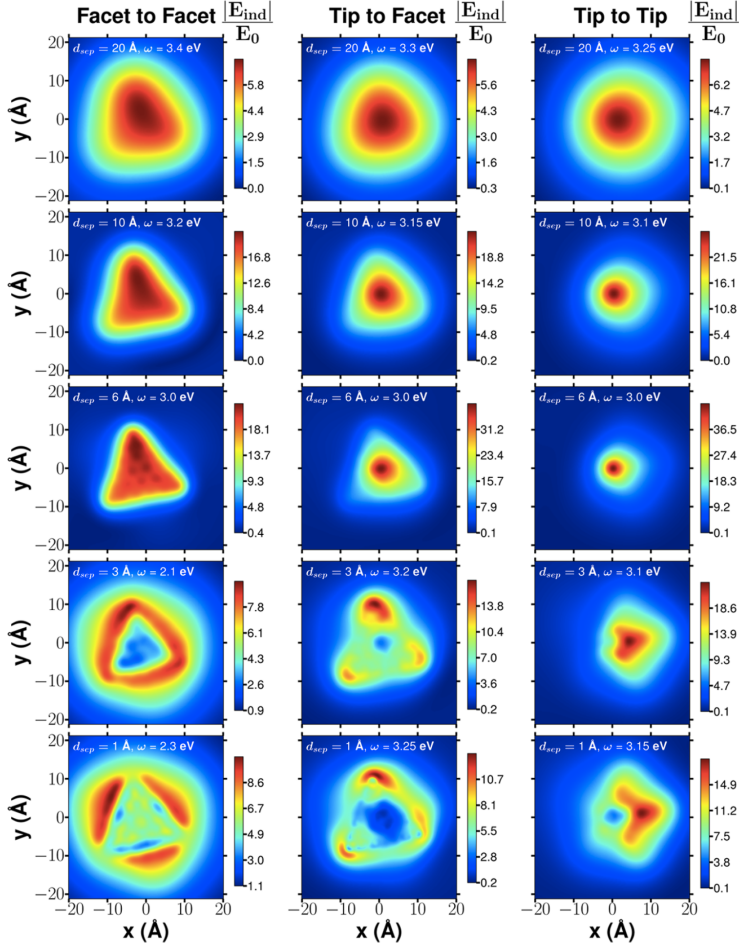
Figure 5.5: Local induced-field enhancement at resonance in the midplane of the gap between two Na$_{380}$ clusters for our three configurations, face-to-face gap (left column), tip-to-face (middle column) and tip-to-tip (right column). The incident planewave is polarized along the dimer axis. From top to bottom each case shows a decreasing separation distance for each configuration, from $d_{sep} = 20$ Å (largely separated particles, on the top row) to $d_{sep} = 1$ Å (interpenetrating situation on the bottom row). The influence of the atomic scale features at the nanogaps is directly noticeable.

We can finally conclude by saying that with our first-principles full-atomistic TDDFT

calculations we have demonstrated that the field localization and enhancement inside the plasmonic nanogaps can be very different depending on whether the distribution of the atoms at the gap defines a flat surface, or presents atomic-scale tip-like protrusions. In fact, we have demonstrated that the distribution of the near-field close to plasmonic nanoparticles presents subnanometric hot spots that reflect atomic-scale features at the nanoparticle surface.

It is important to underlight that not only the local field but also the low energy far-field spectrum is affected by the clusters mutual configuration. This is evident if we compare the TDDFT and JM results. In fact, although the JM detects the presence of the CTP mode in the absorption spectrum, it fails to capture the dependence of this mode on the detailed features of the cavity, see Fig 5.4. The reason being that, the CTP mode involves the polarization of the whole connected dimer, and appears as a consequence of the tunneling current established across the gap. It appears then clear that while approaching the clusters the atomic-scale structure might be particularly important for the tunnelling current to happen.

Further proves of the relation between the CTP mode and the current flowing through the whole dimer are given and amply explained in Section 5.2 where we explicitly relate the electron current with the CTP mode dispersion for clusters that are left free to rearrange their atoms during the approaching and retracting process.

5.2 Metal-Nanocontacts Structure Evolution

Another key aspect to understand the behavior of particles brought in close proximity is given by the possibility of atoms inside the particles and in particular in the plasmonic cavity to rearrange. Depending on the plasticity of the material considered the relaxed structures can vary dramatically from the ideal ones. When two metallic surfaces are approached and put into contact, the formation of small metal necks or nanojunctions connecting them is a very likely process[229] that has been theoretically predicted[229,230] and experimentally observed.[229,231–233] This work comes as a natural continuation of the study described in section 5.1 where frozen clusters are considered. Here, we perform a deeper exploration on how the optical response of plasmonic cavities simultaneously correlates with their structural properties and transport properties,[3] going beyond a macroscopic description[234] and looking at the atomic-scale regime where the effects of quantum transport at the interface must be taken into account.[235–237] Small metal neck formation and nanojunction structures are at the root of friction phenomena in metal surfaces[238] and give rise to quantized transport following discontinuous changes in the contact cross-section.[229,239–241] Here, we will show that these rearrangements at the atomic scale also have noticeable influence on the optical properties of the nanostructures.

In this study we correlate migration or repositioning of atoms in a metal neck, variation in conductance and change in the optical response. An observation of discontinuous changes in the plasmonic response of the system accompanying each plastic deformation event indeed confirms such correlation. This connection between quantized transport and the evolution of the plasmonic response has also been pointed out in a recent report[242] that considers the optical response of a small Na_{261} nanorod as it is stretched. In order to address the complex correlation of electronics and optics in subnanometric junctions where

the majority of the atoms in the system are allowed to adapt to the geometrical boundary conditions, we performed atomistic quantum mechanical calculations of the electronic structure, the optical response, and the structural evolution of a plasmonic cavity. The plasmonic cavity in our simulations is formed by two large sodium clusters, containing 380 atoms each of them, in close proximity. While Na is not the most relevant material from a technological points of view, we think that the properties observed here can be extrapolated, with care, to other metallic systems. The use of sodium allows performing larger calculations, in terms of the number of atoms, as compared to other more technologically relevant materials like, for example, gold. This increases the relevance of our results, since the number of atoms involved in the structural reorganizations of the neck is indeed a small percentage of those contained in the system.

Our approach consists in tracing the energetics, the geometry and the optical response of the two metallic clusters which gradually get closer while allowing atoms to rearrange. Eventually, the two particles are retracted until complete separation. For each approaching and retracting step the geometry is optimized. Structural relaxations, using forces obtained from DFT SIESTA calculations, are performed.

5.2.1 System Configuration and Computational Details

Fig. 5.6 shows the single cluster optimized structure. The cluster contains 380 Sodium atoms with a lateral dimension of $\sim$24 Å. The structural relaxation is performed first for an isolated cluster. After the clusters were brought together and each cluster was allowed to relax in response to the presence of its neighbor. Most distant atoms in the cluster dimer were kept at fixed positions to simulate attachment to a bulky substrate All the structural relaxations were performed using standard DFT as implemented in the SIESTA code.[6,7] The starting icosahedral geometry has been obtained, as in the case described in section 5.1, from a configuration optimized with empirical potential[224] and available at the Cambridge Cluster Database (CCD).[225] However, in this case the Perdew-Burke-Erzenhof density functional (GGA-PBE) was used.[243] We also used norm-conserving pseudopotentials[244] to effectively describe the core electrons and to perform the geometry relaxation calculations for the single-cluster structure as well as for all the other configurations including the two-clusters-system evolution. We used the DZP basis set of numerical atomic orbitals generated using an energy shift of 100 meV. The fineness of the real-space grid used to compute the Hartree and exchange-correlation contributions to the energy and Hamiltonian corresponds to a plane-wave cut-off of 130 Ry. Structural relaxations were stopped when forces acting on all atoms were smaller than 0.02 eV/Å.
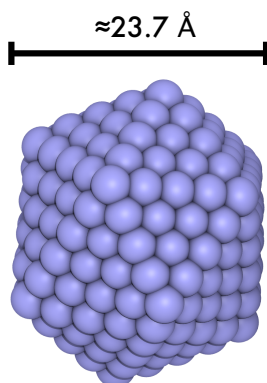
Figure 5.6: Optimized geometry of the icosahedral Na_{380} cluster.

LDA vs GGA Relaxed Structure

The LDA-CA and the GGA-PBE DFT functionals can provide quite different results in terms of equilibrium geometry of the dimer. However, for the single-cluster case the relaxed structure obtained using GGA-PBE is very similar to the one calculated with the LDA-CA potential and it is characterized by the presence of planar facets, sharp edges and single-atom vertices.
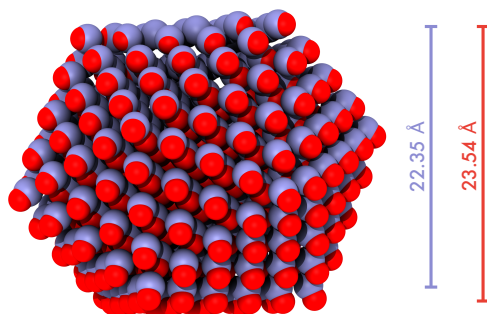
Figure 5.7: The single-cluster relaxed structure is shown. Purple atoms refer to the geometry optimized using LDA-CA functional. Red atoms correspond to the geometry optimized using GGA-PBE functional. The top facets of the two structure are aligned.

In Fig. 5.7 we compare the resulting structures obtained for the single Na_{380} cluster using the above mentioned functionals. The structure obtained with the GGA-PBE (red atoms) functional shows a slightly lower density than the one calculated with LDA-CA (purple atoms) functional. The higher sodium density found with GGA translates in a smaller interlayer distance, about 10%. This 10% corresponds to an average elongation per bond of $\sim$0.17 Å. The difference is due to the well-known underestimation of the Na

lattice parameter by LDA.[226] The overall linear dimension of the cluster is 22.35 Å for LDA and 23.54 Å for GGA, see Fig. 5.7. The difference in cluster size affects obviously the optical frequencies of the plasmonic modes for the single cluster and for the two-cluster system. In Section 5.1 and following the LDA functional was consistently used in the DFT and TDDFT calculations. The underestimation of the volume with LDA gives rise to a large redshift on the resonance energies, nevertheless, the spectrum features are preserved. Thus, for the study presented in section 5.1 the use of the LDA functional in SIESTA does not change the overall conclusions. The real need for the use of a more sophisticated functional lies in the necessity of having reliable geometries at a DFT level once the two cluster interact strongly. This greater importance of the functional choice in the DFT calculations (versus the choice of functional for TDDFT kernel) is also verified in our study of the silver clusters.[20]

Once the single cluster optimized geometry is found, the two clusters are placed in a mirror-like geometry 16 Å apart and we decrease the distance between them in small steps of 0.2 Å, as shown in Fig. 5.8 panel a), and, eventually the two clusters are again moved apart, Fig. 5.8 panel b). We monitor the interparticle distance using the Nominal Gap Size (NGS), defined as the distance between the two cluster inner facets if the system would remain unrelaxed. Thus, a nominal size gap of zero value would correspond to the superposition of the atoms forming the two opposing facets in the absence of relaxation. The distance between the outer facets of the two clusters is chosen as calculational parameter. The atoms belonging to the outer facets, Fig. 5.9(a), are not allowed to move during the relaxation steps allowing us to define unambiguously the displacement applied to the system, and in turn the nominal gap size (NGS), Fig. 5.9(b).

Deformation steps of 0.2 Å during the approach/retraction events were chosen as a compromise between computational convenience and a sufficiently small deformation in each step, so that we always keep the system reasonably close to a local minimum configuration. Importantly, this deformation is distributed uniformly along the whole structure, translating into a rather small (<0.5%) modification of the bond lengths. The system is then allowed to relax so that the excess of energy created by the deformation can be dissipated and the system evolves into the closest local energy minimum. This procedure is similar to that followed in other ab initio DFT studies of the formation and evolution of metal junctions and nanocontacts[245, 246] and mimics a situation in which the system is slowly deformed at low temperature. The heat transport away from the (nanosized) contact region is supposed to be sufficiently efficient to keep the cavity cold in spite of the work being done in the system. This is a reasonable assumption for instance in STM cavities at cryogenic temperatures.
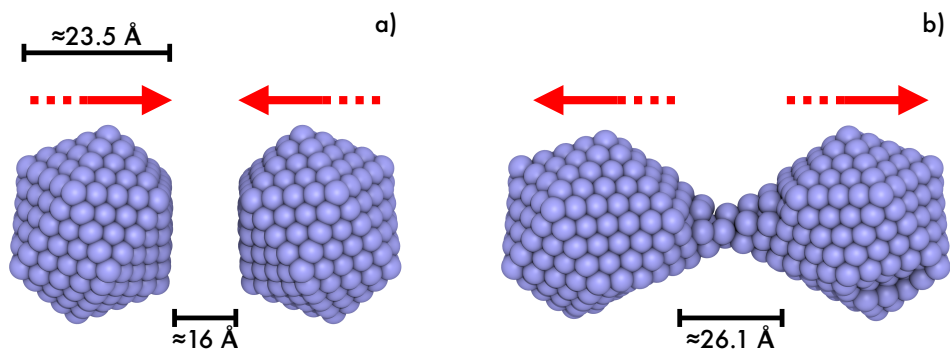
Figure 5.8: Example of two configurations, while approaching and retracting the two clusters. The distance at the bottom indicates the value of the nominal gap size.

(a)   (b)
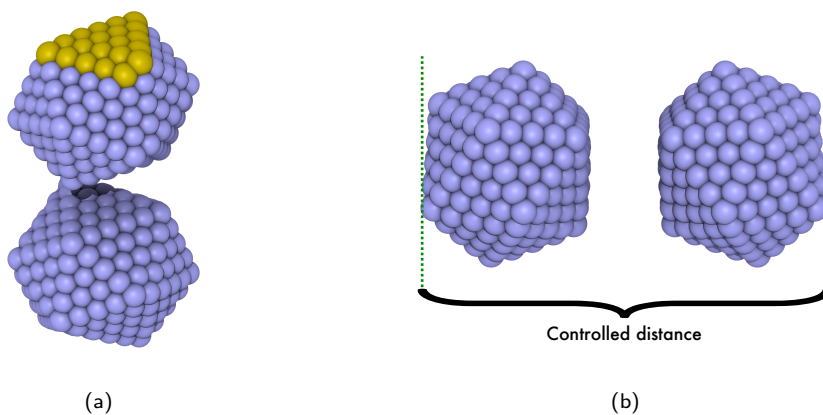
Figure 5.9: In panel (a) we show the atoms in the outer facets of both clusters (the atoms in the facet of the upper cluster have been highlighted in yellow) that are kept fixed during the relaxation process. In panel (b) the external facet distance used to determine the Nominal Gap Size (NGS) is used.

Before computing the polarizability, for each relaxed structure, a DFT ground-state calculation has to be performed employing the LDA functional – in order to ensure consistency with the following TDDFT-ALDA calculation. ALDA has proven to provide accurate results for the optical properties of sodium clusters.[247–252] Fig. 5.10 the steps followed in this work is summarized.
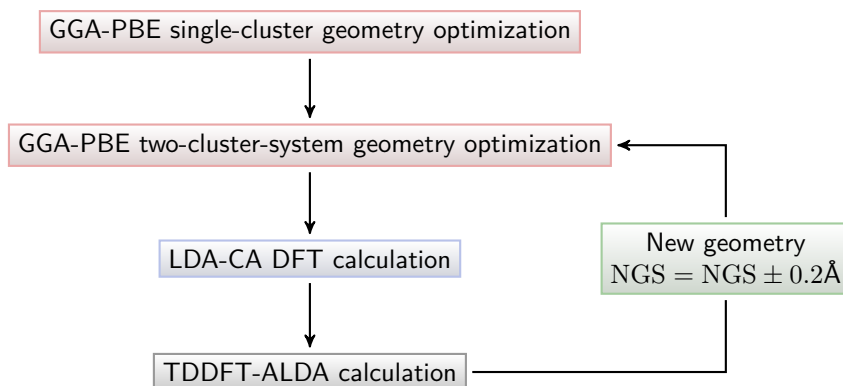
Figure 5.10: Calculation process. NGS = Nominal Gap Size.

5.2.2 TOTAL ENERGY: JUMP-TO-CONTACT INSTABILITY AND JUNCTION CREATION

DFT relaxation calculations provide us with the relaxed geometry and the system total energy. System total energy results are shown in Fig. 5.11, together with some of the most emblematic system configurations. Red data in Fig. 5.11 describe the evolution of the total energy of the system as we approach the two clusters. The initial intercluster distance of 16 Å is large enough to avoid direct interaction between the nanoparticles. The cavity between the clusters is initially symmetric with the two clusters opposing planar facets. When we start approaching the clusters, the total energy remains essentially constant until a NGS of 7.5 Å. From this separation the total energy starts to slowly decrease until a NGS of 6.3 Å. The next step in the approaching process is characterized by a big drop in energy due to the so-called jump-to-contact. The two clusters are now in contact nullifying practically the actual interparticle gap that drops down to about 3.2 Å and remain fairly constant closing to 3.0 Å as the two clusters get closer together. The abrupt reduction of the energy at the jump-to-contact point is mostly due to the reduction of the surface energy of both clusters (two facets disappear). However, this happens at the expense of a large elastic deformation of the clusters. By further approaching the two clusters, we reduce the elastic deformation of the system, and correspondingly, the total energy decreases. Eventually the system suffers some reorganizations which are also reflected (although they are somewhat less obvious than the jump-to-contact). For example, the stacking of the atomic layers at the interface, initially imposed by the mirror symmetry of our starting geometry, gets optimized as we push the two clusters together. Later, the particles start to deform to try to reduce further their surface area by increasing the contact cross-section. Although the jump-to-contact effect is a quite general behavior which is routinely taken into account in the interpretation of data from scanning probe microscopies, the details of the jump-to-contact process strongly depend on the size and shape of the facets and the effective elastic constants of the systems being brought into contact. This can be seen in Fig. 5.12 which compare the total energy for the face-to-face with the tip-to-tip case. In the tip-to-tip case, we do not observe any jump-to-contact instability. This is due to the small surfaces associated with the tip apex. Bringing the two tips together causes a very

small reduction on the surface of the system, and, thus, it does not compensate for a large elastic deformation. The tip-to-tip configuration in shown in the inset in Fig. 5.12.

Once the two clusters are clumped together at a nominal size gap of ~3.5 Å, comparable to the interlayer distance in bulk sodium, we start pulling them apart (blue circles in Fig. 5.11). During the retraction process the whole structure evolves creating and thinning a neck that connects the two clusters until a monatomic chain is formed and, eventually, until a complete separation of the clusters is achieved (point m in Fig. 5.11). In agreement with previous studies, the evolution of the contact structure takes place via an alternation of elastic and plastic deformation events.[229, 233, 241, 245, 246, 253] The contact is elongated until the accumulated elastic energy is sufficient to produce atomic rearrangements, mainly driven by the atoms in the neck area. During these plastic events the energy of the system decreases abruptly. Thus, there is a one-to-one correspondence between the discontinuities of total energy in Fig. 5.11 and the changes in the configuration of the metal neck. It is striking to note the dramatic contrast between the distance at which the jump-to-contact takes place and the clusters "touch" for the first time during the approaching process (close to point a in Fig. 5.11) and the distance at which they finally detach (indicated by a vertical green dashed line). A nominal gap distance of 32.3 Å is needed to separate completely the clusters. The results shown in Fig. 5.11 underline that the geometry of the system strongly departs from the idealized situation in which two clusters simply change their relative position. It is interesting to note that the final geometry of the two clusters once they separate is very different from the initial one. The symmetric face-to-face configuration (panel a in Fig. 5.11) is substituted by an asymmetric tip-to-tip like configuration (panel m in Fig. 5.11). The system total energy after the clusters detached is considerably higher than the initial one. Moreover, once the monoatomic neck is formed at 29.3 Å by increasing the NGS the monoatomic neck gets stretched and breaks only at 32.3 Å. This elongation of 2.8 Å is distributed among the few atoms in the monoatomic neck.

In summary, the total energy results show how strong is the atomic reorganization while approaching and retracting. In particular, while approaching, the two clusters jump to contact leading the two inner faces of the clusters to clump together. The retracting event is characterized by many small discontinuities in the total energy due to atomic reorganization affecting mainly the neck region.

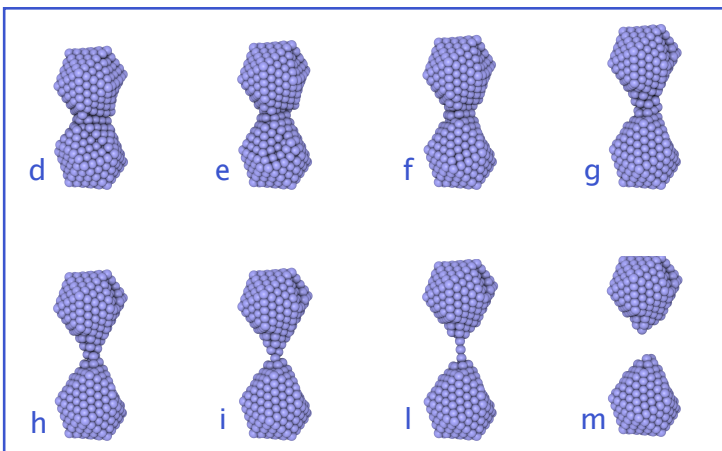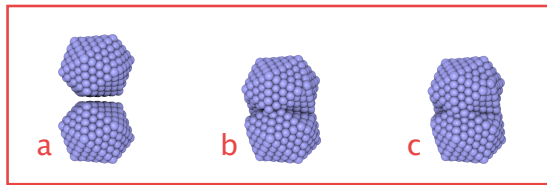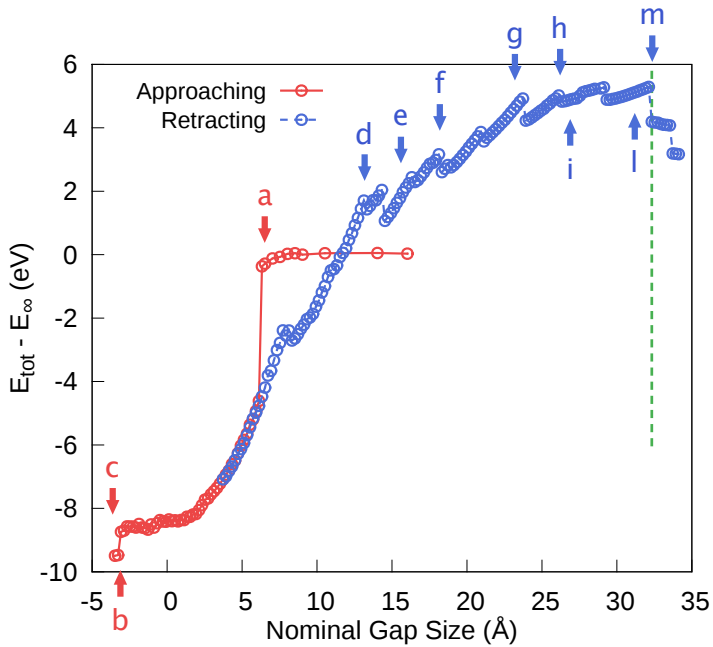Figure 5.11: Total energy of a plasmonic cavity formed by two Na$_{380}$ clusters as a function of the NGS between them during approaching and retracting. Red circles represent the approaching process, while blue circles indicate the retracting process. Latin letters indicate the correspondence between some of the total energy points in the graph and the dimer configurations shown in the panels below.
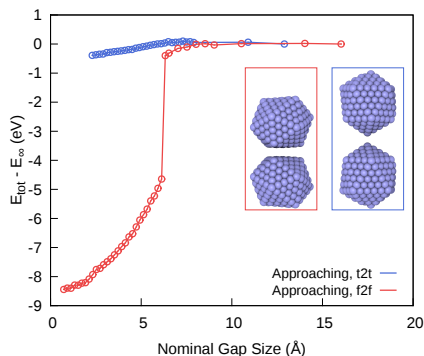
Figure 5.12: Comparison total energy versus distance for the tip-to-tip (t2t) and facet-to-facet (f2f) configurations. The t2t curve does not show any jump-to-contact as the two clusters are approached. In the insets the f2f and t2t geometries are shown.

5.2.3 Analysis of Forces and Stresses

In our calculations, during approaching and retracting, the atoms on the external facets are not allowed to relax, thus, the forces acting in these atoms will be different from zero in general. The sum of the forces, along the axis direction, acting on the atoms belonging to the external facets while the two clusters are approaching are shown in Fig. 5.13. The data in blue represent the total force acting on one of the facet, as shown in inset panel of Fig. 5.13.
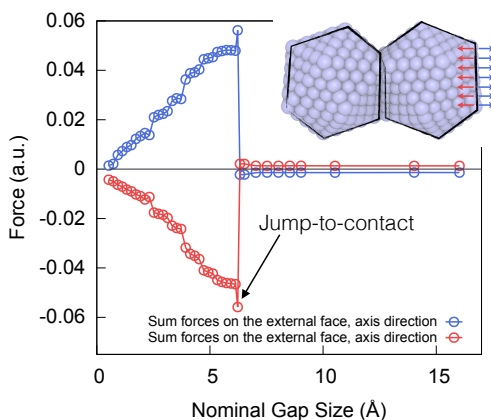
Figure 5.13: The forces analysis acting on one of the external facet is shown. The atoms belonging to the facet are not allowed to relax. After the jump-to-contact instability the force acting on the facet increasing considerably and pushes the external facets of the two clusters inwards. In the inset the colored arrows indicate the direction of the force acting on the facet.

Before the jump-to-contact, the forces on the two external faces are small. After the jump-to-contact the forces acting on the fixed atoms increase suddenly changing sign. The origin of the change of sign is not clear from our analysis. The evolution total energy in Fig. 5.11 does not show any energy barrier that could explain the change in sign. Before the jump-to-contact instability the total force points outwards pushing the two clusters apart from each other however, the intensity of this force is really small and within the chosen threshold value used for the SIESTA geometry optimization calculations. After the jump-to-contact the force is pushing inward the external facets. The two clusters elongate resulting in an important force acting on the clusters. The increases of the forces on the external faces of the two clusters after the jump-to-contact indicates a large stretching. The increase in the total energy of the system due to this stretching is compensated by the decrease in energy due the decrease of the total surface of the dimer once the two inner facets of the clusters come into contact. This is also the reason why no jump-to-contact can be observed when the tip-to-tip configuration is considered. The sharpness of the tips does not allow a favorable configuration as in the case of the facet-to-facet dimer configuration.

5.2.4 Optical Properties of a Forming Plasmonic Cavity

The optical absorption of the forming plasmonic cavity has been calculated while the clusters where approaching. To explore the role of atomic relaxation while creating the plasmonic cavity we compare the optical spectrum with the case of unrelaxed clusters. In Fig. 5.14 panel a, the polarizability for the unrelaxed case is shown, no relaxation of the clusters is allowed and only the distance between the clusters is modified. In Fig. 5.14 panel b the reported optical absorption takes into account the relaxation of the atoms following the atomic-scale restructuring shown in Fig. 5.11 (red dots). The resonant plasmonic modes of the forming cavity, as obtained from the calculated polarizability of the system, are displayed as a function of the NGS in both situations. For the unrelaxed case the NGS correspond to the actual distance between the clusters' inner facets. The component of the polarizability parallel to the dimer axis in response to a field in the same direction is considered here, that we take hereafter as z. In both cases, and depending on the separation, we can identify three distinct resonances[170, 212–214, 219, 220, 234] as introduced previously in section 5.1. A single intense so-called BDP resonance around 3 eV dominates the response at large intercluster distances when the two clusters interact weakly. At distances above ~15 Å the energy of the resonant mode converge to that of the single cluster BDP mode, with the two clusters behaving basically as isolated entities. The BDP shows an induced charge distribution characterized by a capacitive coupling of charges of opposite sign at both sides of the cavity, as schematically depicted in the right drawing of the top panel in Fig. 5.14. In this regime two dipoles appear in the clusters and interact with each other. When both clusters are in contact, so that free charges can efficiently move across the junction, we enter a conductive coupling regime characterized by the so-called Charge Transfer Plasmon (CTP)[234] and the associated high-energy Charge Transfer Plasmon (CTP') modes. The conducting link of the CTP through the junction of the clusters produces a screening of the charges in the cavity and thus, redistributes the induced charge density to produce a net dipole that extends to the whole dimer structure, as depicted in the top-left scheme in Fig.

5.14 (see also Fig. 5.18). As the distance between the clusters decreases the BDP mode slightly disperses towards lower frequency. The BDP resonance red-shifts and the Coulomb interactions among the clusters increase. This shift is due to the strong interaction of the parallel induced dipoles along the dimer axis, which hybridize[254] lowering the energy of the resulting optically active mode. In this capacitive (weak interaction) regime both unrelaxed and relaxed cases show the same dependence on the interparticle distance. The BDP mode is present until the clusters are brought to a distance of about 6.1 Å. At this point, for the unrelaxed dimer (see Fig. 5.14a), the BDP mode is quenched and higher energy modes start gaining intensity. If the clusters are approached further we observe a smooth transition from the capacitive to the conductive coupling regime. For separation distances right below 6 Å the electron tunnelling current at relevant frequencies gradually starts flowing, giving rise to the progressive emergence of the CTP resonance.[170, 210, 213, 220] This transition region is frequently referred to as the quantum tunnelling regime of plasmonic cavities.[214] At a distance comparable to the sodium interlayer distance, $\sim$3.0 Å, the clusters become chemically bonded and a clear contact is established. Under those conditions, a substantial current can be established and the CTP appears fully developed. The situation shown in Fig. 5.14b for the relaxed dimer is strikingly different. The relaxed dimer undergoes a jump-to-contact instability (see red dots in Fig. 5.11) that dramatically modifies the evolution of the optical spectrum. The transition regime, found between 6 and 3 Å for the unrelaxed dimer, has almost completely disappeared in the relaxed case. There are no stable geometries for those intermediate gap sizes, and thus, the resistive tunnelling (transition) regime cannot be clearly identified in the optical response in this case.
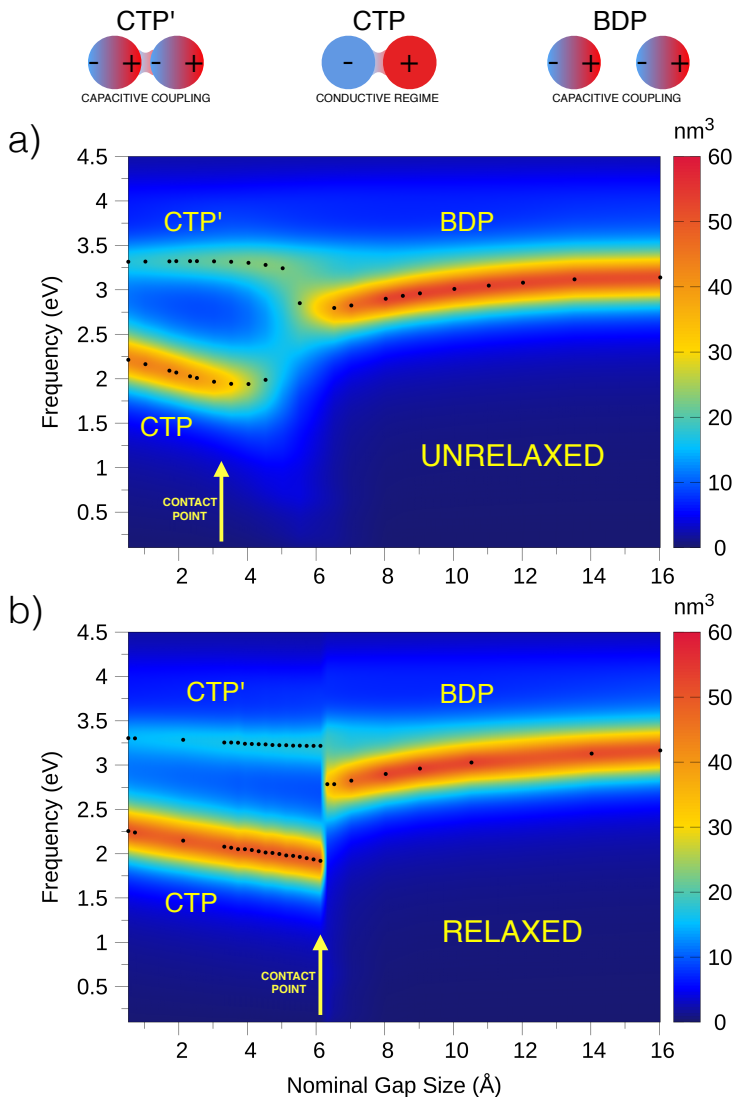
Figure 5.14: Evolution of the imaginary part of the polarizability of a Na_{380} dimer (external field applied along the dimer axis) as the clusters approach, plotted as a function of the NGS and photon energy. Both unrelaxed (a) and relaxed (b) geometries of the cluster dimer are considered. The dark dots indicate the position of the maximum of the peak in the polarizability for those distances for which the optical response has been computed. The arrow lines indicate the contact point for the two cases, that is, the distance at which the clusters merge into one single larger object. In the top panel the schematic representation of the induced charge of the modes that dominate the optical response before contact (bonding dipolar plasmon mode, BDP) and after contact (charge transfer plasmon mode, CTP) is shown.

Our results indicate that the effect of the jump-to-contact must be considered when exploring and interpreting the optical response of metallic particles in close proximity, particularly when large atomic-scale reconfigurations can be expected. Importantly, this phenomenon can hinder the appearance of a smooth transition between the capacitive and charge-transfer regimes in the optical response of plasmonic cavities. Finally, below 2 Å of nominal gap size the conductive coupling regime of the junction is fully developed in both the unrelaxed and relaxed cases, with the CTP and the CTP' resonances converging to similar values of energy, around 2.25 and 3.3 eV, respectively. This underlines the fact that the details of atom rearrangements at the cluster interface might not be so important in the determination of the optical response once the two clusters are fully chemically bonded.

5.2.5 Nanocontact Formation: Optics Driven by Individual Atoms

Fig. 5.15 shows the optical polarizability of the junction during the retraction process. Surprisingly, as the two clusters retract the CTP and CTP' modes dominate the spectrum for most separation distances, all the way to nominal interparticle distances of several tens of Angstroms. This is in clear contrast with the results obtained in the previous section (approaching situation), and it is a result of the structural evolution of the junction, characterized by the formation of a thin conducting neck among the clusters [as shown in the panels (d)–(l) of Fig. 5.11]. As the clusters get separated, the neck gets longer and thinner. As a consequence, the charge transfer modes disperse towards lower energies (due to the overall elongation of the system). Moreover, as the neck's cross-section is reduced, the intensity of the CTP' mode increases at the expense of the lower-energy CTP resonance, consistent with calculations of stretched clusters.[242] As the current flowing across the neck diminishes, the CTP' mode converges toward the BDP mode while the CTP mode tends to disappear.

While the polarizability of the approaching situation in Fig. 5.14 only shows a clear discontinuity associated with the jump-to-contact instability of the cavity, the retracting situation shows a completely different behavior as a function of the separation distance. During retraction the optical spectrum is characterized by the appearance of many discontinuities both in the spectral position and in the intensity of the resonances.

A careful inspection of Fig. 5.11 reveals that these discontinuities happen at exactly the same nominal distances where jumps in the total energy are detected. Some of the most visible jumps are highlighted with arrows of different colors and marked with Greek letters in Fig. 5.15a, and the corresponding polarizability is plotted in detail in Fig. 5.15b, which extract the spectral lines from the contour plot in Fig. 5.11. Each panel shows spectra corresponding to distances before and after one of the jumps, identified in the contour plot of Fig. 5.15a with the corresponding colored dots and arrows. Consecutive curves correspond to configurations in which the interparticle distance is changed by 0.2 Å. In each panel there are several, almost indistinguishable, spectra of the same color. This highlights that noticeable changes in the spectrum are indeed linked to the plastic deformation events in the neck, and not to the small rearrangements during elastic deformation. At each jump we observe clear changes in the intensities, widths, and positions of the resonance peaks. The jumps affect primarily the low energy resonance, CTP, although they are also visible in the CTP' mode. They are owing to the atomic reorganization in the neck region and they

are specially visible for distances above $\sim$20 Å due to the small cross-section of the neck. Remarkably, for such thin necks, even single atom movements produce visible changes in the optical response of the system, clearly associated with the quantized nature of the conductance through the junction neck – paragraph 5.21. The jump at 29.3 Å indicates the formation of a well-ordered monatomic neck, that is, the clusters are connected by a single row of atoms. The formation of such structures has been observed for many metals, for example, in the case of Au, for which these monatomic wires have even been visualized by electron microscopy.[229, 231–233, 255, 256]
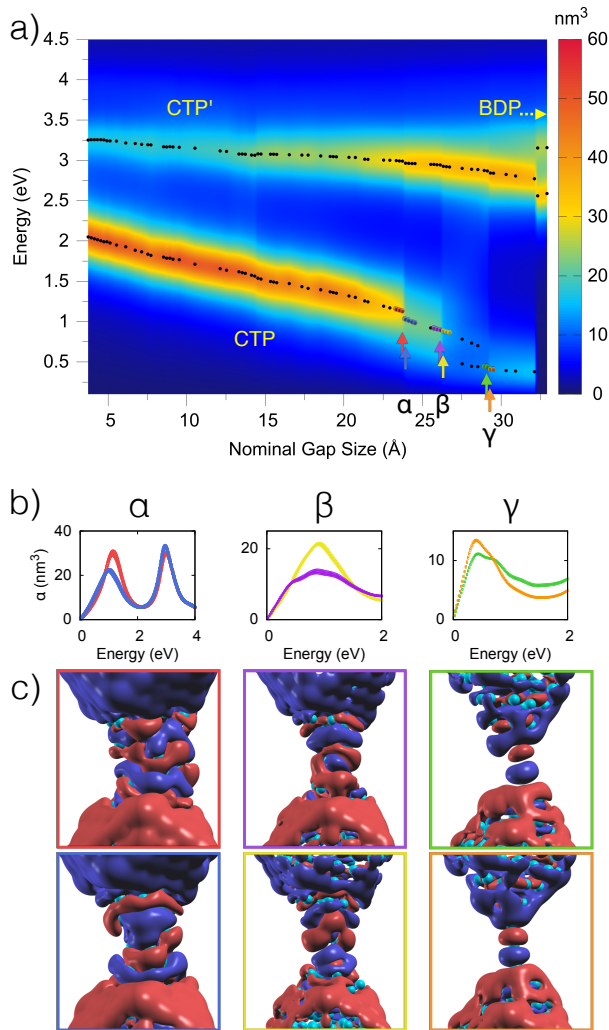
Figure 5.15: (a) Evolution of the resonances in the polarizability of a plasmonic junction as a function of the NGS and energy, as the clusters forming the junction move apart (i.e., move toward larger NGS). The dots indicate the positions of the peak maxima in the polarizability for the considered configurations. Panels in (b) show the spectral lines of the polarizability at distances before and after each of the jumps highlighted in panel (a) by means of Greek letters and colored arrows and dots. The colors of the lines of the spectra correspond to the colors of those arrows and dots, thus, indicating whether a given spectrum corresponds to a configuration before or after the jump. (c) Imaginary part of the induced charge density distribution around the junction for the three selected distances in (a) and (b), before (top) and after (bottom) the spectral jumps.

5.2.6 MODES SPLITTING AFTER CLUSTER SEPARATION

Once the two clusters totally separate, breaking the neck, the final system structure differ considerably from the initial one. The initial face-to-face mirror symmetric configuration is replaced by an asymmetric tip-to-tip configuration (see panel m in Fig. 5.11). With the rupture of the connecting neck, the CTP and CTP' modes that dominated the optical response of the system during the whole retraction process disappear as no charge transfer can exist between the two clusters. Two new modes appear in the spectrum. The lower energy resonance found at ∼2.6 eV has a density change pattern that recalls the BDP mode with the largest charge accumulations around the central gap as shown in Fig. 5.16 panel (a). However, the resonance appears red-shifted compared to the BDP mode which is found at ∼3.1 eV, see Fig. 5.14. The higher energy resonance arising at ∼3.2 eV has a more complex charge distribution, corresponding to a higher order mode showing charge accumulations both in the tips inside the cavity and in the facets of the clusters, see Fig. 5.16 pane; (b).
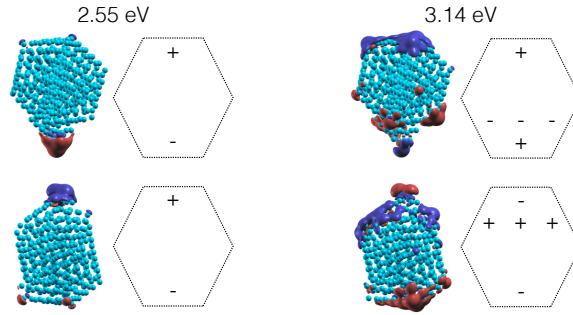
Figure 5.16: Imaginary part of the induced charge density distribution for the frequencies of the two plasmon resonances found after breaking the connecting neck and final separation of the clusters.

5.2.7 ELECTRONIC CURRENT

In Chapter 1 in the paragraph 1.3.10 we described how the electronic current in a finite object can be calculated starting from the density change. Since we are dealing with a finite object we can use the continuity equation and an integration region like the one shown in Fig. 5.17 to define the current that flows across a chosen plane. In particular, starting from the density change, the maximum current flowing through the gap can be computed from equation E.11, here repeated,

$$|I_{max}(\omega_0)| = \omega_0 \sqrt{\delta Q'(\omega_0)^2 + \delta Q''(\omega_0)^2}. \tag{5.8}$$

Where $\delta Q'$ and $\delta Q''$ are, respectively, the real and imaginary part of the total charge calculated inside the volume defined in Fig. 5.17. $\delta Q(\omega)$ is calculated by integrating the

density change $\delta n(\mathbf{r}, \omega)$ over this real space volume.

By changing the integration volume we can obtain a map of the maximum current passing through the different planes dividing the dimer system. Such results are shown in Fig. 5.18 where we explore the real space distribution of the induced charge together with the correspondent current for the CTP and CTP' modes for a nominal gap size of 6.1 Å, right after the jump-to-contact instability. The isosurfaces in the density change plots correspond to $\sim 10\%$ of the maximum value of the induced density. The corresponding electron current plots (graph to the right of each charge density plot) show the modulus of the current flowing through (x,y) planes (i.e., perpendicular to the dimer axis) as a function of z, the coordinate along the dimer axis. It is important to stress that such current maps do not refer to a given instant of time as we work in frequency domain. The density charge associated with the CTP forms a dipolar pattern over the whole system having a single node placed at the center of the system, as shown in Fig. 5.18. Thus, the charge accumulation does not take place in the cavity interfaces but, rather, extends to the whole system. Correspondingly, the current associated with the CTP resonance has its maximum at the gap center. On the other hand, the CTP' mode presents two dipolar patterns on each cluster with nodes of the induced charge density in the center of the system as well as in the middle of each cluster. The charge distribution in this case is somewhat similar to what one can expect for the BDP mode. However, the current reveals a key piece of information to rule out this interpretation. In the case of the CTP' resonance the maxima of the current are found both in the center of the system as well as within each cluster. This is indeed confirming that there is charge transfer among both clusters also in this high energy mode. Thus, the observed induced density pattern is better interpreted as the second optically active mode of a metal rod.

Moreover, during retraction it becomes relevant to follow the current flowing through the forming neck connecting the two clusters – paragraph 5.2.9. Due to the neck size, small atomic movement in the neck section can give rise to considerable variations in the current and eventually to changes in the polarizability.
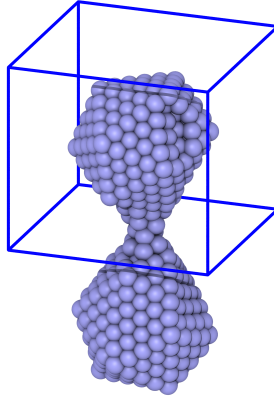
Figure 5.17: Chosen volume to calculate the current passing through the neck.
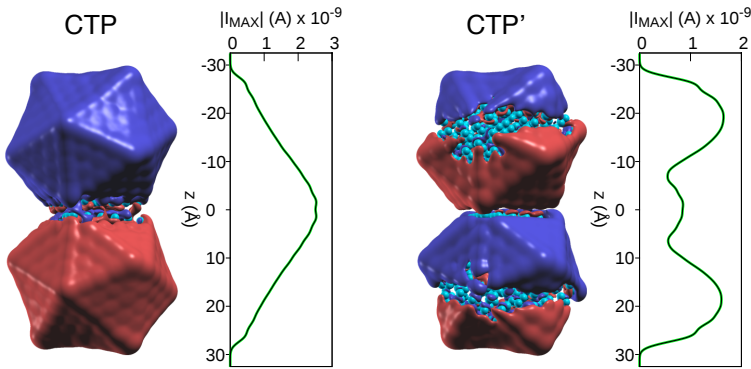
Figure 5.18: The imaginary part of the induced density and the corresponding modulus of the electron current are shown. The modulus of maximum of the current, $|I_{max}|$, represents the current flowing through each cross sectional [i.e., (x,y)] plane along the dimer axis. An external electric field of magnitude of 1×10^{-9} atomic units is assumed here with a polarization parallel to the junction main axis. The nominal gap size is 6.1 Å, corresponding to the jump-to-contact configuration in the relaxed case.

5.2.8 NECK CROSS-SECTION

Before analysing the current flowing through the neck is important to define a way to effectively measure the neck cross-section. In order to do so we decided to use the distribution of the ground-state electron density $\rho(\mathbf{r})$. The density is computed in an (x,y) plane passing through the middle of the junction and the neck cross-section A_{cs} is obtained as the area in which the electron density is larger than a given threshold value ρ_{th} (see Fig. 5.19). In

other words, we use the integral,

$$A_{cs} = \int \int f(\mathbf{r}) \mathrm{d}x \mathrm{d}y$$

$$\text{where} \ \ f(\mathbf{r}) = 1 \quad \text{if} \ \ |\rho(\mathbf{r})| > \rho_{th}$$

$$\text{where} \ \ f(\mathbf{r}) = 0 \quad \text{if} \ \ |\rho(\mathbf{r})| < \rho_{th}.$$

In practice, in our discretized 2D plane the points for which $|\rho(\mathbf{r})| > \rho_{th}$ are counted and the number is compared to the total number of points in the surface. The value of ρ_{th} is arbitrary and was chosen here so that the radius of an isolated Na atom is 2.88 Å, a reasonable value if compared to the Na bulk density (characterized by a Wigner-Seitz radius $r_s \sim 2.12\text{Å}$) and we take into account the spillage of charge towards vacuum in a finite object. In any case, the specific value of the cross-section assigned to a particular neck structure is irrelevant (as far as reasonable), the importance of this method is the ability to continuously monitor the cross-section change as the structure evolves, see Fig. 5.20 in section 5.2.9. In Fig. 5.19 we can clearly see the three atoms forming the neck. The cross-section tool is particularly useful when the neck is composed of many atoms arranged in a complex manner.
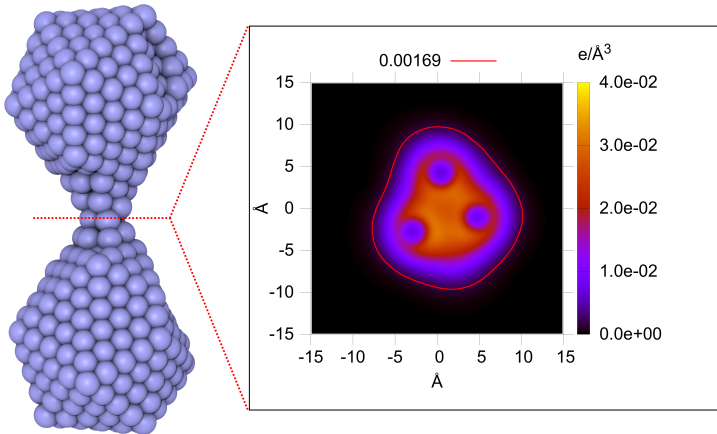
Figure 5.19: The neck section is calculated by analyzing the electron density in a (x, y) plane cutting the center of the neck. The right panel shows the 2D electron density distribution in that plane (red dashed line). The red solid curve represents the isocontour corresponding to a 0.00169 $e/\text{Å}^3$ threshold density. The cross-section is defined as the area of the region limited by such isocontour. We can clearly see that the neck cross-section is formed in this case by three Na atoms.

5.2.9 CURRENT QUANTIZATION

During the retraction process when the nominal gap size is around 23 Å the intensity of the CTP resonance suffers an abrupt decrease, becoming broader between 27 and 29.3 Å, see

Fig. 5.15. Afterward, simultaneously to the monatomic neck formation, the CTP resonance gets sharper with a consequent regain in intensity. This evolution is due to a combination of several effects, the most important being the quantization of electron transport in the metal neck. Such quantization is a well-known effect due to the small cross-section of the contact, comparable to the electron wavelength.[257] As a result of the lateral confinement, the electronic energy levels in a thin metal nanowire or neck get quantized and, at a given energy, only a discrete number of bands (or "channels" using the standard terminology in quantum transport) can contribute to the electron transport. Thus, under a small, static bias, if the electron injection from the electrodes (in our case the clusters) is efficient and the neck structure is sufficiently long and ordered, we can expect each channel at the Fermi level to contribute to the transport with a quantum of conductance $G_0 = 2e^2/h$,[257] with h the Planck's constant and e the electron charge. In the presence of defects or strong scattering in the connections to the electrodes, the transmission probability of the channels gets reduced.[257]

To establish a more direct connection between the computed current as a function of the gap separation within the junction and the well-known quantization of transport in metal nanocontacts, in Fig. 5.20 we show the current flowing through the neck for the CTP while retracting (left axis of the graph) plotted in relationship with the neck cross-section (right axis of the graph). As can be seen, there is an almost perfect correlation between the changes in the current and the evolution of the neck cross-section. Such correlation has been already well established in the case of low-frequency driving-fields being applied to the necks. It has been observed in the formation of metal nanocontacts in Scanning Tunnelling Microscopy (STM) and break-junctions experiments and corroborated by many calculations.[229] Here we show this correlation at the optical frequencies.

With these ideas at hand, we can easily explain the observed behaviors. The abrupt jump in the intensity of the CTP peak around 23 Å (α jump) is caused by the sudden reduction of the neck's cross-section, as can be clearly seen in Fig. 5.15c and in Fig. 5.20. As expected, the reduction of the cross-section reduces the number of conduction channels and, therefore, the electric current flowing through the junction (this is confirmed in Fig. 5.21, discussed later in detail). The resonance peak also shifts to slightly lower energies. The origin of the intensity jump at $\sim$27 Å (β jump) is also similar: a cross-section reduction that translates onto a sudden decrease of the current as can be seen in Fig. 5.15c and Fig. 5.21. After this jump at 27 Å, the neck develops into a less ordered structure, creating a region of high scattering that hampers the electron transport between the clusters. As a consequence the CTP resonance broadens. Finally, once the relatively defect-free monatomic wire is formed, the transport through the neck becomes completely ballistic, i.e. all the electrons that are injected to the monatomic wire get across the junction, and the peak in the polarizability becomes more defined again.

These quantization effects can also be observed in the shape of the distributions of induced charge density as the neck evolves during retraction. In panel (c) of Fig. 5.15 the imaginary part of the induced density associated with the CTP mode is plotted for those configurations immediately before and after the α, β, and γ jumps (indicated by the colored arrows in the polarizability plot). Although the density change has a quite complex distribution, it is possible to follow the evolution of the patterns toward simpler schemes of charge oscillation after each jump. The induced density presents a complex distribution and nodal structure, with a decreasing number of nodes as the cross-section of the neck

gets thinner, a fact that reflects the larger number of open conduction channels for the wider structures. Subtle changes in the structure that have a direct translation in the optical response can also be observed in these density plots. For example, in the case of the γ jump, Fig. 5.15, the three-atoms-long monatomic wire becomes more straight and the connections to the cluster more symmetric. This slightly increases the current flowing through the structure and produces the aforementioned changes in the plasmonic response.

To fully account for the connection between high-frequency electron transport and optical response of the plasmonic junction, we have calculated the current through the junction as a function of the nominal gap size. In Fig. 5.21 the results for the modulus of the current passing through a plane cutting the center of the junction are shown – calculated as described in section 5.2.7 and in appendix E. Here we present the current computed at the frequencies of the main resonances of the polarizability: BDP, CTP and CTP'.

The current during the approach process is shown by red solid circles, corresponding first to the BDP mode and, later, to the CTP mode once the clusters are in contact. The current for the BDP mode is negligible until the jump-to-contact event takes place. Once the clusters are connected the current can flow through the whole system and therefore its value increases dramatically. The current calculated for the CTP resonance increases almost linearly as we decrease the NGS.

The values of the current across the junction at the energies of the CTP and CTP' resonances, while retracting the clusters and the neck is getting thinner, are plotted, respectively, in blue and yellow. The current related to the CTP resonance decreases monotonously as we elongate the system. As commented above, its evolution is characterized by abrupt jumps whenever the neck suffers a plastic deformation. The current eventually reaches a plateau associated with the formation of a well-defined monatomic neck. Interestingly, once the monatomic neck is formed, a further neck stretching does not affect considerably the current. This can be expected since the conductance of such small necks mostly depends on the cross-section, which is fixed for the monatomic wire. The current associated with the CTP' mode follows the same trends than that of the CTP, although it shows a less pronounced dependence on the overall elongation of the system. Obviously, once the clusters separate, the current transfer from one cluster to the other is negligible.

The arrows in Fig. 5.21 indicate the position of the jumps shown in Fig. 5.15a. Except for the last jump at 29.3 Å, the other two jumps observed in the polarizability (Fig. 5.15) and in the total energy (Fig. 5.11) show a clearly correlated sudden change in the current. This points toward a remarkable effect of a few atoms (or even a single atom), whose motion influences the overall optical response of the whole system (containing 760 atoms in our case). This observation can be of utmost importance in the control and manipulation of optical signal in subnanometric junctions, which are clearly affected by this type of physical processes at the atomic scale.
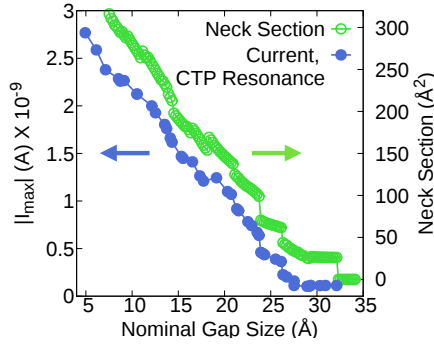
Figure 5.20: The figure shows the one-to-one correspondence between the jumps in the current for the CTP mode and the cross-section of the metal neck. An external electric field of 1×10^{-9} atomic units is assumed with a polarization parallel to the junction main axis.
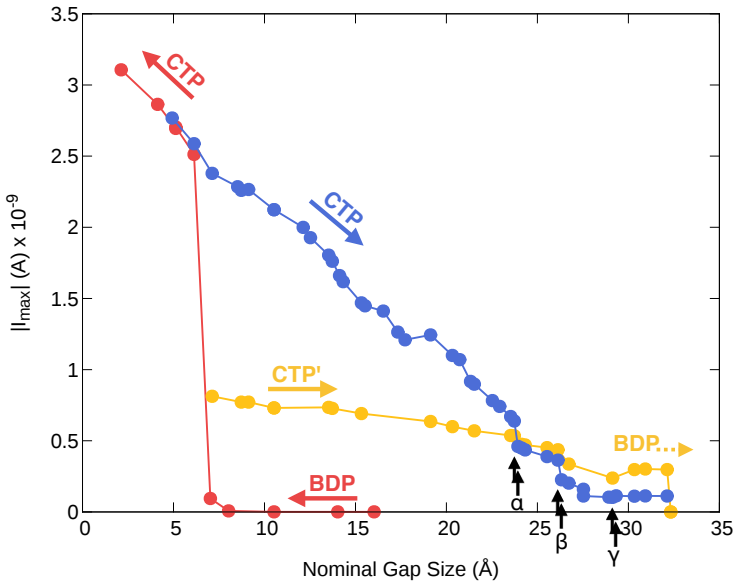
Figure 5.21: Modulus of the current flowing through a plasmonic junction as a function of the nominal gap size. The current is evaluated at a cross-sectional plane passing through the center of the cavity (and cutting the center of the neck when present). Colored arrows indicate the direction of the process (approaching, in red, and retracting, in blue and yellow). The current is computed at the resonance frequency of the different modes of the cavity, as indicated by the labels and described in the text. Black arrows indicate the position at which the spectral jumps in Fig. 5.15 occur.

5.2.10 QUANTUM TRANSPORT REVEALED BY OPTICS

The results in Fig. 5.21 and Fig. 5.20 together with the optical response results shown in Fig. 5.18 and in Fig. 5.15 allow us to establish a correlation between the changes in the current and the evolution of the neck cross-section at optical frequencies. Atomic-scale structural reorganizations are crucial to determine the optical properties of plasmonic cavities. Besides the importance of jump-to-contact events, that can almost completely eliminate any signature of the plasmonic tunnelling regime, the effects are particularly dramatic when a metal nanocontact is formed across the cavity. This is due to the strong dependence of the plasmonic response of the system on the quantized current flowing through the connecting neck.

The mechanical response of atom-sized necks is characterized by sudden rearrangements of the atomic structure, which frequently involve just a few atoms in the thinner part of the contact. Since the electron transport through thin metal nanocontacts is quantized, the corresponding changes of the current flowing across the junction are necessarily discontinuous. Our calculations demonstrate that this common observation under small applied Direct Current (DC) biases can be extrapolated to the optical frequencies of plasmon resonances in a cavity, at least for the short ballistic contacts considered here. These jumps in the current translate onto abrupt changes in the plasmonic response of the system. Thus, the discontinuous evolution of the spectral position, width, and intensity of the CTP mode observed in our simulations is a direct consequence of the transport quantization in the connecting neck. Finally, more disordered structures translate into broader and dimmer CTP resonances.

We can unambiguously establish the following cause-effect relationships: plastic deformation of the neck during elongation $\rightarrow$ cross-section reduction $\rightarrow$ abrupt drop of the current $\rightarrow$ decrease of the intensity of the CTP mode.

5.2.11 CONDUCTANCE AT OPTICAL FREQUENCIES

In the previous paragraph we analyzed the current however, for the low energy CTP mode, it was also possible to define the conductance. The conductance is defined as the ratio between the current flowing across and the bias applied to a particular structure. The conductance is frequently used to characterize the DC transport properties of nanowires. For wires of atom-sized cross-sections the DC conductance can be quantized, i.e. it appears in multiples of the quantum of conductance G_0 ($G_0 = 2e^2/h$ with h Planck's constant and e the electron charge).[257] Thus, in principle, it is also possible to calculate the neck conductance at optical frequencies from the knowledge of the current passing through the neck, Eq. 5.8, and the total potential drop between the two clusters. The total potential is $V_{tot}(\mathbf{r}; \omega_0) = V_{ind}(\mathbf{r}; \omega_0) + V_{ext}(\mathbf{r}; \omega_0)$ where

$$V_{ind}(\mathbf{r}; \omega_0) = \int \frac{\delta n(\mathbf{r}'; \omega_0)}{|\mathbf{r} - \mathbf{r}'|} d\mathbf{r}'. \tag{5.9}$$

and

$$V_{ext}(\mathbf{r}; \omega_0) = \mathbf{E}_0(\omega_0) \cdot \mathbf{r}. \tag{5.10}$$

Here we do not consider the contribution coming from the exchange-correlation potential (V_{xc}). V_{xc} negative contribution is supposed to be small compare to V_{ext} and leads to a

higher conductance. The total potential in real space and frequency domain is a complex number as well as the density change and the current. Thus, the result in this case will be a complex number reflecting the capacitive component of the impedance of the system.

In order to extract the potential drop across the junction in a meaningful way it is necessary a constant potential inside each cluster. This condition is met for configurations having a monatomic neck and at low frequencies. When the neck becomes wider and the energy of the mode increases is not possible anymore to define a potential drop restricted to the neck, i.e., the mismatch between the transmission through the neck and the clusters themselves is not sufficiently large that the potential drop localizes mainly along the neck. In particular, the imaginary part of the potential strongly varies inside the clusters. Due to this behavior of the imaginary part of the potential profile it is not possible to define a voltage drop for wide contacts. Thus, we focus on configurations formed by clusters connected by monatomic chains. In such cases the voltage drop is extracted from the total voltage of a real-space 3D-point-grid. The number of points in real space with the same voltage are counted and plotted. The result is shown in Fig. 5.22. On the x-axis we have the value of the total potential and on the y-axis the recurrence of this value for all the grid points. In particular, in Fig. 5.22(a) the results for the real part of the total potential $V'_{tot} = V'_{ind} + V_{ext}$ are shown, while in Fig. 5.22(b) the results imaginary part $V''_{tot} = V''_{ind}$ are plotted. For the example in Fig. 5.22 − 29.3Å NGS − for both real and imaginary part is possible to determine the voltage drop which is given by the difference of the voltage between the two main peaks in each histogram. The peak are so sharp and well defined because the voltage is constant inside each cluster as can be seen in Fig. 5.23. For the two-cluster system with bigger neck the peaks of the imaginary part get broaden making impossible to define a potential drop. Interestingly, for the real part even for relative big necks is still possible to define a potential drop.
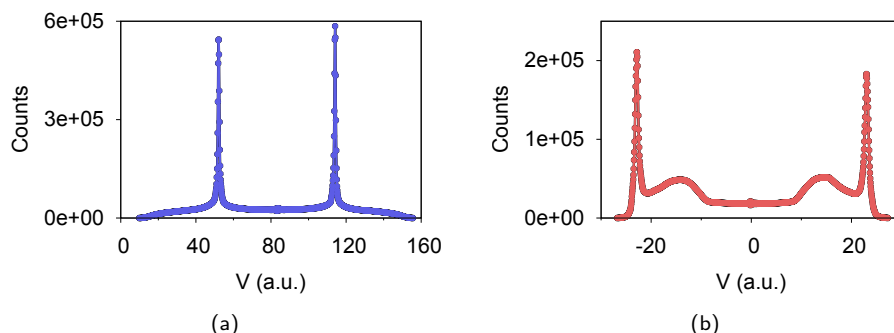
Figure 5.22: Voltage Analysis. In panel (a) the real part of the total potential is plotted, while in panel (b) we plot the imaginary part of the total potential. On the x-axis the value of the total potential is shown while on the y-axis the recurrence of this value valuated for all the grid points.

In Fig. 5.23(a) and 5.23(b) the real and imaginary parts of the total electrostatic potential calculated along the path in panel 5.23(c) are plotted. In particular, Fig. 5.23(a) corresponds to the system with a NGS of 31.3 Å while Fig. 5.23(b) is for a system with

a NGS of 34.1 Å. As can be clearly seen, a bias drop across the monatomic chain can be meaningfully defined for these geometries. The computed conductances for these two cases are:

$$G(\omega_{\text{CTP}}) = (4.52 + i2.21)\text{x}10^{-5}\text{S}, \ d = 31.3\text{Å}$$

$$G(\omega_{\text{CTP}}) = (4.13 + i2.35)\text{x}10^{-5}\text{S}, \ d = 34.1\text{Å}.$$

The corresponding moduli $|G(\omega_{\text{CTP}})|$ of the conductance are, respectively, 5.03 x 10^{-5} S (0.65 G_0) for d = 31.3 Å and 4.75 x 10^{-5} S (0.61 G_0) for d = 34.1 Å, where G_0 = 7.75 x 10^{-5} S is the quantum of conductance.
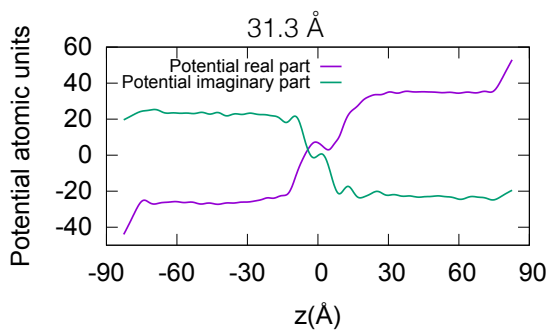
(a)
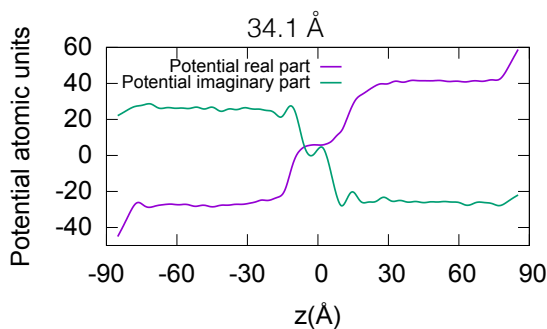
(b)
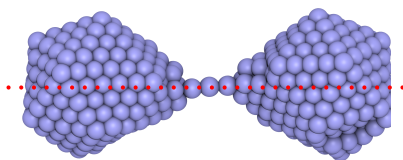
(c)

Figure 5.23: In panels (a) and (b) we can find the real and imaginary parts of the total electrostatic potential ($V_{tot} = V_{ext} + V_{ind}$) when a external field of 1 a.u. is applied along the dimer axis. Panel (a) corresponds to a the dimer system at a NGS of 31.3 Å while in panel (b) the NGS is 34.1 Å. The profiles are calculated along the line shown in panel (c) and for the CTP resonance frequency.

5.3 REAL TIME PLASMONIC MODE EVOLUTION

The real-space density-change distributions shown through all the previous sections correspond to the imaginary component of the complex density change, which can be directly related to the imaginary part of the polarizability and, thus, to the optical absorption. Therefore, although they can serve to characterize the resonant mode at a particular frequency, they may not give a complete picture of the time evolution of the oscillating charge in the system. The real and imaginary are related through the Kramers-Kroenig relation as explained in paragraph 1.3.4. For this, both the real and imaginary part of the polarizability are necessary. In real space and real time the calculated density change is a real quantity. In order to obtain the density change in real time a Fourier transform of $\delta n(\omega)$ has to be performed,

$$\delta n(t) = \frac{1}{2\pi} \int \delta n(\omega) \mathrm{e}^{i\omega t} \mathrm{d}\omega. \tag{5.11}$$

If we consider a sinusoidal external electric field

$$\mathbf{E} = E_0 \cos(\omega_{res} t) \tag{5.12}$$

the density change in real time become

$$\delta n(\mathbf{r}, t; \omega_{res}) = \delta n'(\mathbf{r}, \omega_{res}) \cos(\omega_{res}) + \delta n''(\mathbf{r}, \omega_{res}) \sin(\omega_{res}) \tag{5.13}$$

where ω_{res} is the resonance frequency. In Eq. 5.13 the density in real time depends on both real and imaginary part of the density change in frequency domain. In order to further understand how real and imaginary part play a role in determining the real-time density change is worth it to analyze the shape of the real and imaginary curve of the cross-section spectrum. For a spectral function made of a single excitation the corresponding imaginary part of the cross-section spectrum has a maximum of the Lorentzian peak that coincides with a zero in the real part of the cross-section spectrum, Fig. 5.24(a) – Equations 1.80 and 1.81. However, when dealing with a system having multiple resonances and especially at low frequencies the resulting cross-section spectrum can have a more complex shape due to the proximity of the different resonances. Depending on the broadening factor, peaks in the imaginary of the cross section can merge while in the real part the shape of the curve can change considerable. In particular, even at resonance the real part can be different from zero and have a non-negligible intensity as compared to the imaginary part, Fig. 5.24(b). Thus, for some systems the real part of $\delta n(\omega)$ can contribute strongly to the real-time density-change evolution.

This is the case for the CTP low energy mode seen in the polarizability once the monoatomic neck is formed, that shows a large real part of the induced charge density even at resonance. In Fig. 5.25 the density change real-time evolution of the CTP mode shows the "interaction" between real and imaginary part of the density change in frequency domain. The black arrows indicate the time direction while the green arrows indicate the direction and intensity of the external electric field in each step. At $t = 0$ and $t = \pi/\omega_{res}$ the distribution is solely the real part $\delta n'(\mathbf{r}, \omega_{res})$, while at $t = \pi/2\omega_{res}$ it is given by the imaginary part $\delta n''(\mathbf{r}, \omega_{res})$. At resonance the imaginary part represents the out-of-phase (resonant) component of the total density change while the real part of the density change

oscillates in phase with the external electric driving field. The sequence of images shown in Fig. 5.24 describes the evolution in time of the CTP mode across the cavity when there is a monatomic wire connecting the clusters. At $t = \pi/2\omega_{res}$ we find the imaginary part of the induced charge, that characterizes the mode resonant at that frequency. As expected, the dipole pattern extents over the whole system with the presence of a node in the center of the junction indicating the expected charge transfer among the clusters. In contrast, the real part, found at $t = 0$ and $t = \pi/\omega_{res}$, presents a pattern formed by dipoles placed on each cluster which resembles a BDP mode.

From a physical point of view what we see here is quite transparent. The monatomic wire across the junction represents a bottleneck for electron conduction as compared to the facile movement of charges within each of the clusters. As a consequence, electrons can easily move across each of the clusters and react fast to the applied external field. However, when they reach the gap in the center of the system they accumulate there, since the movement of charge across that gap is limited by the monatomic chain, which provides just a single channel for electron conduction.
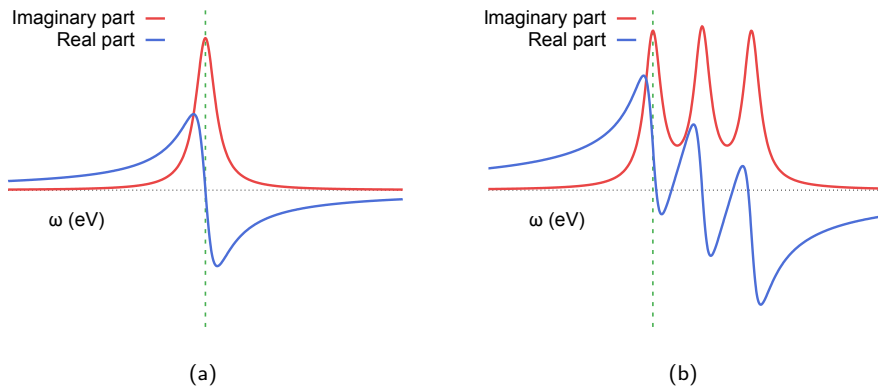
Figure 5.24: Example of the real and imaginary parts typical of the polarizability function. Real and imaginary part are related by the Kramers-Kroenig relation, see paragraph 1.3.4. In panel (a) an example involving a single excitation is shown. In panel (b) a 3-resonance system is shown. The real part is affected by the presence of many resonances close in energy.
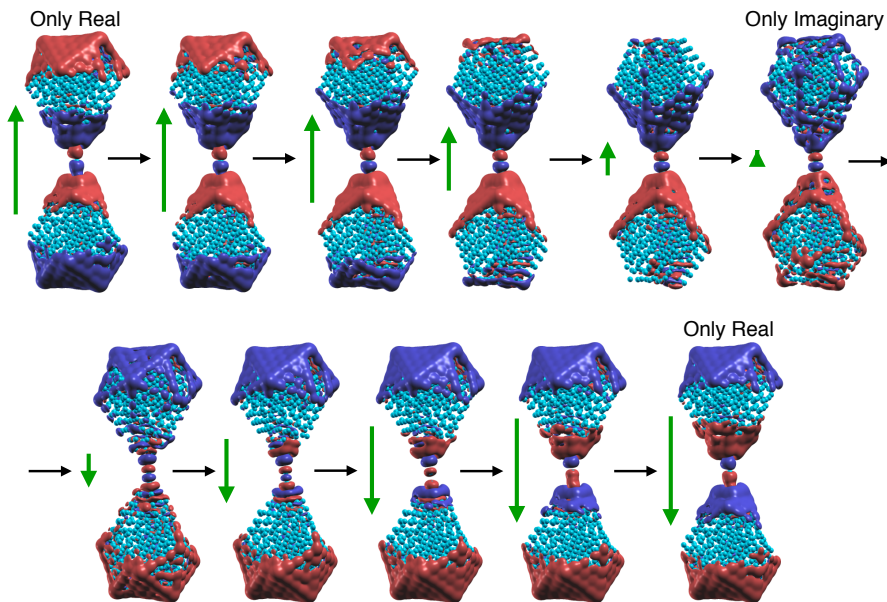
Figure 5.25: Real time evolution of the density change, for the CTP mode. The two clusters are connected by a small monatomic chain in this case

5.4 CONCLUSIONS

In summary, in Section 5.1 we provided new insights into the limits of plasmonic localization where first-principles full-atomistic TDDFT calculations were used to demonstrate that the field localization and enhancement inside the plasmonic nanogaps can be very different depending on whether the distribution of the atoms at the gap defines a flat surface, or presents atomic-scale tip-like protrusions. We showed that, due to the features of the field enhancement at the atomic scale, a description of the plasmonic response based on smooth interface profiles that does not account for the atomistic structural details, either classical or quantum, might not be able to address this atomic-scale near-field regime. Such sensitivity to the atomic details of a structure could explain the lack of reproducibility between apparently similar experiments,[258] but could also provide a root for further optimization of morphologies. The resolution in optics depends on atomic-scale features at the nanoparticle(s) surface and it has important consequences for the limits of optical resolution in field-enhanced spectroscopies[259, 260] and microscopies.[189, 261]

In Section 5.2 we analyzed the effects on the optical properties of atomic reorganization during the approaching process and the retracting process for the same two-cluster system. We showed that the internal atomic reorganization meanly at the plasmon cavity is of fundamental importance to predict the optical behavior. In particular, during the two processes we observed

- Jump-to-contact instability during the approach process.
- Nanocontact formation during the retraction process.

Both effects affect the optical properties. But whereas the former clearly influences the optical properties, de facto making the tunneling region observed in section 5.1 to disappear, the latter shows us the less trivial relation between discontinuous neck-cross-section reduction, jumps in the neck current and jumps in the optical properties. Thus showing that the far field response also depends on the atomic configuration when, the rearrangement involves atoms in the junction of the dimer. In this case, even a small rearrangement of one atom can lead to a considerable change in current flowing through the whole dimer and, thus, affect the absorption spectrum. This is due to the particular structure of such tiny necks, in which the current quantization effects are reflected in the plasmonic response of the system.

A similar connection between quantized transport and the evolution of the plasmonic response has also been pointed out recently.[242] In spite of the smaller scale of the systems treated, discontinuities in the computed DC transport across the junction are related to the intensities of the plasmonic peaks. In our work, the discontinuity of AC quantum transport is revealed in the optical fingerprint of both a snap-to-contact situation in a forming plasmonic junction, as well as during retraction in a nanojunction connected by atom-sized metal contacts. The correlation is clearly demonstrated, showing that remarkably, optics follows the atoms. This is important in the design of subnanometric-scale optical modulators that rely in slight changes of the optical response against tiny configurational modifications. In our case we have analyzed relatively small icosahedral sodium clusters, however, we expect to find a similar behavior for other materials suitable for electronic applications, such as gold. The effect of a single atom in the optical properties of a nanoscopic object as the one reported here, which can be probably extended to somewhat larger objects, has important

consequences in optical engineering, molecular electronics, and photochemistry, where the optical response can now be tailored by a few atoms.

The present study is particularly relevant in light of recent progress in fabrication and processing techniques. As the dimensions of nanoscale architectures are progressively reduced, we are facing a regime where the actual distribution of the atoms in a system matters.[262] The fact that optics might follow the atoms is of utmost importance in optical engineering and optoelectronics, targeting optical modulators or electroactive control of optical signals, where instabilities and modifications of the performance can be attributed to atomic-scale features.[263]

6 | Plasmon Identification in Molecules

For solids, plasmons are defined as charge oscillations that appear whenever the real part of the dielectric function is zero, and the imaginary part is sufficiently small that a clear resonance peak is observed. However, when we consider finite objects like molecules the usual definition is not easy to apply. The peaks observed in the spectrum of finite systems can be thought as single electron-hole (e-h) excitations and collective excitations. The former can be pictured within the classical point particle concept as a result of a chaotic, uncorrelated motion of electrons, while the latter can be pictured as a results of a correlated motion of a group of electrons, resulting in a motion of their center of mass.[264] Some of the latter should be plasmons, corresponding to "classical" charge oscillations. How can we distinguish between these two different kinds of absorption peaks? Some authors have associated peaks appearing in the interacting cross section and absent in the non-interacting one with plasmonic peaks. However, this identification is risky since the effect of the interacting kernel in the response function can give rise to strong modifications of the position and spatial distribution of electron-hole transitions with respect to those obtained from the KS response. Moreover, the induced real-space density and induced potential distribution showing the typical multipolar pattern are plotted as further justification of the plasmonic character for such excitations. However, a better definition, able also to *quantify* the nature of the different resonances in the interacting absorption spectrum, is needed.

In this chapter, we show that the non-interacting absorption spectrum is not the correct quantity to be compared with the full optical spectrum, particularly in order to address the "plasmonic" character of the observed excitations. Recently, several authors addressed the identification of plasmonic excitations in molecules to find a way to define and identify plasmons in molecules.[26–28] Bernadotte et al.[26] exploited the fact that the peaks renormalization due to the Coulomb interaction between electrons is different for peaks of different nature and used this fact to track excitations with collective character. More recently, Bursi et al.[27] and Casanova et al.[28] suggested the classification of electronic transitions by means of some ad hoc quantities to make the classification more clear and feasible. However, as we will show in this chapter a clear way to define plasmons in molecules has not been found yet. We show this by testing the mentioned proposals in the case of a sodium chains.

In particular, in this chapter we have tried to go through different proposed methods in order to understand and define the origin of the peaks observed in the interacting response.

We have considered a system consisting of a Sodium chain for simplicity and we have compared our findings with the results available in the literature.[26–28] Furthermore, in the quest for a better identification criterion, we have calculated the momentum transfer for each excitation and we have used these results to show that plasmon resonances are present in a Sodium chain and are in good agreement with the theoretical predictions obtained for a 1D electron gas model. Even if the adopted system is simple, the analysis of the results can be considered as having a more general validity and indeed shows the presence of plasmonic-like excitations. Unfortunately, the momentum analysis, although useful for the characterization of the optical excitations, is cumbersome and a better analysis method is yet to be found.

6.0.1 DIELECTRIC FUNCTION IN THE DOMINANT PRODUCT FRAMEWORK

Before introducing the methodology used to identify "plasmonic" resonances in molecules, it is useful to define the dielectric function in our framework. In Section 1.4.1 we introduced the concept of dielectric function ϵ which for bulk systems is connected to the concept of plasmons. For bulk systems the zeros of the real part of the dielectric function give the frequency of the plasmonic resonance. Here we show that this idea cannot be applied to find the plasmonic mode frequencies in finite systems. We can write the dielectric function ϵ as

$$\epsilon^{\mu\nu}(\omega) = \iint F^{\mu}(\mathbf{r})\epsilon(\mathbf{r}, \mathbf{r}', \omega)F^{\nu}(\mathbf{r}')d\mathbf{r}d\mathbf{r}' \ , \tag{6.1}$$

where F's are dominant products and μ and ν are the dominant product indices. Within RPA we can now substitute Equation 1.135 in 6.1 and obtain

$$\epsilon^{\mu\nu}(\omega) = \iint F^{\mu}(\mathbf{r})\left[\delta(\mathbf{r}-\mathbf{r}') - \int K_H(\mathbf{r}-\mathbf{r}'')F^{\mu'}(\mathbf{r}'')\chi^0_{\mu',\nu'}(\omega)F^{\nu'}(\mathbf{r}')d\mathbf{r}''\right]F^{\nu}(\mathbf{r}')d\mathbf{r}d\mathbf{r}'$$

$$= \iint F^{\mu}(\mathbf{r})\delta(\mathbf{r}-\mathbf{r}')F^{\nu}(\mathbf{r}')d\mathbf{r}d\mathbf{r}'$$

$$- \int\int\int F^{\mu}(\mathbf{r})K_H(\mathbf{r}-\mathbf{r}'')F^{\mu'}(\mathbf{r}'')\chi^0_{\mu',\nu'}(\omega)F^{\nu'}(\mathbf{r}')F^{\nu}(\mathbf{r}')d\mathbf{r}d\mathbf{r}'d\mathbf{r}'' \ . \tag{6.2}$$

We finally write

$$\epsilon^{\mu\nu}(\omega) = S^{\mu\nu} - K_H^{\mu\mu'}\chi^0_{\mu'\nu'}(\omega)S^{\nu'\nu}$$

where $S^{\mu\nu} = \int F^{\mu}F^{\nu}d\mathbf{r}$ is the overlap matrix between product functions.

The dielectric function depends on the linear response function and on the finite parameter η introduced in Eq. 1.78. This dependence does not allow to identify plasmons in molecules. In Fig. 6.1 the dipole integral calculated from the eigenvalues obtained by diagonalizing the $\epsilon^{\mu\nu}(\omega)$ matrix defined in Eq. 6.0.1, and the polarizability are plotted. The results shown in Fig. 6.1 were obtained for the benzene molecule, however, the observed trend is general and valid for all finite systems. The parameter η determines whether or not the curve representing the real part of the dielectric function crosses the x axis. Consequently, unless the "real" value of η, which is connected to the life-time of the excitation,

for each excitation is known, it becomes impossible to identify plasmons in our system. For bulk systems this is not a problem because the width of the peak, and so the behavior of the real part of the dielectric function is given by the whole bunch of excitations and not anymore by η.
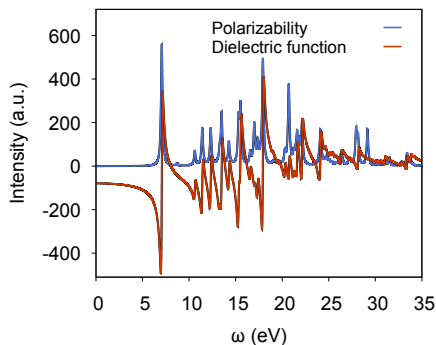
Figure 6.1: The imaginary part of the polarizability (blue curve) and the real dielectric function (red curve) for Benzene are shown.

6.1 System: 1D Sodium Chain

In the previous section we have shown the inadequacy of the dielectric function to identify plasmons in molecules. Here, we are going to show an alternative approach to the problem. As proof of concept we consider a simple system consisting of a sodium chain of 20 atoms with interatomic distance of 3.2 Å. This system was first analyzed by Bernadotte et al.[26] allowing us to directly compare our results to theirs.

6.1.1 Calculation Details

The SIESTA ground state calculation was performed using a DZP basis set with an energyshift of 100 meV. The Random Phase Approximation (RPA) is used as the kernel for the TDDFT calculation, i.e. the TDDFT kernel in Eq. 1.82 is given by the Hartree kernel excluding the exchange-correlation part. This was selected in order to simplify as much as possible the kernel and keeping in mind that the Hartree part of the kernel is accountable for creating plasmonic excitations.[47] Furthermore, the Hartree part of the kernel is mostly responsible for the peak renormalization producing a strong blueshift in the spectrum while, the exchange-correlation term usually produces a minor redshift.

6.1.2 Low Energy Resonant Modes

The sodium-chain optical cross-section spectrum is shown in Fig. 6.2. The resonances visible above 4 eV are given by the out-of-axis components of the polarizability (α_{xx} and α_{zz}). However, for the 1D chain and for the purpose of this work the most interesting peaks are observed at low energy, where a series of peaks are found at 0.584 eV, at 1.466

eV, at 2.142 eV, at 2.712 eV and at 3.181 eV, see Fig. 6.2(b). The low-energy peak at 0.584 eV is found to be very close to the first high-intensity peak presented by Bernadotte et al.[26] who proved the peak to have a plasmonic nature.

For our study we have decided to consider the peak at 0.584 eV and the other two resonances at 0.513 eV and 0.576 eV presenting very low oscillator strength, see Section 1.3.7 for the definition of oscillator strength. The High Intensity (HI) resonance at 0.584 eV has an associated oscillation strength, of 5.661. While, the resonances at 0.513 eV and 0.576 eV show respectively an oscillator strength of 0.034, and 0.019, and thus are not visible in Fig. 6.2(b). Our aim is to show the different character of these resonances lying very close in energy to each other in order to mark the line between plasmonic and non-plasmonic resonances.

Let us start by analyzing the imaginary part of the density change shown in Fig. 6.3, calculated according to Eq. 1.56. Obviously, the isovalue chosen for the plots of the three electronic density plots in Fig. 6.3 is very different, due to their very different oscillator strength. However, at this point we are not interested in the intensity of the resonance, but rather in the pattern depicted by the induced density. The three plots for the three different resonances present very different density distributions. The HI resonance at 0.584 eV shows a dipolar pattern distributed along the whole molecule. Such pattern of the induced electron density is the one expected for a low energy plasmon resonance. The other two maps of the induced densities (0.513 eV, 0.576 eV) have a completely different pattern characterized by more rapid oscillations in the sign of the density change that are not expected at these low energies, although they could appear for high energy plasmon peaks. This first analysis on the induced density indeed highlights some differences among the three resonances considered here. In the following Sections we will consider the same resonances and perform a more detailed analysis of their features.
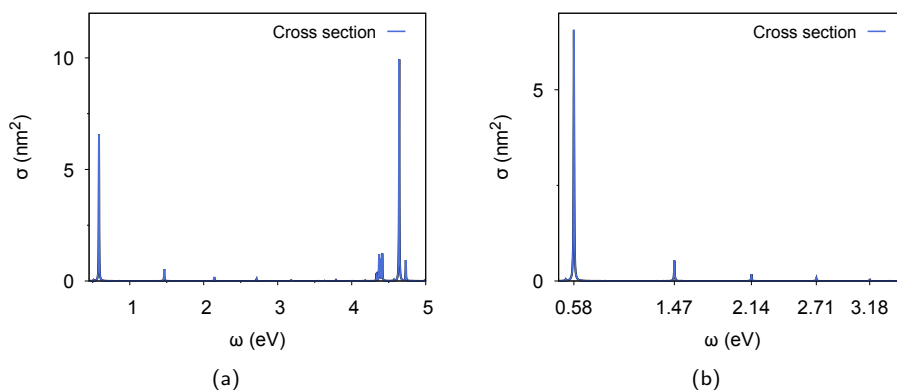
Figure 6.2: Cross section for the 20 atoms sodium chain. Panel (a), from 0.45 eV to 5 eV. Panel (b), from 0.45 eV to 3.5 eV.
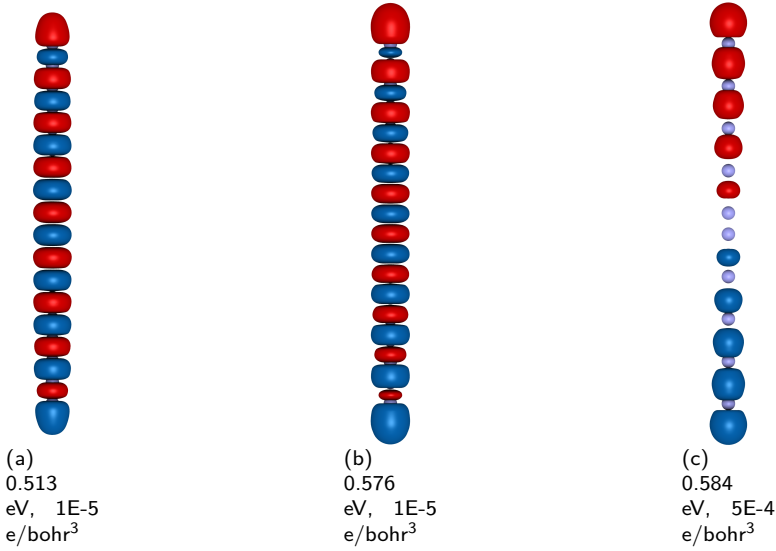
Figure 6.3: The imaginary part of the density change for three different resonances for the system Na_{20} is plotted. At the bottom we indicate the energy at which each resonance is found. The isovalue chosen for the plot in panel (c) is 5E-4 e/bohr^3, the isovalue chosen for the other two plots is set to 1E-5 e/bohr^3 (50 times smaller).

6.2 EIGENVECTORS ANALYSIS

The notion of a plasmon as a collective electronic mode can lead to the idea that plasmon peaks should be composed by many electron-hole transitions. In contrast, non-plasmonic excitations are thought as having a larger weight on a particular electron-hole transition. To exploit this intuitive idea we decided to analyze the eigenvectors of the interacting response, as given by the Casida's formulation (section 1.3.11) in terms of KS e-h excitations. Notice that KS excitations correspond to the Casida's eigenvectors in the absence of the interaction kernel. The hope is that the resulting expansion would indicate the plasmonic nature of the different transitions. From Casida's equation, see Section 1.3.11, we can define the interacting transition density $\phi^I(\mathbf{r})$ as

$$\phi^I(\mathbf{r}) = \sum_{EF} c_{EF}^I \psi^E(\mathbf{r}) \psi^F(\mathbf{r}) \tag{6.3}$$

where $\psi^E(\mathbf{r})$ and $\psi^F(\mathbf{r})$ are the KS wavefunctions (E and F indicate respectively unoccupied and occupied orbitals) and the coefficients c^I's are given by

$$c_{EF}^I = \sum_{E'F'} \tilde{S}_{EF,E'F'}^{-1/2} F_I^{E'F'}. \tag{6.4}$$

The matrix S is defined in Eq. 1.118. c_{EF}^I's are the expansion coefficients connecting non-interacting and interacting transition eigenvectors. F_I's are the Casida eigenvectors

and form an orthonormal basis set, see again Section 1.3.11. Thus, the optical cross section 1.96 (σ) can be written as follows,

$$\sigma = \frac{2}{3} \sum_{i=1}^{3} \int |\phi^I(\mathbf{r})\mathbf{r}_i|^2 \mathrm{d}\mathbf{r} \tag{6.5}$$

$$\times \left[\frac{1}{\omega_I - \omega + i\eta} - \frac{1}{\omega_I + \omega + i\eta} \right]$$

If we combine equations 6.3, 6.4 and 6.5 we obtain,

$$\sigma = \frac{2}{3} \sum_{i=1}^{3} \int \left| \sum_{EF,E'F'} S_{EF,E'F'}^{-1/2} F_I^{E'F'} \psi^E(\mathbf{r})\psi^F(\mathbf{r})\mathbf{r}_i \right|^2 \mathrm{d}\mathbf{r} \tag{6.6}$$

$$\times \left[\frac{1}{\omega_I - \omega + i\eta} - \frac{1}{\omega_I + \omega + i\eta} \right] \tag{6.7}$$

For the non-interacting system the F_I matrix built out of the Casida's eigenvectors ($F_I^{EF,E'F'}$) is diagonal and the cross section becomes,

$$\sigma = \frac{2}{3} \sum_{i;EF} (f_E - f_F)(\epsilon_F - \epsilon_E) \int \left| \psi^E(\mathbf{r})\psi^F(\mathbf{r})\mathbf{r}_i \right|^2 \mathrm{d}\mathbf{r} \tag{6.8}$$

$$\times \left[\frac{1}{\omega_I - \omega + i\eta} - \frac{1}{\omega_I + \omega + i\eta} \right]. \tag{6.9}$$

When the kernel is switched on in the Casida's equation, the resulting eigenvectors F_I^{EF} mix the Kohn-Sham states

$$\phi^I(\mathbf{r}) = \left[\mathbf{S}^{-1/2}\mathbf{F} \right]_{EF}^I \psi^E(\mathbf{r})\psi^F(\mathbf{r}) \tag{6.10}$$

In Fig. 6.4 we show the results of the expansion of $\phi^I(\mathbf{r})$ in terms of the KS electron-hole transitions for the sodium chain. The three resonances, 0.513 eV, 0.576 eV and 0.584 eV, were analyzed. In Fig. 6.4 the x-axis goes from channel 1 up to channel 900. Each channel indicates a different Kohn-Sham transition. The x-axis is ordered according to increasing energy. Thus, the channel number 1 correspond to the HOMO-LUMO DFT transition. The total number (900) is given by the number of the occupied states times the number of the unoccupied states. The y-axis indicates the modulus of the coefficients c_{EF}^I. Fig. 6.4(a), Fig. 6.4(b) and Fig. 6.4(c) do not show any important variation in the distribution pattern, no qualitative difference is visible in the expansion distribution over the 900 transition states. The fact that the excitation at 0.584 eV has a high oscillator strength is not reflected in the way this interacting excitation is expanded in terms of Kohn-Sham electron-hole pairs.

However, if we only consider the first 30 Kohn-Sham transitions, see Fig.6.5, we notice a clear difference in the distribution of the coefficients. In this range, the HI peak presents one transition channel that dominates the expansion, (HOMO-LUMO transition). The plasmonic resonance at 0.584 eV is dominated by the transition 1, while the other two resonances have the strongest components at the 4, 5 and 6 KS transitions. In the

same plot the density distribution $(\psi^E(\mathbf{r})\psi^F(\mathbf{r}))$ associated with the transitions 1, 4, 5 and 6 is presented above each transition. In particular, the density associated with the transition 1 $(\psi^{HOMO}(\mathbf{r})\psi^{LUMO}(\mathbf{r}))$, shown in detail in Fig. 6.6, shows a dipolar distribution similar to the one showed in the density change (Fig. 6.3). The results show that the plasmonic resonance at 0.584 eV, well visible in the cross section (Fig. 6.2(a)), has a dominant contribution from the HOMO-LUMO Kohn-Sham transition. To explain this fact we consider a particle in a 1D box. The particle wavefunction is $\propto \cos(k_n x)$ where $k_n = n\pi/L$ and L is the length of the box. The resulting transition wavefunction calculated multiplying two wavefunctions having the quantum n differing by 1 is proportional to $\cos(\frac{2n+1}{L}\pi x) + \cos(-\frac{\pi}{L}x)$, see Fig.6.7, and shows a clear dipolar electron distribution. Thus, for a monoatomic chain as in the case of sodium 20, the main plasmonic resonance can be expected to have a strong (probably dominant) contribution coming from the HOMO-LUMO KS transition. These results show that the information provided by the expansion of the Casida's eigenvectors does not give us any clear information about the plasmonic nature of the peak. Moreover, the initial intuition of a plasmon made out of many Kohn-Sham transitions does not hold necessarily, even in the simple situation of sodium chain.

(a)

(b)

(c)
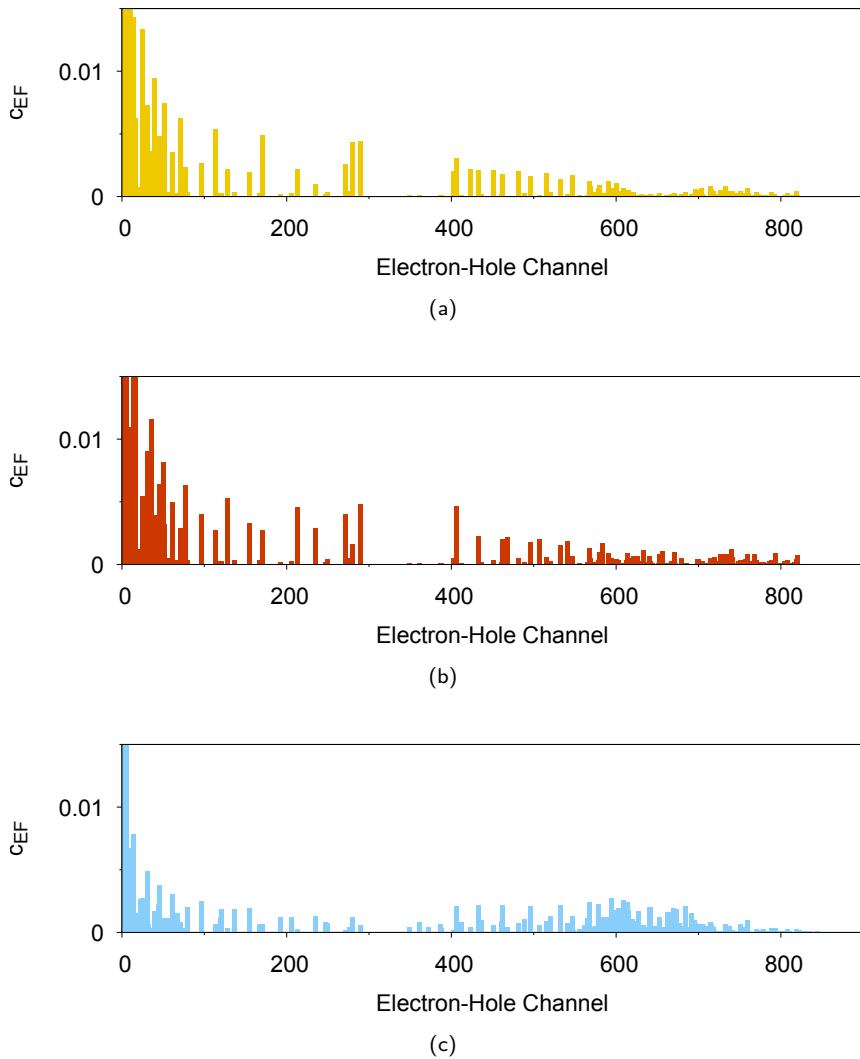
Figure 6.4: Interacting resonance expansion in terms of Kohn-Sham transitions. The 900 transitions between occupied and unoccupied KS levels are indicated in the x-axis. In panel (a), (b) and (c) we show the results respectively for the modes at frequency 0.513 eV, 0.576 eV, 0.584 eV.
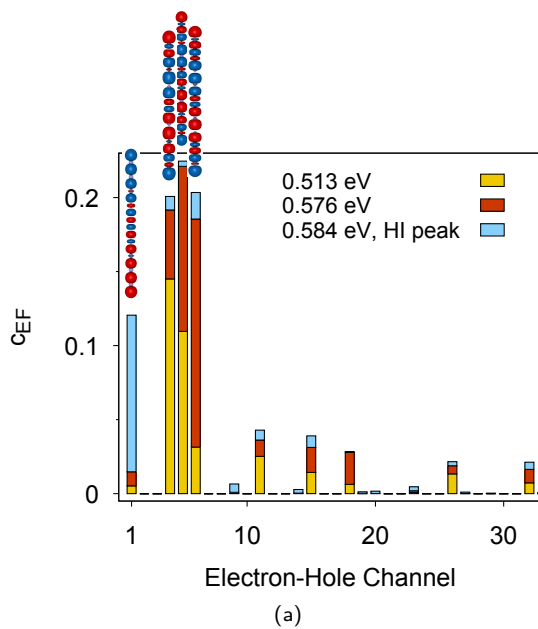
Figure 6.5: Expansion coefficients, in terms of the first 30 KS excitations, for the optical transitions obtained using Casida's equation at 0.513 eV, 0.576 eV and 0.584 eV.
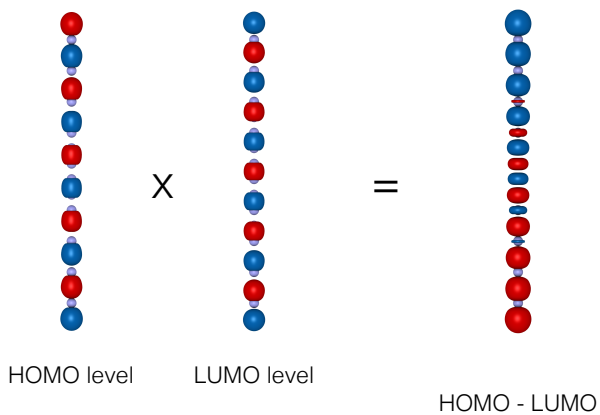
Figure 6.6: HOMO and LUMO KS wavefunctions and the associated HOMO- LUMO transition.
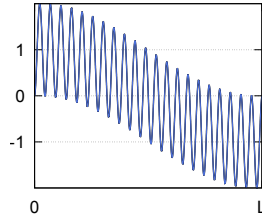
Figure 6.7: Density change associated with the lowest energy e-h transition in a simple particle in a 1D box model, $\cos((2n+1)\pi/L) + \cos(-\pi/L)$

In Fig. 6.8 we present the same analysis for three other different resonances, at the energies 1.439 eV, 1.441 eV and 1.466 eV. The three resonances have an oscillator strength respectively $<10^{-3}$, equal to 0.003 and 0.460. The peak at 1.466 eV can be seen in the cross section in Fig. 6.2. The three different frequencies have very different expansion coefficients as shown in Fig. 6.8 however, no general rule can be extracted in order to differentiate the nature of the three oscillations. Even in this case the resonance with the largest oscillator strength has strong contributions only from a few KS transitions.
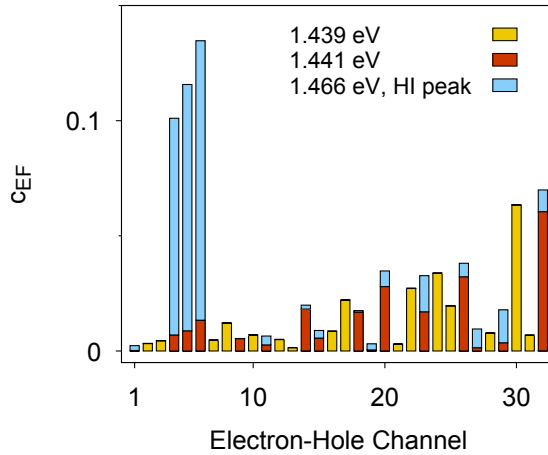
Figure 6.8: Expansion coefficients, in terms of the first 30 KS excitations, for the optical transitions obtained using Casida's equation at 1.439 eV, 1.441 eV and 1.466 eV.

6.2.1 TRANSITION DENSITY: REAL-SPACE MAP

Fig. 6.9 shows the real-space representation of Casida's interacting transition density ϕ^I for some resonances Is. For all the plots an isovalue of the density equal to $5 \cdot 10^{-5} e/\text{Å}^3$ is used. Many resonant frequencies are considered, some at low energy, less than 1 eV, and some at higher energy, around 1.5 eV. Only two of the twelve modes show a distribution pattern that we could describe as "plasmonic", in the sense that they correspond to relatively

long wavelength oscillations of the density that extent over the whole structure. The two "plasmonic" modes detected in Fig. 6.2 and shown in Fig. 6.9(c) and Fig. 6.9(i) have, respectively, one and three nodes. The resonance at 1.466 eV shows a low oscillator strength (0.456 eV) due to the small total dipole. The patterns corresponding to the other transitions cannot be classified as "plasmonic" according to the description above.
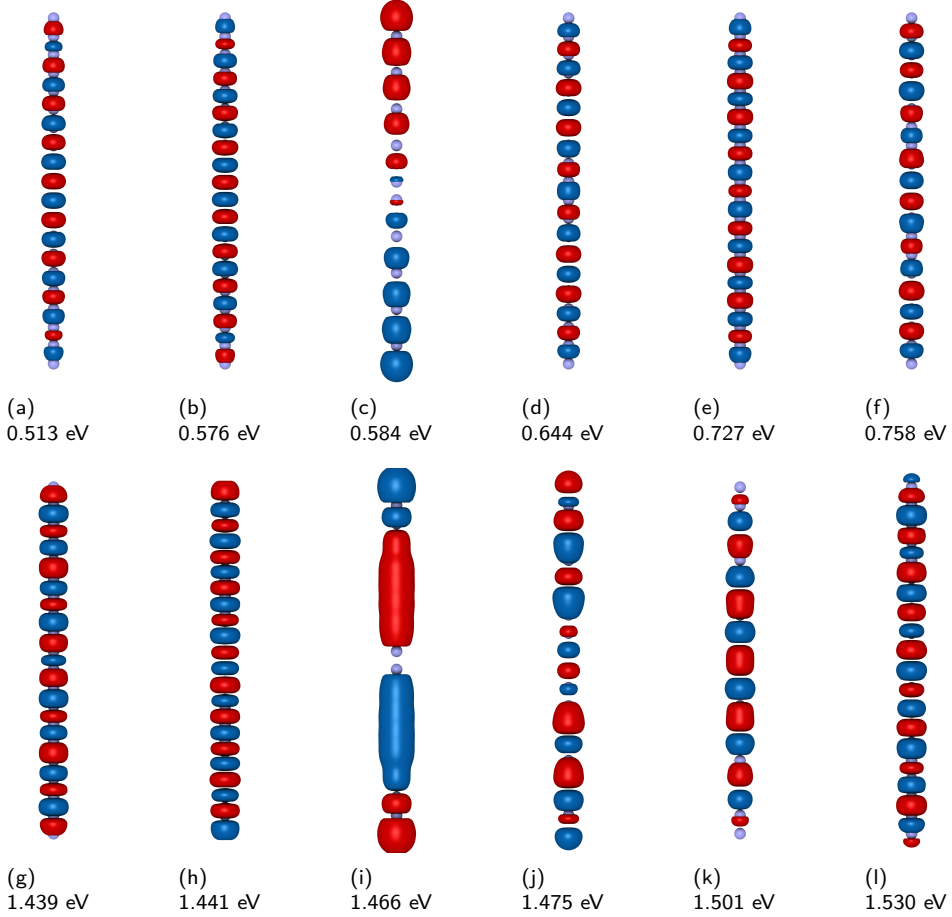
Figure 6.9: The interacting transition density ϕ^I defined in Eq. 6.10 is plotted in real-space for several transitions in a Na$_{20}$ chain. The energy of the modes is indicated at the bottom of each plot.

Recently, Casanova et al.[28] used the so-called *Transition Inverse Participation Ratio* (TIPR). The TIPR labelled as τ is defined as

$$\tau = \left(\sum_{i=1}^{n_{occ}} \lambda_i^4 \right)^{-1} \tag{6.11}$$

λ_i corresponding to transition occupation numbers and are calculated by applying the Single Value Decomposition (SVD) procedure to the transition density matrix T.[28] The *transition inverse participation ratio* is defined in the natural transition orbital. Using SVD, the transition matrix can be re-written as $T = U\Lambda V^\dagger$ where λ_i are the diagonal elements of the matrix Λ. For each excitation we calculate a τ. In particular, the value τ varies from 1 to the number of occupied states. A value of τ close to 1 features single e-h transition while, higher values of τ would indicate higher plasmonic character for that excitation.

In our framework, we can perform the SVD procedure on the C matrix, which elements are $c_{I,EF} = \sum_{E'F'} \widetilde{S}^{-1/2}_{EF,E'F'} F_I^{E'F'}$. The results for the transition inverse participation ratio τ that we calculated for the Sodium chain are shown in Table 6.1. The numbers in blue are the two plasmonic frequency analyzed previously. We cannot see any significant variation of τ for the different excitations. Actually, the excitation at 0.584 eV, which we saw to have a plasmonic character, has a τ of 1.006. In our case, for our system consisting of a Sodium chain, the transition inverse participation ratio does not help to characterize the nature of the excitations. In our analysis of the Casida's eigenvectors presented in Section 6.2 we found that the high intensity excitation at 0.584 eV is given mainly by the HOMO-LUMO KS transition. Thus, it is not surprising to find a τ value of 1 for that excitation. In fact, the SVD procedure projects the problem in a new basis set – the so-called natural orbital's basis set. This new basis set is smaller than the KS e-h transition basis set. However, it does not seem to be able to identify plasmons in molecules, at least in our sodium chain. Moreover, it is interesting to notice that the excitation at 1.466 eV in Table 6.1 has a tau value of 2.996. This value is very close to what is observed in Fig. 6.8.

Frequency (eV)	τ
0.513	1.938
0.576	2.113
0.584	1.006
0.664	1.756
0.727	2.359
0.758	1.624
1.439	2.421
1.441	2.574
1.466	2.996
1.475	1.887
1.501	1.428
1.530	2.286

Table 6.1: Results for τ transition inverse part ratio.

6.3 COMPARISON TO THE DISPERSION OF ELECTRONIC STRUCTURE IN THE INFINITE NA CHAIN

A further analysis can be made by comparing the electronic excitations in an infinite 1D chain. Optical fields carry a very small momentum. For this reason, optical excitations are frequently described as "vertical excitations", meaning that in a bulk system, where electron momentum is well defined, they must take place only between states characterized by the same crystalline momentum (or Bloch wavevector). In a finite system things become slightly more complicated. Scattering at the surfaces mixes states with different momenta (for example, $\mathbf{k}$ and $-\mathbf{k}$ in a 1D chain as the one considered here) and selection rules inspired by the optical vertical transitions might be relaxed. In any case, it frequently becomes difficult to assign a momentum to the resulting quantized electronic states. Under these conditions, it becomes interesting to analyze the infinite system, and consider how its electronic structure should be modified when the boundaries, and the corresponding quantization, of a finite object are taken into account. We start by comparing the band structure calculated for an infinite Na chain with the "band structure" for the Na_{20} chain. For the finite system the momentum is assigned to each Kohn-Sham orbitals by performing a Fast Fourier Transform (FFT), see Appendix G, of the wavefunction. The results in Fig. 6.10 show the band structure of a sodium infinite chain with the band structure calculated from the 20 atoms sodium chain. In particular in Fig. 6.10(b) the first Brillouin Zone (BZ) is considered. The Fermi energy is set to 0 eV. For long chains the bands will converge to the infinite chain limit. The agreement is good, allowing us to calculate a momentum transfer for each excitation.
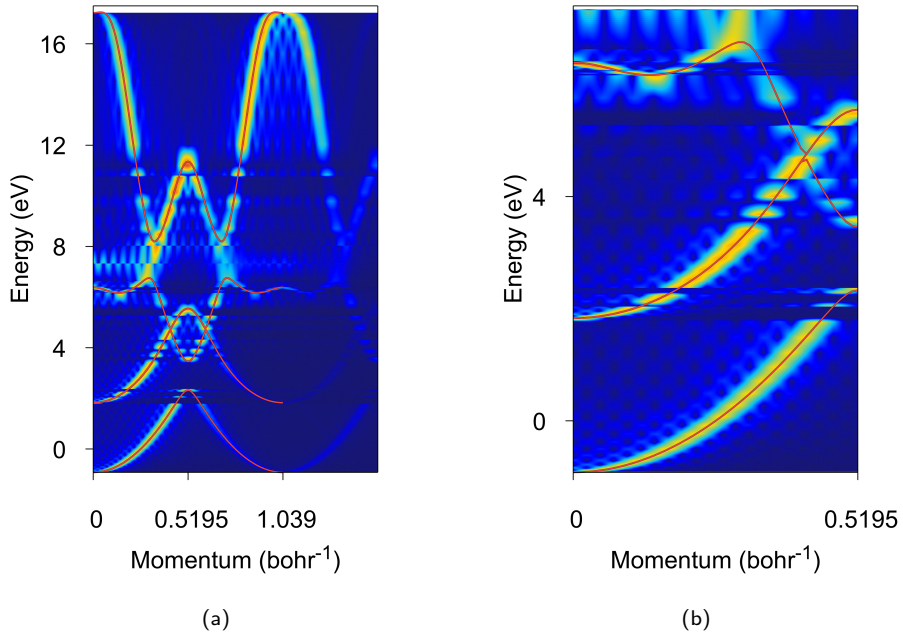
Figure 6.10: Comparison between the band structure for an infinite sodium chain (red line) and The Fourier transform of the levels of a Na_{20} chain (colormap).

6.4 MOMENTUM-TRANSFER ANALYSIS OF THE ELECTRONIC EXCITATIONS IN A FINITE SODIUM CHAIN

The band structure obtained for the finite Sodium chain is in good agreement with the one of an infinite Sodium chain. In the same manner, we can associate a momentum exchange for each excitation by Fourier transforming the real-space functions ϕ^I. This procedure provides information about the momentum transferred during the electronic excitation. Such kind of analysis for a given excitation provides a function of momentum. In Fig. 6.11 we show the Fourier transform of ϕ^I for the transition at 0.584 eV. Although many momenta contribute to this function, it is possible to extract the momentum exchange with the maximum contribution. In Fig. 6.11 on the x-axis is indicated the momentum transfer q. The dashed line indicates the value of the momentum transfer with the higher intensity, which for this transition is equal to 0.032 bohr^{-1}.
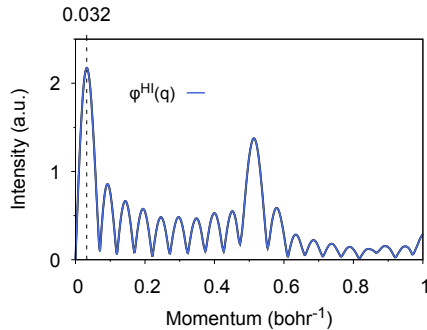
Figure 6.11: FFT of the function ϕ_{HI}. The main contribution is given by the momentum equal to 0.032 bohr^{-1}.

The same analysis was done for all the excitations. In Fig. 6.12 a map of the Fourier transform of ϕ^I for the excitations up to 3 eV is shown. These data show clearly the 1D electron gas plasmon as described in section 1.4.2, the peaks that we will see to have a plasmonic character are indicated with red dots. We can go one step further and extract the q component contributing the most at each $\phi^I(q)$ and assign it to each ϕ^I. The resulting analysis is shown in Fig. 6.13 as red dots. The light blue dots, instead, represent the KS e-h continuum. Finally, the blue curve is calculated using Eq. 1.148 for a Fermi momentum (K_F) equal to 0.496 bohr^{-1}. The value 0.496 bohr^{-1} for K_F was extracted from the momentum analysis of the KS eigenfunction corresponding to the HOMO level for the Na$_{20}$ system. We can see the good agreement between the group of red dots departing from the origin and entering in the e-h continuum, and the blue theoretical curve. Unfortunately, once the group of red dots enter the e-h continuum region is not possible anymore to follow the plasmon dispersion due to the coupling of the "plasmonic" excitations with the e-h excitations. The "plasmonic" modes inside the e-h region cannot be distinguished from the non-plasmonic e-h excitations. This result is a clear mark of the "plasmonic" nature of the low energy excitation peaks present in the cross-section plot, see Fig. 6.2. Note that there is another group of peaks around 4.5 eV that disperses from $q = 0$ towards the e-h continuum region. This, most likely, indicates the presence of another high-energy plasmon mode arising from high-energy features of the sodium band structure and that cannot be described solely by the 1D electron gas theory.
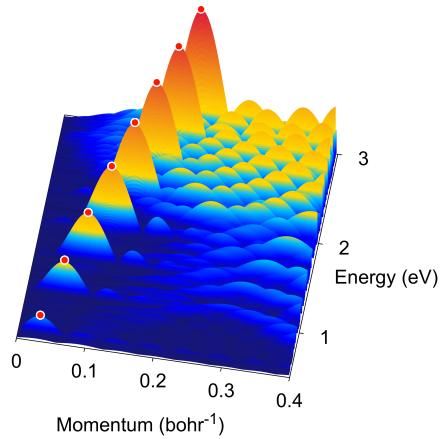
Figure 6.12: Map of the Fourier transform of the ϕ^I functions up to 3 eV. Color code indicates the modulus of the Fourier transform.
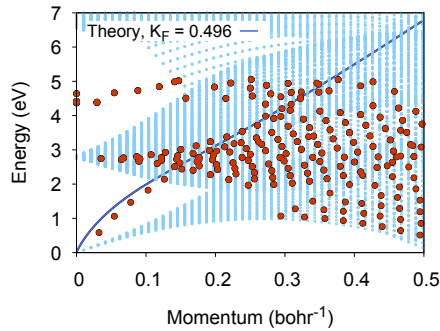
Figure 6.13: The light blue dots represent the electron-hole continuum of an infinite Na chain, while the red dots indicate the electronic excitations in a finite 20 atom Na chain as a function of the momentum transfer assigned to each transition The blue curve represents the theoretical plasmon curve as described in Equation 1.148 for a value of the Fermi momentum equal to 0.496 bohr^{-1}.

A study to calculate the momentum transfer for each excitation of the Na chain has already been done by the Bernadotte et al.[26] In that work they assign the momentum transfer by visual a inspection of the TDDFT transition density. In our study we calculated the plasmon dispersion for the Na$_{20}$ in a more systematic way by defining a procedure based on the application of the Fourier transform on the interacting transition density $\phi^I(\mathbf{r})$ calculated within the Casida's framework. The momentum transfer is then chosen by selecting the momentum component with the most weight.

6.5 COULOMBIC RESTORING FORCE RATIO

A collective electronic oscillation, such as a plasmon, implies a considerable charge displacement. Thus, we expect the coulomb kernel (K) connecting the non-interacting (χ_0) and the interacting response functions (χ) $(\chi = (\chi_0^{-1} - K)^{-1})$ to contribute differently in the case of plasmon modes. With this idea in mind we decided to study in more depth the existing relation between the "plasmonic" modes and kernel renormalization.

In the Casida's formulation, the kernel contribution can be easily separated. As we show in 6.14 we can split the Casida's matrix into two terms, the first term on the right side (highlighted by the dark green line) is the non-interacting "Kohn-Sham" contribution while the second term on the right side (highlighted by the yellow line) contains the kernel and accounts for the electronic interactions. The dynamic screening introduced by the kernel plays an important role in the collective electronic motion unlike in the case of single electron-hole excitations.[26] Different non-interacting transitions respond differently as the kernel is adiabatically switched on, and plasmon-like excitations are strongly renormalized by the kernel.[26] With the above mentioned considerations it seems then possible to quantify a plasmonicity of different excitations by calculating what we called the *Coulombic Restoring Force ratio* (R_{CRF}). The quantity R_{CRF} is given by the ratio between the interacting expectation value and non-interacting expectation value of a given excitation. The two expectation values are taken for the Casida's states $|S^{-1/2}F_I\rangle$. High values of the CRF ratio correspond to excitations that undergo a strong renormalization.

$$
\Omega_{EF}(\omega) = \overbrace{\boxed{\delta_{EF,E'F'}(\epsilon_E - \epsilon_F)}}^{\Omega_{nonint}}
$$

$$
+ \overbrace{\boxed{2\sqrt{(f_E - f_F)(\epsilon_F - \epsilon_E)}K_{EF,E'F'}(\omega)\sqrt{(f_{E'} - f_{F'})(\epsilon_{F'} - \epsilon_{E'})}}}^{\Omega_{int}}
$$

$$
\boxed{\langle S^{-1/2}F_I|\,\Omega_{int}\,|S^{-1/2}F_I\rangle} \;/\; \boxed{\langle S^{-1/2}F_I|\,\Omega_{nonint}\,|S^{-1/2}F_I\rangle} \;=\; R_{CRF}
$$

Figure 6.14

The results obtained are shown in Fig. 6.15(a). The excitations addressed as "plasmonic" excitations from the analysis on the momentum transfer performed in Section 6.4 and having a high oscillator strength, have also a high R_{CRF}. However, we also note that some low intensity peaks in the cross-section can possess high R_{CRF}. This is due to the fact that the cross-section by definition is proportional to the dipolar component of the induced density distribution. It is in fact possible to have a "plasmonic" excitation with multiple nodes and so a weak associated dipole moment. Note that the high energy resonances found above 4 eV are excited by fields perpendicular to the chain axis.

In section 6.4 we discussed the impossibility of detecting "plasmonic" resonances once they enter the e-h continuum, this fact is evident in Fig. 6.13. However, if we take the results from Fig. 6.4 and we filter out those resonances with low R_{CRF} we are able, at least partially, to determine the energy of the "plasmonic" resonances even when they couple with the e-h continuum, see Fig. 6.15(b).

We also note that we see what it looks like a splitting of the plasmonic mode inside the e-h continuum. One branch is indeed following the theoretical curve for the 1D electron gas plasmon (blue curve) while the other branch does not disperse and reaches a plateau value around 3.5 eV. The reason of this "plasmonic" splitting is unknown.

The two studies performed, on the momentum transfer on one side, see Section 6.4, and on the R_{CRF} ratio on the other, together provide a way to gain information about the "plasmonic" character of the resonances, even after they penetrate the e-h continuum.
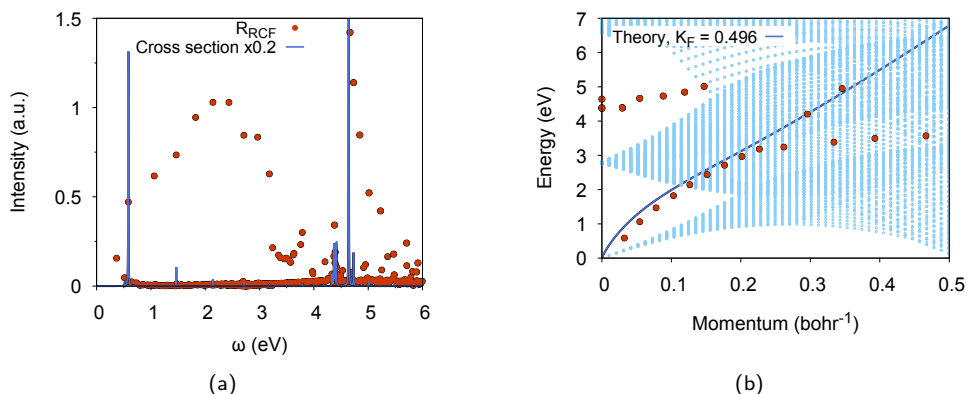
Figure 6.15: In panel (a) the cross section (blue line) is plotted together with the value of the R_{CRF} ratio (red dots) for each energy eigenvalue. In panel (a) the plasmon dispersion is plotted in the momentum energy plane. The red dots indicate the Na_{20} chain electronic excitations with high oscillator strength value. The light blue dots indicate the e-h continuum while the blue line represents the theoretical plasmon curve as described in Equation 1.148 for a value of the Fermi momentum equal to 0.496 bohr^{-1}.

In a recent publication, Bursi et al.[27] introduced what they called *plasmonicity index*, which is a very similar quantity to the CRF ratio just introduced. The idea behind was the same, to measure Coulomb energy related to the modes induced density. Their findings for a system consisting of a sodium chain are very similar to the ones presented in Fig. 6.15(a). However, although our results on the CRF ratio seem to be qualitatively and quantitatively able to define the level of plasmonicity of a system excitation, it was not possible to find transitions with a low CRF ratio and a large oscillator strength. No single e-h excitation has a large enough oscillator strength to be clearly visible in the polarizability/cross section spectrum. More complex systems will have more unpredictable behavior and the study presented here, analysing several characteristic of excitations, becomes even more relevant.

6.6 CONCLUSIONS

In this chapter we tested several definitions of plasmonicity character of molecular resonances. For this purpose we considered a simple Sodium chain containing 20 atoms and we calculated the optical properties employing the Casida's approach (Section 1.3.11). The

eigenvectors obtained by solving the Casida's equation (1.114) contain information about the KS transitions involved in each optical excitation.

Firstly, we looked at the number of KS transitions involved. Our initial idea was based on the notion of plasmons as a collective participation of single-electron transition. In particular, a high number of KS states involved in a given excitation would be a mark of high plasmonicity for that excitation. This kind of analysis proved not to be adequate, and we showed that the basis set given by KS orbitals cannot be used as a mean to measure the collectiveness of an excitation.

The second step consisted in analyzing the momentum transferred in each excitation. Although our system is a finite object, we proved that it is possible by means of the Fourier transform to gather information about the momentum exchanged associated with the excitations. In particular, in the Fourier transform of a given excitation we picked the momentum with higher weight and we assigned it to that excitation. At least in the sodium chain we studied, the results confirmed the existence of plasmonic modes. It was possible, in fact, to observe the theoretically expected 1D plasmon mode typical of a 1D free electron gas system.

Finally, in Section 6.5 we presented the *Coulombic Restoring Force ratio* (R_{CRF}) as calculated in Eq. 6.14. The larger the value of R_{CRF} the higher is the Coulomb interaction for an excitation, which leads to a high renormalization of that excitation, typical of plasmonic modes.[26] The results support the findings obtained with the momentum transfer analysis. Indeed, plasmonic modes possess high values of R_{CRF}. The results from the analysis on the momentum transfer and the R_{CRF} made possible to follow the 1D plasmonic mode well within the e-h continuum. In particular, a splitting of the plasmonic mode inside the e-h continuum was observed.

This study showed that in finite systems is not trivial to characterize the nature of an excitation. In fact, the definition of plasmons for bulk systems does not hold anymore and a deeper analysis is needed to have a better understanding of the nature of the excitations.

7 | CONCLUSIONS

In this PhD thesis we applied *ab initio* Density Functional Theory (DFT) and Linear Response Time-Dependent Density Functional Theory (LR-TDDFT) to study the ground-state and optical properties of some selected finite systems and molecules. The SIESTA (Spanish Initiative for Electronic Simulations with Thousands of Atoms)[6,7] code has been the DFT code used for calculating the ground-state properties of the systems. The optical properties were calculated using the MBPT-LCAO (Many Body Perturbation Theory - Linear Combination Atomic Orbitals)[17–19] code. MBPT-LCAO is a non-commercialized many-body perturbation-theory code that we develop in our research group in Donostia - San Sebastian and featuring efficient algorithms such as

- the generation of an efficient and accurate product basis set,

- efficient procedure to apply the noninteracting linear response matrix on a vector.

- Iterative method to obtain interacting TDDFT spectra.

It is designed to work in tandem with SIESTA – the SIESTA ground-state calculations provide the input to be used in the MBPT-LCAO code. The code has been used to calculate the optical properties of a large variety of systems, be able to treat systems containing thousands of atoms.

In particular, in Chapter 3 of this thesis we analyzed the optical properties of graphene nanoflakes. The study of the optical properties comprehended the analysis of the polarizability, optical cross section and induced density. We considered square and hexagonal graphene nanoflakes because, while the former possess both ZigZag (ZZ) and ArmChair (AC) edges, the latter can be designed to have only ZZ or only AC edges. This gave us the possibility to relate the optical behavior with the presence of a specific type of edge. The sizes of the flakes considered vary from a minimum of $\sim$10 Å ($\sim$40 Carbon atoms) to a maximum of $\sim$60 Å ($>$1000 atoms), in lateral dimensions. The flakes were saturated with Hydrogen atoms.

For all the flakes, two main peaks were observed in the polarizability spectrum. These peaks are related to the π and σ plasmons characteristic of infinite graphene. The origin of the peaks was explained and their energy position was monitored for the three different geometries (square, hexagonal ZZ and hexagonal AC) and for many flake sizes.

The main position of the π and σ plasmons was found to be basically independent of the geometry considered and, thus, of the type of edge of the flake. However, both plasmons redshifted as we increased the size of the flakes. For systems containing $\sim$1000

carbon atoms the position in frequency of the plasmons seems to have converged within tens of meV. Thus, we do not expect an important shift in the plasmon peak positions by further increasing the flake size. In fact, the optical spectrum of the flake ZZ $C_{1014}H_{78}$ is in good agreement with the experimental results from Geim et al.,[131] specially for the lower energy plasmon, i.e. π plasmon, which was found in our polarizability spectra at about 4.8 eV.

The optical gap, i.e. the first optically active excitation, is another interesting quantity we monitored in our work. To perform the study we used the ALDA kernel which shows limitations in describing the optical gap. Square flakes with more that ∼30 carbon atoms have zero optical gap. The reason behind the absence of optical gap in square flakes has been related to the band structure of ZZ graphene nanoribbons. For ZZ and AC hexagonal flakes the optical gap is finite and decreases rapidly as the flakes get bigger. As we increased the size, the optical gap is redshifted and eventually, for very big flakes, approaches the zero limit, typical for graphene. For ZZ flakes the HOMO-LUMO gap and the optical gap approach zero faster than in AC flakes. Most likely this is due to the presence of ZZ edges. Moreover, DFT HOMO-LUMO gap energy and TDDFT optical gap energy have been compared to understand the role of the interaction kernel, ZZ flakes showed a stronger electron screening.

The plots of the induced density for the three geometries and for three different selected energy windows helped us once more to underline the different behavior of the two types of edges. For certain energy ranges in ZZ flakes the density change is concentrated on the edge atoms. In the last part of Chapter 3 we investigated the effects of the edges in the low-energy regime by changing the saturating atoms in ZZ flakes. We functionalized the edges with oxygen, fluorine and hydroxyl group.

In Chapter 4 we focused on the tunability of low-energy resonances by changing the total net charge in triangular Polycyclic Aromatic Hydrocarbons (PAHs). PAH molecules are made of aromatic benzene rings and can be regarded as nanoflakes of graphene. They bear a close resemblance to the so-called graphene quantum dots.[150] The fact that these molecules can be chemically synthesized and are defect-free makes the PAHs potentially attractive for nanodevices. Our calculations showed that even the addition or removal of a single electronic charge can cause the rising of new resonances at visible and near-infrared frequencies in the optical cross section. In particular, this is true for AC triangular flakes where a finite HOMO-LUMO gap exists. The degenerate KS orbitals at the Fermi energy prevent ZZ PAHs from behaving in the same way, and therefore no new resonances were found after doping the material. In order to complete this study a finite temperature had to be considered in the TDDFT calculations. In fact, the low-energy features visible in the spectra after doping are connected to the partially filled KS levels at the Fermi energy as has been proved in Chapter 4.

In Chapter 5 our efforts were focused on analyzing the plasmonic cavity formed by two icosahedral sodium nanoclusters. Each cluster contained 380 sodium atoms arranged to minimize the total energy of the isolated particles. In the first study[170] we left the two cluster geometries untouched and we played with the intercluster distance that separated the two particles. At distances greater than ∼15 Å we can consider the two clusters to be decoupled. Each cluster's polarizability was not heavily influenced by the presence of the other cluster. As we decreases the interparticle distance the two clusters started to interact. We analyzed in detail the evolution of the dimer plasmonic modes in relation

to the interparticle distance and for different cluster-cluster orientations: face-to-face, tip-to-face and tip-to-tip configurations. We also studied the cavity by plotting the induced field real-space distribution at the plasmonic mode frequencies. The analysis has shown the presence of three major plasmonic modes:

- The Bonding Dipolar Plasmon (BDP)

- The Charge Transfer Plasmon (CTP)

- The high-energy Charge Transfer Plasmon (CTP')

The first one is the characteristic mode of the isolated cluster renormalized by the presence of the neighboring particle. It is visible while we are in the so-called capacity regime, when the clusters are placed far apart, and it redshifts as we decrease the intercluster distance. In this regime no current flows between the two clusters. As we decreased the intercluster distance, we eventually entered in the so-called tunnelling regime, the BDP mode slowly disappears and the CTP along with the CTP' become visible. A more intense CTP corresponding to a larger tunnelling current is found for the face-to-face configuration. The CTP mode blueshifted as we keep decreasing the interparticle distance. At the BDP plasmon frequencies, inside the nanocavity a strong localized and enhanced electric field is present, due to the Coulomb coupling between induced charges across the gap. With our first-principles full-atomistic TDDFT approach we showed that the plasmonic field in the cavity can be very dependent on the interparticle distance but also on the mutual orientation of the two objects, for such small interparticle distances the atomistic structure of the junction determines the details of the near-field distribution.

In a following study again described in detail in Chapter 5 we considered the same system consisting of two sodium clusters but, this time we included the possibility for the atoms to rearrange while we change the interparticle distance. To monitor the distance between the clusters we defined the so-called Nominal Gap Size (NGS), which was defined as the distance between the two cluster inner facets if the system would remain unrelaxed. Starting from a NGS of 16 Å we approached the two clusters in steps of 0.2 Å and at each step we performed a SIESTA calculation aimed at optimizing the dimer structure – each cluster geometry is relaxed in response to the presence of its neighbor.

We obtained a plasmonic mode dispersion very different to that where each cluster was kept frozen. In particular, the so-called jump-to-contact instability alters the optical response at small separations dramatically. Around a NGS of 6 Å the attraction between the two flat surfaces in the cavity was strong enough to get them to contact, resulting in a consequent elongation of each cluster. We then kept pushing the two clusters one against the other, almost to the point to form a single roundish big sodium cluster. At a NGS of about 3.5 Å we started the retracting process. Due to the plasticity of our sodium clusters during the retracting process we showed the formation of a nanocontact. A neck connecting the two clusters is formed and becomes thinner and thinner as the distance between the NGS increases as to the point of becoming of monoatomic cross-section. Finally, as we reached a NGS of ∼32 Å the two clusters separate completely.

During the approach and retraction processes we monitored the total energy of the system and the optical response. The jump-to-contact instability led to an abrupt passage from the capacity regime to the resistive regime as such, the total energy of the system changed quickly and the BDP mode suddenly was quenched while both CTP and CTP'

modes appear. The jump-to-contact process wipes out the transition tunnelling regime found theoretically when the clusters were not allowed to relax. The resistive regime characterized by the presence of intense CTP and CTP' modes is characterized by current flowing through the entire dimer.

A less trivial relation between jump in the total energy and discontinuity in the optical cross section is also observed during the retraction process. The contact formation process was not a continuous process, instead it was made by a series of discontinuous processes. In order to investigate further this fact, we calculated the geometrical cross-section of the neck and the current passing through the neck for different NGS. In the analysis presented in Chapter 5 we could associate the neck-cross-section reduction with jumps in the neck current and jumps in the optical properties. We showed that single-atomic reorganization played an important role, even in the far field – the current quantization in the junction region for such small necks reflects in the plasmonic response of the system.

Our study has clearly demonstrated that optics follows the atoms. This is important in the design of subnanometric-scale optical modulators that rely in changes of the optical response against tiny configurational modifications. Our analysis was done for small icosahedron sodium clusters, however, we expect to find a similar behavior for other materials, suitable for electronic applications, such as gold.[265]

In Chapter 6 we asked ourselves whether it is possible to find an operational definition for plasmons in finite systems within the DFT/ TDDFT framework. For bulk systems, plasmons are defined as the frequency at which we have zeros in the macroscopic dielectric function. In finite systems is not possible to define a macroscopic dielectric function and so we need to find another way to identify plasmons. For the current study we considered a system consisting of a sodium chain. Owing to the simplicity of the Na_{20} chain we could perform several types of analysis suggested by different authors.[26–28] The reason to use this system is that it is a simple 1D system and that we could find a publication of a similar study[26] giving us the possibility to readily compare our results to theirs. In order to tackle the problem of the origin of plasmons in molecules we employed the Casida's approach, that provides information about the KS transitions contributing to a given excitation. Moreover, an FFT analysis on Casida's eigenvectors has been performed. From the analysis we were able to define a momentum transfer for a given excitation in a finite system. The analysis on the results have shown the presence of the expected 1D electron gas plasmon. A supporting analysis on the so-called transition density ϕ_I clarified the difference in electron density real-space distribution between electron-hole (e-h) excitations and plasmonic transitions. In order to enable the detection of plasmons without the need of analyzing the real-space or momentum distribution of ϕ_I, we defined a single quantity called *Coulombic Restoring Force ratio* (R_{CRF}). R_{CRF} measures the Coulomb matrix elements of the different Casida's eigenvectors. Indeed, all the plasmonic resonances spotted in the previous analysis showed a strong R_{CRF} value.

A | LINEAR RESPONSE THEORY

Using the results from Appendix B we can write,

$$\hat{\rho}_I(t) = \hat{\rho}_0 - i \int_{-\infty}^{t} \left[\hat{H}_{1,I}(t'), \hat{\rho}_I(t)\right] \mathrm{d}t. \tag{A.1}$$

This equation has to be solved iteratively. However, since the perturbation $H_{1,I}$ is chosen to be *small* we can restrict ourselves to the first order in the perturbation. This means that equation A.1 in Schrödinger representation becomes

$$\hat{\rho}_S(t) \approx \hat{\rho}_0 - i \int_{-\infty}^{t} \mathcal{U}_{H_0} \left[\hat{H}_{1,I}(t'), \hat{\rho}_0\right] \mathrm{d}t \, \mathcal{U}_{H_0}^{\dagger}. \tag{A.2}$$

The integration limits goes from ∞ to t. $t' < t$ where t is observation time ensuring *causality*. Only times t' before the observation time t affect our observation. The ensemble average of the expectation value for a given operator $\hat{O}$ is written as

$$
\begin{aligned}
\langle \hat{O} \rangle &= \sum_i p_i \langle \Psi_i | \hat{O} | \psi_i \rangle = \sum_{i,j,k} p_i \langle \Psi_i | n_j \rangle \langle n_j | \hat{O} | n_k \rangle \langle n_k | \Psi_i \rangle \\
&= \sum_{j,k} \langle n_k | \hat{\rho} | n_j \rangle \langle n_j | \hat{O} | n_k \rangle = \sum_{j,k} \rho_{kj} O_{jk} = \mathrm{Tr}(\rho \, O),
\end{aligned}
\tag{A.3}
$$

where we used the Complete OrthoNormal System (CONS) $\{|n\rangle\}$ and the definition of density operator $\hat{\rho} = \sum_i p_i |\Psi_i\rangle \langle \Psi_i|$. Where $\langle \Psi_i | \hat{O} | \psi_i \rangle$ is the expectation value for the operator $\hat{O}$ in the pure state $|\Psi_i\rangle$. Consequently, it is possible to obtain the expectation value $\langle \ldots \rangle$ of the operator $\hat{O}$ at a given time using A.2 and A.3

$$
\begin{aligned}
\langle \hat{O} \rangle_t &= \mathrm{Tr}(\rho(\mathrm{t}) \, \hat{O}) = \langle \hat{O} \rangle_0 - i \int_{-\infty}^{t} \mathrm{Tr}\left(\mathcal{U}_{H_0} \left[\hat{H}_{1,I}(t'), \hat{\rho}_0\right] \mathcal{U}_{H_0}^{\dagger} \hat{O} \right) \mathrm{d}t' \\
&= \langle \hat{O} \rangle_0 - i \int_{-\infty}^{t} \mathrm{Tr}\left(\hat{\rho}_0 \left[\hat{O}_I, \hat{H}_{1,I}(t')\right] \right) \mathrm{d}t'.
\end{aligned}
\tag{A.4}
$$

where we used twice the cyclic properties for matrix trace, $\mathrm{Tr}(ABCD) = \mathrm{Tr}(BCDA)$.

A.1 EIGENSTATE TIME-EVOLUTION

A state in Interaction representation is defined as

$$|\Psi_I(t)\rangle \stackrel{\text{def}}{=} e^{i\hat{H}_{0,S}t} |\Psi_S(t)\rangle = \mathcal{U}_{H_0}^{\dagger} |\Psi_S(t)\rangle \tag{A.5}$$

so that the Schrödinger equation $i\frac{\partial}{\partial t} |\Psi_S(t)\rangle = \hat{H}_S |\Psi_S(t)\rangle = (\hat{H}_0 + \hat{H}_{1,S}(t)) |\Psi_S(t)\rangle$ can be re-written as

$$i\frac{\partial}{\partial t}\big(\mathcal{U}_{H_0} |\Psi_I(t)\rangle\big) = \hat{H}_S |\Psi_S(t)\rangle = (\hat{H}_0 + \hat{H}_{1,S}(t))\mathcal{U}_{H_0} |\Psi_I(t)\rangle$$

$$\mathcal{U}_{H_0}\hat{H}_0 |\Psi_I(t)\rangle + i\mathcal{U}_{H_0}\frac{\partial}{\partial t} |\Psi_I(t)\rangle = \hat{H}_0 \mathcal{U}_{H_0} |\Psi_I(t)\rangle + \hat{H}_{1,S}(t)\mathcal{U}_{H_0} |\Psi_I(t)\rangle \tag{A.6}$$

$$i\frac{\partial}{\partial t} |\Psi_I(t)\rangle = \hat{H}_{1,I}(t) |\Psi_I(t)\rangle$$

where $\hat{H}_{1,I}(t) = \mathcal{U}_{H_0}^{\dagger}\hat{H}_{1,S}\mathcal{U}_{H_0}$. We can integrate with respect to t and we get

$$|\Psi_I(t)\rangle = |\Psi_0\rangle - i \int_{-\infty}^{t} \hat{H}_{1,I}(t') |\Psi_I(t')\rangle \, dt' \tag{A.7}$$

where $|\Psi_0\rangle = |\Psi_I(t=-\infty)\rangle$. For small $H_{1,I}(t)$ we can stop at the first order in the expansion

$$|\Psi_I(t)\rangle \approx |\Psi_0\rangle - i \int_{-\infty}^{t} \hat{H}_{1,I}(t') |\Psi_0\rangle \, dt'. \tag{A.8}$$

Thus, the expectation value of an observable $\hat{O}(t)$ at any time t can be written as

$$\langle \hat{O}_I \rangle_t = \left[\langle\Psi_0| + i\int_{-\infty}^{t} \langle\Psi_0| \hat{H}_{1,I}(t') dt' \right] \hat{O}_I(t) \left[|\Psi_0\rangle - i\int_{-\infty}^{t} \hat{H}_{1,I}(t') |\Psi_0\rangle \, dt' \right]$$

$$= \langle \hat{O}_I(t) \rangle_0 + i\int_{-\infty}^{t} \left[\langle\Psi_0| \hat{O}_I(t)\hat{H}_{1,I}(t') |\Psi_0\rangle - \langle\Psi_0| \hat{H}_{1,I}(t')\hat{O}_I(t) |\Psi_0\rangle \right] dt'$$

$$= \langle \hat{O}_I(t) \rangle_0 - i\int_{-\infty}^{t} \langle [\hat{O}_I(t)\hat{H}_{1,I}(t')] \rangle\big|_0 \, dt'$$

$$\tag{A.9}$$

A.2 KUBO FORMULA

Let us consider the time-dependent perturbing part of the Hamiltonian represented in Interacting picture $\hat{H}_{1,I}(t)$ to be functional of $\hat{A}(t)$ and depending on the field $F(t)$

$$\hat{H}_1(t) = \hat{A}(t)F(t). \tag{A.10}$$

Then we get

$$\Delta \langle \hat{O}(t) \rangle = \langle \hat{O} \rangle_t - \langle \hat{O} \rangle_0 = -i \int_{-\infty}^t F(t') \text{Tr} \left(\hat{\rho}_0 \left[\hat{O}_I, \hat{A}_I(t') \right] \right) dt$$
$$= -i \int_{-\infty}^t F(t') \left\langle \left[\hat{O}_I, \hat{A}_I(t') \right] \right\rangle_0 dt'. \tag{A.11}$$

Of our interest is the case in which $\hat{H}_1(t)$ depends on the density ρ, $\hat{H}_1(t) = \int \rho(\mathbf{r}, t) \phi(\mathbf{r}, t) d\mathbf{r}$. In this case

$$\Delta \langle \hat{\rho}(\mathbf{r}, t) \rangle = -i \int_{-\infty}^t \int \phi(\mathbf{r}', t') \left\langle \left[\hat{\rho}_I(\mathbf{r}, t), \hat{\rho}_I(\mathbf{r}', t') \right] \right\rangle_0 d\mathbf{r}' dt'$$
$$= \int_{-\infty}^\infty \int (-i) \theta(t - t') \left\langle \left[\hat{\rho}_I(\mathbf{r}, t), \hat{\rho}_I(\mathbf{r}', t') \right] \right\rangle_0 \phi(\mathbf{r}', t') d\mathbf{r}' dt', \tag{A.12}$$

where the integral is extended to $+\infty$ but the $\theta(t - t')$ is introduced

$$\theta(t - t') = \begin{cases} 1, & t' < t \\ 0, & t' \geq t \end{cases}. \tag{A.13}$$

In A.12 the change in density due to the perturbation depends linearly on the potential ϕ. The formula connects the external perturbation and the response of the system and it depends only on the unperturbed system. From equation A.12 we can define

$$\chi(\mathbf{r}, t; \mathbf{r}', t') = (-i) \theta(t - t') \left\langle \left[\hat{\rho}_I(\mathbf{r}, t), \hat{\rho}_I(\mathbf{r}', t') \right] \right\rangle_0. \tag{A.14}$$

This result is known as *Kubo formula*. χ defined as in equation A.14 is also called *retarded Green function*, or *retarded response function*, or *retarded propagator* or *correlation function*. For a time-independent H_0 we have *time invariance* and we can write

$$\chi(\mathbf{r}, t; \mathbf{r}', t') = \chi(\mathbf{r}, \mathbf{r}', t - t') \rightarrow \chi(\mathbf{r}, t). \tag{A.15}$$

Using A.12, A.14, A.15 and by Fourier transforming equation A.12 we obtain,

$$\Delta \langle \hat{\rho}(\mathbf{r}, t) \rangle = \frac{1}{2\pi} \int \Delta \langle \hat{\rho}(\mathbf{r}, \omega) \rangle e^{i\omega t} d\omega$$
$$= \frac{1}{4\pi^2} \int_{-\infty}^\infty \int \int \int \chi(\mathbf{r}, \mathbf{r}', \omega) e^{i\omega(t-t')} \phi(\mathbf{r}', \omega') e^{i\omega' t'} d\mathbf{r}' d\omega d\omega' dt' \tag{A.16}$$
$$= \frac{1}{2\pi} \int \int \chi(\mathbf{r}, \mathbf{r}', \omega) \phi(\mathbf{r}', \omega) d\mathbf{r}' e^{i\omega t} d\omega$$

obtaining

$$\Delta \langle \hat{\rho}(\mathbf{r}, \omega) \rangle = \int \chi(\mathbf{r}, \mathbf{r}', \omega) \phi(\mathbf{r}', \omega) d\mathbf{r}'. \tag{A.17}$$

In particular we can obtain a more explicit version of the linear response function in frequency domain. If we use the complete set of eigenstates of the Hamiltonian $\hat{H}$, e.i. $\hat{H} |n\rangle = E_n |n\rangle$ and fact that

$$\hat{\rho}_I(\mathbf{r}, t) = \mathcal{U}_{H_0}^\dagger \hat{\rho}_I(\mathbf{r}, 0) \mathcal{U}_{H_0} = e^{i\hat{H}_{0,s}t} \hat{\rho}_I(\mathbf{r}', 0) e^{-i\hat{H}_{0,s}t} \tag{A.18}$$

we can write

$$
\begin{aligned}
\chi(\mathbf{r}, \mathbf{r}', \omega) = \lim_{\eta \to 0} -i \sum_n \int \theta(t) \Bigg[& \langle \Psi_0 | e^{iE_0 t} \hat{\rho}_I(\mathbf{r}, 0) e^{-iE_n t} | \Psi_n \rangle \langle \Psi_n | \hat{\rho}_I(\mathbf{r}', 0) | \Psi_0 \rangle \\
& - \langle \Psi_0 | \hat{\rho}_I(\mathbf{r}', 0) | \Psi_n \rangle \langle \Psi_n | e^{iE_n t} \hat{\rho}_I(\mathbf{r}, 0) e^{-iE_0 t} | \Psi_0 \rangle \Bigg] e^{-\omega t} e^{\eta t} \mathrm{d}t \\
= \lim_{\eta \to 0} -i \sum_n \int_{-\infty}^0 \Bigg[& e^{-it(E_{n0} + \omega + i\eta)} \langle \Psi_0 | \hat{\rho}_I(\mathbf{r}, 0) | \Psi_n \rangle \langle \Psi_n | \hat{\rho}_I(\mathbf{r}', 0) | \Psi_0 \rangle \\
& - e^{-it(-E_{n0} + \omega + i\eta)} \langle \Psi_0 | \hat{\rho}_I(\mathbf{r}', 0) | \Psi_n \rangle \langle \Psi_n | \hat{\rho}_I(\mathbf{r}, 0) | \Psi_0 \rangle \Bigg] \mathrm{d}t \\
= \lim_{\eta \to 0} \sum_n \Bigg[& \frac{\langle \Psi_0 | \hat{\rho}_S(\mathbf{r}) | \Psi_n \rangle \langle \Psi_n | \hat{\rho}_S(\mathbf{r}') | \Psi_0 \rangle}{\omega + E_{n0} + i\eta} \\
& - \frac{\langle \Psi_0 | \hat{\rho}_S(\mathbf{r}') | \Psi_n \rangle \langle \Psi_n | \hat{\rho}_S(\mathbf{r}) | \Psi_0 \rangle}{\omega - E_{n0} + i\eta} \Bigg]
\end{aligned}
$$

$$(A.19)$$

where the factor $e^{-\eta t}$ and the limit $\lim_{\eta \to 0}$ are introduced. η is taken positive and real. This is equivalent to consider the Hamiltonian $H = H_0 + e^{-\eta|t|} H_1$. In this case for $t \pm \infty$ the system is described by the non-interacting Hamiltonian H_0. Starting from $t = -\infty$ the perturbation is switched on and will increase until $t = 0$, while, for times following $t = 0$ the oscillation will decay. The limit for $\eta \to 0$ means in the perturbation to be turned on infinitely slowly (adiabatically), in this case any purposeful result has to be independent of the factor η.[266] The perturbative adiabatic approach is a mathematical trick employed to follow the development of the H_0 eigenstates as the perturbative Hamiltonian term H_1 is switched-on so to obtain reliable interacting eigenstates.[266] However, it can be shown that the TDDFT linear response theory is valid also for sudden switched-on potential, nevertheless the factor $e^{-\eta t}$ is necessary in order to perform the integration in frequency domain and it does not come from a potential adiabatically switched-on.[267] In equation A.19 the η factor appears as imaginary infinitesimals at the denominator in the response function. We can finally define the oscillator strength as

$$F_i = \langle \Psi_n | \hat{\rho}_S(\mathbf{r}') | \Psi_0 \rangle. \tag{A.20}$$

A.3 NON-INTERACTING RESPONSE FUNCTION (χ_0), LEHMANN REPRESENTATION

It is useful to introduce the so-called non-interacting response function $\chi_0(\mathbf{r}, \mathbf{r}', t)$ which describes the linear response of a system of independent particles. In this approximation we can extract a concise form for the response functions depending on the system orbital wavefunctions. In order to do that, it is convenient to use the second-quantization formalism in equation A.19. In second quantization the creation and annihilation operators are introduced

$$a_i | \Psi_n \rangle = \sqrt{f_i} | \Psi_{n,-i} \rangle \qquad a_i^\dagger | \Psi_n \rangle = \sqrt{f_i + 1} | \Psi_{n,+i} \rangle, \tag{A.21}$$

where f_i is the occupation of the ith-level. Moreover, the density is defined in term of creation ($\psi^\dagger$) and annihilation (ψ) field operators

$$\hat{\rho}_S(\mathbf{r}) = \psi^\dagger(\mathbf{r})\psi(\mathbf{r}) \qquad \psi(\mathbf{r}) = \sum_i \phi_i(\mathbf{r})a_i \qquad \psi^\dagger(\mathbf{r}) = \sum_i \phi_i^*(\mathbf{r})a_i^\dagger, \qquad \text{(A.22)}$$

where $a^\dagger$ and a are the creation and annihilation operators respectively and $\phi_i(\mathbf{r})$ are single-particle wave functions. We can re-write the oscillator strength terms (equation A.20) as

$$\begin{aligned}
\langle \Psi_n | \psi^\dagger(\mathbf{r})\psi(\mathbf{r}) | \Psi_0 \rangle &= \sum_{j,k} \langle \Psi_n | \phi_j^*(\mathbf{r})a_j^\dagger \phi_k(\mathbf{r})a_k | \Psi_0 \rangle \\
&= \sum_{j,k} \phi_j^*(\mathbf{r})\phi_k(\mathbf{r})\sqrt{f_j+1}\sqrt{f_k}\, \langle \Psi_n | \Psi_{0,-k+j} \rangle
\end{aligned} \qquad \text{(A.23)}$$

$$\langle \Psi_0 | \psi^\dagger(\mathbf{r})\psi(\mathbf{r}) | \Psi_n \rangle = \sum_{j,k} \phi_j^*(\mathbf{r})\phi_k(\mathbf{r})\sqrt{f_j}\sqrt{f_k+1}\, \langle \Psi_{0,-j+k} | \Psi_n \rangle \qquad \text{(A.24)}$$

Substituting the terms A.23 and A.24 in equation A.19 we obtain the so-called Lehmann representation[267]

$$\begin{aligned}
\chi_0(\mathbf{r},\mathbf{r}',\omega) &= \sum_{j,k} \frac{(f_j+1)f_k \phi_k^*(\mathbf{r})\phi_j(\mathbf{r})\phi_j^*(\mathbf{r}')\phi_k(\mathbf{r}')}{\omega + E_{jk} + i\eta} \\
&\quad - \frac{(f_k+1)f_j \phi_j^*(\mathbf{r}')\phi_k(\mathbf{r}')\phi_k^*(\mathbf{r})\phi_j(\mathbf{r})}{\omega - E_{kj} + i\eta} \\
&= \sum_{j,k} \frac{(f_k-f_j)\phi_k^*(\mathbf{r})\phi_j(\mathbf{r})\phi_j^*(\mathbf{r}')\phi_k(\mathbf{r}')}{\omega - E_{kj} + i\eta}.
\end{aligned} \qquad \text{(A.25)}$$

B | Von Neumann Equation

Starting from the Schrödinger equation,

$$i\frac{\partial}{\partial t}\left|\Psi_S(t)\right\rangle = \hat{H}_S\left|\Psi_S(t)\right\rangle \qquad\qquad i\frac{\partial}{\partial t}\left\langle\Psi_S(t)\right| = -\left\langle\Psi_S(t)\right|\hat{H}_S \qquad (\text{B.1})$$

being $\hat{H}_S = \hat{H}_S^\dagger$. If we evolve the density operator defined as $\hat{\rho}(t) = \sum_{i=1}^N p_i\left|\Psi_S(t)\right\rangle\left\langle\Psi_S(t)\right|$ we find the Von Neumann equation,

$$
\begin{aligned}
i\frac{\mathrm{d}}{\mathrm{d}t}\hat{\rho}_S(t) &= \sum_{i=1}^N p_i\left[\left(i\frac{\mathrm{d}}{\mathrm{d}t}\left|\Psi_S(t)\right\rangle\right)\left\langle\Psi_S(t)\right| + \left|\Psi_S(t)\right\rangle\left(i\frac{\mathrm{d}}{\mathrm{d}t}\left\langle\Psi_S(t)\right|\right)\right]\\
&= \sum_{i=1}^N p_i\left[\hat{H}_S\left|\Psi_S(t)\right\rangle\left\langle\Psi_S(t)\right| - \left|\Psi_S(t)\right\rangle\left\langle\Psi_S(t)\right|\hat{H}_S\right] = \left[\hat{H}_S, \hat{\rho}_S(t)\right]
\end{aligned}
\qquad (\text{B.2})
$$

Equation B.2 is defined in Schrödinger representation. However, we can re-write it in Interaction representation. In this representation we assume the Hamiltonian can be split into a time-independent part $\hat{H}_0^S$ (e.i. $\partial_t\hat{H}_{0,S}t = 0$) and a time-dependent part $H_{1,S}(t)$. A state in Interaction representation is defined as

$$\left|\Psi_I(t)\right\rangle \overset{\text{def}}{=} e^{i\hat{H}_{0,S}t}\left|\Psi_S(t)\right\rangle = \mathcal{U}_{H_0}^\dagger\left|\Psi_S(t)\right\rangle \qquad (\text{B.3})$$

If we re-write equation B.2 in Interaction representation we get

$$
\begin{aligned}
i\frac{\mathrm{d}}{\mathrm{d}t}\hat{\rho}_I(t) &= i\left[iH_{0,S}\mathcal{U}_{H_0}^\dagger\hat{\rho}_S(t)\mathcal{U}_{H_0} + \mathcal{U}_{H_0}^\dagger\frac{\mathrm{d}}{\mathrm{d}t}\hat{\rho}_S(t)\mathcal{U}_{H_0} - i\mathcal{U}_{H_0}^\dagger\hat{\rho}_S(t)\mathcal{U}_{H_0}H_{0,S}\right]\\
&= -H_{0,S}\mathcal{U}_{H_0}^\dagger\hat{\rho}_S(t)\mathcal{U}_{H_0} + \mathcal{U}_{H_0}^\dagger\left[\hat{H}_{0,S} + \hat{H}_{1,S}, \hat{\rho}_S(t)\right]\mathcal{U}_{H_0}\\
&\quad + \mathcal{U}_{H_0}^\dagger\hat{\rho}_S(t)\mathcal{U}_{H_0}H_{0,S} = \mathcal{U}_{H_0}^\dagger\left[\hat{H}_{1,S}, \hat{\rho}_S(t)\right]\mathcal{U}_{H_0}\\
&= \left[\hat{H}_{1,I}, \hat{\rho}_I(t)\right]
\end{aligned}
\qquad (\text{B.4})
$$

C | Residue Theorem

The residue theorem or Cauchy's residue Theorem is employed to calculate the complex line integral an integrand of the form $f(z) = g(z)/(z-z_0)^n$ where $g(z)$ is an analytic function. The Residue (Res) is defined as the coefficient a_{-1} of the Laurent series. The residue theorem reads

$$\oint_c f(z)\mathrm{d}z = 2\pi i \sum_{i=1}^{k} \mathrm{Res}(f, a_k). \qquad \text{(C.1)}$$

D | Important Relations

D.1 Commutators

D.1.1 $[\hat{r}, \hat{p}] = i$

With the momentum operator in position space defined as $\hat{p} = -i\nabla$ the commutator becomes

$$[\hat{r}, \hat{p}]f(r) = -i\hat{r}\nabla f(r) + i\nabla(\hat{r}f(r))$$
$$= -i\hat{r}\nabla f(r) + i(\nabla\hat{r})f(r) + i\hat{r}(\nabla f(r)) = i(\nabla\hat{r})f(r) = i \tag{D.1}$$

D.1.2 $i[\hat{H}, \hat{r}] = \hat{p}$

For an Hamiltonian whose potential part does not depend on momentum $\hat{H} = \frac{p^2}{2} + V(\mathbf{r}, t)$ and using D.1 then

$$i[\hat{H}, \hat{r}] = \frac{i}{2}\left(\hat{p}[\hat{p}, \hat{r}] + [\hat{p}, \hat{r}]\hat{p}\right) = \hat{p}. \tag{D.2}$$

The same result can be calculated starting from the Heisemberg equation $\frac{d\hat{O}}{dt} = i[\hat{H}, \hat{O}]$ substituting with the observable $\hat{O}$ with $\hat{r}$ and using the Ehrenfest's theorem $\frac{d\langle\hat{r}\rangle}{dt} = \langle\hat{p}\rangle$.

D.2 f-SUM (TRK) RULE

The derivation f-sum rule or Thomas-Reiche-Kuhn (TRK) rule uses the relations D.1 and D.2.

$$
\begin{aligned}
-i \langle 0| [\hat{r}, \hat{p}] |0\rangle = \langle 0|0\rangle &= N_e \\
&= -i \Big(\sum_n \langle 0| \hat{r} |n\rangle \langle n| \hat{p} |0\rangle - \sum_m \langle 0| \hat{p} |m\rangle \langle m| \hat{r} |0\rangle \Big) \\
&= -i \Big(\sum_n \langle 0| \hat{r} |n\rangle \langle n| i[\hat{H}, \hat{r}] |0\rangle - \sum_m \langle 0| i[\hat{H}, \hat{r}] |m\rangle \langle m| \hat{r} |0\rangle \Big) \\
&= \sum_n \langle 0| \hat{r} |n\rangle \langle n| \hat{H}\hat{r} - \hat{r}\hat{H} |0\rangle - \sum_m \langle 0| \hat{H}\hat{r} - \hat{r}\hat{H} |m\rangle \langle m| \hat{r} |0\rangle \\
&= \sum_n (E_n - E_0) \langle 0| \hat{r} |n\rangle \langle n| \hat{r} |0\rangle - \sum_m (E_m - E_0) \langle 0| \hat{r} |m\rangle \langle m| \hat{r} |0\rangle \\
&= \sum_n 2(E_n - E_0) \, | \langle n| \hat{r} |0\rangle |^2.
\end{aligned}
$$

$$(D.3)$$

In the derivation we used the fact the fact that $\sum_n |n\rangle \langle n|$ twice, where $|n\rangle$ are the eigenfunctions of $\hat{H}$ as well as $|0\rangle$. N_e is the normalization condition of the ground state $|0\rangle$ and is equal to the total number of electrons in the system.

E | ELECTRIC CURRENT

From equation 1.109 we can calculate the total amount of charge displaced δQ within a given volume in real space Ω. Thus, we can write

$$\delta Q(t, \omega_0) = E_0 \cos(\omega_0 t) \int_\Omega n'(\mathbf{r}, \omega_0) d\mathbf{r} - iE_0 \sin(\omega_0 t) \int_\Omega n''(\mathbf{r}, \omega_0) d\mathbf{r} \qquad \text{(E.1)}$$

$$= E_0 \big[\delta Q'(\omega_0) \cos(\omega_0 t) - i\delta Q''(\omega_0) \sin(\omega_0 t) \big]. \qquad \text{(E.2)}$$

The current is defined as the time derivative of the total amount of charge $I = dQ/dt$,

$$\delta I(t, \omega_0) = -\omega_0 \delta Q'(\omega_0) \sin(\omega_0 t) - i\omega_0 \delta Q''(\omega_0) \cos(\omega_0 t). \qquad \text{(E.3)}$$

The average current over a period T can be calculated by means of the Root Mean Square (RMS),

$$I_{RMS}(\omega_0) = \frac{1}{T} \int_T \delta I(\omega_0)^2 dt = \frac{1}{T} \int_T \delta I(\omega_0)^2 dt \qquad \text{(E.4)}$$

$$= \frac{1}{T} \omega_0^2 \Big[\delta Q'(\omega_0)^2 \int_T \sin^2(\omega_0 t) dt + \delta Q''(\omega_0)^2 \int_T \cos^2(\omega_0 t) dt \qquad \text{(E.5)}$$

$$+ 2\delta Q'(\omega_0) \delta Q''(\omega_0) \int_T \sin(\omega_0 t) \cos(\omega_0 t) dt \Big]. \qquad \text{(E.6)}$$

$$\int_T \sin^2(\omega_0 t) dt = \frac{t}{2} - \frac{\sin(2\omega_0 t)}{4\omega_0} \Big|_0^T = \frac{T}{2} \qquad \text{(E.7)}$$

$$\int_T \cos^2(\omega_0 t) dt = \frac{t}{2} - \frac{\sin(2\omega_0 t)}{4\omega_0} \Big|_0^T = \frac{T}{2} \qquad \text{(E.8)}$$

$$\int_T \sin(\omega_0 t) \cos(\omega_0 t) dt = -\frac{\cos^2(\omega_0 t)}{2\omega_0} \Big|_0^T = 0 \qquad \text{(E.9)}$$

so that

$$I_{RMS}(\omega_0) = \frac{\omega_0}{\sqrt{2}} \sqrt{\delta Q'(\omega_0)^2 + \delta Q''(\omega_0)^2}. \qquad \text{(E.10)}$$

While the modulus of the maximal current flowing through the system is given by the relation $I_{RMS} = |\frac{I_{max}}{\sqrt{2}}|$

$$|I_{max}(\omega_0)| = \omega_0 \sqrt{\delta Q'(\omega_0)^2 + \delta Q''(\omega_0)^2}. \qquad \text{(E.11)}$$

Alternatively, one can arrive to the same conclusion calculating the current in frequency domain.

$$I(\omega) = \int \left[\frac{\mathrm{d}Q(t)}{\mathrm{d}t}\right]e^{-i\omega t}\mathrm{d}t = \int \frac{\mathrm{d}}{\mathrm{d}t}\left[\frac{1}{2\pi}\int Q(\omega')e^{i\omega' t}\mathrm{d}\omega'\right]e^{-i\omega t}\mathrm{d}t$$
$$= \frac{i}{2\pi}\iint \omega'Q(\omega')e^{-it(\omega-\omega')}\mathrm{d}\omega'\mathrm{d}t = \int \omega'Q(\omega')\delta(\omega-\omega')\mathrm{d}\omega' = i\omega Q(\omega). \tag{E.12}$$

Thus,

$$|I(\omega)| = \omega\delta Q(\omega). \tag{E.13}$$

Equation E.13 shows that the modulus of the current in frequency domain is equivalent to the modulus of the maximum current in time domain, Equation E.11.

F | FUNCTIONAL DERIVATIVES

When dealing with functional is important to have clear the concept of functional derivatives. The approximated form for the potential in DFT is the functional derivative of the energy functional over the density and the kernel in TDDFT is in again the functional derivative of the potential respect with the density. Let us consider a functional F of a function ϕ where ϕ is a function of the variable $\mathbf{r}$. The functional derivative $\frac{\delta F[\phi]}{\delta \phi(\mathbf{r})}$ is defined through the relation

$$\delta F[\phi] = \int \frac{\delta F[\phi]}{\delta \phi(\mathbf{r})} \delta \phi(\mathbf{r}) \mathrm{d}\mathbf{r}. \tag{F.1}$$

Thus, the functional variation δF is given by the sum of local changes over the whole range of $\mathbf{r}$ values. If we defined the function variation $\delta \phi$ to be localized at a given point point, i.e. $\delta \phi(\mathbf{r}) = \epsilon \delta(\mathbf{r} - \mathbf{r}')$ we can write

$$F[\phi(\mathbf{r}) + \epsilon \delta(\mathbf{r} - \mathbf{r}')] - F[\phi(\mathbf{r})] = \int \frac{\delta F[\phi]}{\delta \phi(\mathbf{r})} \epsilon \delta(\mathbf{r} - \mathbf{r}') \mathrm{d}\mathbf{r} = \frac{\delta F[\phi]}{\delta \phi(\mathbf{r}')} \epsilon. \tag{F.2}$$

So for small variation of the $\delta \phi$ we obtain

$$\frac{\delta F[\phi(\mathbf{r})]}{\delta \phi(\mathbf{r}')} = \lim_{\epsilon \to 0} \frac{\delta F[\phi(\mathbf{r}) + \epsilon \delta(\mathbf{r} - \mathbf{r}')] - \delta F[\phi(\mathbf{r})]}{\epsilon} = \left[\frac{\mathrm{d}F}{\mathrm{d}\epsilon} \right]_{\epsilon=0}. \tag{F.3}$$

Relation F.3 is important for practical the evaluation of functional derivative. For example, if we consider $F[\phi] = \int \phi(\mathbf{r})^n \mathrm{d}\mathbf{r}$ by using F.3 we can easily obtain

$$\frac{\delta F[\phi]}{\delta \phi(\mathbf{r})} = n[\phi(\mathbf{r})]^{n-1}. \tag{F.4}$$

More generally, if we consider a generic functional F which is functional of a function ϕ and its derivative $\nabla \phi$,

$$F[\phi] = \int f(\phi(\mathbf{r}), \nabla \phi(\mathbf{r})) \mathrm{d}\mathbf{r} \tag{F.5}$$

we can write the variation in the functional using Taylor expansion as

$$\delta F[\phi] = \frac{\delta F[\phi]}{\delta \phi} \delta \phi + \frac{\delta F[\phi]}{\delta \nabla \phi} \delta \nabla \phi = \int \left[\frac{\partial f}{\partial \phi} \delta \phi + \frac{\partial f}{\partial \nabla \phi} \delta \nabla \phi \right] d\mathbf{r}$$

$$= \int \frac{\partial f}{\partial \phi} \delta \phi \, d\mathbf{r} + \frac{\partial f}{\partial \nabla \phi} \delta \phi \Big|_{-\infty}^{+\infty} - \int \nabla \cdot \frac{\partial f}{\partial \nabla \phi} \delta \phi \, d\mathbf{r} = \int \left[\frac{\partial f}{\partial \phi} - \nabla \cdot \frac{\partial f}{\partial \nabla \phi} \right] \delta \phi d\mathbf{r}.$$
$$(F.6)$$

Where we used the integration for parts and the fact that $\delta \phi(-\infty) = \delta \phi(\infty) = 0$. The functional derivative with respect to the ϕ function is obtained by comparing equation F.6 with equation F.1,

$$\frac{\delta F}{\delta \phi(\mathbf{r})} = \frac{\partial f}{\partial \phi} - \nabla \cdot \frac{\partial f}{\partial \nabla \phi}. \tag{F.7}$$

G | FAST FOURIER TRANSFORM (FFT)

In the MBPT-LCAO code the FFTW library[268, 269] is used to calculate the Fourier transform of functions in a 3D real-space grid. It is important to know how the function distributed in real-space grid characterized by a given Δr defining the finess of the grid is related to the Fourier Transform algorithm used in the FFTW subroutine. Let's consider a 1D continuous function $f(r)$ (the extension to the 3D case is trivial) and its Fourier transform $F(k)$,

$$F(k) = \int f(r)e^{-irk}\mathrm{d}r \tag{G.1}$$

Equation G.1 can be discretized in the following way,

$$F_k = \sum_r f_r e^{-irk}\Delta r \tag{G.2}$$

The Fast Fourier Transform (FFT) calculated as in FFTW library reads[268, 269]

$$F_m = \sum_{n=0}^{N-1} f_n e^{-i\frac{2\pi}{N}nm} \tag{G.3}$$

No information about the real-space or reciprocal-space grid is delivered. The input function f_n is characterize by being discretized with N points with n going from 0 to $N-1$. In the same way the output F_m is a N dimension 1D array. The m index runs from 0 to $N-1$.

In order to compare equation G.3 with equation G.2 the continuous variable r and k are re-writing so that $r_n = r_0 + n\Delta r$ and $k_m = m\Delta k$. r_0 is the offset of my real-space function and Δr and Δk are the increments for the continuous variables r and k respectively. We can then write equation G.2 as,

$$F(k_m) = \sum_{n=0}^{N-1} f(r_n)e^{-i(r_0+n\Delta r)(m\Delta k)}\Delta r \tag{G.4}$$

$$= \sum_{n=0}^{N-1} f(r_n)e^{-i(nm\Delta r\Delta k + r_0 m\Delta k)}\Delta r \tag{G.5}$$

Comparing equation G.3 and equation G.5 and extracting the nm term we get,

$$\Delta r \Delta k = \frac{2\pi}{N} \qquad (G.6)$$

Thus we get,

$$
\begin{aligned}
F(k_m) &= \sum_{n=0}^{N-1} f(r_n) e^{-i\frac{2\pi}{N}(nm + r_0 m \frac{1}{\Delta r})} \Delta r \\
&= \left[e^{-i\frac{2\pi}{N} r_0 m \frac{1}{\Delta r}} \Delta r \right] \left[\sum_{n=0}^{N-1} f(r_n) e^{-i\frac{2\pi}{N} nm} \right]
\end{aligned} \qquad (G.7)
$$

The relation G.6 connecting Δr with Δk is important when converting the output coming from FFTW subroutine to momentum domain corresponding to our input function in real space in order to have the right discretization of the grid in momentum domain. Moreover, it tells you which support in real space ($N\Delta r$) is needed to have the wanted grid in reciprocal domain.

H | Linear Response Function in Momentum Domain

In space domain and in first quantization the density operator is defined as

$$n(\mathbf{r}) = \sum_i \delta(\mathbf{r} - \mathbf{r}_i). \tag{H.1}$$

The same operator in momentum space reads

$$n_{\mathbf{k}} = \int \sum_i \delta(\mathbf{r} - \mathbf{r}_i) e^{-i\mathbf{k}\cdot\mathbf{r}} \mathrm{d}\mathbf{r}. \tag{H.2}$$

In second quantization $n(\mathbf{r}) = \psi^\dagger(\mathbf{r})\psi(\mathbf{r})$ where $\psi(\mathbf{r})$ is the field operator defined as in equation A.22. The field operator can be re-written in momentum domain as[67]

$$\psi(\mathbf{r}) = \frac{1}{\sqrt{V}} \sum_{\mathbf{k}} e^{i\mathbf{k}\cdot\mathbf{r}} a_{\mathbf{k}}, \qquad\qquad \psi^\dagger(\mathbf{r}) = \frac{1}{\sqrt{V}} \sum_{\mathbf{k}} e^{-i\mathbf{k}\cdot\mathbf{r}} a_{\mathbf{k}}^\dagger, \tag{H.3}$$

$$a_{\mathbf{k}} = \frac{1}{\sqrt{V}} \int \psi(\mathbf{r}) e^{-i\mathbf{k}\cdot\mathbf{r}} \mathrm{d}\mathbf{r}. \tag{H.4}$$

$a_{\mathbf{k}}$ is the annihilation operator which destroys a particle of momentum $\mathbf{q}$. Thus, we can write the density operator as

$$n(\mathbf{r}) = \sum_{\mathbf{k},\mathbf{k}'} a_{\mathbf{k}}^\dagger a_{\mathbf{k}'} e^{i(\mathbf{k}'-\mathbf{k})\cdot\mathbf{r}}, \tag{H.5}$$

and its Fourier transform is

$$n_{\mathbf{q}} = \frac{1}{V} \int \sum_{\mathbf{k},\mathbf{k}'} a_{\mathbf{k}}^\dagger a_{\mathbf{k}'} e^{i(\mathbf{k}'-\mathbf{k})\cdot\mathbf{r}} e^{-i\mathbf{q}\cdot\mathbf{r}} \mathrm{d}\mathbf{r} = \frac{1}{V} \sum_{\mathbf{k},\mathbf{k}'} a_{\mathbf{k}}^\dagger a_{\mathbf{k}'} \int e^{i(\mathbf{k}'-\mathbf{k}-\mathbf{q})\cdot\mathbf{r}} \mathrm{d}\mathbf{r}$$
$$= \sum_{\mathbf{k},\mathbf{k}'} a_{\mathbf{k}}^\dagger a_{\mathbf{k}'} \delta(\mathbf{k}' - \mathbf{k} - \mathbf{q}) = \sum_{\mathbf{k}} a_{\mathbf{k}}^\dagger a_{\mathbf{k}+\mathbf{q}}. \tag{H.6}$$

The Hermitian conjugate of $n_{\mathbf{q}}$ becomes

$$n_{\mathbf{q}}^\dagger = \sum_{\mathbf{k}} a_{\mathbf{k}+\mathbf{q}}^\dagger a_{\mathbf{k}} = n_{-\mathbf{q}}. \tag{H.7}$$

Physically, the operator $n_{\mathbf{q}}$ acts on the ket destroying a particle with wavevector $\mathbf{k} + \mathbf{q}$, $a_{\mathbf{k}+\mathbf{q}}$, and creating another particle with $\mathbf{k}$, $a_{\mathbf{k}}$. Where $\mathbf{q}$ is momentum exchanged. The operator $n_{\mathbf{q}}^{\dagger}$ works similarly, destroying a particle with momentum $\mathbf{k}$, $a_{\mathbf{k}}$, and creating a particle of momentum $\mathbf{k} + \mathbf{q}$, $a_{\mathbf{k}+\mathbf{q}}$.

We can now use the operator $n_{\mathbf{q}}$ and $n_{\mathbf{q}}^{\dagger}$ to write the linear response function,

$$\chi(\mathbf{q}, -\mathbf{q}, t) = \chi(\mathbf{q}, t) = (-i)\theta(t) \left\langle \left[n_{\mathbf{q}}(t), n_{\mathbf{q}}^{\dagger}(0) \right] \right\rangle_{0}. \tag{H.8}$$

Where $\mathbf{q}$ represents the momentum transferred during the interaction between projectile and target.

I | INELASTIC SCATTERING

Let us consider a projectile (electron) hitting a target (specimen). We can calculate the probability of interchange of energy and momentum between the projectile and target. In this case the electron approaching with energy E_i and momentum $\mathbf{k}_i$ is scattered. The final energy and momentum of the outgoing electron is E_f and $\mathbf{k}_f$, respectively. If we consider the initial ground state of the target $|0\rangle$ and the final excited state as $|n\rangle$ we can write the state of the whole system before and after the event as $|\mathbf{k}_i\rangle \otimes |0\rangle = |0, \mathbf{k}_i\rangle$ and $|\mathbf{k}_f\rangle \otimes |n\rangle = |n, \mathbf{k}_f\rangle$, respectively. The Hamiltonian describing the interaction between the incoming electron and all the electrons in the target is $H'(\mathbf{r}) = \sum_i V(\mathbf{r} - \mathbf{r}_i)$ being the target a collection of points charges with density $n(\mathbf{r}) = \sum_i \delta(\mathbf{r} - \mathbf{r}_i)$. The Fermi golden rule tells us that the ratio (probability per unit of time) of an event where the electron exchange momentum $\mathbf{k}_f - \mathbf{k}_i$ and energy $\omega_n - \omega_0 = \omega_{n0}$ with the target is

$$R = 2\pi \sum_n |\langle n, \mathbf{k}_f| H'(\mathbf{r}) |0, \mathbf{k}_i\rangle|^2 \delta(\omega + \omega_{n0}). \tag{I.1}$$

$H'(\mathbf{r})$ can be written as $\frac{1}{(2\pi)^3} \int H'(\mathbf{k}) e^{i\mathbf{k}\cdot\mathbf{r}} d\mathbf{k}$ where

$$H'(\mathbf{k}) = \int \sum_i V(\mathbf{r} - \mathbf{r}_i) e^{-i\mathbf{k}\cdot\mathbf{r}} d\mathbf{r} = \sum_i e^{-i\mathbf{k}\mathbf{r}_i} \int V(\mathbf{r} - \mathbf{r}_i) e^{-i\mathbf{k}\cdot(\mathbf{r}-\mathbf{r}_i)} d\mathbf{r} = n(\mathbf{k})V(\mathbf{k}) \tag{I.2}$$

where $\sum_i e^{-i\mathbf{k}\mathbf{r}_i} = n(\mathbf{k}) = \int \sum_i \delta(\mathbf{r} - \mathbf{r}_i) e^{-i\mathbf{k}\cdot\mathbf{r}} d\mathbf{r}$. Thus we can write

$$\langle n, \mathbf{k}_f| H'(\mathbf{r}) |0, \mathbf{k}_i\rangle = \frac{1}{(2\pi)^3} \int \langle n, \mathbf{k}_f| n(\mathbf{k})V(\mathbf{k}) |0, \mathbf{k}_i\rangle e^{i\mathbf{k}\cdot\mathbf{r}} d\mathbf{k} \tag{I.3}$$

$$= \frac{1}{(2\pi)^3} \iint e^{i\mathbf{k}_f\cdot\mathbf{r}} \langle n| n(\mathbf{k})V(\mathbf{k}) |0\rangle e^{-i\mathbf{k}_i\cdot\mathbf{r}} e^{i\mathbf{k}\cdot\mathbf{r}} d\mathbf{r} d\mathbf{k} \tag{I.4}$$

$$= \int \langle n| n(\mathbf{k})V(\mathbf{k}) |0\rangle \delta(\mathbf{k}_i - \mathbf{k}_f - \mathbf{k}) d\mathbf{k} \tag{I.5}$$

$$= V(-\mathbf{q}) \langle n| n(-\mathbf{q}) |0\rangle = V(\mathbf{q}) \langle n| n^\dagger(\mathbf{q}) |0\rangle. \tag{I.6}$$

We used $\mathbf{q} = \mathbf{k}_f - \mathbf{k}_i$ and the that fact that $V(-\mathbf{q}) = V(\mathbf{q})$ and $n(-\mathbf{q}) = n^\dagger(\mathbf{q})$. $\mathbf{q}$ represents the momentum transferred. The ratio R can be re-written as

$$R(\mathbf{q}, \omega) = 2\pi|V(\mathbf{q})|^2 \sum_n |\langle n| n^\dagger(\mathbf{q}) |0\rangle|^2 \delta(\omega + \omega_{n0}) = 2\pi|V(\mathbf{q})|^2 S(\mathbf{q}, \omega) \tag{I.7}$$

where $S(\mathbf{q}, \omega) = \sum_n |\langle n| n^\dagger(\mathbf{q}) |0\rangle|^2 \delta(\omega + \omega_{n0})$ is the dynamical structure factor. If we introduced the Coulomb interaction $V(\mathbf{r} - \mathbf{r}_i) = \frac{1}{|\mathbf{r} - \mathbf{r}_i|}$ we find

$$R(\mathbf{q}, \omega) = 2\pi |V(\mathbf{q})|^2 \sum_n |\langle n| n^\dagger(\mathbf{q}) |0\rangle|^2 \delta(\omega + \omega_{n0}) = 32\pi^3 \frac{1}{q^4} S(\mathbf{q}, \omega) \qquad \text{(I.8)}$$

with $V(\mathbf{q}) = 4\pi/q^2$. Using the inverse procedure used in appendix A we can correlate the dynamical structure factor with the density-density correlation function

$$S(\mathbf{q}, \omega) = \sum_n \langle 0| n(\mathbf{q}) |n\rangle \langle n| n^\dagger(\mathbf{q}) |0\rangle \delta(\omega + \omega_{n0}) \qquad \text{(I.9)}$$

$$= \frac{1}{2\pi} \int \langle 0| n(\mathbf{q}, t) n^\dagger(\mathbf{q}, 0) |0\rangle e^{-i\omega t} \mathrm{d}t \qquad \text{(I.10)}$$

where

$$S(\mathbf{q}, t) = \langle 0| n(\mathbf{q}, t) n^\dagger(\mathbf{q}, 0) |0\rangle = \langle 0| \sum_i e^{-i\mathbf{q} \cdot \mathbf{r}_i(t)} \sum_j e^{i\mathbf{q} \cdot \mathbf{r}_j(0)} |0\rangle \qquad \text{(I.11)}$$

$$= \langle 0| \sum_{i,j} e^{-i\mathbf{q} \cdot (\mathbf{r}_i(t) - \mathbf{r}_j(0))} |0\rangle \qquad \text{(I.12)}$$

J | Derivation of Casida's Equation

From Petersilka-Gossmann-Gross[16] equation we can write

$$\chi = \chi_0 + \chi_0 K \chi \tag{J.1}$$

and

$$\frac{\delta n}{\delta V_{ext}} = \frac{\delta n}{\delta V_0} + \frac{\delta n}{\delta V_0} K \frac{\delta n}{\delta V_{ext}} , \tag{J.2}$$

where the Kernel $K = \delta V_{ext}/\delta n$. Let us express the $\chi_0(\mathbf{r}, \mathbf{r}', \omega)$ in the e-h basis

$$\chi_0(\mathbf{r}, \mathbf{r}', \omega) = \sum_{nm, n'm'} \chi_0^{nm, n'm'}(\omega) \psi_n(\mathbf{r}) \psi_m(\mathbf{r}) \psi_{n'}(\mathbf{r}') \psi_{m'}(\mathbf{r}') , \tag{J.3}$$

where

$$\chi_0^{nm, n'm'} = \delta_{nn'} \delta_{mm'} \left[\frac{f_n - f_m}{\omega - (E_n - E_m)} \right] \tag{J.4}$$

and

$$\chi_0^{nm, n'm'} = \left[\frac{f_n - f_m}{\omega - (E_m - E_n)} - \frac{f_n - f_m}{\omega + (E_m - E_n)} \right] . \tag{J.5}$$

At this points we can write the density as

$$\delta n(\mathbf{r}, \omega) = \sum_{ij} \psi_i \psi_j \delta n_{ij}(\omega) , \tag{J.6}$$

$$\delta n_{ij}(\omega) = \left[\frac{f_i - f_j}{\omega - (E_j - E_i)} - \frac{f_i - f_j}{\omega + (E_j - E_i)} \right] K^{ijkl} \delta n_{kl}(\omega) , \tag{J.7}$$

$$\delta n_{ij}(\omega) = \frac{(f_i - f_j)[(E_j - E_i) + \omega] - (f_i - f_j)[\omega - (E_j - E_i)]}{\omega^2 + (E_j - E_i)^2} K^{ijkl} \delta n_{kl}(\omega) , \tag{J.8}$$

$$\delta n_{ij}(\omega) = \frac{(E_j - E_i)(f_i - f_j) + (E_j - E_i)(f_i - f_j)}{\omega^2 - (E_j - E_i)^2} K^{ijkl} \delta n_{kl}(\omega) \, , \qquad \text{(J.9)}$$

$$[\omega^2 - (E_j - E_i)^2] \delta n_{ij}(\omega) = 2(E_j - E_i)(f_i - f_j) K^{ijkl} \delta n_{kl}(\omega) \, . \qquad \text{(J.10)}$$

If $j > i$ the $E_j - E_i > 0$ and $f_i - f_j > 0$. Finally we can rearrange J.10 and to obtain the so-called Casida's equation[64]

$$\left[(E_j - E_i)^2 \delta_{ik} \delta_{jl}(\omega) - 2(E_j - E_i)(f_i - f_j) K^{ijkl} \right] \delta n_{kl}(\omega) = \omega^2 \delta n_{ij}(\omega) \, . \qquad \text{(J.11)}$$

K | SIESTA Input File

In Fig. K.1 and Fig. K.2 I show an example of a SIESTA input file for a finite and a periodic system, respectively. In Fig. K.1 the first two lines contain the name of the system and its nickname used to name the output files, respectively. Afterwards, the number of atoms (*NumberOfAtoms*) and the number of atomic species (*NumberOfSpecies*) in the system are specified. The parameter *PAO.EnergyShift* (PseudoAtomic Orbital Energy Shift) definea the orbital spatial extension. This specifies the shift of the energy of the orbitals due to the confinement to a finite-range The default value is 272 meV. An energyshift of 100 meV as the one indicated in Fig.K.1 generates more extended orbitals. *PAO.BasisSet* is used to choose the basis set multiplicity. The defines the number of Pseudo-Atomic Orbitals (PAO) for the atomic species involved in the calculation. In this example the minimum basis set Single-ζ (SZ) is chosen. More details about *PAO.EnergyShift* and *PAO.BasisSet* are found in Sections 2.2.2 and 2.2.3. Furthermore, in Chapter 3 a convergence study with respect to PAO.BasisSet and PAO.EnergyShift is shown for graphene flakes. The *MeshCutOff* is an energy value that defines the fineness of the 3D real space grid. The default value is 100 Ry = 50 Hartree and corresponds to a distance between points of 0.628 bohr = 0.332 Å. A wave function $\psi(\mathbf{r})$ in a 3D real-space grid that can be seen as given by a combination of plane waves $C(\mathbf{q})$, $\psi(\mathbf{r}) = \sum_{q_{cutoff}} C(\mathbf{q})e^{i\mathbf{r}\cdot\mathbf{q}}$. The q_{cutoff} determines the fineness of the 3D real-space grid through the relation $\Delta\mathbf{r} = 2\pi/q_{cutoff}$. For a plane wave $q_{cutoff} = \sqrt{2E_{cutoff}}$. *XC.functional* and *XC.authors* define the approximation for the Exchange-Correlation (XC) functional. The next group of parameters determines the conditions to reach convergence in the Self-Consistent Field (ΔSCF) cycle. *MD.TypeOfRun*, *MD.NumCGsteps* and *UseSaveData* together with the *GeometryConstraints* block define the geometry optimization procedure. In particular, with the *GeometryConstraints* block is possible to fix the position of any atom in any of the three directions. In the block *ChemicalSpeciesLabel* the species and the labels for each specie are indicated. Finally, the *AtomicCoordinatesAndAtomicSpecies* block contains the geometry of the system. The flag *AtomicCoordinatesFormat* specifies the units for the positions of the atoms. The logical flag *COOP.Write* if set to ".true." enables the generation of the *SystemLabel.fullBZ.WFSX* and *SystemLabel.HSX*. These files are necessary to generate COOP/COHP curves, (projected) densities of states, etc., with the utility Util/COOP/mprop. *WriteDenchar* is used to generate *SystemLabel.PLD* and *SystemLabel.DIM*. Those files are needed to run the Denchar utility which generate 2D and 3D valence charge densities and/or wavefunctions in real space. *WFS.Band.min* and *WFS.Band.max* define the lowest and highest orbital index of the wavefunction to be

written in $SystemLabel.bands.WFSX$.

The input file shown in Fig. K.2 is for calculating the ground-state properties and band structure of a graphene sheet. In the input file for a periodic-system we need to define the periodic lattice, thus, we have to specify the lattice constant ($LatticeConstant$) and the block $LatticeVectors$ that contains the three lattice vectors in units of the lattice constant. The logical flag $WriteBands$, if sets to ".true.", writes the electronic bands of the system, i.e. the eigenenergies as a function of the $\mathbf{k}$ vector. $BandLinesScale$ specifies the way the coordinates for the k vectors are given, if sets to pi/a the Cartesian coordinates are given in units of π/a, where a is the lattice constant. The alternative option is $ReciprocalLatticeVectors$, in this case the coordinates for the $\mathbf{k}$ vectors are given in reciprocal-lattice-vector coordinates. $SolutionMethod$ defines the method to solve of the Kohn-Sham Hamiltonian. The next block called $kgrid\_Monkhorst\_Pack$ contains the information about the real-space supercell. The reciprocal unit cell is defined by the real-space supercell and defines the k-sampling grid. The fourth column contains the grid displacement for each grid coordinate. Finally, the $Bandlines$ block defines the number of points and the directions in k-space along which the energy bands are calculated.

```
SystemName                    Na10_chain
SystemLabel                   Na10_chain
NumberOfAtoms                 10
NumberOfSpecies               1

PAO.EnergyShift               100 meV
PAO.BasisSize                 SZ
MeshCutOff                    100 Ry

XC.functional      GGA
XC.authors         PBE

DM.Tolerance                  1e-5
DM.MixingWeight               0.08
MaxSCFIterations              150
DM.NumberPulay                4

MD.TypeOfRun CG
MD.NumCGsteps 200
UseSaveData true

%block GeometryConstraints
  position from 1 to 5   0.0  0.0  1.0
  position from 1 to 5   1.0  0.0  0.0
%endblock GeometryConstraints

%block ChemicalSpeciesLabel
1  11  Na      # Species index, atomic number, species label
%endblock ChemicalSpeciesLabel

AtomicCoordinatesFormat   Ang
%block AtomicCoordinatesAndAtomicSpecies
    0.00000000   0.000000000    0.00000000   1
    0.00000000  -3.20000000     0.00000000   1
    0.00000000   3.20000000     0.00000000   1
    0.00000000  -6.40000000     0.00000000   1
    0.00000000   6.40000000     0.00000000   1
    0.00000000  -9.60000000     0.00000000   1
    0.00000000   9.60000000     0.00000000   1
    0.00000000 -12.80000000     0.00000000   1
    0.00000000  12.80000000     0.00000000   1
    0.00000000 -16.00000000     0.00000000   1
%endblock AtomicCoordinatesAndAtomicSpecies

### Exports .WFSX, .HSX
COOP.Write                .true.
### Exports .DIM and .PLD files
WriteDenchar              .true.
### WFS.Band.Min    10
### WFS.Band.Max    11
```

Figure K.1: SIESTA .fdf format input file for a linear "molecule" composed of 10 Na atoms.

```
SystemName          graphene
SystemLabel         graphene
NumberOfAtoms       2
NumberOfSpecies     1

PAO.EnergyShift         50 meV

DM.Tolerance    1e-5
DM.MixingWeight         0.10
MaxSCFIterations        150

%block ChemicalSpeciesLabel
 1  6  C      # Species index, atomic number, species label
%endblock ChemicalSpeciesLabel

LatticeConstant        2.4595 Ang

%block LatticeVectors
  0.8660    0.5    0.0
  0.8660   -0.5    0.0
  0.0       0.0   10.0
%endblock LatticeVectors


WriteBands          true
BandLinesScale      pi/a
SolutionMethod      diagon

%block kgrid_Monkhorst_Pack
  10   0   0    0.5
   0  10   0    0.5
   0   0   1    0.5
%endblock kgrid_Monkhorst_Pack

%block BandLines
1   1.1547     0.6666    0.000    K
30  0.0        0.000     0.000    \Gamma
30  1.1547     0.000     0.000    M
30  1.1547     0.6666    0.000    K
%endblock BandLines

AtomicCoordinatesFormat  Ang
%block AtomicCoordinatesAndAtomicSpecies
    -1.420      0.000      0.000      1
     0.000      0.000      0.000      1
%endblock AtomicCoordinatesAndAtomicSpecies


### Exports .WFSX, .HSX
COOP.Write              .true.
```

Figure K.2: SIESTA .fdf format input file for the graphene periodic system.

Bibliography

[1] W. Kohn. "Nobel lecture: Electronic structure of matter—wave functions and density functionals". *Rev. Mod. Phys.*, 71:1253–1266 (1999). doi:10.1103/RevModPhys.71.1253. URL http://link.aps.org/doi/10.1103/RevModPhys.71.1253.

[2] J. Peng, et al. "Graphene quantum dots derived from carbon fibers". *Nano Letters*, 12(2):844–849 (2012). doi:10.1021/nl2038979. URL http://pubs.acs.org/doi/abs/10.1021/nl2038979.

[3] F. Wen, et al. "Charge transfer plasmons: Optical frequency conductances and tunable infrared resonances". *ACS Nano*, 9(6):6428–6435 (2015). doi:10.1021/acsnano.5b02087. URL http://dx.doi.org/10.1021/acsnano.5b02087. PMID: 25986388.

[4] P. J. Schuck, et al. "Improving the mismatch between light and nanoscale objects with gold bowtie nanoantennas". *Phys. Rev. Lett.*, 94:017402 (2005). doi:10.1103/PhysRevLett.94.017402. URL http://link.aps.org/doi/10.1103/PhysRevLett.94.017402.

[5] P. Mühlschlegel, et al. "Resonant optical antennas". *Science*, 308(5728):1607–1609 (2005).

[6] J. M. Soler, et al. "The siesta method for ab initio order-n materials simulation". *J. Phys.: Condens. Matter*, 14:2745–2779 (2002).

[7] D. Sánchez-Portal, et al. "Density-functional method for very large systems with lcao basis sets". *Int. J. of Quantum Chem.*, 65:453–461 (1997).

[8] J. J. Mortensen, L. B. Hansen, and K. W. Jacobsen. "Real-space grid implementation of the projector augmented wave method". *Phys. Rev. B*, 71:035109 (2005). doi:10.1103/PhysRevB.71.035109. URL http://link.aps.org/doi/10.1103/PhysRevB.71.035109.

[9] S. R. Bahn and K. W. Jacobsen. "An object-oriented scripting interface to a legacy electronic structure code". *Comput. Sci. Eng.*, 4(3):56–66 (2002). ISSN 1521-9615. doi:10.1109/5992.998641.

[10] M. Valiev, et al. "Nwchem: A comprehensive and scalable open-source solution for large scale molecular simulations". *Computer Physics Communications*,

181(9):1477 – 1489 (2010). ISSN 0010-4655. doi:http://dx.doi.org/10.1016/j.cpc.2010.04.018. URL http://www.sciencedirect.com/science/article/pii/S0010465510001438.

[11] X. Gonze, et al. "Abinit: First-principles approach to material and nanosystem properties". *Computer Physics Communications*, 180(12):2582 – 2615 (2009). ISSN 0010-4655. doi:http://dx.doi.org/10.1016/j.cpc.2009.07.007. URL http://www.sciencedirect.com/science/article/pii/S0010465509002276. 40 {YEARS} {OF} CPC: A celebratory issue focused on quality software for high performance, grid and novel computing architectures.

[12] URL http://undsci.berkeley.edu/article/0_0_0/howscienceworks_02.

[13] L. H. Thomas. "The calculation of atomic fields". *Proc. Cambridge Phil. Soc.*, 23(5):542–548 (1927).

[14] E. Fermi. "Un metodo statistico per la determinazione di alcune prioprietà dell'atomo". *Rend. Accad. Naz. Lincei.*, 6:602–607 (1927).

[15] E. Runge and E. K. U. Gross. "Density-functional theory for time-dependent systems". *Phys. Rev. Lett.*, 52:997–1000 (1984). doi:10.1103/PhysRevLett.52.997. URL http://link.aps.org/doi/10.1103/PhysRevLett.52.997.

[16] M. Petersilka, U. J. Gossmann, and E. K. U. Gross. "Excitation energies from time-dependent density-functional theory". *Phys. Rev. Lett.*, 76:1212–1215 (1996). doi:10.1103/PhysRevLett.76.1212. URL http://link.aps.org/doi/10.1103/PhysRevLett.76.1212.

[17] P. Koval, D. Foerster, and O. Coulaud. "A parallel iterative method for computing molecular absorption spectra". *Journal of Chemical Theory and Computation*, 6(9):2654–2668 (2010). doi:10.1021/ct100280x. URL http://dx.doi.org/10.1021/ct100280x. PMID: 26616067.

[18] D. Foerster, P. Koval, and D. Sánchez-Portal. "An $o(n^3)$ implementation of hedin's gw approximation for molecules". *The Journal of Chemical Physics*, 135:074105 (2011).

[19] URL http://mbpt-domiprod.wikidot.com.

[20] P. Koval, et al. "Optical response of silver clusters and their hollow shells from linear-response tddft". *Journal of Physics: Condensed Matter*, 28(21):214001 (2016). URL http://stacks.iop.org/0953-8984/28/i=21/a=214001.

[21] P. Koval, D. Foerster, and D. Sánchez-Portal. "Fully self-consistent gw and quasiparticle self-consistent gw for molecules". *Phys. Rev. B*, 89:155417 (2014). doi:10.1103/PhysRevB.89.155417. URL http://link.aps.org/doi/10.1103/PhysRevB.89.155417.

[22] M. P. Ljungberg, et al. "Cubic-scaling iterative solution of the bethe-salpeter equation for finite systems". *Phys. Rev. B*, 92:075422 (2015). doi:10.1103/PhysRevB.92.075422. URL http://link.aps.org/doi/10.1103/PhysRevB.92.075422.

[23] K. S. Novoselov, et al. "Electric field effect in atomically thin carbon films". *Science*, 306(5696):666–669 (2004). doi:10.1126/science.1102896. URL `http://www.sciencemag.org/content/306/5696/666.abstract`.

[24] K. S. Novoselov, et al. "Two-dimensional atomic crystals". *Proceedings of the National Academy of Sciences of the United States of America*, 102(30):10451–10453 (2005). doi:10.1073/pnas.0502848102. URL `http://www.pnas.org/content/102/30/10451.abstract`.

[25] K. Bolotin, et al. "Ultrahigh electron mobility in suspended graphene". *Solid State Communications*, 146(9–10):351 – 355 (2008). ISSN 0038-1098. doi:http://dx.doi.org/10.1016/j.ssc.2008.02.024. URL `http://www.sciencedirect.com/science/article/pii/S0038109808001178`.

[26] S. Bernadotte, F. Evers, and C. R. Jacob. "Plasmons in molecules". *The Journal of Physical Chemistry C*, 117(4):1863–1878 (2013). doi:10.1021/jp3113073. URL `http://dx.doi.org/10.1021/jp3113073`.

[27] L. Bursi, et al. "Quantifying the plasmonic character of optical excitations in nanostructures". *ACS Photonics*, 3(4):520–525 (2016). doi:10.1021/acsphotonics.5b00688. URL `http://dx.doi.org/10.1021/acsphotonics.5b00688`.

[28] D. Casanova, J. M. Matxain, and J. M. Ugalde. "Plasmonic resonances in the al13–cluster: Quantification and origin of exciton collectivity". *The Journal of Physical Chemistry C*, 120(23):12742–12750 (2016). doi:10.1021/acs.jpcc.6b03210. URL `http://dx.doi.org/10.1021/acs.jpcc.6b03210`.

[29] M. Pelton, J. Aizpurua, and G. Bryant. "Metal-nanoparticle plasmonics". *Laser & Photonics Reviews*, 2(3):136–159 (2008). ISSN 1863-8899. doi:10.1002/lpor.200810003. URL `http://dx.doi.org/10.1002/lpor.200810003`.

[30] I. Romero, et al. "Plasmons in nearly touching metallic nanoparticles: singular response in the limit of touching dimers". *Opt. Express*, 14(21):9988–9999 (2006). doi:10.1364/OE.14.009988. URL `http://www.opticsexpress.org/abstract.cfm?URI=oe-14-21-9988`.

[31] E. Townsend and G. W. Bryant. "Plasmonic properties of metallic nanoparticles: The effects of size quantization". *Nano Letters*, 12(1):429–434 (2012). doi:10.1021/nl2037613. URL `http://dx.doi.org/10.1021/nl2037613`. PMID: 22181554.

[32] F. Furche. "On the density matrix based approach to time-dependent density functional response theory". *The Journal of Chemical Physics*, 114(14):5982–5992 (2001). doi:http://dx.doi.org/10.1063/1.1353585. URL `http://scitation.aip.org/content/aip/journal/jcp/114/14/10.1063/1.1353585`.

[33] Y. Li and C. Ullrich. "Time-dependent transition density matrix". *Chemical Physics*, 391(1):157 – 163 (2011). ISSN 0301-0104. doi:http://dx.doi.org/10.1016/j.chemphys.2011.02.001. URL `http://www.sciencedirect.com/science/article/pii/S0301010411000358`. Open problems and new solutions in time dependent density functional theory.

[34] M. Born and J. R. Oppenheimer. "On the quantum theory of molecules". *Ann. Physik*, 84(458) (1927).

[35] P. Hohenberg and W. Kohn. "Inhomogeneous electron gas". *Phys. Rev.*, 136:B864–B871 (1964). doi:$10.1103/\mathrm{PhysRev}.136.\mathrm{B}864$. URL http://link.aps.org/doi/10.1103/PhysRev.136.B864.

[36] W. Pauli. "Nobel lecture: Exclusion principle and quantum mechanics". *Nobelprize.org Nobel Media AB 2014. Web. 29 Nov 2016*. URL http://www.nobelprize.org/nobel_prizes/physics/laureates/1945/pauli-lecture.html.

[37] T. Tsuneda. *Density Functional Theory in Quantum Chemistry*. Springer Japan (2014).

[38] E. Fermi. "On quantizing an ideal monatomic gas". *Z. Phys.*, 36(902) (1926).

[39] E. Fermi. "Statistical method to determine some properties of atoms". *Rendiconti Lincei*, 6:602–607 (1927).

[40] R. G. Parr. *Density Functional Theory of Atoms and Molecules*. Springer Netherlands (1989).

[41] M. Levy. "Universal variational functionals of electron densities, first-order density matrices, and natural spin-orbitals and solution of the v-representability problem". *Proceedings of the National Academy of Sciences*, 76(12):6062–6065 (1979). URL http://www.pnas.org/content/76/12/6062.abstract.

[42] M. Levy. "Electron densities in search of hamiltonians". *Phys. Rev. A*, 26:1200–1208 (1982). doi:$10.1103/\mathrm{PhysRevA}.26.1200$. URL http://link.aps.org/doi/10.1103/PhysRevA.26.1200.

[43] Y. A. Wang, N. Govind, and E. A. Carter. "Orbital-free kinetic-energy density functionals with a density-dependent kernel". *Phys. Rev. B*, 60:16350–16358 (1999). doi:$10.1103/\mathrm{PhysRevB}.60.16350$. URL http://link.aps.org/doi/10.1103/PhysRevB.60.16350.

[44] H. Levämäki, et al. "Alternative to the kohn-sham equations: The pauli potential differential equation". *Phys. Rev. A*, 92:062502 (2015). doi:$10.1103/\mathrm{PhysRevA}.92.062502$. URL http://link.aps.org/doi/10.1103/PhysRevA.92.062502.

[45] L. Novotny and B. Hecht. *Principles of Nano-Optics*. Cambridge University Press (2006). ISBN 9780511813535. URL http://dx.doi.org/10.1017/CBO9780511813535. Cambridge Books Online.

[46] M. A. L. Marques, et al. *Time-Dependent Density Functional Theory*, volume Lecture Notes in Physics 706. Springer-Verlag Berlin Heidelberg (2006).

[47] P. Fulde. *Electron Correlations in Molecules and Solids*, volume 100. Springer Berlin Heidelberg (1995).

[48] J. P. Perdew and A. Zunger. "Self-interaction correction to density-functional approximations for many-electron systems". *Phys. Rev. B*, 23:5048–5079 (1981). doi:10.1103/PhysRevB.23.5048. URL http://link.aps.org/doi/10.1103/PhysRevB.23.5048.

[49] J. P. Perdew and Y. Wang. "Accurate and simple analytic representation of the electron-gas correlation energy". *Phys. Rev. B*, 45:13244–13249 (1992). doi:10.1103/PhysRevB.45.13244. URL http://link.aps.org/doi/10.1103/PhysRevB.45.13244.

[50] J. P. Perdew, K. Burke, and M. Ernzerhof. "Generalized gradient approximation made simple". *Phys. Rev. Lett.*, 77:3865–3868 (1996). doi:10.1103/PhysRevLett.77.3865. URL http://link.aps.org/doi/10.1103/PhysRevLett.77.3865.

[51] Y. Zhang and W. Yang. "Comment on "generalized gradient approximation made simple"". *Phys. Rev. Lett.*, 80:890–890 (1998). doi:10.1103/PhysRevLett.80.890. URL http://link.aps.org/doi/10.1103/PhysRevLett.80.890.

[52] Z. Wu and R. E. Cohen. "More accurate generalized gradient approximation for solids". *Phys. Rev. B*, 73:235116 (2006). doi:10.1103/PhysRevB.73.235116. URL http://link.aps.org/doi/10.1103/PhysRevB.73.235116.

[53] B. Hammer, L. B. Hansen, and J. K. Nørskov. "Improved adsorption energetics within density-functional theory using revised perdew-burke-ernzerhof functionals". *Phys. Rev. B*, 59:7413–7421 (1999). doi:10.1103/PhysRevB.59.7413. URL http://link.aps.org/doi/10.1103/PhysRevB.59.7413.

[54] J. P. Perdew, et al. "Restoring the density-gradient expansion for exchange in solids and surfaces". *Phys. Rev. Lett.*, 100:136406 (2008). doi:10.1103/PhysRevLett.100.136406. URL http://link.aps.org/doi/10.1103/PhysRevLett.100.136406.

[55] J. A. White and D. M. Bird. "Implementation of gradient-corrected exchange-correlation potentials in car-parrinello total-energy calculations". *Phys. Rev. B*, 50:4954–4957 (1994). doi:10.1103/PhysRevB.50.4954. URL http://link.aps.org/doi/10.1103/PhysRevB.50.4954.

[56] D. Bylander and L. Kleinman. "White and bird's formulation of gradient-corrected exchange-correlation potentials applied to atoms". *Journal of Computational Physics*, 136(2):599 – 602 (1997). ISSN 0021-9991. doi:http://dx.doi.org/10.1006/jcph.1997.5784. URL http://www.sciencedirect.com/science/article/pii/S0021999197957843.

[57] L. C. Balbás, J. L. Martins, and J. M. Soler. "Evaluation of exchange-correlation energy, potential, and stress". *Phys. Rev. B*, 64:165110 (2001). doi:10.1103/PhysRevB.64.165110. URL http://link.aps.org/doi/10.1103/PhysRevB.64.165110.

[58] A. Gaiduk. *Theory of Model Kohn-Sham Potentials and its Applications*. Ph.D. thesis, The University of Western Ontario (2013).

[59] C. V. Caillie and R. D. Amos. "Geometric derivatives of density functional theory excitation energies using gradient-corrected functionals". *Chemical Physics Letters*, 317(1–2):159 – 164 (2000). ISSN 0009-2614. doi:http://dx.doi.org/10.1016/S0009-2614(99)01346-9. URL `http://www.sciencedirect.com/science/article/pii/S0009261499013469`.

[60] G. Malloci, et al. "Electronic and optical properties of families of polycyclic aromatic hydrocarbons: A systematic (time-dependent) density functional theory study". *Chemical Physics*, 384(1–3):19 – 27 (2011). ISSN 0301-0104. doi:http://dx.doi.org/10.1016/j.chemphys.2011.04.013. URL `http://www.sciencedirect.com/science/article/pii/S0301010411001327`.

[61] G. Onida, L. Reining, and A. Rubio. "Electronic excitations: density-functional versus many-body green's-function approaches". *Rev. Mod. Phys.*, 74:601–659 (2002). doi:10.1103/RevModPhys.74.601. URL `http://link.aps.org/doi/10.1103/RevModPhys.74.601`.

[62] K. V. I. *Equations of Mathematical Physics*. Marcel Dekker (1971).

[63] B. Bransden and C. Joachain. *Physics of Atoms and Molecules*. Pearson Education. Prentice Hall (2003). ISBN 9780582356924. URL `https://books.google.es/books?id=ST_DwIGZeTQC`.

[64] M. E. Casida. *Recent Advances in Density Functional Theory*. D. P. Chong (World Scientific, Singapore) (1995).

[65] A. Sakko, et al. "Time-dependent density functional approach for the calculation of inelastic x-ray scattering spectra of molecules". *The Journal of Chemical Physics*, 133(17):174111 (2010). doi:http://dx.doi.org/10.1063/1.3503594. URL `http://scitation.aip.org/content/aip/journal/jcp/133/17/10.1063/1.3503594`.

[66] L. Van Hove. "Correlations in space and time and born approximation scattering in systems of interacting particles". *Phys. Rev.*, 95:249–262 (1954). doi:10.1103/PhysRev.95.249. URL `http://link.aps.org/doi/10.1103/PhysRev.95.249`.

[67] C. Kittel. *Quantum theory of solids*. Wiley (1963). URL `https://books.google.es/books?id=zgBRAAAAMAAJ`.

[68] P. Nozieres and D. Pines. *Theory Of Quantum Liquids*. Advanced Books Classics Series. Westview Press (1999). ISBN 9780813346533. URL `https://books.google.es/books?id=q3wCwaV-gmUC`.

[69] D. T. Haar. "Foundations of statistical mechanics". *Rev. Mod. Phys.*, 27:289–338 (1955). doi:10.1103/RevModPhys.27.289. URL `http://link.aps.org/doi/10.1103/RevModPhys.27.289`.

[70] O. F. Sankey and D. J. Niklewski. "Ab initio multicenter tight-binding model for molecular-dynamics simulations and other applications in covalent systems". *Phys. Rev. B*, 40:3979–3995 (1989). doi:10.1103/PhysRevB.40.3979. URL `https://link.aps.org/doi/10.1103/PhysRevB.40.3979`.

[71] URL `http://departments.icmab.es/leem/siesta/`.

[72] URL `https://launchpad.net/siesta`.

[73] URL `http://departments.icmab.es/leem/siesta/Documentation/Manuals/manuals.html`.

[74] E. Artacho, et al. "The siesta method; developments and applicability". *Journal of Physics: Condensed Matter*, 20(6):064208 (2008). URL `http://stacks.iop.org/0953-8984/20/i=6/a=064208`.

[75] R. Bauernschmitt, et al. "Calculation of excitation energies within time-dependent density functional theory using auxiliary basis set expansions". *Chemical Physics Letters*, 264(6):573 – 578 (1997). ISSN 0009-2614. doi:http://dx.doi.org/10.1016/S0009-2614(96)01343-7. URL `http://www.sciencedirect.com/science/article/pii/S0009261496013437`.

[76] S. Hamel, M. E. Casida, and D. R. Salahub. "Assessment of the quality of orbital energies in resolution-of-the-identity hartree–fock calculations using demon auxiliary basis sets". *The Journal of Chemical Physics*, 114(17):7342–7350 (2001). doi:http://dx.doi.org/10.1063/1.1358865. URL `http://scitation.aip.org/content/aip/journal/jcp/114/17/10.1063/1.1358865`.

[77] G. te Velde, et al. "Chemistry with adf". *Journal of Computational Chemistry*, 22(9):931–967 (2001). ISSN 1096-987X. doi:10.1002/jcc.1056. URL `http://dx.doi.org/10.1002/jcc.1056`.

[78] X. Blase and P. Ordejón. "Dynamical screening and absorption within a strictly localized basis implementation of time-dependent lda: From small clusters and molecules to aza-fullerenes". *Phys. Rev. B*, 69:085111 (2004). doi:10.1103/PhysRevB.69.085111. URL `http://link.aps.org/doi/10.1103/PhysRevB.69.085111`.

[79] D. Foerster. "Elimination, in electronic structure calculations, of redundant orbital products". *The Journal of Chemical Physics*, 128(3):034108 (2008). doi:http://dx.doi.org/10.1063/1.2821021. URL `http://scitation.aip.org/content/aip/journal/jcp/128/3/10.1063/1.2821021`.

[80] D. Foerster and P. Koval. "On the kohn–sham density response in a localized basis set". *J. Chem. Phys.*, 131:044103 (2009).

[81] P. Koval, D. Foerster, and O. Coulaud. "Fast construction of the kohn–sham response function for molecules". *physica status solidi (b)*, 247(8):1841–1848 (2010). ISSN 1521-3951. doi:10.1002/pssb.200983811. URL `http://dx.doi.org/10.1002/pssb.200983811`.

[82] X. Ren, et al. "Resolution-of-identity approach to hartree–fock, hybrid density functionals, rpa, mp2 and gw with numeric atom-centered orbital basis functions". *New Journal of Physics*, 14(5):053020 (2012). URL `http://stacks.iop.org/1367-2630/14/i=5/a=053020`.

[83] Y. Saad. *Iterative methods for sparse linear systems*. SIAM: Philadelphia, PA: 2000.

[84] V. Frayssé, et al. "Algorithm 842: A set of gmres routines for real and complex arithmetics on high performance computers". *ACM Trans. Math. Softw.*, 31(2):228–238 (2005). ISSN 0098-3500. doi:10.1145/1067967.1067970. URL `http://doi.acm.org/10.1145/1067967.1067970`.

[85] I. C. F. Ipsen and D. C. Meyer. "The idea behind krylov methods". 105(10):889–899 (1998).

[86] M. A. Marques, M. J. Oliveira, and T. Burnus. "Libxc: A library of exchange and correlation functionals for density functional theory". *Computer Physics Communications*, 183(10):2272 – 2281 (2012). ISSN 0010-4655. doi:http://dx.doi.org/10.1016/j.cpc.2012.05.007. URL `http://www.sciencedirect.com/science/article/pii/S0010465512001750`.

[87] A. K. Geim. "Graphene: Status and prospects". *Science*, 324(5934):1530–1534 (2009). doi:10.1126/science.1158877. URL `http://www.sciencemag.org/content/324/5934/1530.abstract`.

[88] R. R. Nair, et al. "Fine structure constant defines visual transparency of graphene". *Science*, 320(5881):1308–1308 (2008). ISSN 0036-8075. doi:10.1126/science.1156965. URL `http://science.sciencemag.org/content/320/5881/1308`.

[89] A. A. Balandin, et al. "Superior thermal conductivity of single-layer graphene". *Nano Letters*, 8(3):902–907 (2008). doi:10.1021/nl0731872. URL `http://dx.doi.org/10.1021/nl0731872`. PMID: 18284217.

[90] A. N. Grigorenko, M. Polini, and K. S. Novoselov. "Graphene plasmonics". *Nature Photon.*, 6:749–758 (2012). doi:10.1038/nphoton.2012.262. URL `http://www.nature.com/nphoton/journal/v6/n11/full/nphoton.2012.262.html`.

[91] K. S. Novoselov, et al. "A roadmap for graphene". *Nature*, 490(7419):192–200 (2012). URL `http://dx.doi.org/10.1038/nature11458`.

[92] G.-P. Guo, et al. "Quantum computation with graphene nanoribbon". *New Journal of Physics*, 11:123005 (2009).

[93] P. R. Wallace. "The band theory of graphite". *Phys. Rev.*, 71:622–634 (1947). doi:10.1103/PhysRev.71.622. URL `http://link.aps.org/doi/10.1103/PhysRev.71.622`.

[94] I. Snook and A. Barnard. *Graphene Nano-Flakes and Nano-Dots: Theory, Experiment and Applications*. Dr. Sergey Mikhailov (Ed.) InTech (2011). ISBN 978-953-307-152-7. doi:10.5772/15541. URL `http://www.intechopen.com/books/physics-and-applications-of-graphene-theory/graphene-nano-flakes-and-nano-dots-theory-experiment-and-applications`.

[95] A. H. Castro Neto, et al. "The electronic properties of graphene". *Rev. Mod. Phys.*, 81:109–162 (2009). doi:10.1103/RevModPhys.81.109. URL `http://link.aps.org/doi/10.1103/RevModPhys.81.109`.

[96] K. S. Novoselov, et al. "Two-dimensional gas of massless dirac fermions in graphene". *Nature*, 438:197–200 (2005).

[97] L. Ci, et al. "Controlled nanocutting of graphene". *Nano Research*, 1:116–122 (2008). ISSN 1998-0124. doi:10.1007/s12274-008-8020-9. URL http://dx.doi.org/10.1007/s12274-008-8020-9.

[98] S. Dutta and S. K. Pati. "Novel properties of graphene nanoribbons: a review". *J. Mater. Chem.*, 20:8207–8223 (2010). doi:10.1039/C0JM00261E. URL http://dx.doi.org/10.1039/C0JM00261E.

[99] C. Berger, et al. "Electronic confinement and coherence in patterned epitaxial graphene". *Science*, 312(5777):1191–1196 (2006). doi:10.1126/science.1125925. URL http://www.sciencemag.org/content/312/5777/1191.abstract.

[100] X. Li, et al. "Chemically derived, ultrasmooth graphene nanoribbon semiconductors". *Science*, 319(5867):1229–1232 (2008). doi:10.1126/science.1150878. URL http://www.sciencemag.org/content/319/5867/1229.abstract.

[101] P. Ruffieux, et al. "On-surface synthesis of graphene nanoribbons with zigzag edge topology". *Nature*, 531(7595):489–492 (2016). URL http://dx.doi.org/10.1038/nature17151.

[102] X. Jia, et al. "Controlled formation of sharp zigzag and armchair edges in graphitic nanoribbons". *Science*, 323(5922):1701–1705 (2009). doi:10.1126/science.1166862. URL http://www.sciencemag.org/content/323/5922/1701.abstract.

[103] Y. Zhu, A. L. Higginbotham, and J. M. Tour. "Covalent functionalization of surfactant-wrapped graphene nanoribbons". *Chemistry of Materials*, 21(21):5284–5291 (2009). doi:10.1021/cm902939n. URL http://pubs.acs.org/doi/abs/10.1021/cm902939n.

[104] X. Geng, et al. "Aqueous-processable noncovalent chemically converted graphene–quantum dot composites for flexible and transparent optoelectronic films". *Advanced Materials*, 22(5):638–642 (2010). ISSN 1521-4095. doi:10.1002/adma.200902871. URL http://dx.doi.org/10.1002/adma.200902871.

[105] N. G. Shang, et al. "Controllable selective exfoliation of high-quality graphene nanosheets and nanodots by ionic liquid assisted grinding". *Chem. Commun.*, 48:1877–1879 (2012). doi:10.1039/C2CC17185F. URL http://dx.doi.org/10.1039/C2CC17185F.

[106] X. Feng, W. Pisula, and K. Müllen. "Large polycyclic aromatic hydrocarbons: Synthesis and discotic organization". *Pure Appl. Chem.*, 81(12):2203–2224 (2009). doi:10.1351/PAC-CON-09-07-07. URL http://www.iupac.org/publications/pac/81/12/2203/.

[107] S. Zhu, et al. "Control the size and surface chemistry of graphene for the rising fluorescent materials". *Chem. Commun.*, 48:4527–4539 (2012). doi:10.1039/C2CC31201H. URL http://dx.doi.org/10.1039/C2CC31201H.

[108] J. Lee, et al. "Uniform graphene quantum dots patterned from self-assembled silica nanodots". *Nano Letters*, 12(12):6078–6083 (2012). doi:10.1021/nl302520m. URL `http://pubs.acs.org/doi/abs/10.1021/nl302520m`.

[109] R. Yamaguchi, et al. "Functionalization of hexa-peri-hexabenzocoronenes: Investigation of the substituent effects on a superbenzene". *Chemistry – An Asian Journal*, 8(1):178–190 (2013). ISSN 1861-471X. doi:10.1002/asia.201200723. URL `http://dx.doi.org/10.1002/asia.201200723`.

[110] K. Brenner, Y. Yang, and R. Murali. "Edge doping of graphene sheets". *Carbon*, 50(2):637–645 (2012). ISSN 0008-6223. doi:10.1016/j.carbon.2011.09.021. URL `http://www.sciencedirect.com/science/article/pii/S0008622311007573`.

[111] J. Chen, et al. "Optical nano-imaging of gate-tunable graphene plasmons". *Nature*, 487(7405):77–81 (2012). URL `http://dx.doi.org/10.1038/nature11254`.

[112] M. Olle, et al. "Yield and shape selection of graphene nanoislands grown on ni(111)". *Nano Letters*, 12(9):4431–4436 (2012). doi:10.1021/nl300897m. URL `http://dx.doi.org/10.1021/nl300897m`. PMID: 22901016.

[113] Q. Cao, et al. "End-bonded contacts for carbon nanotube transistors with low, size-independent resistance". *Science*, 350(6256):68–72 (2015). ISSN 0036-8075. doi:10.1126/science.aac8006. URL `http://science.sciencemag.org/content/350/6256/68`.

[114] S. E. Stein and R. L. Brown. ".pi.-electron properties of large condensed polyaromatic hydrocarbons". *Journal of the American Chemical Society*, 109(12):3721–3729 (1987). doi:10.1021/ja00246a033. URL `http://pubs.acs.org/doi/abs/10.1021/ja00246a033`.

[115] Z. Z. Zhang, K. Chang, and F. M. Peeters. "Tuning of energy levels and optical properties of graphene quantum dots". *Phys. Rev. B*, 77:235411 (2008). doi:10.1103/PhysRevB.77.235411. URL `http://link.aps.org/doi/10.1103/PhysRevB.77.235411`.

[116] F. Libisch, C. Stampfer, and J. Burgdörfer. "Graphene quantum dots: Beyond a dirac billiard". *Phys. Rev. B*, 79:115423 (2009). doi:10.1103/PhysRevB.79.115423. URL `http://link.aps.org/doi/10.1103/PhysRevB.79.115423`.

[117] A. D. Guclu, P. Potasz, and P. Hawrylak. "Optical properties of graphene quantum dots with fractionally filled degenerate shell of zero energy states". *AIP Conference Proceedings*, 1399(1):771–772 (2011). doi:10.1063/1.3666604. URL `http://link.aip.org/link/?APC/1399/771/1`.

[118] H. P. Heiskanen, M. Manninen, and J. Akola. "Electronic structure of triangular, hexagonal and round graphene flakes near the fermi level". *New Journal of Physics*, 10(10):103015 (2008). URL `http://stacks.iop.org/1367-2630/10/i=10/a=103015`.

[119] A. Kuc, T. Heine, and G. Seifert. "Structural and electronic properties of graphene nanoflakes". *Phys. Rev. B*, 81:085430 (2010). doi:10.1103/PhysRevB.81.085430. URL http://link.aps.org/doi/10.1103/PhysRevB.81.085430.

[120] M. Wimmer, A. R. Akhmerov, and F. Guinea. "Robustness of edge states in graphene quantum dots". *Phys. Rev. B*, 82:045409 (2010). doi:10.1103/PhysRevB.82.045409. URL http://link.aps.org/doi/10.1103/PhysRevB.82.045409.

[121] A. M. Silva, et al. "Graphene nanoflakes: Thermal stability, infrared signatures, and potential applications in the field of spintronics and optical nanodevices". *The Journal of Physical Chemistry C*, 114(41):17472–17485 (2010). doi:10.1021/jp105728p. URL http://pubs.acs.org/doi/abs/10.1021/jp105728p.

[122] V. Barone, et al. "Accurate prediction of the electronic properties of low-dimensional graphene derivatives using a screened hybrid density functional". *Accounts of Chemical Research*, 44(4):269–279 (2011). doi:10.1021/ar100137c. URL http://pubs.acs.org/doi/abs/10.1021/ar100137c.

[123] C. Cocchi, et al. "Optical properties and charge-transfer excitations in edge-functionalized all-graphene nanojunctions". *The Journal of Physical Chemistry Letters*, 2(11):1315–1319 (2011). doi:10.1021/jz200472a. URL http://pubs.acs.org/doi/abs/10.1021/jz200472a.

[124] H. Zheng and W. Duley. "First-principles study of edge chemical modifications in graphene nanodots". *Phys. Rev. B*, 78:045421 (2008). doi:10.1103/PhysRevB.78.045421. URL http://link.aps.org/doi/10.1103/PhysRevB.78.045421.

[125] H. Zheng and W. Duley. "The relation between carbon-hydrogen bond lengths and bond angles". *Phys. Rev. B*, 78:155118 (2008). doi:10.1103/PhysRevB.78.155118. URL http://link.aps.org/doi/10.1103/PhysRevB.78.155118.

[126] F. H. L. Koppens, D. E. Chang, and F. J. García de Abajo. "Graphene plasmonics: A platform for strong light–matter interactions". *Nano Letters*, 11(8):3370–3377 (2011). doi:10.1021/nl201771h. URL http://pubs.acs.org/doi/abs/10.1021/nl201771h.

[127] C. W. N. Cumper. "The relation between carbon-hydrogen bond lengths and bond angles". *Trans. Faraday Soc.*, 54:1261–1265 (1958). URL http://pubs.rsc.org/en/Content/ArticleLanding/1958/TF/tf9585401261.

[128] W. Humphrey, A. Dalke, and K. Schulten. "VMD – Visual Molecular Dynamics". *Journal of Molecular Graphics*, 14:33–38 (1996).

[129] J. Stone. An Efficient Library for Parallel Ray Tracing and Animation. Master's thesis, Computer Science Department, University of Missouri-Rolla (1998).

[130] E. Artacho, et al. "Linear-scaling ab-initio calculations for large and complex systems". *Phys. Stat. Sol. (b)*, 215:809 (1999).

[131] M. H. Gass, et al. "Free-standing graphene at atomic resolution". *Nature Nanotechnology*, 3:676–681 (2008).

[132] X. Zhu and H. Su. "Scaling of excitons in graphene nanoribbons with armchair shaped edges". *The Journal of Physical Chemistry A*, 115(43):11998–12003 (2011). doi: 10.1021/jp202787h. URL `http://pubs.acs.org/doi/abs/10.1021/jp202787h`.

[133] V. Barone, O. Hod, and G. E. Scuseria. "Electronic structure and stability of semi-conducting graphene nanoribbons". *Nano Letters*, 6(12):2748–2754 (2006). doi: 10.1021/nl0617033. URL `http://pubs.acs.org/doi/abs/10.1021/nl0617033`. PMID: 17163699.

[134] H. E. Lieb. "Two theorems on the hubbard model". *Phys. Rev. Lett.*, 62:1201–1204 (1989).

[135] J. Fernández-Rossier and P. J. J. "Magnetism in graphene nanoislands". *Phys. Rev. Lett.*, 99:177204 (2007).

[136] Y.-W. Son, M. L. Cohen, and S. G. Louie. "Energy gaps in graphene nanoribbons". *Phys. Rev. Lett.*, 97:216803 (2006).

[137] M. Fujita, et al. "Peciliar localized state at zigzag graphite edge". *J. Phys. Soc. Jpn.*, 65:1920–1923 (1996).

[138] A. Kokalj. "Computer graphics and graphical user interfaces as tools in simulations of matter at the atomic scale". *Computational Materials Science*, 28(2):155 – 168 (2003). ISSN 0927-0256. doi:http://dx.doi.org/10.1016/S0927-0256(03)00104-6. URL `http://www.sciencedirect.com/science/article/pii/S0927025603001046`. Proceedings of the Symposium on Software Development for Process and Materials Design.

[139] A. Manjavacas, et al. "Tunable molecular plasmons in polycyclic aromatic hydrocarbons". *ACS Nano*, 7(4):3635–3643 (2013). doi:10.1021/nn4006297. URL `http://dx.doi.org/10.1021/nn4006297`. PMID: 23484678.

[140] R. Zia, et al. "Plasmonics: the next chip-scale technology". *Materials Today*, 9(7–8):20 – 27 (2006). ISSN 1369-7021. doi:http://dx.doi.org/10.1016/S1369-7021(06)71572-3. URL `http://www.sciencedirect.com/science/article/pii/S1369702106715723`.

[141] N. Engheta. "Circuits with light at nanoscales: Optical nanocircuits inspired by metamaterials". *Science*, 317(5845):1698–1702 (2007). ISSN 0036-8075. doi:10.1126/science.1133268. URL `http://science.sciencemag.org/content/317/5845/1698`.

[142] S. I. Bozhevolnyi, et al. "Channel plasmon subwavelength waveguide components including interferometers and ring resonators". *Nature*, 440(7083):508–511 (2006). URL `http://dx.doi.org/10.1038/nature04594`.

[143] A. Manjavacas and F. J. García de Abajo. "Robust plasmon waveguides in strongly interacting nanowire arrays". *Nano Letters*, 9(4):1285–1289 (2009). doi:10.1021/nl802044t. URL `http://dx.doi.org/10.1021/nl802044t`. PMID: 18672946.

[144] K. Li, M. I. Stockman, and D. J. Bergman. "Self-similar chain of metal nanospheres as an efficient nanolens". *Phys. Rev. Lett.*, 91:227402 (2003). doi: 10.1103/PhysRevLett.91.227402. URL http://link.aps.org/doi/10.1103/PhysRevLett.91.227402.

[145] A. Polman. "Plasmonics applied". *Science*, 322(5903):868–869 (2008). ISSN 0036-8075. doi:10.1126/science.1163959. URL http://science.sciencemag.org/content/322/5903/868.

[146] M. I. Stockman. "Nanoplasmonics: The physics behind the applications". *Phys. Today*, pages 39–44 (2011).

[147] M. Grzelczak, et al. "Shape control in gold nanoparticle synthesis". *Chem. Soc. Rev.*, 37:1783–1791 (2008). doi:10.1039/B711490G. URL http://dx.doi.org/10.1039/B711490G.

[148] M. P. Pileni. "Control of the size and shape of inorganic nanocrystals at various scales from nano to macrodomains". *The Journal of Physical Chemistry C*, 111(26):9019–9038 (2007). doi:10.1021/jp070646e. URL http://dx.doi.org/10.1021/jp070646e.

[149] A. Kuzyk, et al. "Dna-based self-assembly of chiral plasmonic nanostructures with tailored optical response". *Nature*, 483(7389):311–314 (2012). URL http://dx.doi.org/10.1038/nature10889.

[150] J. Shen, et al. "Graphene quantum dots: emergent nanolights for bioimaging, sensors, catalysis and photovoltaic devices". *Chem. Commun.*, 48:3686–3699 (2012). doi:10.1039/C2CC00110A. URL http://dx.doi.org/10.1039/C2CC00110A.

[151] J. Roncali. "Synthetic principles for bandgap control in linear π-conjugated systems". *Chemical Reviews*, 97(1):173–206 (1997). doi:10.1021/cr950257t. URL http://dx.doi.org/10.1021/cr950257t. PMID: 11848868.

[152] J. Wu, W. Pisula, and K. Müllen. "Graphenes as potential material for electronics". *Chemical Reviews*, 107(3):718–747 (2007). doi:10.1021/cr068010r. URL http://dx.doi.org/10.1021/cr068010r. PMID: 17291049.

[153] X. Feng, et al. "Supramolecular organization and photovoltaics of triangle-shaped discotic graphenes with swallow-tailed alkyl substituents". *Advanced Materials*, 20(14):2684–2689 (2008). ISSN 1521-4095. doi:10.1002/adma.200800642. URL http://dx.doi.org/10.1002/adma.200800642.

[154] R. Rieger and K. Müllen. "Forever young: polycyclic aromatic hydrocarbons as model cases for structural and optical studies". *Journal of Physical Organic Chemistry*, 23(4):315–325 (2010). ISSN 1099-1395. doi:10.1002/poc.1644. URL http://dx.doi.org/10.1002/poc.1644.

[155] D. S. McKay, et al. "Search for past life on mars: Possible relic biogenic activity in martian meteorite alh84001". *Science*, 273(5277):924–930 (1996). ISSN 0036-8075. doi:10.1126/science.273.5277.924. URL http://science.sciencemag.org/content/273/5277/924.

[156] K. Zhang, et al. "Far-infrared emission spectra of selected gas-phase pahs: Spectroscopic fingerprints". *Science*, 274(5287):582–583 (1996). ISSN 0036-8075. doi:10.1126/science.274.5287.582. URL http://science.sciencemag.org/content/274/5287/582.

[157] G. Malloci, et al. "Time-dependent density functional study of the electronic spectra of oligoacenes in the charge states -1, 0, +1, and +2". *Chemical Physics*, 340(1–3):43 – 58 (2007). ISSN 0301-0104. doi:http://dx.doi.org/10.1016/j.chemphys.2007.07.046. URL http://www.sciencedirect.com/science/article/pii/S0301010407003084.

[158] Z. Fei, et al. "Gate-tuning of graphene plasmons revealed by infrared nano-imaging". *Nature*, 487(7405):82–85 (2012). URL http://dx.doi.org/10.1038/nature11253.

[159] T. Nagao, et al. "One-dimensional plasmon in an atomic-scale metal wire". *Phys. Rev. Lett.*, 97:116802 (2006). doi:10.1103/PhysRevLett.97.116802. URL http://link.aps.org/doi/10.1103/PhysRevLett.97.116802.

[160] J. W. Keller and M. Coplan. "Electron energy loss spectroscopy of c60". *Chemical Physics Letters*, 193(1):89 – 92 (1992). ISSN 0009-2614. doi:http://dx.doi.org/10.1016/0009-2614(92)85687-6. URL http://www.sciencedirect.com/science/article/pii/0009261492856876.

[161] O. Stéphan, et al. "Dielectric response of isolated carbon nanotubes investigated by spatially resolved electron energy-loss spectroscopy: From multiwalled to single-walled nanotubes". *Phys. Rev. B*, 66:155422 (2002). doi:10.1103/PhysRevB.66.155422. URL http://link.aps.org/doi/10.1103/PhysRevB.66.155422.

[162] M. Jablan, H. Buljan, and M. Soljačić. "Plasmonics in graphene at infrared frequencies". *Phys. Rev. B*, 80:245435 (2009). doi:10.1103/PhysRevB.80.245435. URL http://link.aps.org/doi/10.1103/PhysRevB.80.245435.

[163] D. Varsano, et al. "A tddft study of the excited states of dna bases and their assemblies". *The Journal of Physical Chemistry B*, 110(14):7129–7138 (2006). doi:10.1021/jp056120g. URL http://dx.doi.org/10.1021/jp056120g. PMID: 16599476.

[164] C.-F. Chen, et al. "Controlling inelastic light scattering quantum pathways in graphene". *Nature*, 471(7340):617–620 (2011). URL http://dx.doi.org/10.1038/nature09866.

[165] Z. Fang, et al. "Gated tunability and hybridization of localized plasmons in nanostructured graphene". *ACS Nano*, 7(3):2388–2395 (2013). doi:10.1021/nn3055835. URL http://dx.doi.org/10.1021/nn3055835. PMID: 23390960.

[166] S. Thongrattanasiri, F. H. L. Koppens, and F. J. García de Abajo. "Complete optical absorption in periodically patterned graphene". *Phys. Rev. Lett.*, 108:047401 (2012). doi:10.1103/PhysRevLett.108.047401. URL http://link.aps.org/doi/10.1103/PhysRevLett.108.047401.

[167] J. M. Pitarke, et al. "Theory of surface plasmons and surface-plasmon polaritons". *Rep. Prog. Phys.*, 70:1 (2007).

[168] S. A. Maier. *Plasmonics: Fundamentals and Applications*. Springer (2007).

[169] S. M. Morton, D. W. Silverstein, and L. Jensen. "Theoretical studies of plasmonics using electronic structure methods". *Chemical Reviews*, 111(6):3962–3994 (2011). doi:10.1021/cr100265f. URL http://dx.doi.org/10.1021/cr100265f. PMID: 21344862.

[170] M. Barbry, et al. "Atomistic near-field nanoplasmonics: Reaching atomic-scale resolution in nanooptics". *Nano Letters*, 15(5):3410–3419 (2015).

[171] H. Xu, et al. "Spectroscopy of single hemoglobin molecules by surface enhanced raman scattering". *Phys. Rev. Lett.*, 83:4357–4360 (1999). doi:10.1103/PhysRevLett.83.4357. URL http://link.aps.org/doi/10.1103/PhysRevLett.83.4357.

[172] R. Alvarez-Puebla, L. M. Liz-Marzán, and F. J. G. de Abajo. "Light concentration at the nanometer scale". *The Journal of Physical Chemistry Letters*, 1(16):2428–2434 (2010). doi:10.1021/jz100820m. URL http://dx.doi.org/10.1021/jz100820m.

[173] D. Jimenez de Aberasturi, A. B. Serrano-Montes, and L. M. Liz-Marzán. "Modern applications of plasmonic nanoparticles: From energy to health". *Adv. Opt. Mater.*, 3:602–617 (2015).

[174] S. Oldenburg, et al. "Nanoengineering of optical resonances". *Chemical Physics Letters*, 288(2–4):243 – 247 (1998). ISSN 0009-2614. doi:http://dx.doi.org/10.1016/S0009-2614(98)00277-2. URL http://www.sciencedirect.com/science/article/pii/S0009261498002772.

[175] W. L. Barnes, A. Dereux, and E. T. W. "Surface plasmon subwavelength optics". *Nature*, 424:824–830 (2003).

[176] J. Kern, et al. "Atomic-scale confinement of resonant optical fields". *Nano Letters*, 12(11):5504–5509 (2012). doi:10.1021/nl302315g. URL http://dx.doi.org/10.1021/nl302315g. PMID: 22984927.

[177] D. R. Ward, et al. "Optical rectification and field enhancement in a plasmonic nanogap". *Nat Nano*, 5(10):732–736 (2010). URL http://dx.doi.org/10.1038/nnano.2010.176.

[178] D. O. Sigle, et al. "Monitoring morphological changes in 2d monolayer semiconductors using atom-thick plasmonic nanocavities". *ACS Nano*, 9(1):825–830 (2015). doi:10.1021/nn5064198. URL http://dx.doi.org/10.1021/nn5064198. PMID: 25495220.

[179] M. Danckwerts and L. Novotny. "Optical frequency mixing at coupled gold nanoparticles". *Phys. Rev. Lett.*, 98:026104 (2007). doi:10.1103/PhysRevLett.98.026104. URL http://link.aps.org/doi/10.1103/PhysRevLett.98.026104.

[180] N. Grillet, et al. "Plasmon coupling in silver nanocube dimers: Resonance splitting induced by edge rounding". *ACS Nano*, 5(12):9450–9462 (2011). doi: 10.1021/nn2041329. URL `http://dx.doi.org/10.1021/nn2041329`. PMID: 22087471.

[181] M. Sun and H. Xu. "A novel application of plasmonics: Plasmon-driven surface-catalyzed reactions". *Small*, 8(18):2777–2786 (2012).

[182] P. Christopher, et al. "Singular characteristics and unique chemical bond activation mechanisms of photocatalytic reactions on plasmonic nanostructures". *Nat Mater*, 11(12):1044–1050 (2012). URL `http://dx.doi.org/10.1038/nmat3454`.

[183] S. Mukherjee, et al. "Hot electrons do the impossible: Plasmon-induced dissociation of h2 on au". *Nano Letters*, 13(1):240–247 (2013). doi:10.1021/nl303940z. URL `http://dx.doi.org/10.1021/nl303940z`. PMID: 23194158.

[184] G. Baffoua and R. Quidant. "Nanoplasmonics for chemistry". *Chem. Soc. Rev.*, 43:3898–3907 (2014).

[185] S. Nie and S. R. Emory. "Probing single molecules and single nanoparticles by surface-enhanced raman scattering". *Science*, 275(5303):1102–1106 (1997). ISSN 0036-8075. doi:10.1126/science.275.5303.1102. URL `http://science.sciencemag.org/content/275/5303/1102`.

[186] K. Kneipp, et al. "Single molecule detection using surface-enhanced raman scattering (sers)". *Phys. Rev. Lett.*, 78:1667–1670 (1997). doi:10.1103/PhysRevLett.78.1667. URL `http://link.aps.org/doi/10.1103/PhysRevLett.78.1667`.

[187] S. Kühn, et al. "Enhancement of single-molecule fluorescence using a gold nanoparticle as an optical nanoantenna". *Phys. Rev. Lett.*, 97:017402 (2006). doi: 10.1103/PhysRevLett.97.017402. URL `http://link.aps.org/doi/10.1103/PhysRevLett.97.017402`.

[188] P. Anger, P. Bharadwaj, and L. Novotny. "Enhancement and quenching of single-molecule fluorescence". *Phys. Rev. Lett.*, 96:113002 (2006). doi: 10.1103/PhysRevLett.96.113002. URL `http://link.aps.org/doi/10.1103/PhysRevLett.96.113002`.

[189] R. Zhang, et al. "Chemical mapping of a single molecule by plasmon-enhanced raman scattering". *Nature*, 498(7452):82–86 (2013). URL `http://dx.doi.org/10.1038/nature12151`.

[190] E. Ozbay. "Plasmonics: Merging photonics and electronics at nanoscale dimensions". *Science*, 311:189–193 (2006).

[191] J.-S. Huang, et al. "Impedance matching and emission properties of nanoantennas in an optical nanocircuit". *Nano Letters*, 9(5):1897–1902 (2009). doi:10.1021/nl803902t. URL `http://dx.doi.org/10.1021/nl803902t`. PMID: 19338279.

[192] J. C. Prangsma, et al. "Electrically connected resonant optical antennas". *Nano Letters*, 12(8):3915–3919 (2012). doi:10.1021/nl3007374. URL `http://dx.doi.org/10.1021/nl3007374`. PMID: 22800440.

[193] A. Stolz, et al. "Nonlinear photon-assisted tunneling transport in optical gap antennas". *Nano Letters*, 14(5):2330–2338 (2014). doi:10.1021/nl404707t. URL `http://dx.doi.org/10.1021/nl404707t`. PMID: 24697629.

[194] M. Moskovits. "Surface-enhanced spectroscopy". *Rev. Mod. Phys.*, 57:783–826 (1985). doi:10.1103/RevModPhys.57.783. URL `http://link.aps.org/doi/10.1103/RevModPhys.57.783`.

[195] F. Neubrech, et al. "Resonant plasmonic and vibrational coupling in a tailored nanoantenna for infrared detection". *Phys. Rev. Lett.*, 101:157403 (2008).

[196] H. Xu, et al. "Electromagnetic contributions to single-molecule sensitivity in surface-enhanced raman scattering". *Phys. Rev. E*, 62:4318–4324 (2000). doi:10.1103/PhysRevE.62.4318. URL `http://link.aps.org/doi/10.1103/PhysRevE.62.4318`.

[197] L. Jensen, C. M. Aikens, and G. C. Schatz. "Electronic structure methods for studying surface-enhanced raman scattering". *Chem. Soc. Rev.*, 37:1061–1073 (2008). doi:10.1039/B706023H. URL `http://dx.doi.org/10.1039/B706023H`.

[198] F. Le, et al. "Metallic nanoparticle arrays: A common substrate for both surface-enhanced raman scattering and surface-enhanced infrared absorption". *ACS Nano*, 2(4):707–718 (2008). doi:10.1021/nn800047e. URL `http://dx.doi.org/10.1021/nn800047e`. PMID: 19206602.

[199] M. Banik, et al. "Surface-enhanced raman trajectories on a nano-dumbbell: Transition from field to charge transfer plasmons as the spheres fuse". *ACS Nano*, 6(11):10343–10354 (2012). doi:10.1021/nn304277n. URL `http://dx.doi.org/10.1021/nn304277n`. PMID: 23092179.

[200] R. F. Aroca. "Plasmon enhanced spectroscopy". *Phys. Chem. Chem. Phys.*, 15:5355–5363 (2013).

[201] H. A. Atwater and A. Polman. "Plasmonics for improved photovoltaic devices". *Nature Materials*, 9:205–213 (2010).

[202] X. Li, et al. "Dual plasmonic nanostructures for high performance inverted organic solar cells". *Advanced Materials*, 24:3046–3052 (2012).

[203] A. Berrier, et al. "Ultrafast active control of localized surface plasmon resonances in silicon bowtie antennas". *Opt. Express*, 18(22):23226–23235 (2010). doi:10.1364/OE.18.023226. URL `http://www.opticsexpress.org/abstract.cfm?URI=oe-18-22-23226`.

[204] S. Lal, S. E. Clare, and N. J. Halas. "Nanoshell-enabled photothermal cancer therapy: Impending clinical impact". *Accounts of Chemical Research*, 41(12):1842–1851 (2008). doi:10.1021/ar800150g. URL `http://dx.doi.org/10.1021/ar800150g`. PMID: 19053240.

[205] L. Polavarapua and L. M. Liz-Marzán. "Towards low-cost flexible substrates for nanoplasmonic sensing". *Phys. Chem. Chem. Phys.*, 15:5288–5300 (2013).

[206] M. Virk, et al. "Thermal plasmonic sensor platform: Resistive heating of nanohole arrays". *NanoLett.*, 14:3544–3549 (2014).

[207] M. Li, S. K. Cushingab, and N. Wu. "Plasmon-enhanced optical sensors: a review". *Analyst*, 140:386–406 (2015).

[208] J. A. Fan, et al. "Self-assembled plasmonic nanoparticle clusters". *Science*, 328:1135–1138 (2010).

[209] R. M. Stöckle, et al. "Nanoscale chemical analysis by tip-enhanced raman spectroscopy". *Chem. Phys. Lett.*, 318:131–136 (2000).

[210] D. Marinica, et al. "Quantum plasmonics: Nonlinear effects in the field enhancement of a plasmonic nanoparticle dimer". *Nano Letters*, 12(3):1333–1339 (2012). doi:10.1021/nl300269c. URL http://dx.doi.org/10.1021/nl300269c. PMID: 22320125.

[211] Y. Luo, et al. "Surface plasmons and nonlocality: A simple model". *Phys. Rev. Lett.*, 111:093901 (2013). doi:10.1103/PhysRevLett.111.093901. URL http://link.aps.org/doi/10.1103/PhysRevLett.111.093901.

[212] J. Zuloaga, E. Prodan, and P. Nordlander. "Quantum description of the plasmon resonances of a nanoparticle dimer". *Nano Letters*, 9(2):887–891 (2009). doi:10.1021/nl803811g. URL http://dx.doi.org/10.1021/nl803811g. PMID: 19159319.

[213] R. Esteban, et al. "Bridging quantum and classical plasmonics with a quantum-corrected model". *Nat Commun*, 3:825 (2012). URL http://dx.doi.org/10.1038/ncomms1806.

[214] K. J. Savage, et al. "Revealing the quantum regime in tunnelling plasmonics". *Nature*, 491(7425):574–577 (2012). URL http://dx.doi.org/10.1038/nature11653.

[215] S. F. Tan, et al. "Quantum plasmon resonances controlled by molecular tunnel junctions". *Science*, 343(6178):1496–1499 (2014). ISSN 0036-8075. doi:10.1126/science.1248797. URL http://science.sciencemag.org/content/343/6178/1496.

[216] J. Zuloaga, E. Prodan, and P. Nordlander. "Quantum plasmonics: Optical properties and tunability of metallic nanorods". *ACS Nano*, 4(9):5269–5276 (2010). doi:10.1021/nn101589n. URL http://dx.doi.org/10.1021/nn101589n. PMID: 20698558.

[217] C. Ciracì, et al. "Probing the ultimate limits of plasmonic enhancement". *Science*, 337(6098):1072–1074 (2012). URL http://science.sciencemag.org/content/337/6098/1072.abstract.

[218] L. Stella, et al. "Performance of nonlocal optics when applied to plasmonic nanostructures". *The Journal of Physical Chemistry C*, 117(17):8941–8949 (2013). doi: 10.1021/jp401887y. URL http://dx.doi.org/10.1021/jp401887y.

[219] P. Zhang, et al. "*Ab initio* nanoplasmonics: The impact of atomic structure". *Phys. Rev. B*, 90:161407 (2014). doi:10.1103/PhysRevB.90.161407. URL http://link.aps.org/doi/10.1103/PhysRevB.90.161407.

[220] R. Esteban, et al. "A classical treatment of optical tunneling in plasmonic gaps: extending the quantum corrected model to practical situations". *Faraday Discuss.*, 178:151–183 (2015). doi:10.1039/C4FD00196F. URL http://dx.doi.org/10.1039/C4FD00196F.

[221] A. Varas, et al. "Anisotropy effects on the plasmonic response of nanoparticle dimers". *The Journal of Physical Chemistry Letters*, 6(10):1891–1898 (2015). doi:10.1021/acs.jpclett.5b00573. URL http://dx.doi.org/10.1021/acs.jpclett.5b00573. PMID: 26263265.

[222] O. J. F. Martin and C. Girard. "Controlling and tuning strong optical field gradients at a local probe microscope tip apex". *Applied Physics Letters*, 70(6):705–707 (1997). doi:http://dx.doi.org/10.1063/1.118245. URL http://scitation.aip.org/content/aip/journal/apl/70/6/10.1063/1.118245.

[223] F. Marchesin, et al. "Plasmonic response of metallic nanojunctions driven by single atom motion: Quantum transport revealed in optics". *ACS Photonics*, 3(2):269–277 (2016). doi:10.1021/acsphotonics.5b00609. URL http://dx.doi.org/10.1021/acsphotonics.5b00609.

[224] J. N. Murrell and R. E. Mottram. "Potential energy functions for atomic solids". *Molecular Physics*, 69(3):571–585 (1990). doi:10.1080/00268979000100411. URL http://dx.doi.org/10.1080/00268979000100411.

[225] D. J. Wales, et al. "The cambridge cluster database". URL http://www-wales.ch.cam.ac.uk/CCD.html.

[226] M. M. Dacorogna and M. L. Cohen. "First-principles study of the structural properties of alkali metals". *Phys. Rev. B*, 34:4996–5002 (1986). doi:10.1103/PhysRevB.34.4996. URL http://link.aps.org/doi/10.1103/PhysRevB.34.4996.

[227] K. H. Su, et al. "Interparticle coupling effects on plasmon resonances of nanogold particles". *Nano Letters*, 3(8):1087–1090 (2003). doi:10.1021/nl034197f. URL http://dx.doi.org/10.1021/nl034197f.

[228] W. Rechberger, et al. "Optical properties of two interacting gold nanoparticles". *Optics Communications*, 220:137–141 (2003).

[229] N. Agraït, A. L. Yeyati, and J. M. van Ruitenbeek. "Quantum properties of atomic-sized conductors". *Physics Reports*, 377(2–3):81 – 279 (2003). ISSN 0370-1573. doi:http://dx.doi.org/10.1016/S0370-1573(02)00633-6. URL http://www.sciencedirect.com/science/article/pii/S0370157302006336.

[230] U. Landman, et al. "Atomistic mechanisms and dynamics of adhesion, nanoindentation, and fracture". *Science*, 248(4954):454–461 (1990). ISSN 0036-8075. doi:10.1126/science.248.4954.454. URL http://science.sciencemag.org/content/248/4954/454.

[231] H. Ohnishi, Y. Kondo, and K. Takayanagi. "Quantized conductance through individual rows of suspended gold atoms". *Nature*, 395(6704):780–783 (1998). URL http://dx.doi.org/10.1038/27399.

[232] A. I. Yanson, et al. "Formation and manipulation of a metallic wire of single gold atoms". *Nature*, 395(6704):783–785 (1998). URL http://dx.doi.org/10.1038/27405.

[233] S. V. Aradhya, et al. "Correlating structure, conductance, and mechanics of silver atomic-scale contacts". *ACS Nano*, 7(4):3706–3712 (2013). doi:10.1021/nn4007187. URL http://dx.doi.org/10.1021/nn4007187. PMID: 23521342.

[234] O. Pérez-González, et al. "Optical spectroscopy of conductive junctions in plasmonic cavities". *Nano Letters*, 10(8):3090–3095 (2010). doi:10.1021/nl1017173. URL http://dx.doi.org/10.1021/nl1017173. PMID: 20698622.

[235] P. Song, P. Nordlander, and S. Gao. "Quantum mechanical study of the coupling of plasmon excitations to atomic-scale electron transport". *The Journal of Chemical Physics*, 134(7):074701 (2011). doi:http://dx.doi.org/10.1063/1.3554420. URL http://scitation.aip.org/content/aip/journal/jcp/134/7/10.1063/1.3554420.

[236] P. Song, et al. "Quantum plasmonics: Symmetry-dependent plasmon-molecule coupling and quantized photoconductances". *Phys. Rev. B*, 86:121410 (2012). doi:10.1103/PhysRevB.86.121410. URL http://link.aps.org/doi/10.1103/PhysRevB.86.121410.

[237] V. Kulkarni and A. Manjavacas. "Quantum effects in charge transfer plasmons". *ACS Photonics*, 2(7):987–992 (2015). doi:10.1021/acsphotonics.5b00246. URL http://dx.doi.org/10.1021/acsphotonics.5b00246.

[238] B. Bhushan, J. N. Israelachvili, and U. Landman. "Nanotribology: friction, wear and lubrication at the atomic scale". *Nature*, 374(6523):607–616 (1995). URL http://dx.doi.org/10.1038/374607a0.

[239] T. N. Todorov and A. P. Sutton. "Jumps in electronic conductance due to mechanical instabilities". *Phys. Rev. Lett.*, 70:2138–2141 (1993). doi:10.1103/PhysRevLett.70.2138. URL http://link.aps.org/doi/10.1103/PhysRevLett.70.2138.

[240] N. Agraït, J. G. Rodrigo, and S. Vieira. "Conductance steps and quantization in atomic-size contacts". *Phys. Rev. B*, 47:12345–12348 (1993). doi:10.1103/PhysRevB.47.12345. URL http://link.aps.org/doi/10.1103/PhysRevB.47.12345.

[241] J. A. Torres and J. J. Sáenz. "Conductance and mechanical properties of atomic-size metallic contacts: A simple model". *Phys. Rev. Lett.*, 77:2245–2248 (1996). doi:10.1103/PhysRevLett.77.2245. URL http://link.aps.org/doi/10.1103/PhysRevLett.77.2245.

[242] T. P. Rossi, et al. "Quantized evolution of the plasmonic response in a stretched nanorod". *Phys. Rev. Lett.*, 115:236804 (2015). doi:10.1103/PhysRevLett.115.236804. URL http://link.aps.org/doi/10.1103/PhysRevLett.115.236804.

[243] J. P. Perdew, K. Burke, and M. Ernzerhof. "Generalized gradient approximation made simple". *Phys. Rev. Lett.*, 77:3865–3868 (1996). doi:10.1103/PhysRevLett.77.3865. URL http://link.aps.org/doi/10.1103/PhysRevLett.77.3865.

[244] N. Troullier and J. L. Martins. "Efficient pseudopotentials for plane-wave calculations". *Phys. Rev. B*, 43:1993–2006 (1991). doi:10.1103/PhysRevB.43.1993. URL http://link.aps.org/doi/10.1103/PhysRevB.43.1993.

[245] A. Nakamura, et al. "Density functional simulation of a breaking nanowire". *Phys. Rev. Lett.*, 82:1538–1541 (1999). doi:10.1103/PhysRevLett.82.1538. URL http://link.aps.org/doi/10.1103/PhysRevLett.82.1538.

[246] P. Jelínek, et al. "First-principles simulations of the stretching and final breaking of al nanowires: Mechanical properties and electrical conductance". *Phys. Rev. B*, 68:085403 (2003). doi:10.1103/PhysRevB.68.085403. URL http://link.aps.org/doi/10.1103/PhysRevB.68.085403.

[247] A. Rubio, et al. "*Ab Initio* photoabsorption spectra and structures of small semiconductor and metal clusters". *Phys. Rev. Lett.*, 77:247–250 (1996). doi:10.1103/PhysRevLett.77.247. URL http://link.aps.org/doi/10.1103/PhysRevLett.77.247.

[248] I. Vasiliev, S. Öğüt, and J. R. Chelikowsky. "*Ab Initio* excitation spectra and collective electronic response in atoms and clusters". *Phys. Rev. Lett.*, 82:1919–1922 (1999). doi:10.1103/PhysRevLett.82.1919. URL http://link.aps.org/doi/10.1103/PhysRevLett.82.1919.

[249] I. Vasiliev, S. Öğüt, and J. R. Chelikowsky. "First-principles density-functional calculations for optical spectra of clusters and nanocrystals". *Phys. Rev. B*, 65:115416 (2002). doi:10.1103/PhysRevB.65.115416. URL http://link.aps.org/doi/10.1103/PhysRevB.65.115416.

[250] A. Tsolakidis, D. Sánchez-Portal, and R. M. Martin. "Calculation of the optical response of atomic clusters using time-dependent density functional theory and local orbitals". *Phys. Rev. B*, 66(235416) (2002).

[251] M. A. L. Marques, et al. *Time-Dependent Density Functional Theory*, volume Lecture Notes in Physics 706. Springer, Berlin Heidelberg (2006).

[252] 2006, editor. *Structure and Properties of Atomic Nanoclusters*. Imperial College Press (Alonso, Julio A.).

[253] G. Rubio, N. Agraït, and S. Vieira. "Atomic-sized metallic contacts: Mechanical properties and electronic transport". *Phys. Rev. Lett.*, 76:2302–2305 (1996). doi:10.1103/PhysRevLett.76.2302. URL http://link.aps.org/doi/10.1103/PhysRevLett.76.2302.

[254] E. Prodan, et al. "A hybridization model for the plasmon response of complex nanostructures". *Science*, 302(5644):419–422 (2003). ISSN 0036-8075. doi:10.1126/science.1089171. URL http://science.sciencemag.org/content/302/5644/419.

[255] M. R. Sørensen, M. Brandbyge, and K. W. Jacobsen. "Mechanical deformation of atomic-scale metallic contacts: Structure and mechanisms". *Phys. Rev. B*, 57:3283–3294 (1998). doi:10.1103/PhysRevB.57.3283. URL http://link.aps.org/doi/10.1103/PhysRevB.57.3283.

[256] T. Kizuka. "Atomic configuration and mechanical and electrical properties of stable gold wires of single-atom width". *Phys. Rev. B*, 77:155401 (2008). doi:10.1103/PhysRevB.77.155401. URL http://link.aps.org/doi/10.1103/PhysRevB.77.155401.

[257] S. Datta. *Electronic Transport in Mesoscopic Systems*. Cambridge University Press (1995). ISBN 9780511805776. URL http://dx.doi.org/10.1017/CBO9780511805776. Cambridge Books Online.

[258] B. Pettinger, et al. "Tip-enhanced raman spectroscopy: Near-fields acting on a few molecules". *Annual Review of Physical Chemistry*, 63(1):379–399 (2012). doi:10.1146/annurev-physchem-032511-143807. URL http://dx.doi.org/10.1146/annurev-physchem-032511-143807. PMID: 22263910.

[259] A. Hartschuh, et al. "High-resolution near-field raman microscopy of single-walled carbon nanotubes". *Phys. Rev. Lett.*, 90:095503 (2003). doi:10.1103/PhysRevLett.90.095503. URL http://link.aps.org/doi/10.1103/PhysRevLett.90.095503.

[260] J. M. Gerton, et al. "Tip-enhanced fluorescence microscopy at 10 nanometer resolution". *Phys. Rev. Lett.*, 93:180801 (2004). doi:10.1103/PhysRevLett.93.180801. URL http://link.aps.org/doi/10.1103/PhysRevLett.93.180801.

[261] T.-a. Yano, et al. "Tip-enhanced nano-raman analytical imaging of locally induced strain distribution in carbon nanotubes". *Nat Commun*, 4 (2013). URL http://dx.doi.org/10.1038/ncomms3592.

[262] D. R. Ward, et al. "Electromigrated nanoscale gaps for surface-enhanced raman spectroscopy". *Nano Letters*, 7(5):1396–1400 (2007). doi:10.1021/nl070625w. URL http://dx.doi.org/10.1021/nl070625w. PMID: 17430009.

[263] A. Emboras, et al. "Atomic scale plasmonic switch". *Nano Letters*, 16(1):709–714 (2016). doi:10.1021/acs.nanolett.5b04537. URL http://dx.doi.org/10.1021/acs.nanolett.5b04537. PMID: 26670551.

[264] U. Kreibig and M. Vollmer. *Optical properties of metal clusters*. Number v. 25 in Springer series in materials science. Springer (1995). ISBN 9780387578361. URL `https://books.google.es/books?id=jYhRAAAAMAAJ`.

[265] W. Dednam, et al. "Modeling contact formation between atomic-sized gold tips via molecular dynamics". *Journal of Physics: Conference Series*, 574(1):012045 (2015). URL `http://stacks.iop.org/1742-6596/574/i=1/a=012045`.

[266] A. Fetter and J. Walecka. *Quantum Theory of Many-particle Systems*. Dover Books on Physics. Dover Publications (2003). ISBN 9780486428277. URL `https://books.google.es/books?id=0wekf1s83b0C`.

[267] E. Gross and K. Burke. *Basics*, pages 1–13. Springer Berlin Heidelberg, Berlin, Heidelberg (2006). ISBN 978-3-540-35426-0. doi:10.1007/3-540-35426-3_1. URL `http://dx.doi.org/10.1007/3-540-35426-3_1`.

[268] M. Frigo and S. G. Johnson. "The design and implementation of fftw3". *Proceedings of the IEEE*, 93(2):216–231 (2005). ISSN 0018-9219. doi:10.1109/JPROC.2004. 840301.

[269] M. Frigo and S. G. Johnson. *FFTW*, version 3.3.3 edition (2012).

Resumen (Summary in Spanish)

El desarrollo de este proyecto de tesis está basado en el estudio de las propiedades ópticas de nano-estructuras de interés físico por medio de teorías $ab\ initio$. Las teorías $ab\ initio$ nos permiten estudiar una amplia gama de sistemas cambiando solamente unos parámetros que dependen del sistema sin tener que reconsiderar la metodología de trabajo de la teoría.

En particular, se ha usado la Teoría del Funcional de la Densidad (DFT) para obtener información sobre la estructura electrónica de los materiales estudiados. Mientras que la Teoría del Funcional de la Densidad Tiempo-Dependiente (TDDFT) nos ha permitido estudiar en detalle como los electrones de dichos materiales se comportan cuando son sometidos a un campo eléctrico. Las dos teorías $ab\ initio$, DFT y TDDFT han crecido en popularidad debido a la mayor potencia de los ordenadores y su favorable complejidad computacional, es decir, a que el coste computacional aumenta siguiendo potencias de exponentes relativamente bajos del número de átomo en el sistema.

En este proyecto hemos empleado el método y código DFT SIESTA (Spanish Initiative for Electronic Simulations with Thousands of Atoms). SIESTA es un método y código DFT de licencia GPL que se empezó a desarrollar en los años noventa y que todavía tiene una comunidad de desarrolladores que siguen ampliando y mejorando el código. Con SIESTA hemos calculado las propiedades electrónicas de estado del estado de base de los sistemas. Estas propiedades incluyen las curvas de dispersión energía-momento, las energías de los niveles electrónicos, la energía total, la densidad electrónica, la geometría de equilibrio, etc.

La propiedades ópticas que han sido el objeto principal de esta investigación han sido calculadas y estudiadas por medio del código MBPT-LCAO (Many Body Perturbation Theory with Linear Combination Atomic Orbitals), un código que todavía no se distribuye al público en general y que está en desarrollo, siendo su principal desarrollador el Dr. Peter Koval. A pesar de que el código MBPT-LCAO está diseñado para trabajar en conjunto con SIESTA, es decir que los ficheros de salida de un cálculo DFT de SIESTA son leídos por MBPT-LCAO como ficheros de entrada para el cálculo TDDFT, es posible usarlo por separado. El código, por medio de la teoría de pertubaciones de muchos-cuerpos y TDDFT, permite calcular el gap de energía, las energías de excitaciones, la densidad inducida, el potencial eléctrico inducido, la corriente inducida, etc.

Específicamente, en este trabajo me he centrado en el cálculo y estudio de la polarizabilidad, de la sección óptica, de la densidad electrónica inducida y de la corriente inducida, para sistemas finitos y moléculas. En esta tesis el código MBPT-LCAO ha sido utilizado para calcular sistemas que contienen más de mil átomos.

A continuación expongo el resumen de las diferentes partes que componen esta tesis.

En la introducción de esta tesis se hace un resumen del trabajo realizado.

En el capítulo uno se revisa la teoría relativa al DFT y TDDFT, donde se exponen las ideas fundamentales de las teorías y se introducen y deducen las ecuaciones usadas para calcular las propiedades de interés. En la parte relacionada con la DFT se introduce el concepto de que la densidad electrónica determina completamente las propiedades del estado fundamental de cualquier sistema electrónico, así como las ecuacioned Kohn-Sham (KS) que nos permiten estudiar las propiedades electrónicas de sistemas con muchos electrones. En el apartado de TDDFT se presenta la función de respuesta lineal y su relación con la polarizabilidad, la cual nos da información sobre como el sistema físico interactúa y responde a una perturbación eléctrica.

En el capítulo dos se presenta una visión en conjunto de los dos códigos. En una primera parte se describe el código SIESTA enseñando unos ejemplos de fichero de entrada para hacer los cálculos.

Después el código TFDDT MBPT-LCAO es analizado, en este caso nos centramos en las características técnicas que permiten obtener una alta eficiencia computacional. Además se describen los métodos de cálculo de la función de respuesta lineal usados para calcular las propiedades ópticas. La función de respuesta lineal puede ser calculada en el código a través de un proceso iterativo o siguiendo el método de Casida. Al mismo tiempo, el código incluye algoritmos eficientes que permiten la generación de una base auxiliar para expandir los productos de orbitales atómico y el cálculo de la respuesta lineal para partículas no interactuantes por medio de un proceso eficiente.

En el capítulo 3 hemos analizado la propiedades ópticas de nanoláminas de grafeno. Este nuevo material aislado por primera vez en el año 2004 tiene propiedades con potenciales aplicaciones industriales en muchas areas tecnológicas. El principal método utilizado hoy en día para la producción de la monocapa de grafeno es la deposición química en fase vapor (CVD), mientras que la producción de nanoláminas en forma de polvo se realiza con técnicas de exfoliación en fase líquida. Los átomos de carbono en el grafeno forman un retículo hexagonal y es esta particular estructura con su configuración electrónica la que proporciona al grafeno propiedades únicas que inclyuen alta movilidad electrónica, alta flexibilidad, alta transparencia, excelentes propiedades mecánicas, buena conductividad térmica, etc. Es evidente que este material es muy prometedor y es por esto que se investiga el grafeno en muchos campos tan diversos como en plasmónica, fotónica, electrónica, almacenamiento de energía, electrónica flexible, ingeniería aeroespacial, tratamiento de señales ópticas, etc.

El estudio de las propiedades ópticas que aquí presentamos incluye el análisis de la polarizabilidad, la seción óptica y la densidad inducida. Hemos considerado láminas de grafeno de dimensiones nanométricas (nanolaminas) de forma rectangular y hexagonal. Las nanoláminas hexagonales tienen dos tipos de borde, ZigZag (ZZ) y ArmChair (AC), mientras que las laminas rectangulares tienes los dos tipos de bordes.

Esto nos ha permitido relacionar el comportamiento óptico con la presencia de un tipo u otro de borde. El tamaño lateral de las nanoláminas varía desde un mínimo de $\sim$10 Å ($\sim$40 átomos) hasta un máximo de $\sim$60 Å. Las nanoláminas han sido saturadas con átomos de hidrógeno.

Todos los espectros de polarizabilidad de las nanoláminas de grafeno presentan dos picos principales. Estos dos picos representan los plasmones π y σ, plasmones típicos de los planos infinitos de grafeno. En el capítulo se explica el origen físico de estos picos y se monitoriza su dependencia en relación a las tres geometrías (rectangular, exagonal ZZ

y exagonal AC) y a sus tamaños.

La posicíon principal de los picos π y σ es independiente de la geometría y en consecuencia del tipo de borde que caracteriza la nanolámina. En general, los picos π y σ están sujetos a un corrimiento al rojo amedida que se aumenta el tamaño de las nanoláminas. La posición del los picos para las nanoláminas ZZ $C_{1014}H_{78}$ concuerda con los valores experimentales de Geim et al.,[131] especialmente para el pico que aparece a menor frecuencia, i.e. el plasmon π, el cual se encuentra a 4.8 eV.

En nuestro análisis de la respuesta óptica de las láminas de grafeno hemos investigado también el gap óptico. El gap óptico es definido como la frecuencia a la cual se encuentra la primera resonancia en el espectro óptico. En las laminas rectangulares el gap óptico es cero para láminas uqe contienen más de ~ 30 átomos de carbono. La razón de esta ausencia del gap óptico se ha podido relacionar con la estructura de bandas en nanocintas de grafeno con borde ZZ. La situación es diferente para las láminas hexagonales. El gap óptico para las láminas es finito y disminuye cuando el tamaño de las láminas aumenta. Los resultados demuestran una diminución más rápida del gap con el tamaño en las láminas con bordes ZZ.

Para completar el estudio de las láminas de grafeno analizamos la densidad electrónica inducida en las laminas en tres rangos de energía. Esto nos ayudó una vez más a enfatizar el comportamiento diferente de los tipos de bordes. En particular, para las láminas ZZ en ciertos rangos de energía la densidad electrónica inducida está concentrada en los átomos de borde.

Al final del capítulo 3 investigamos los efectos con diferentes tipos de átomos de borde. Los efectos en el espectro óptico a baja energía fueron analizados substituyendo el hidrógeno con oxígeno, flúor y con el grupo hidroxilo.

En el capítulo 4 describimos la respuesta óptica a baja energía en hidrocarburos aromáticos policíclicos (PAHs) triangulares. Los PAHs están formados de anillos aromáticos de benceno y pueden ser considerados como láminas de grafeno. Estas moléculas pueden ser sintetizadas químicamente y sin defectos, esto hace que los PAHs sean potencialmente atractivos para la fabricación de dispositivos tecnológicos de tamaño nanométrico. Los cálculos mostraron que la adición o sustracción de solamente un electrón en el sistema de los PAHs triangulares con borde AC permitía la aparición de nuevos picos a baja energía en el espectro óptico. Por el contrario, los PAHs triangulares con borde ZZ no mostraron este comportamiento. Esto se debe a los estados degenerados que se encuentran en la energía de Fermi en los sistemas con bordes ZZ. En PAHs triangulares con borde AC el gap finito entre el HOMO y LUMO permite la creación de nuevas transiciones ópticas cuando al sistema se le añade o se le quita uno o más electrones. Para hacer los cálculos necesarios para llevar acabo este estudio tuvimos que incluir la temperatura en los cálculos de TDDFT. De hecho, los picos generados por el doping del sistema son debidos a que los niveles de Kohn-Sham están parcialmente ocupados alrededor de la energía de Fermi.

En el capítulo 5 analizamos la formación de una cavidad plasmónica formada por dos partículas nanométricas icosaédricas de sodio. Cada partícula contiene 380 átomos de sodio. La respuesta óptica es analizada para diferentes distancias entre las partículas. En un primer estudio no consideramos las relaciones estructurales a medida que la distancia entre las partículas cambia. Las resonancias plasmónicas del sistema fueron monitorizadas para cada distancia entre las partículas. La distancia inicial entre las facetas más cercanas de ambas partículas se fijó en 15 Å, a esta distancia las dos partículas no interactúan y se pueden

considerar que están aisladas. Cuando se disminuye la distancia entre las dos partículas empiezan a interactuar. Los efectos son visibles en el espectro óptico. El análisis incluye los efectos de la orientación entre las partículas. Se han considerado tres orientaciones: *face-to-face*, *tip-to-face* y *tip-to-tip*. Además, se estudió la intensidad y localización del campo eléctrico inducido a la energía de la resonancia plasmónica en función del tamaño y la geometría de la cavidad.

El análisis ha mostrado tres resonancias plasmónicas principales: el *Bonding Dipolar Plasmon* (BDP), el *Charge Transfer Plasmon* (CTP) y el *high-energy Charge Transfer Plasmon* (CTP'). La primera (BDP) es el modo de resonancia característico de la partícula aislada renormalizado por la presencia de la otra partícula. Esta resonancia se encuentra en el régimen capacitivo. A medida que se van acercando las partículas, la resonancia BDP sufre un corrimiento al rojo progresivo. Durante este proceso no hay ninguna corriente que fluye desde una partícula a la otra.

Disminuyendo la distancia entre las partículas aún más entramos en el régimen túnel, la resonancia BDP lentamente desaparece y aparecen dos nuevas resonancias, CTP y CTP'. La configuración *face-to-face* muestra una resonancia CTP más marcada, debido a una mayor corriente túnel que fluye entre las dos partículas. Cuando seguimos acercando las partículas la posición de la resonancia CTP sufre un corrimiento al azul. En la frecuencia de resonancia plasmónica BDP, el acoplamiento Coulombiano entre las cargas inducidas en la cavidad produce un campo eléctrico fuerte y localizado. Sin embargo, en el regimen túnel el campo es totalmente apantallado por la corriente que fluye a través de la cavidad plasmónica.

Las simulaciones atomísticas TDDFT realizadas mostraron como el campo plasmónico dentro de la cavidad puede depender de la distancia entre las partículas pero también de la orientación entre las dos partículas, de hecho, para distancias muy pequeñas entre partículas los detalles a nivel átomico de la estructura de la cavidad determinan la intensidad y localización del campo eléctrico de campo cercano.

En el estudio que sigue, explicado en detalle en el capítulo 5 consideramos el mismo sistema compuesto de dos partículas de sodio, pero esta vez permitimos a los átomos del sistema que se reorganicen a la vez que cambiamos la distancia entre las partículas.

En este caso, como distancia de referencia entre las partículas se ha tomado el *Nominal Gap Size* (NGS), que está definido como la distancia entre las caras internas de las dos partículas en el caso de que las partículas no estuviesen relajadas. Empezamos con un valor del NGS de 16 Å y en intervalos de 0.2 Å, empezamos a juntar las partículas, y por cada posición, hacemos un cálculo DFT con SIESTA para optimizar la geometría de la estructura del dímero. Cada partícula se relaja en respuesta a la presencia de la otra. Las estructuras obtenida son muy diferentes cuando se considera la relajación. Las partículas son muy elásticas y se deforman con facilidad. En particular, observamos la inestabilidad del salto a contacto (*jump-to-contact instability*) durante el acercamiento de las partículas. Alrededor de un valor de NGS de 6 Å la atracción entre las partículas es suficiente para que las dos partículas entren en contacto, resultando en un estiramiento de sus estructuras. Seguimos acercando las partículas una a la otra hasta llegar al punto de formar una única gran nanopartícula.

A una distancia de 3.5 Å empezamos el proceso de alejamiento de las partículas. Debido a la plasticidad de las particulas de sodio durante este proceso describimos la formación de un nanocontacto, ya que observamos la formación de un cuello que conecta las dos

partículas. Si seguimos alejando las dos partículas el cuello se vuelve cada vez mas fino hasta llegar a tener una sección monoatómica.

Finalmente, para un valor del NGS de 32 Å las dos partículas se separan por completo.

Durante los proceso de acercamiento y alejamiento monitorizamos la energía total del sistema. En el punto en el cual ocurre el salto a contacto de las partículas, observamos un cambio repentino de la energía que indica la transición entre el régimen capacitivo y el régimen resistivo. Consecuentemente, la respuesta óptica cambia y observamos como el modo BDP desaparece y aparecen los dos modos CTP y CTP'. El salto a contacto elimina el régimen túnel que aparencía en el cálculo sin relajación estructual, siendo un régimen de transición entre el régimen capacitivo y el resistivo.

El régimen resistivo está caracterizado por la presencia de una corriente que fluye entre las dos partículas.

Además, durante el proceso de alejamiento observamos que los saltos en la energía total están relacionados con cambios discontinuos en la geometría del sistema y en particular en el contacto entre las dos partículas. Para llegar a esta conclusión medimos la sección geométrica del cuello que conecta a las partículas. Observamos que la respuesta óptica presenta dicosntinuidades exactamnete en aquellas distancias en las que la sección geométrica del cuello cambia de moso discontinuo. Finalmente, medimos la corriente que circula a través del cuello y conseguimos relacionar los cambios en la estructura atómica con la energía total del sistema, la sección geométrica del cuello, la respuesta óptica y la corriente de electrones calculada. Mostramos que la reorganicación, incluso la de un solo átomo, juega un papel muy importante a la hora de determinar la respuesta óptica del sistema. Nuestro estudio demuestra claramente que la respuesta óptica viene determinada por la posición de cada uno de los átomos que componen el sistema. Esta observación es de particular importancia en el diseño de dispositivos de tamaño subnanométrico. Aunque el análisis fue desarrollado para partículas de sodio esperamos un comportamiento muy similar en otros metales como el oro que puedan ser más adecuados para aplicaciones electrónicas.

En el capítulo 6 nos preguntamos si es posible posible definir que es un plasmón en un sistema finito. En sistemas periódicos, los plasmones se definen como las frecuencia a la cuales la función dieléctrica macroscópica es cero. Por otro lado, en sistemas finitos esta misma definición no es posible por lo cual hay que buscar otro modo para definir los plasmones en estos sistema.

En este estudio consideramos un sistema formado por una cadena unidimensional de 20 átomos de sodio. Debido a la simplicidad de este sistema hemos podido hacer diferentes tipos de análisis siguiendo sugerencias encontradas en la literatura, así como proponer nuestro propio criterio para medir el carácter plasmónico de una determinada excitación. Además, este sistema nos ha permitido comparar y contrastar los resultados obtenidos directamente con artículos publicados en la bibliografía.

En este apartado los resultados se obtuvieron usando el método Casida, el cual nos da la posibilidad de obtener información relacionada con las transiciones de Kohn-Sham que contribuyen a una excitación óptica específica. Además, el análisis en el espacio de Fourier de los autovectores de Casida calculados nos ha permitido definir el momento transferido durante la excitación óptica en nuestro sistema finito. Los análisis mostraron la presencia de plasmones típicos de un gas de electrones unidimensional. El análisis de la densidad electrónica de transición en el espacio real ha clarificado la diferencia en la densidad entre una excitación electrón-hueco (e-h) u una transición plasmónica.

Finalmente, para poder identificar plasmones sin la necesidad de hacer un análisis en el espacio de momento definimos un parámetro llamado ratio de fuerza restauradora de Coulomb (R_{CRF}). El R_{CRF} calcula, para cada resonacia, el ratio entre la parte de partículas independientes y la parte que depende de la interacción entre los electrones de la matriz de Casida. Nuestros cálculos muestran como el R_{CRF} sirve para determinar de forma eficaz aquellas resonancias con un marcado carácter plasmónico, que habían sido identificadas previamente mediante el análisis delmomento transferido.

Finalmente, en el capítulo 7 resumimos los resultados más importantes obtenidos en este trabajo de tesis doctoral.